POLYPUBLIE
Polytechnique Montréal

POLYTECHNIQUE MONTRÉAL
UNIVERSITÉ D'INGÉNIERIE

Titre: Title: Lift Alteration at Low Angle of Attack Using Plasma Actuation

Auteur: Author: Xin Gu

Date: 2017

Type: Mémoire ou thèse / Dissertation or Thesis

Référence: Citation: Gu, X. (2017). Lift Alteration at Low Angle of Attack Using Plasma Actuation [Ph.D. thesis, École Polytechnique de Montréal]. PolyPublie. https://publications.polymtl.ca/2920/

Document en libre accès dans PolyPublie
Open Access document in PolyPublie

URL de PolyPublie: PolyPublie URL: https://publications.polymtl.ca/2920/

Directeurs de recherche: Advisors: Huu Duc Vo, Éric Laurendeau, & Njuki W. Mureithi

Programme: Program: Génie mécanique

Ce fichier a été téléchargé à partir de PolyPublie, le dépôt institutionnel de Polytechnique Montréal
This file has been downloaded from PolyPublie, the institutional repository of Polytechnique Montréal

https://publications.polymtl.ca

UNIVERSITÉ DE MONTRÉAL

LIFT ALTERATION AT LOW ANGLE OF ATTACK USING PLASMA ACTUATION

XIN GU
DÉPARTEMENT DE GÉNIE MÉCANIQUE
ÉCOLE POLYTECHNIQUE DE MONTRÉAL

THÈSE PRÉSENTÉE EN VUE DE L'OBTENTION
DU DIPLÔME DE PHILOSOPHIAE DOCTOR
(GÉNIE MÉCANIQUE)
DÉCEMBRE 2017

© Xin Gu, 2017.

UNIVERSITÉ DE MONTRÉAL

ÉCOLE POLYTECHNIQUE DE MONTRÉAL

Cette thèse intitulée :

LIFT ALTERATION AT LOW ANGLE OF ATTACK USING PLASMA ACTUATION

présentée par: GU Xin
en vue de l'obtention du diplôme de : Philosophiae Doctor
a été dûment acceptée par le jury d'examen constitué de :

M. TRÉPANIER Jean-Yves, Ph. D, président
M. VO Huu Duc, Ph. D., membre et directeur de recherche
M. MUREITHI Njuki, Ph. D., membre et codirecteur de recherche
M. LAURENDEAU Éric, Ph. D., membre et codirecteur de recherche
M. KAHAWITA René, Ph. D., membre
M. ASGHAR Asad, Ph. D., membre externe

DEDICATION

To my Mother and Father

ACKNOWLEDGEMENTS

The work reported in this thesis was sponsored by Bombardier Aerospace, the Consortium de recherche et d'innovation en aérospatiale au Québec (CRIAQ), and the Natural Sciences and Engineering Research Council (NSERC). Their generous financial support is greatly appreciated.

I would like to thank Professors Huu Duc Vo, Njuki Mureithi, and Eric Laurendeau. Professor Vo gave me much theoretical and technical guidance and support, which helped advance this project as well as enriching my academic knowledge and improving my technical skills. Professor Mureithi provided advice on the experimental setup, instruments especially PIV and data analysis. Professor Laurendeau's industrial insight and expertise in numerical simulation helped me select proper wing geometries and resolve many numerical issues.

I would like to thank the engineers from Bombardier Aerospace, especially Dr. Patrick D Germain, Dr. Reza Sadri for their insightful comments and advices during progress reviews.

I would also like to thank Francis Demers for his help in CFD mesh generation, CATIA design and plasma implementation. I am grateful for many discussions with Xiaofei Xu. I am very pleased to acknowledge the assistance during wind tunnel test from Michaël Joubarne, Javad Hosseini, Fariba Ajalli, Xinlin Li, Andy Bai and Nicolas Wang. I got a lot of help from people in Polytechnique Montreal and am very grateful to Petro Junior Milan, Richard Nguyen, Hassen Denmark, Stephen Olala, Professor Jerome Vetel and Eddy Petro. I would also like to thank Mr. Jean Potvin of École Nationale d'Aérotechnique for his generous help and support during wind tunnel testing.

Last but not least, special thanks for my mother, father and brother, for their continuous encourage, support and love.

RÉSUMÉ

Les surfaces de contrôle des avions traditionnels comprennent les volets, les becs, les ailerons, le plan horizontal et les systèmes mécaniques/pneumatiques associés, ce qui contribue grandement au poids total et à la consommation de carburant des avions. Diverses techniques de contrôle de l'écoulement ont été proposées et étudiées pour remplacer les surfaces de commande de vol traditionnelles, tel que les jets synthétiques et les actionneurs Micro Electro Mechanical Systems. L'actionneur plasma de type décharge par barrière diélectrique (DBD) est une alternative relativement récente qui est potentiellement plus efficace et robuste. Cet actionneur convertit l'électricité directement en quantité de mouvement de l'écoulement près de la surface via une ionisation partielle de l'air. L'actionneur à plasma est simple, facile à intégrer, non intrusif (protrusion faible à nulle) et a un temps de réponse rapide, ce qui le rend idéal pour les applications aérodynamiques.

Le présent travail est une étude avancée de deux nouveaux concepts d'actionnement plasma pour augmenter la portance des ailes à faible angle d'attaque pour la commande de vol sans surfaces mobiles. Le premier est le *plasma Gurney flap*, qui consiste en deux actionneurs plasma placés dans le sens de l'envergure des deux côtés de l'aile près du bord de fuite pour augmenter la courbure des lignes de courant dans la région du bord de fuite. Le second est le *plasma wing tip actuation* pour lequel des actionneurs plasma sont placés le long de la corde dans la région du bout de l'ail pour bout de l'ail pour affecter le tourbillon marginal. Des évaluations individuelles antérieures des deux concepts avaient été faites avec des simulations numériques préliminaires et/ou des tests en soufflerie avec des ailes 2D de conception improvisée de profil asymétrique opérant à de très basse vitesses et angle d'incidence nulle. Les objectifs de ce projet de recherche sont l'évaluation de ces concepts pour des ailes à profils asymétrique et symétrique (pour les plan horizontal) ainsi que leur fonctionnement pour un angle d'incidence non-null et pour des ailes effilées et en flèche, et la prédiction du niveau de force d'actionnement requise pour des ailes et les plan horizontal de forme et taille réalistes dans les conditions d'opération d'un avion de ligne haut-subsonique typique. La méthodologie consiste à monter et faire les tests en soufflerie avec des mesures plus détaillées sur des ailes 2D bien conçues ayant des profils asymétrique et symétrique pour valider des outils de simulations numériques, qui seront ensuite utilisés pour évaluer les concepts pour des ailes 3D et à des conditions d'opération d'avions réels.

Des essais en soufflerie ont été effectués pour des ailes d'essai avec à des angles d'incidence de 0° et 3°, des vitesses de 8 à 20 m/s, donnant un nombre de Reynolds allant de $1{,}33 \times 10^5$ à $3{,}33 \times 10^5$, avec une force d'actionnement de 65 à 100 mN/m. Les paramètres mesurés incluaient le moment de portance, la distribution de pression sur la surface de l'aile et le champ de vecteurs de vitesse (obtenu par la technique PIV) . En parallèle, des simulations CFD ont été réalisées avec ANSYS FLUENT utilisant les modèles de turbulence Sparlart-Allmaras (SA) et Shear Stress Transportation (SST) et un modèle d'actionneur plasma.

Les résultats montrent que les deux concepts d'actionnement plasma peuvent augmenter la portance pour les ailes avec des profils asymétrique et symétrique. Bien que *plasma Gurney flap* donne une meilleure augmentation de portance, son efficacité diminue à plus grande angle d'incidence alors que celle du *plasma wing tip actuation* reste à peu près le même. Les modèles de turbulence SST et SA donnent des prédictions similaires pour le deux concepts d'actionnement plasma, mais les prédictions du SST sont un peu plus proches des données expérimentales. Les résultats ont aussi validé les mécanismes d'augmentation de portance des deux concepts.

Les simulations CFD sur des ailes 3D montrent que le *plasma Gurney flap* donnent de meilleures performances sur les ailes effilées et balayées en raison de la réduction de la composante de vitesse de l'actionneur normale à l'actionneur plasma. Finalement, les simulations pour une aile et un plan horizontal de géométrie et échelle réalistes à des conditions de vols réelles indiquent que pour remplacer les surfaces de commande de vol traditionnelles, les actionneurs plasma doivent avoir une force d'actionnement effective de l'ordre de 25 à 70 N/m aux conditions de croisière haute-subsonique et d'environ 100 N/m aux conditions d'atterrissage et de décollage. Cependant, à force d'actionnement équivalente, le *plasma wing tip actuation* n'apporte pas de contribution signifiante à l'augmentation de la portance.

ABSTRACT

Traditional aircraft control surfaces consist of flaps, slats, ailerons, tail planes, and associated mechanical/pneumatic systems, which greatly contribute to the total weight and fuel consumption of airplanes. Various flow control devices have been proposed and studied to replace traditional flight control surfaces, such as synthetic jets and Micro Electro Mechanical Systems actuators. The recently developed dielectric barrier discharge (DBD) plasma actuator is potentially a more effective and robust alternative. The DBD plasma actuator converts electricity directly into flow momentum near the surface through partial ionization of air. The plasma actuator is simple, easy to integrate, non-intrusive (low to zero protrusion) and has a fast response time, which makes it ideal for aerodynamic applications.

The present work greatly advances the study of two novel plasma actuation concepts for lift enhancement of wings at low angle of attack for flight control without movable surfaces. The first is the plasma Gurney flap which consists of two spanwise DBD actuators placed on both sides of the wing near the trailing edge to change the flow curvature in the trailing edge region. The second is plasma wing tip actuation, in which chordwise DBD actuators are placed in the wing tip region to alter the wing tip vortex. Prior individual assessments of each concept had been carried out with preliminary CFD simulations and/or wind experiments using roughly built 2D extruded wings with an asymmetrical airfoil at very low speed and zero angle of attack. The objectives of this research are to assess these concepts for wings with both asymmetrical as well as symmetrical profiles (for use as tail planes); evaluate their effectiveness at a non-zero angle of attack and for tapered and swept wings; and predict the actuation requirements for full-scale realistic wings and tail planes under operating conditions of a typical high-subsonic commercial airliner.

The methodology consists of setting up and carrying out more detailed wind tunnel experiments on well-designed 2D extruded wings with asymmetrical and symmetrical profiles to validate numerical tools, which are then used to assess the concepts for 3D wing geometries and at real aircraft operating conditions.

Wind tunnel tests were carried out for test wings at 0° and 3° angle of attack, velocity from 8 to 20 m/s, Reynolds numbers ranging from 1.33×10^5 to 3.33×10^5, equipped with plasma actuators operating at actuation strength ranging from 55 to 90 mN/m. The measured parameters include lift moment, surface pressure distribution and velocity vector field (through PIV). In parallel, CFD

simulations were carried out with ANSYS FLUENT using Sparlart-Allmaras (SA) and Shear Stress Transportation (SST) turbulence models and an engineering plasma actuator model. The results also validate the mechanisms behind the increase in lift by the two plasma actuation concepts.

The results showed that both plasma actuation concepts can increase lift for wings with asymmetrical and symmetrical profiles with the plasma Gurney flap providing much higher lift increase than the plasma wing tip actuation. However, the plasma Gurney flap effectiveness decreases at higher angle of attack while that of the wing tip plasma actuator remains about the same. The SST and SA turbulence models give similar predictions for the two plasma actuation concepts, with SST providing a slightly closer match with test data. CFD simulations on 3D wings show that the plasma Gurney flap has better performance on tapered and swept wings because of the reduction of velocity component normal to plasma actuator. Finally, CFD simulations for realistic wing and tail plane geometries at real fight conditions indicate that an effective plasma actuation strength required for the plasma Gurney flap to replace the flight control surfaces would be on the order of 25 – 70 N/m at high subsonic cruise conditions, and about 100 N/m at landing/takeoff conditions. For the same actuation strength, the contribution to lift increase by the plasma wing tip actuation concept is not significant.

TABLE OF CONTENTS

DEDICATION III
ACKNOWLEDGEMENTS IV
RÉSUMÉ V
ABSTRACT VII
TABLE OF CONTENTS IX
LIST OF TABLES XI
LIST OF FIGURES XII
LIST OF SYMBOLS AND ABBREVIATIONS XIX
LIST OF APPENDICES XXI
CHAPTER 1 INTRODUCTION 1
1.1 Background 1
1.2 Lift Alteration Concepts at Low Angle of Attack 3
1.3 Objectives 5
1.4 Thesis Outline 6
CHAPTER 2 LITERATURE REVIEW 7
2.1 Streamline Curvature Technique 7
2.2 Tip Vortex Management 16
2.3 Plasma Actuation for In-Flight Application 29
2.4 Plasma Model 31
CHAPTER 3 METHODOLOGY 34
3.1 General Approach 34
3.2 Experimental Study 35
3.2.1 Wind Tunnel 35
3.2.2 Wings 37
3.2.3 Plasma Actuators 41
3.2.4 Endplates 45
3.2.5 Force Measurements 48
3.2.6 Pressure Measurements 49
3.2.7 PIV Setup 50
3.2.8 LabVIEW Program 51

3.2.9 Data Reduction 52
3.3 Numerical Study 54
3.3.1 Test Wing Simulations 59
3.3.2 Tapered & Swept Wing Simulations 63
3.3.3 Realistic Wing Simulations 64
CHAPTER 4 EXPERIMENTAL & CFD RESULTS 67
4.1 Wings without Actuation 67
4.2 Wings with Plasma Gurney Flap 73
4.2.1 Asymmetrical Wing (AG) 73
4.2.2 Symmetrical Wing (NG) 79
4.3 Wings with Plasma Wing Tip Actuation 83
4.3.1 Asymmetrical Wing (AT) 83
4.3.2 Symmetrical Wing (NT) 89
4.4 Discussion 92
CHAPTER 5 CFD STUDY ON REAL WING GEOMETRIES AND REAL FLIGHT CONDITIONS 95
5.1 Performance of Plasma Gurney Flap on Tapered & Swept Wings 95
5.2 CFD Tool Assessment at High Speed 97
5.3 Assessment of Plasma Actuation Concepts for Full-scale Aircraft 101
5.4 Discussion 116
CHAPTER 6 CONCLUSION AND RECOMMENDATIONS 118
BIBLIOGRAPHY 120
APPENDICES 128

LIST OF TABLES

Table 3-1 Solver settings in FLUENT 56
Table 5-1 Comparison of CFD simulation with data from literatures 101

LIST OF FIGURES

Figure 1-1 Dielectric barrier discharge plasma actuator [6] 2
Figure 1-2 Plasma Gurney flap concept [12] 4
Figure 1-3 Plasma wing tip actuation concept [6] 5
Figure 2-1 Source of lift and lift alteration through streamline curvature change 7
Figure 2-2 Coanda circulation control at trailing edge (a) streamlines (b) section lift coefficients [14] 8
Figure 2-3 Schematic of wings with trailing edge suction [16] 9
Figure 2-4 A schematic of ZNMF jet [17] 9
Figure 2-5 Virtual aero-shaping airfoil model with a ZNMF jet [3] 10
Figure 2-6 UAV model upper surface geometry with sensors and synthetic jets [20] 11
Figure 2-7 (a) Streamlines from LDA measurement with Gurney flap (b) corresponding C_L vs α measurements [23] 11
Figure 2-8 Gurney flap near main-element trailing edge of two-element airfoil [26] 13
Figure 2-9 C_l vs α of vertical trailing edge plasma Gurney flap on NACA0012 airfoil [40] 14
Figure 2-10 (a) NACA0012 with Gurney flap and plasma actuator; (b) corresponding C_l vs α measurements [42] 15
Figure 2-11 Measured velocity vectors at trailing edge of NACA4424 with plasma Gurney flap with background velocity deducted [12] 15
Figure 2-12 Plasma Gurney flap from Feng [43] 16
Figure 2-13 Perspective view of the velocity from experiment and simulation [44] 17
Figure 2-14 Effect of tip vortex induced downwash on angle of attack and drag [45] 17
Figure 2-15 General shapes of four typical wing tip extensions [46] 18
Figure 2-16 (a) Typical winglet configuration [47] and (b) the flow and force near the wing tip[48] 19
Figure 2-17 A general layout of the Whitcomb winglet [49] 19
Figure 2-18 A wing model (a) and the relative lift increase by wing tip blowing (b) [55] 21
Figure 2-19 Blowing configurations tested for a square tip (a) and a rounded tip (b) [56] 21
Figure 2-20 Wing with pulse jet and vortex center position with varying flow rate [57] 22
Figure 2-21 Wing model and the suction holes [58] 22
Figure 2-22 Wing model and wind tunnel set up [60] 23

Figure 2-23 (a) Combined dual synthetic jet and (b) its effect on tip vortex footprint of a NACA0015 wing suction side [61] 24
Figure 2-24 Wing geometry and plasma actuator locations [6] 25
Figure 2-25 Vorticity contours downstream of trailing edge without and with plasma [6] 26
Figure 2-26 Wing tip plasma actuator configurations and experimental results [64] 26
Figure 2-27 Force coefficients as a function of wing tip plasma actuator induced velocity [65] 27
Figure 2-28 Schematic of the DBD plasma actuator arrangements (left) and the effect on trailing edge downstream tip vortex vorticity (right) [66] 28
Figure 2-29 Schematic of wing tip plasma actuators [67] 28
Figure 2-30 High speed influence on the relative plasma actuator performance and corresponding drop as a function of scaling number *K* [69] 30
Figure 2-31 Wind tunnel layout (a) and experimental setup [70] 31
Figure 2-32 A multi-network model for a DBD plasma actuator [73] 32
Figure 2-33 Time average spatial distribution of the force from plasma actuator [74] 33
Figure 3-1 Top and side elevation view of closed-loop wind tunnel 36
Figure 3-2 Wind tunnel test section 36
Figure 3-3 Airfoil profiles (a) Aerospatiale-A (b) NACA 0012 37
Figure 3-4 Design of Aerospatiale-A extruded wing for plasma Gurney flap (AG) 38
Figure 3-5 Design of NACA 0012 extruded wing for plasma Gurney flap (NG) 38
Figure 3-6 Design of Aerospatiale-A wing for wing tip plasma actuator (AT) 39
Figure 3-7 Design of NACA 0012 wing for wing tip plasma actuator (NT) 39
Figure 3-8 Assembled Aerospatiale-A wing with plasma Gurney flap (AG) 40
Figure 3-9 Assembled Aerospatiale-A wing with wing tip plasma actuators (AT) 40
Figure 3-10 Schematic of plasma actuators 41
Figure 3-11 Negative saw tooth input signal for plasma actuator electrodes 42
Figure 3-12 Positions of plasma Gurney flap for the NG and AG wings 43
Figure 3-13 Geometrical layout of plasma Gurney flap on the suction side 43
Figure 3-14 Geometrical layout of plasma wing tip actuators (left: top view; right: cross section view from upstream) 44
Figure 3-15 Plasma distribution for wing tip plasma actuators 45
Figure 3-16 Characterisation of plasma actuators 45

Figure 3-17 Wing models with endplates 46
Figure 3-18 Test model and L-shaped force balance 47
Figure 3-19 Angle of attack measurement for test model 47
Figure 3-20 Schematic and picture of L-shaped force balance 49
Figure 3-21 Calibration setup for L-shaped force balance 49
Figure 3-22 Schematic of PIV setup for plasma Gurney flap 51
Figure 3-23 Display Panel of LabVIEW Acquisition Program 52
Figure 3-24 PIV averaged vector map from Dynamic Studio 54
Figure 3-25 Computed streamlines from MATLAB 54
Figure 3-26 Instantaneous vorticity fields for plasma actuator in quiescent air from (a) measured PIV and (b) CFD [77] 56
Figure 3-27 Body force implementation for the AG wing 57
Figure 3-28 Body force implementation for AT wing 58
Figure 3-29 Plasma body force distribution of AG wing 58
Figure 3-30 Plasma body force distribution of AT wing 58
Figure 3-31 Schematic of fluid domain 59
Figure 3-32 Flow domain and boundary conditions for wind tunnel simulations 59
Figure 3-33 Mesh topology for wings in wind tunnel 60
Figure 3-34 Mesh topology and surface mesh of AG wing 60
Figure 3-35 Mesh topology and surface mesh of AT wing 61
Figure 3-36 Cross section mesh (spanwise plane) for AG wing and surface mesh for AT wing 61
Figure 3-37 Lift coefficients of experiments and simulations for NACA0012 with wing tip 62
Figure 3-38 Extruded, tapered and swept wings with plasma Gurney flap 63
Figure 3-39 M6w and M6t wings with two plasma actuation concepts 65
Figure 3-40 Fluid domain and boundary conditions for realistic wing simulations 66
Figure 3-41 Surface mesh for the realistic wing simulations 66
Figure 4-1 Moments comparison of TEST versus CFD for AG wing (AOA = 0°) 67
Figure 4-2 Moments comparison of TEST versus CFD for AT wing (AOA = 0°) 68
Figure 4-3 Pressure distribution of experiments and simulations for AT wing (AOA = 0°) 69
Figure 4-4 Pressure distribution of experiments and simulations for wing NT (AOA = 0°) 70
Figure 4-5 Effect of AOA on lift moments of TEST and CFD for AG wing 71

Figure 4-6 Effect of AOA on lift moments of TEST and CFD for AT wing.....71
Figure 4-7 Pressure distribution of experiments and simulations for AT wing (AOA = 3°).....72
Figure 4-8 Effect of plasma Gurney flap on AG wing at AOA = 0°, F_B =55 mN/m.....73
Figure 4-9 Predicted mid-span pressure distribution of AG wing (8 m/s, AOA = 0°) 74
Figure 4-10 Predicted mid-span pressure distribution of AG wing (15 m/s, AOA = 0°) 74
Figure 4-11 Predicted mid-span pressure distribution of AG wing (20 m/s, AOA = 0°) 75
Figure 4-12 Streamlines near trailing edge of AG wing from CFD and PIV (8 m/s, AOA = 0°) 76
Figure 4-13 Streamlines near trailing edge of AG wing from CFD and PIV (15 m/s, AOA = 0°) 77
Figure 4-14 Streamlines near trailing edge of AG wing from CFD and PIV (20 m/s, AOA = 0°) 77
Figure 4-15 Effect of AOA on plasma Gurney flap for AG wing at 8 m/s, F_B = 55 mN/m 78
Figure 4-16 Streamlines near trailing edge of AG wing at 20 m/s, AOA = 0° and 3°.....78
Figure 4-17 Streamlines near trailing edge of AG wing at 20 m/s without plasma, AOA = 0° & 3° 79
Figure 4-18 Effect of plasma Gurney flap on NG wing at AOA = 0°, F_B = 60 mN/m.....80
Figure 4-19 Mid-span pressure distributions for NG wing (AOA = 0°, F_B = 60 mN/m) 81
Figure 4-20 Streamlines near trailing edge of NG wing from CFD and PIV (8 m/s, AOA = 0°) 82
Figure 4-21 Streamlines near trailing edge of NG wing from CFD and PIV (12 m/s, AOA = 0°) 82
Figure 4-22 Streamlines near trailing edge of NG wing (15 m/s, AOA = 0°) 83
Figure 4-23 Effect of wing tip actuation on lift moment for wing AT (AOA = 0°, F_B =65 mN/m) 84
Figure 4-24 Effect of wing tip actuation on lift moment for AT wing (AOA = 0°, F_B =90 mN/m) 84
Figure 4-25 Predicted (CFD) spanwise lift change by plasma for AT wing (AOA = 0°, F_B = 65 mN/m) 85
Figure 4-26 Predicted (CFD) contours of wake vorticity one chord downstream for AT wing (AOA = 0°) without (left) and with plasma actuation (right, F_B =65 mN/m).....86
Figure 4-27 Predicted (CFD) local AOA at 0.1chord upstream leading edge of AT wing with and without plasma (AOA = 0°, F_B =65 mN/m) 87

Figure 4-28 Effect of AOA on wing tip actuation effectiveness for AT wing (F_B = 65 mN/m) ..88
Figure 4-29 Predicted (CFD) local AOA at 0.1chord upstream leading edge of AT wing with and without plasma (AOA = 3°, F_B =65 mN/m) 88
Figure 4-30 Effect of wing tip actuation on lift moment for NT wing (AOA = 0°, F_B =80 mN/m) 89
Figure 4-31 Spanwise lift for symmetrical wing with wing tip actuation (AOA = 0°, F_B = 80 mN/m) 90
Figure 4-32 Predicted (CFD) contours of wake vorticity one chord downstream for NT wing (AOA = 0°) without and with plasma actuation (right, F_B =80 mN/m).....91
Figure 4-33 Predicted (CFD) local AOA at 0.1chord upstream leading edge of NT wing without and with plasma (AOA = 0°, F_B =80 mN/m).....92
Figure 4-34 Comparison of lift increase by plasma Gurney flap with existing data 94
Figure 4-35 Comparison of moment increase by wing tip plasma actuators with existing data...94
Figure 5-1 Effect of 3D wing geometry on plasma Gurney flap effectiveness (20 m/s, AOA = 0°, F_B= 100 mN/m).....95
Figure 5-2 Velocity triangles at trailing edges of extruded, tapered and swept wings 96
Figure 5-3 Effect of velocity on lift for AT wing with and without plasma Gurney flap.....96
Figure 5-4 Predicted streamlines near trailing edges (CFD) of AT, ATtap and ATsw wings at mid-span (20 m/s, AOA = 0°, F_B= 100 mN/m).....97
Figure 5-5 Pressure contour by FLUENT (left) compared with WIND results [84] (right) for M6 wing (Mach = 0.84, AOA = 3.06°, Re = 1.172×10^7).....98
Figure 5-6 Pressure distributions of FLUENT, WIND, and experiment at 20% span for wing M6 (Mach = 0.84, AOA = 3.06°, Re = 1.172×10^7).....99
Figure 5-7 Pressure distributions of FLUENT, WIND, and experiment at 65% span for wing M6 (Mach = 0.84, AOA = 3.06°, Re = 1.172×10^7).....99
Figure 5-8 Pressure distributions of FLUENT, WIND, and experiment at 80% span for wing M6 (Mach = 0.84, AOA = 3.06°, Re = 1.172×10^7).....100
Figure 5-9 Pressure distributions of FLUENT, WIND, and experiment at 99% span for wing M6 (Mach = 0.84, AOA = 3.06°, Re = 1.172×10^7).....100
Figure 5-10 Moment and lift for M6t and M6w wings.....102

Figure 5-11 Moment coefficient increase for M6w wing with plasma Gurney flap (AOA = 3°, Mach = 0.84, Re = 4.94×10^7) 102
Figure 5-12 Pressure contours for M6w wing suction side without (left) and with (right) plasma Gurney flap (AOA = 3°, Mach = 0.84, Re = 4.94×10^7, F_B= 20 N/m) 103
Figure 5-13 Mach number contours for M6w wing mid-span without (left) and with (right) plasma Gurney flap (AOA = 3°, Mach = 0.84, Re = 4.94×10^7, F_B= 20 N/m) 103
Figure 5-14 Pressure distributions for M6w wing with and without plasma Gurney flap at different spanwise positions (AOA = 3°, Mach = 0.84, Re = 4.94×10^7, F_B= 20 N/m) 104
Figure 5-15 Middle-span streamlines for M6w wing with and without plasma Gurney flap (AOA = 3°, Mach = 0.84, Re = 4.94×10^7, F_B=5 and 20 N/m) 105
Figure 5-16 Lift coefficient increase for M6t wing with plasma Gurney flap (AOA = 0°, Mach = 0.84, Re = 1.54×10^7) 106
Figure 5-17 Pressure distributions for M6t wing with and without plasma Gurney flap at different spanwise positions (AOA = 0°, Mach = 0.84, Re = 1.54×10^7, F_B =20 N/m) 107
Figure 5-18 Mid-span streamlines for M6t wing with and without plasma Gurney flap (AOA=0°, Mach = 0.84, Re = 1.54×10^7, F_B=5 and 20 N/m) 107
Figure 5-19 One chord downstream of trailing edge vorticity contours for M6w wing with and without plasma wing tip actuation (AOA=3°, Mach = 0.84, Re = 4.94×10^7, F_B=20 and 40 N/m) 109
Figure 5-20 One chord downstream of trailing edge vorticity contours for M6t wing with and without plasma wing tip actuation (AOA=0°, Mach = 0.84, Re = 1.54×10^7, F_B=20 and 40 N/m) 110
Figure 5-21 Local AOA at 0.1 chord upstream leading edge of M6w wing with and without plasma wing tip actuation (AOA = 3°, Mach = 0.84, Re = 4.94×10^7) 111
Figure 5-22 Local AOA at 0.1 chord upstream leading edge of M6t wing with and without plasma wing tip actuation (AOA = 0°, Mach = 0.84, Re = 1.54×10^7) 111
Figure 5-23 Moment coefficient increase for M6w wing with plasma Gurney flap (AOA = 3°, Mach = 0.3, Re = 6.21×10^7) 112
Figure 5-24 Lift coefficient increase for M6t wing with plasma Gurney flap (AOA = 0°, Mach = 0.3, Re = 1.93×10^7) 113

Figure 5-25 Pressure distributions for M6w wing with and without plasma Gurney flap at different spanwise positions (AOA = 3°, Mach = 0.3, Re = 6.21×10^7, F_B=20 N/m) 113
Figure 5-26 Mid-span streamlines for M6w wing with and without plasma Gurney flap (AOA = 3°, Mach = 0.3, Re = 6.21×10^7, F_B=20 N/m).....114
Figure 5-27 Pressure distributions for M6t wing with and without plasma Gurney flap at different spanwise positions (AOA = 0°, Mach = 0.3, Re = 1.93×10^7, F_B=20 N/m) 115
Figure 5-28 One chord downstream of trailing edge vorticity contours for M6w wing with and without plasma wing tip actuation (AOA = 3°, Mach = 0.3, Re = 6.21×10^7).....116
Figure 5-29 One chord downstream of trailing edge vorticity contours for M6t wing with and without plasma wing tip actuation (AOA = 0°, Mach = 0.3, Re = 1.93×10^7).....116

LIST OF SYMBOLS AND ABBREVIATIONS

Symbols

a	force balance ratio
AR	aspect ratio
C_μ	blowing momentum coefficient
C_L	lift coefficient
C_M	moment coefficient
C_p	pressure coefficient
c	wing chord
d	dielectric thickness
E	electric field strength
F_B	plasma actuation strength
f	frequency
RH	relative humidity
L_1	distance from wing root to balance pivot
L_2	distance from scale to balance pivot
M	molar mass
$\dot{m}$	jet mass flow rate
p	pressure
q_c	charge density
q	free stream dynamic pressure
R	universal gas constant
$\overline{\mathrm{R}}$	balance average reading
Re	Reynold number
S	area
T	temperature
U	velocity
V	applied voltage
x	wing chordwise location
μ	ion mobility

ρ	density
v_d	drift velocity of the momentum imparting ions

Subscript

atm	atmosphere
d	dry air
j	jet
N	normal component
s	static
sw	swept wing
t	total
tap	taper wing
v	vapor
∞	free stream

Abbreviations

AOA	angle of attack
AG	extruded Aerospatiale-A wing with plasma Gurney flap
AT	extruded Aerospatiale-A wing with wing tip plasma actuator
CFD	Computational Fluid Dynamics
NG	extruded NACA0012 wing with plasma Gurney flap
NT	extruded NACA0012 wing with wing tip plasma actuator
SA	Spalart-Allmaras
SST	Shear Stress Transportation

LIST OF APPENDICES

APPENDIX A – WIND TUNNEL CHARACTERISATION 128
APPENDIX B – WIND TUNNEL TEST 136
APPENDIX C – PLASMA CHRACTERLISATION 140
APPENDIX D – MESH STUDY 145
APPENDIX E – CFD RESULTS WITH TRANSITION SST MODEL 148
APPENDIX F – PLASMA IMPLEMENTATION 152
APPENDIX G –ESTIMATION OF LIFT/MOMENT REQUIREMENT FOR BOEING 737 .. 154

CHAPTER 1 INTRODUCTION

1.1 Background

The world commercial aircraft market has grown rapidly in recent decades, as a result of expanding trade and travel between different countries and regions. At the same time, as climate change and impending energy shortage become more serious, there is a great demand for a reduction in pollution and fuel consumption associated with aircraft operation, for which weight reduction is a key contributor. The replacement of the traditional lift augmentation and flight control surfaces, namely flaps, slats, ailerons, elevator and rudder, and associated mechanical/pneumatic systems would greatly contribute to weight savings and/or provide additional volume for fuel storage contributing to flight range extension as well as reduction production and operating costs of the aircraft.

Flow control technology using pneumatic actuators to blow the boundary layers over the wing (Coanda effect) [1] or boundary layer suction [2] for lift increase and drag reduction have been tested for several decades. However, the weight and complexity/cost associated with integrating the associated systems (pressurised air/vacuum source, valves and piping) have prevented any significant implementation of these systems in commercial aviation. The integration issues may be resolved with recent electrically driven micro-actuation technology such as synthetic jets [3] which add momentum in the boundary layer with zero net mass addition and MEMS (Micro Electro-Mechanical Systems) actuators such as micro-balloons [4] and micro-flaps [5] for altering surface roughness. However, the robustness of these actuators in a harsh aircraft operating environment and resulting maintenance issues reduce the particular application of this technology.

The aerodynamic plasma actuator is a recent technology which came shortly after the advent of MEMS actuators and is very promising for practical application of flow control technology in aircraft applications. It is a simple solid-state device that allows conversion of electrical energy directly into flow acceleration through partial air ionization. The most common form of this actuator is the DBD (dielectric barrier discharge) actuator. As illustrated in Figure 1-1 [6], a DBD actuator essentially consists of two axially offset electrodes separated by one or multiple layers of dielectric materials. When an AC voltage of several kilovolts and several kilohertz is applied at the electrodes, ionized particles are formed in the air which are then accelerated by the electric field

between the two electrodes. These ions collide with neutral air particles imparting momentum resulting in flow acceleration in the thin layer (on the order of a millimetre thick) of air next to the surface. More details on the physics of DBD plasma actuators can be found in reference [7]. The simplicity and solid-state nature of DBD actuators make them potentially robust with high bandwidth while their thinness and purely electrical nature could make their integration and maintenance potentially much simpler than other actuators. Finally, since the exposed electrode is very thin and can be made flush with the aerodynamic surface, the actuator would not interfere with the flow when not in use.

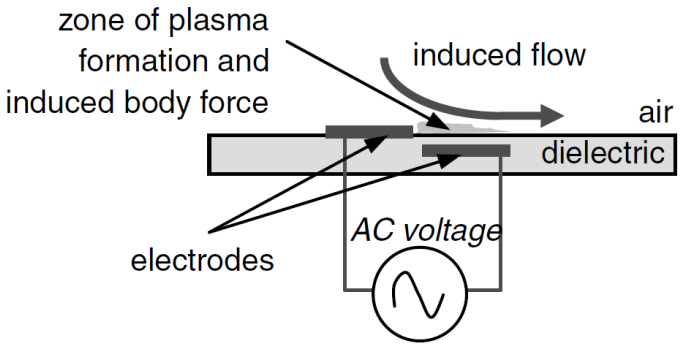

Figure 1-1 Dielectric barrier discharge plasma actuator [6]

The first proposed application for DBD plasma was in fact to suppress boundary layer separation on wing profiles at high angle of attack (AOA) by placing DBD actuators at the leading edge, injecting momentum downstream [8]. This application would allow for the elimination of slats and flaps by allowing the aircraft to take off and land at higher angle of attack. Later suggested applications of DBD plasma actuators consist of controlling boundary layer separations on low pressure turbine's blades [9], delaying boundary layer transition [10] for drag reduction and delaying rotating stall in axial compressors [11]. However, achieving moderate lift change on wings and tail planes with plasma actuators for flight control without movable surfaces (ailerons, rudder and elevators), which is the subject of this research, is more difficult and has been less investigated.

1.2 Lift Alteration Concepts at Low Angle of Attack

Flow control applications aim at placing actuators in strategic environment to have macroscopic effect with limited actuator input power. In this respect, most flow control applications in aeronautics have placed the actuators near boundary layer separation points where small perturbations can have a large impact. This has been particularly true for plasma actuators, for which current achievable strength is still relatively weak, for stall delay in wings at high angle of attack, where the boundary layer on the suction side is close to separation. However, flight control at low angle of attack with plasma actuators present a particular challenge in that the boundary layer is well attached to the wing/empennage surface and thus much less sensitive to the relatively weak flow perturbations from these actuators. For this reason, the first attempt involved implementing a ramp on the wing surface for inducing boundary layer separation which can then be suppressed with a plasma actuator to alter lift. However, this solution is far from desirable as it imposes a nominal drag penalty on the aircraft. Two flow control concepts for altering lift at low angle of attack without nominal performance penalty were later developed and investigated at École Polytechnique de Montréal, and are described below.

The first concept studied by Ueno [12] relies on modifying streamline curvature at the airfoil trailing edge to increase lift. As illustrated in Figure 1-2, this concept consists of placing two spanwise plasma actuators near the trailing edge of an airfoil, one on the suction side adding momentum downstream and the other on the pressure side injecting momentum upstream. This combination effectively curves the flow at the trailing edge in the same manner as a permanently installed Gurney flap for enhancement of lift, but which can be turned on and off as needed. This concept was hence referred to as the plasma Gurney flap. Ueno installed the plasma Gurney flap on a ten-inch chord 2-D extruded wing with a NACA 4424 profile and tested it in a low speed wind tunnel with an incoming flow velocity range of $6 - 16$ m/s for a Reynolds number ranging from 1.2×10^5 to 3.0×10^5. While the actuator strength was not explicitly given, it can be estimated to be around 20 mN/m based on the nature of the dielectric used in the actuator and the actuator input signal suggested. Force measurements and PIV flow visualization were conducted. His results showed that the plasma Gurney flap leads to an increase of 0.02 to 0.18 in lift coefficient and that the final effect is approximately the sum of the effect of each of the two actuators.

The second concept is plasma wing tip actuation, studied by Boesch *et al.* [6]. It consists of placing plasma actuators around the wing tip, as illustrated in Figure 1-3, adding momentum in the

direction opposite that of the tip vortex to diffuse the latter. The tip vortex induces downwash near the wing tip resulting in lift decrease and drag increase for the wing. The reduction of these effects through a more diffused tip vortex increases lift. Conversely, the concept can be applied to a symmetrical airfoil at zero angle of attack (zero nominal lift) such as in the case of aircraft tail planes to induce a tip vortex and generate different lift for yaw and pitch control. CFD simulations were carried out by Boesch *et al.* [6] for a finite six-inch chord 2D wing with a NACA 4418 profile and a rounded wing tip at zero angle of attack in a wind tunnel setting with an incoming velocity of 15 m/s for a Reynolds number of 1.5×10^5. The simulation results showed that the actuators lead to a significant diffusion of the tip vortex downstream of the trailing edge, resulting in a lift increase of up to 20% with maximum 400 mN/m. Preliminary corresponding wind tunnel experiments with suction and pressure side actuators of limited actuation strength (40 mN/m) showed that for lift change versus incoming velocity the experimental results matched the predicted simulations in trend.

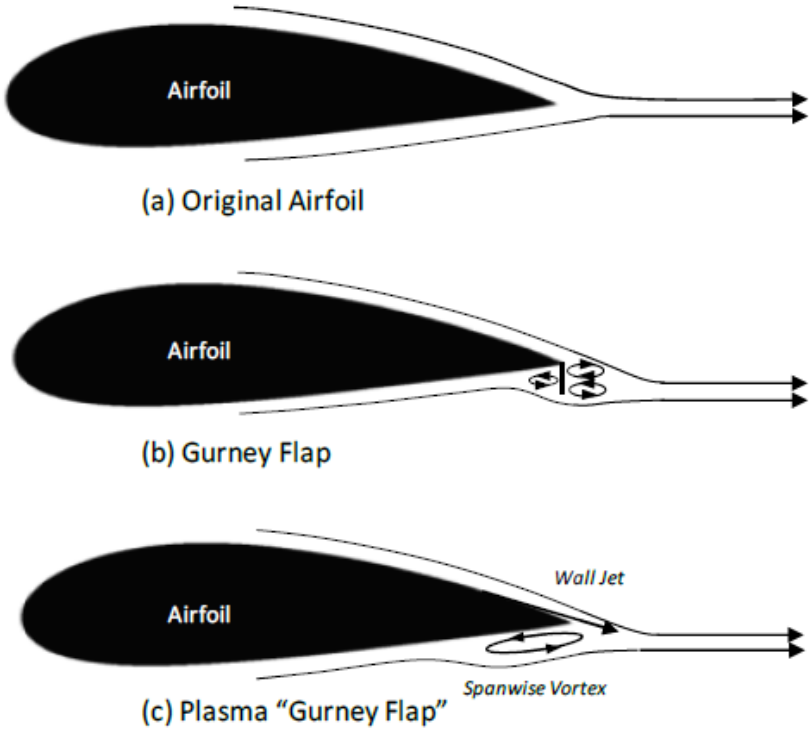

Figure 1-2 Plasma Gurney flap concept [12]

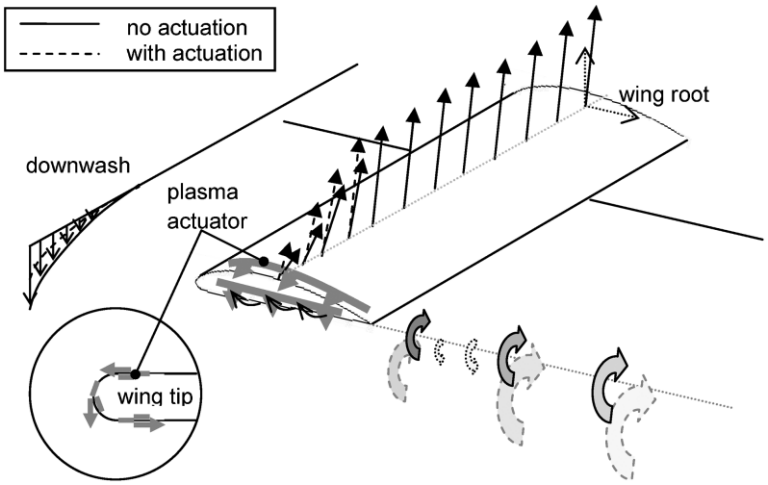

Figure 1-3 Plasma wing tip actuation concept [6]

1.3 Objectives

The previous works on the plasma Gurney flap and plasma wing tip actuation concepts for lift increase at low angle of attack produced promising results [6] [12]. However, these studies were preliminary as the test velocity and Reynolds number were far below realistic aircraft operating conditions. The wing geometries considered were also ideal compared to actual aircraft wings and tail planes operating at non-zero angles of attack. As such, the following research questions need to be addressed for these two concepts to move to the next technology readiness level and eventually into industrial research and development:

- Will these concepts work for zero nominal lift (symmetric) airfoils?
- How does the effectiveness of these concepts change with angle of attack?
- How effective are the plasma Gurney flap and plasma wing tip actuation concepts for more realistic wing geometries (3D tapered swept wings)
- How effective are these concepts for real wing geometries under realistic flight conditions?
- What are the actuation requirements at realistic operating conditions?
- Can these concepts be combined to augment the lift alteration?

To answer these questions, a computational approach combined with wind tunnel experiments is used in this project, to evaluate and assess the effect of these two concepts. Thus, the specific objectives of this project are to:

1) Evaluate the plasma Gurney flap and plasma wing tip actuation concepts for wings with asymmetric and symmetric profiles
2) Assess the effectiveness of these plasma concepts at different angles of attack
3) Assess the effectiveness of these plasma concepts on tapered and swept wings
4) Evaluate the actuation requirements of the two concepts for realistic wings and tail planes of a typical full-scale high subsonic commercial airliner

1.4 Thesis Outline

This thesis is organized as follows: following this introduction, Chapter 2 presents a detailed literature review on lift alteration techniques at low angle of attack, as well as plasma actuation and in-flight application and plasma model. In Chapter 3, the methodology used to attain the above objectives is presented. This is followed by the experimental and CFD results in Chapter 4. In Chapter 5, the validated CFD tools are used to study plasma actuators on realistic wing geometries and realistic in-flight conditions. Finally, Chapter 6 summarizes the conclusions and provides recommendation for future work.

CHAPTER 2 LITERATURE REVIEW

This chapter first provides a brief review of the flow control techniques for lift alteration on wings at low angle of attack. These flow control techniques can be divided into two main categories: streamline curvature control and wing tip vortex management. Then, the plasma actuation for in-flight application and plasma model will be addressed in the end of this chapter.

2.1 Streamline Curvature Technique

Streamline curvature techniques rely on changing the streamline curvature to alter the pressure distribution over the wing. As illustrated in Figure 2-1, lift comes from the larger curvature of streamlines over the top surface of the wing due to air following the latter's shape. A pressure gradient is set up within the flow field to provide the required centripetal force for the fluid particles to turn and follow the required flow path. Since the pressure increases in the direction of curvature and given the fact that the pressure far away from the wing is uniform, the pressure at the upper wing surface with larger streamline curvature must be less than that at the lower wing surface, resulting in lift. Any device that can change the curvature of the flow will alter the lift. This is the principle behind movable flight control surfaces such as ailerons, elevators and rudders.

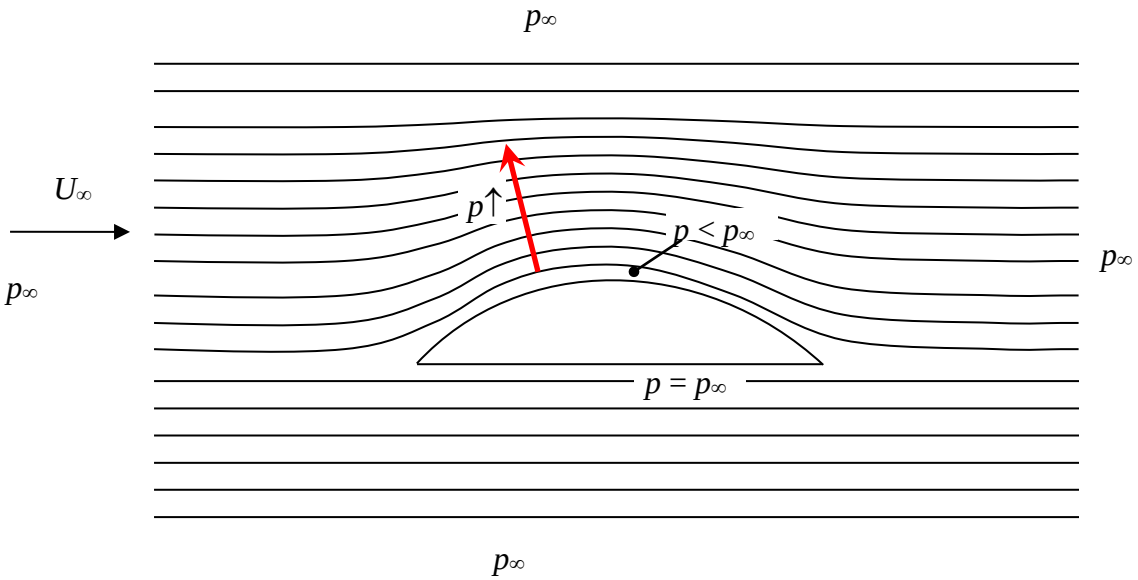

Figure 2-1 Source of lift and lift alteration through streamline curvature change

Several concepts have been developed over the past decades to control lift at low angle of attack through streamline curvature without resorting to movable flight control surfaces. The first is the Coanda jet which is an application of the Coanda effect. The Coanda effect is the tendency of a fluid jet to be attached to a surface, which one can observe from a spinning ping pong ball held in a diagonal stream of air [13]. When applied to airfoils at low angle of attack, a high-speed jet is blown over the suction side near the trailing edge and the jet follows the curved trailing edge surface, as illustrated in Figure 2-2(a). Therefore, the streamlines moving over the wing are bent downwards at the trailing edge, resulting in an increase of lift. Novak *et al.* [14] tested this effect on a 15-inch chord airfoil at zero angle in a flow of 42.50 m/s for a Reynolds number of 1,000,000. They achieved an increase in sectional lift coefficient C_l from 0.5 to 6.8 with a blowing momentum coefficient $C\mu$ from 0 to 0.36 as shown in Figure 2-2(b) ($C\mu=m_jU_j/qS$, where m_j is the jet mass flow rate, U_j is the jet exit velocity, q is free stream dynamic pressure, and S is the model area). However, this technique can introduce noise from the jet and the jet can easily detach from the curved surface, which limits the effectiveness of the concept. Furthermore, the required high-pressure source and pressure cavity built within the wing structure would introduce integration complexity and additional costs.

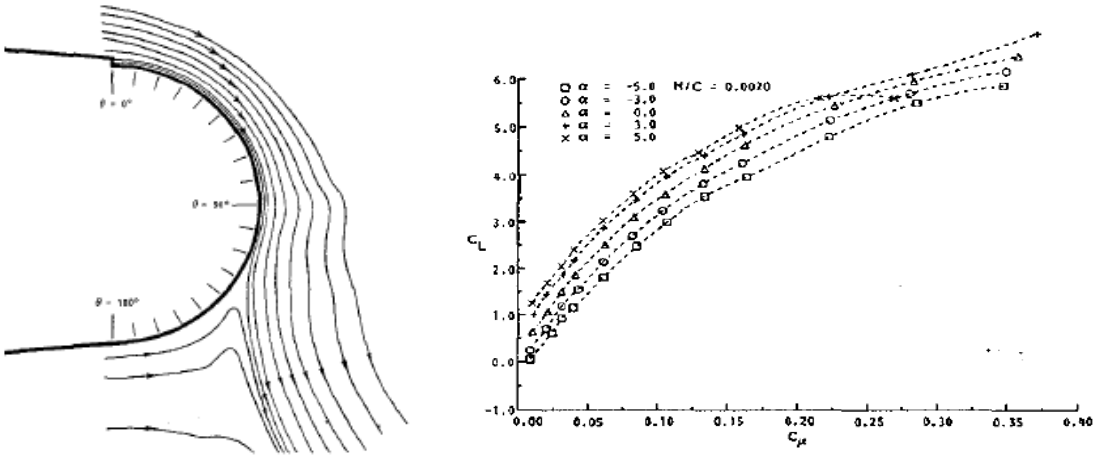

(a) (b)

Figure 2-2 Coanda circulation control at trailing edge (a) streamlines (b) section lift coefficients [14]

Another concept is to modify the apparent local surface curvature and therefore to redirect the external flow. This concept was first developed by Raspet[15] and Hazen *et al.*[16]. Raspet added a suction source with a flow coefficient of 0.0023 on a trailing edge slot covering 65% of the span

of a sailplane. No improvement in the lift/drag ratio was found. By applying trailing edge suction asymmetrically, a rolling behavior was measured which was insufficient for effective lateral control. Hazen *et al*. tested trailing edge suction (shown in Figure 2-3) on a modified eight-inch chord NACA 23015 airfoil and found that lift increased to a limiting values with increasing suction quantity at trailing edge.

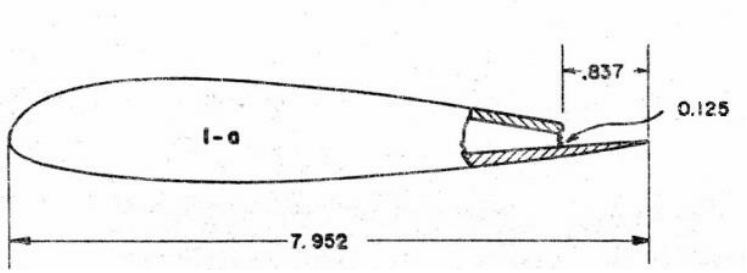

Figure 2-3 Schematic of wings with trailing edge suction [16]

Another technique for generating trapped vortex is the zero-net-mass-flux (ZNMF) or synthetic jet. The ZNMF jet consists of a cavity with an oscillating membrane at one end and an orifice at the other end, as illustrated in Figure 2-4 [17]. In suction mode, the cavity sucks fluid from all direction followed by a blowing mode in which this fluid leaves only in one direction. The result is a directional momentum addition without net mass addition. Chatlynne *et al.* [18] and Amitay *et al.*[19] applied the ZNMF jet to virtually shape the surface of an airfoil and then to reduce pressure drags at low angle of attack with minimum penalty in lift, as shown in Figure 2-5.

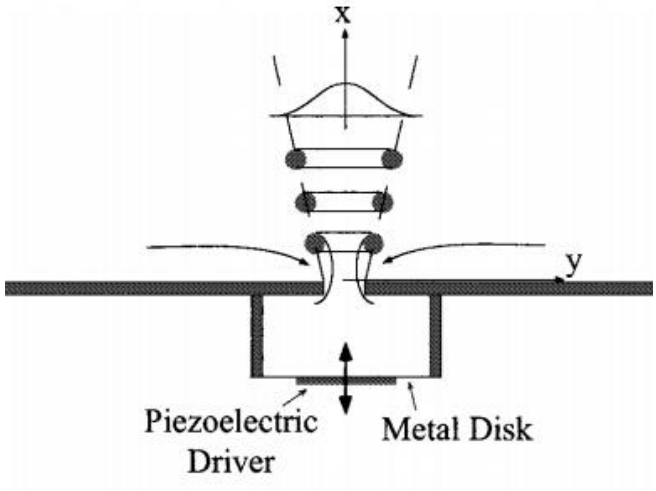

Figure 2-4 A schematic of ZNMF jet [17]

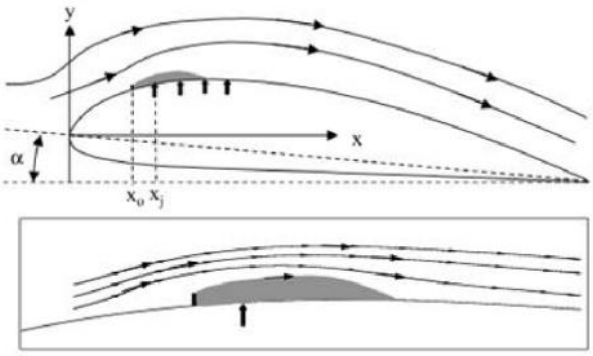

Figure 2-5 Virtual aero-shaping airfoil model with a ZNMF jet [3]

The concept of virtual aero-shaping by ZNMF jets was later applied to a three dimensional wing. Farnsworth *et al*. [20] applied the synthetic jets on a scaled Stingray unmanned aerial vehicle (UAV) in a flow of 30.5 m/s and 25 m/s with a mean aerodynamic chord-based Reynolds number of 185,000. Figure 2-6 illustrates the upper surface geometry of the UAV model with sensors and synthetic jets. The model incorporated twelve pairs of synthetic jets that are issued through rectangular orifices, and the synthetic jets were formed by the periodic motion of a piezoelectric disk mounted on the bottom wall of a sealed cavity. The results showed that the synthetic jets were able to alter the local streamlines on the suction side of wing surfaces and to displace the boundary layer by forming a small quasi-steady interaction region. They obtained a maximum C_L increase of 0.11 with 6 jets turned on at AOA= 2°. However, since the synthetic jet actuators are often very small to achieve high bandwidth as well as ease of integration, they could be subject to clogging in a real aircraft operating environment.

A third strategy for altering lift at low angle of attack is the Gurney Flap. It is a very simple but effective device, which consists of a small flap located at the trailing edge perpendicular to the chord line or pressure surface of an airfoil. Invented by Dan Gurney in early 1970s, this device has been subsequently studied by numerous researchers. Liebeck [21] applied a Gurney flap to a Newman symmetric airfoil and indicated that there was a turning of the flow over the back of the flap and a reverse flow directly behind it. These observations were corroborated in water tunnel experiments at lower Reynolds number by Neuhart and Pendergraft [22].

This flow structure is more precisely shown by Jeffrey *et al.* [23] who carried out laser Doppler anemometry (LDA), surface pressure and force measurements as well as smoke visualization for a single-element wing (Eppler e423 profile) with a Gurney flap, at free stream velocity up to 40 m/s

and at a Reynolds number up to 8.9×10^5. Their results indicated a twin vortex structure downstream of the Gurney flap (see Figure 2-7(a)), with a convex streamline curvature over the trailing edge reducing local pressure on the suction side. In parallel, the flow slowed down with a similar curvature ahead of the Gurney flap near the trailing edge, creating a local pressure rise on the pressure side. The combination of both effects increased the lift and pitching moment. The lift increase was almost proportional to the height of flaps, with maximum lift increase of 71% at AOA=0° and maximum lift increase of 94% at AOA=3°, as shown in Figure 2-7(b).

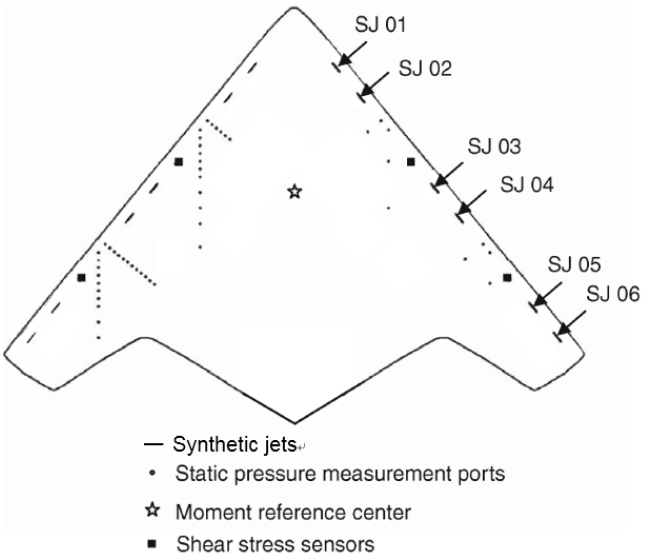

Figure 2-6 UAV model upper surface geometry with sensors and synthetic jets [20]

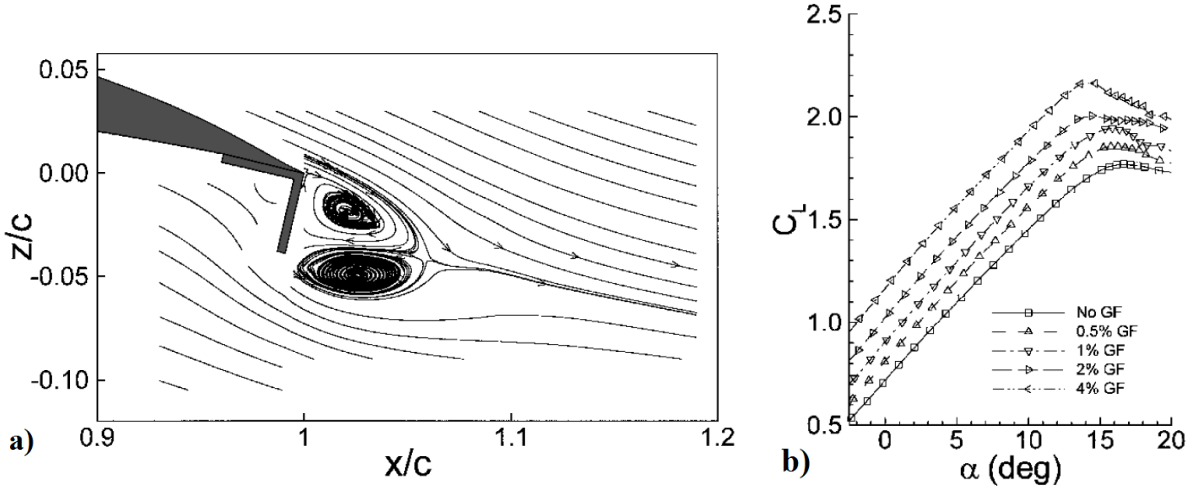

Figure 2-7 (a) Streamlines from LDA measurement with Gurney flap (b) corresponding C_L vs α measurements [23]

Other researchers have also studied the effect of lift and drag of the basic Gurney flap with varying heights, at different angles of attack and at higher Reynolds numbers. Storms *et al.* [24] measured surface pressure distributions and wake profiles on a NACA 4412 with a Gurney flap to obtain lift, drag and pitching moment coefficient. The Gurney flap increased the maximum lift coefficient from 1.49 up to 1.96 (by 32%) and increased the drag at low-to-moderate lift coefficients. Jang *et al.* [25] carried out a numerical study on a similar configuration with an incoming flow Mach number of 0.085 at angles of attack from 0 to 18° and Reynolds number of 1.64×10^6. A maximum lift coefficient increase of 150% was obtained at zero angle of attack with a flap of 3% chord height, but with penalties in drag and moment coefficients. The authors suggested that the height of Gurney flap should be less than 1.25% chord in order to get an increase in lift with little drag increase.

Ross *et al.* [26] studied Gurney flaps with height from 0.125% to 1.25% chord on a two dimensional two-element airfoil NACA 632-215 Mod B with a single slotted, 30%-chord regular flap, as shown in Figure 2-8. The Reynolds number was 3.7×10^6, with a free stream velocity of 69 m/s. Results showed that the maximum lift coefficient could be increased by 12% and maximum lift-to-drag by 40% with a 0.5%-chord flap at 0.5% chord upstream of the trailing edge of main element. Later, Myose *et al.* [27] carried out a detailed study on 2D airfoils, 3D wings, and a reflection plane model. The Reynolds number ranged from 9×10^5 to 2.2×10^6, with an incoming Mach number from 0.12 to 0.19 and an angle of attack ranging from -2 to 20°. For a single-element NACA 0011 airfoil, a Gurney flap of 4%-chord height leaded to an increased zero-angle lift coefficient of 0.8 at $Re=2.2\times10^6$ and Mach=0.13. Results showed that for all of the studied airfoils, Gurney flap can improve the maximum lift coefficient albeit with drag penalties, which is the main disadvantage of the Gurney flap.

Several improvements to the Gurney flap have been proposed. They included serrated [28], segmented [29] and perforated Gurney [30, 31] to mitigate the drag penalty. Some of them can enhance lift (segmented Gurney flap) but some may affect the lift increase as well (perforated Gurney flap). Oscillating Gurney flaps were studied by Tang and Dowekll [32] and Gerontakos and Lee [33] to enhance the maximum lift and pitching-moment coefficients under a wide range of angle of attack. However, the oscillation of flaps required more complex structure, which would be less desirable.

Last but not least, the Gurney flap have also been shown to be effective in other applications, such as rotorcraft blades [34, 35], wind turbines [36, 37] and turbine blades [38, 39].

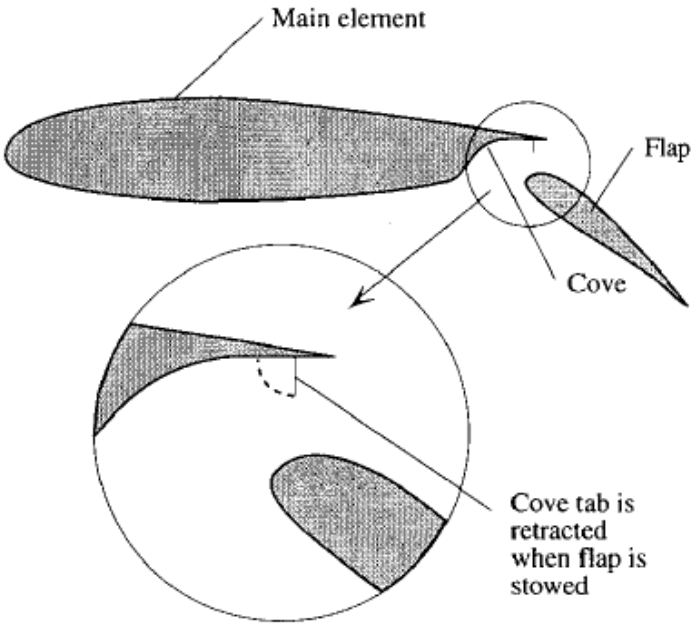

Figure 2-8 Gurney flap near main-element trailing edge of two-element airfoil [26]

With the advent of plasma actuators, several active control concepts have been proposed for lift alteration at low angles of attack. Zhang *et al.* [40] placed plasma actuators on the vertical trailing edge surface of a truncated NACA0012 airfoil in an attempt to replicate the effect of a Gurney flap, as shown in Figure 2-9. Simulations were carried out in ANSYS FLUENT with a phenomenological plasma model from Shyy *et al.* [41] at a free stream velocity of 10 m/s and Reynolds number of 6.84×10^5. The simulation was carried out under two-dimensional steady mode, using SA model. The non-dimensional plasma actuator strength D_c is defined as

$$D_c = \frac{q_c E_0 L}{\rho U_\infty^2} \tag{2.1}$$

where q_c is the charge density, E_0 is the electric field strength, L is the height of electrode, ρ is density and U_∞ is the free stream velocity. In this case, a plasma strength of 9.14 was applied in the simulation. The simulation results showed that the induced jet from plasma actuators resulted in a zero-angle lift coefficient of 0.18. However, the simulated velocity is low and there was no experimental validation of the concept.

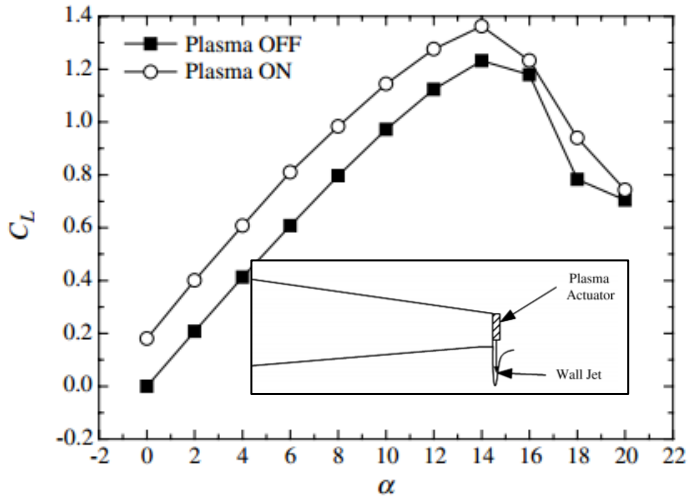

Figure 2-9 C_l vs α of vertical trailing edge plasma Gurney flap on NACA0012 airfoil [40]

Feng *et al.* [42] carried out an experimental study with plasma actuator attached to a physical Gurney flap on NACA 0012, using the flap as the dielectric material, as shown in Figure 2-10(a). The maximum tested velocity and Reynolds number were limited to 5.3 m/s, and 3.5×10^4, respectively. They found that the lift coefficient C_l increased by 0.15 (about 22%) at Re=2.0×10^4 for AOA=0 – 16°, when the actuators was attached to a 7% chord physical Gurney flap (see Figure 2-10(b)).

Ueno [12] developed and tested a new plasma Gurney flap configuration, which avoids the need to truncate the trailing edge as done by Zhang *et al.* [40] which is not aerodynamically desirable as well as limits the width of the DBD actuator that one can fit. As mentioned in Chapter 1, Ueno's configuration consists of two spanwise plasma actuators placed near the trailing edge, one on the suction side inducing the ionic wind downstream and the other on the pressure side inducing upstream ionic wind. Net velocity (velocity minus background velocity) from PIV measurements by Ueno [12] shown in Figure 2-11, indicate that the net effect of trailing edge flow (acceleration of flow over the suction side and deceleration of flow at the pressure side) with this configuration is similar to that of a physical Gurney flap. At tested free stream velocities ranging from 6 m/s to 16 m/s and Reynolds number of 1.2 to 3.0×10^5, this plasma Gurney flap increased the lift coefficient by 0.18 to 0.02 (about 69% to 7%, respectively). Additional tests with each actuator turned on individually indicated that the total effect on lift is the combined effect of each actuator.

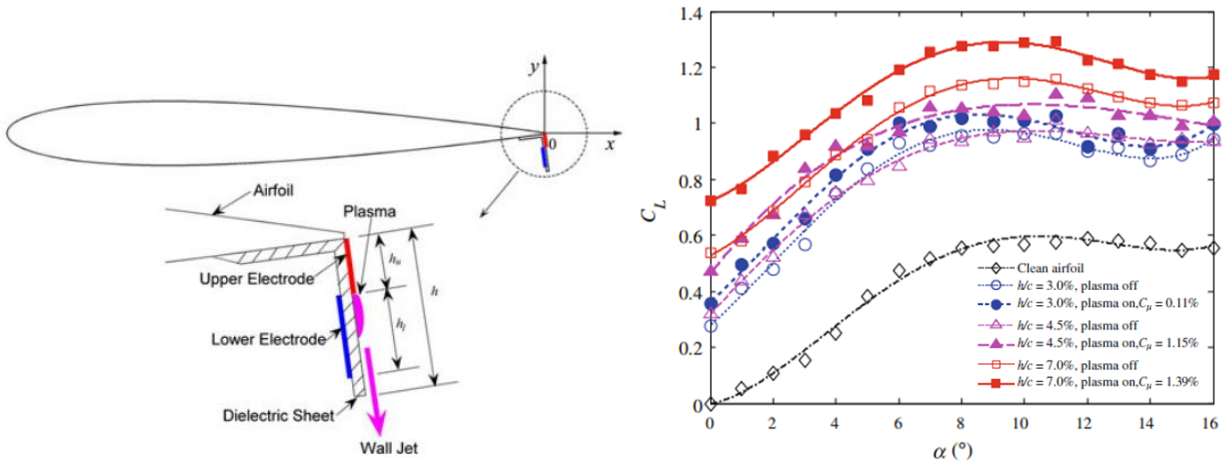

(a) (b)

Figure 2-10 (a) NACA0012 with Gurney flap and plasma actuator; (b) corresponding C_l vs α measurements [42]

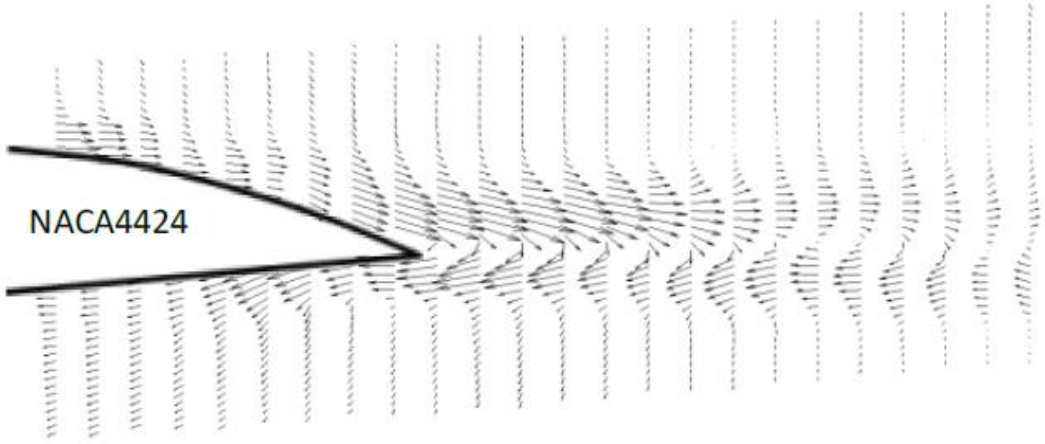

Figure 2-11 Measured velocity vectors at trailing edge of NACA4424 with plasma Gurney flap with background velocity deducted [12]

Recently, Feng [43] proposed a new plasma Gurney flap which consists of two dielectric barrier discharge plasma actuators attached to the airfoil NACA 0012 pressure surface near the trailing edge, as shown in Figure 2-12. 2D numerical study was carried out for NACA 0012 with a chord length of 1 m at background flow speed of 10 m/s and Reynolds number of 6.8×10^5. And it was found that the most significant control effect occurs with only downstream plasma actuators on. The plasma Gurney flap can increase the lift coefficient before the stall, reduce the drag coefficient, and increase the lift-to-drag ratio at small angles of attack. For NACA 0012 airfoil with plasma control, the maximum lift coefficient and the maximum lift-to-drag ratio are increased by about

7.5% and 7.7%, respectively. The plasma Gurney flap have been also simulated on the pressure side of a 3D Unmanned Aerial Vehicle [43], near the trailing edge and along the whole span. The lift coefficient is increased by about 0.09 to 0.12 for the angles of attack from -2 to 16°.

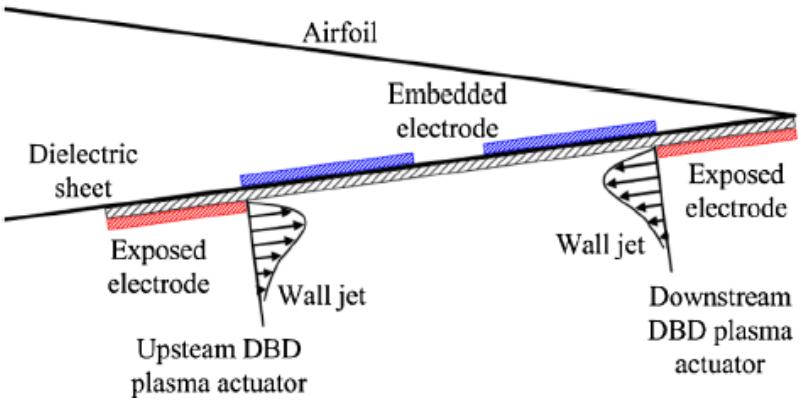

Figure 2-12 Plasma Gurney flap from Feng [43]

In summary, although the streamlines curvature methods for lift increase at low angle of attack show promising results, the mechanical and pneumatic methods all come with some drawbacks that prevent them from being used for practical flight control. Furthermore, apart from the physical Gurney flap[26], none of the proposed concepts have yet been assessed at realistic flight conditions for which the Reynolds number would be on the order of 10^6.

2.2 Tip Vortex Management

The wing tip vortex, also known as trailing edge vortex, is the rotating flow pattern behind a finite wing when generating lift. It comes about as the high pressure air on the pressure side tends toward the lower pressure air on the suction side around the wing tip. Figure 2-13 from Dacles-Mariani *et al.* [44] show the formation and convection of the wing tip vortex through measured and simulated velocity profiles at different axial planes. This vortex induces a downwash that is largest near the wing tip, as shown in Figure 1-3, causing the incoming flow to bend downward, thus reducing the local angle of attack and resulting not only in a lift decrease near the wing tip but also an additional drag, called induced drag, as illustrated in Figure 2-14. These negative effects can be alleviated if the normally concentrated wing tip vortex can be diffused and/or moved further out from the wing tip to reduce the downwash over the outer wing span. A variety of strategies have been developed and studied to achieve these tasks.

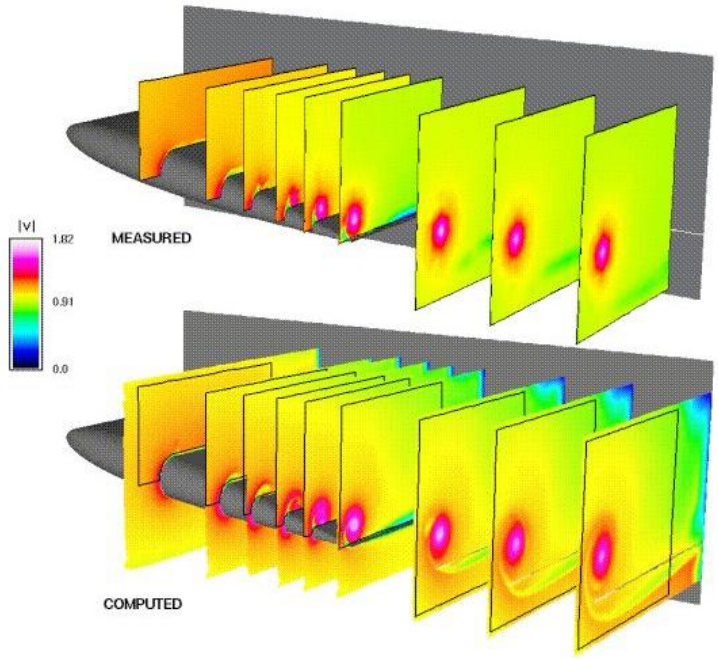

Figure 2-13 Perspective view of the velocity from experiment and simulation [44]

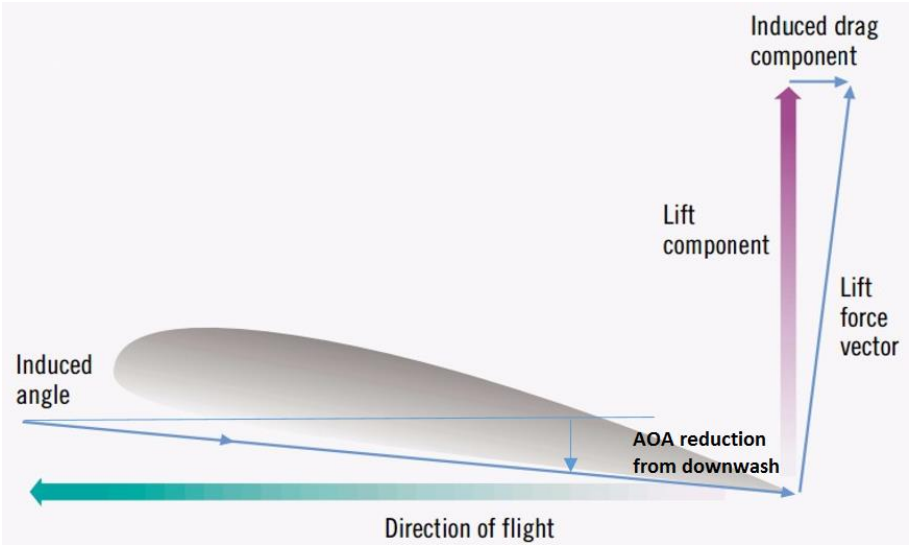

Figure 2-14 Effect of tip vortex induced downwash on angle of attack and drag [45]

One typical strategy is to use wing tip extension to reduce the negative effect of wing tip vortex, mainly by pushing the vortex farther outboard from the wing root, resulting in a reduction of both downwash and lift-induced drag. Various wing tip extensions have been developed [46], including rounded wing tip, spherical wing tip, squared wing tip, booster wing tip, Hoerner wing tip, raked wing tip, endplate, polyhedral wing tip and winglet. Figure 2-15 shows the shapes of four typical wing tip extensions.

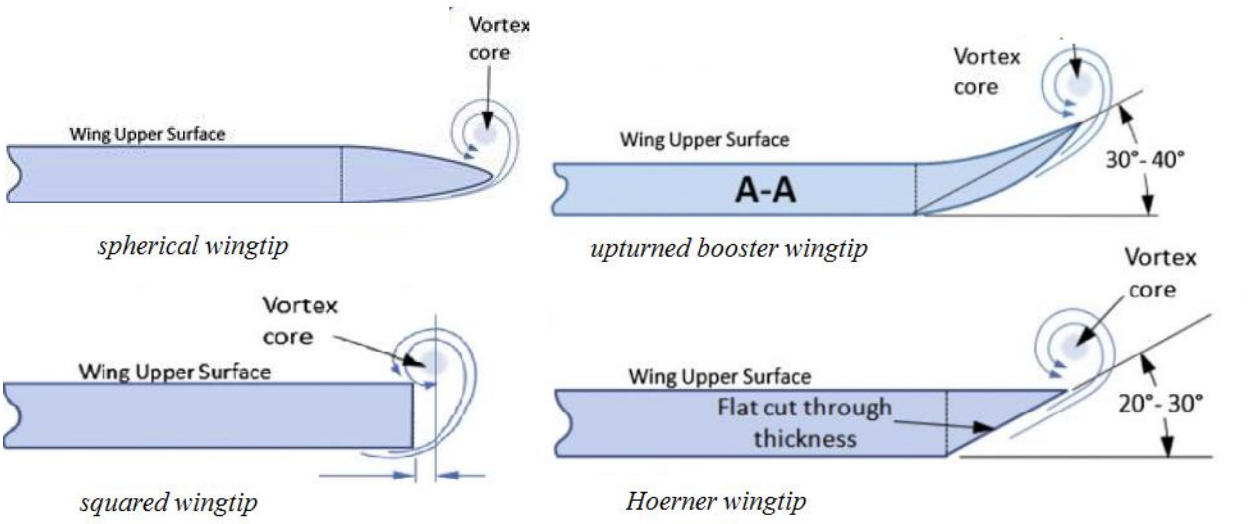

Figure 2-15 General shapes of four typical wing tip extensions [46]

A winglet is a near-vertical extension of the wing tip, which can perform better in term of diffusing the vortex than previous wing tip extensions. A typical winglet is shown in Figure 2-16(a) [47]. A vortex is developed and change the relative wind direction near wing tip, as shown in Figure 2-16(b). If the winglet is fitted to the wing tip with appropriate height and orientation, the lift generated by winglets have a component pointing forward, which can reduce the drag [48].

Whitcomb [49] studied a shifted downstream winglet mounted on the tip of a narrow-body jet transport wing, with a free stream Mach number of 0.78, and Reynolds number 17.2×10^6. The winglet consisted of two spilt winglet located at wing tip with different flap angles. The primary winglet was located rearward above the tips while the smaller secondary one was placed forward below the tips, as shown in Figure 2-17. This winglet configuration reduced the induced drag by about 20%, and increased lift-drag ratio by 9%. The lift-drag ratio was more than twice as that achieved by wing tip extension configuration. Another study by Sohn *et al.* [50] on similar configuration also showed similar results, where the Whitcomb winglet increased the lift coefficient by 9% more than a simple fairing wing tip extension with a free stream velocity of 26 m/s and Reynolds number of 4.12×10^5.

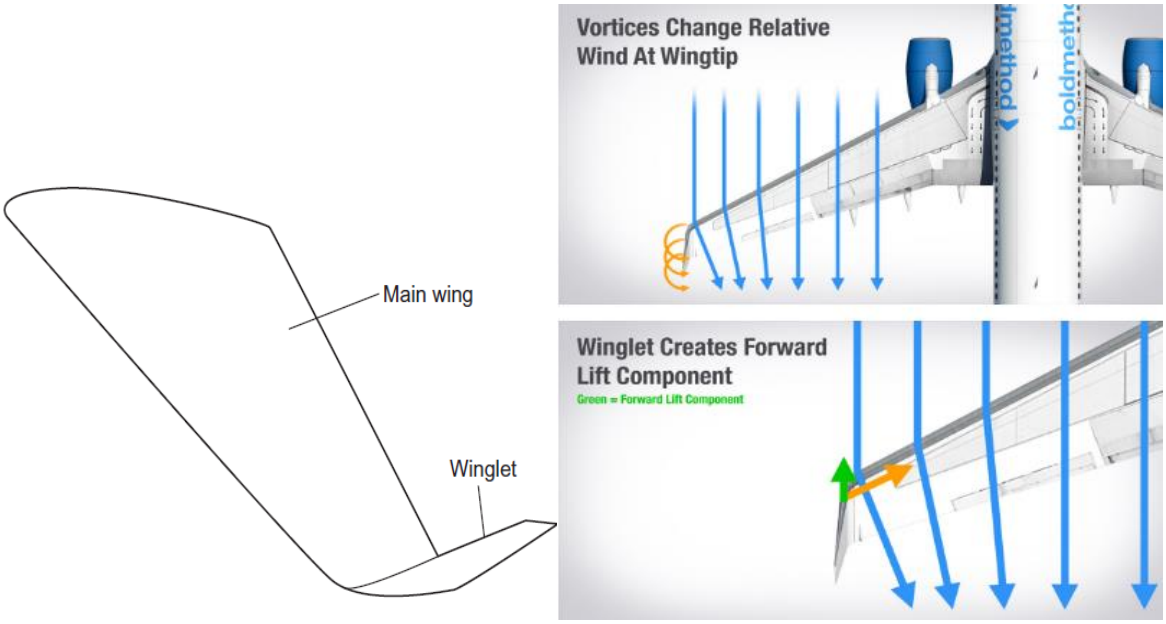

(a) (b)

Figure 2-16 (a) Typical winglet configuration [47] and (b) the flow and force near the wing tip[48]

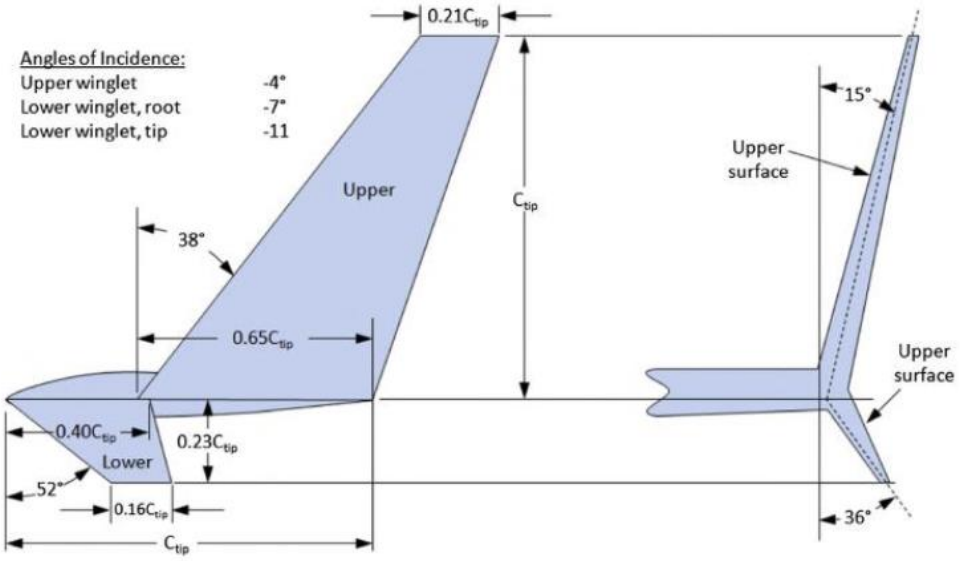

Figure 2-17 A general layout of the Whitcomb winglet [49]

While the passive techniques discussed previously may be effective, they may induce additional drag under off-design conditions unless the devices involved can be retracted, which would incur the same mechanical inconveniences as using movable flight control surfaces. As such, active control techniques that can be easily turned on and off would be more practical. The first technique developed for wing tip vortex control was pneumatic, using jet injection, or wing tip suction. Ayers

and Wilde [51] first proposed the idea of wing tip spanwise blowing in 1956. Later Wu *et al.* [52] studied wing tip blowing from three jet ports on a NACA0012-64 airfoil with AR=1.7, with an inlet flow of 20 m/s, a Reynolds number of 2.46×10^5 and an angle of attack of 5°. The local lift coefficient was found to increase by up to 20% with wing tip blowing.

Schwind and Briggs [53] studied outboard-blowing wing tip jets on several low aspect ratio NACA 0015 half-span wings. In aeronautics, the aspect ratio of a wing is the ratio of its span to its mean chord. It is equal to the square of the wingspan divided by the wing area. The lift was augmented by as much as 120% at low angles of attack in an inlet flow of 64 m/s. They indicated that the lift augmentation by wing tip blowing would reduce with a larger wing aspect ratio, which was later confirmed by Mineck [54] when he studied spanwise blowing on modern-aspect-ratio wings at high speed. The spanwise jets were at the tip of a swept wing with NASA HSNLF(1)-0213 airfoil section at a Mach number of 0.30. The maximum lift increase was only 0.028 (about 1%) at angle of attack of 2.07°.

Tavella [55] studied a thin wing tip jet on a symmetrical NACA 0018 airfoil section (AR=3.14, see Figure 2-18a) and indicated that this concept was very effective for small angles of attack. A maximum lift increase of 88 % was obtained at AOA=2° (see Figure 2-18b). The lift gain due to wing tip blowing was also modulated, which indicated that the lift increase depended on the 2/3 power of the jet blowing intensity. Later, an extensive experimental study was carried out by Margaris and Gursul [56] to study the effect of main parameters on wing tip blowing, such as the jet direction, its vertical and longitudinal position on the tip, the tip shape, the blowing coefficient and the angle of attack. The wing tip jets were installed on a NACA 0015 airfoil section as shown in Figure 2-19. The Reynolds number was about 10^5 and angles of attack were 5 and 10°. It was founded that blowing from the pressure side led to diffused vortex in the near wake, while with blowing from the suction surface producing the opposite effect. The spanwise blowing from pressure side on a rounded wing tip could produce coherent vortex. However, the authors did not carry out force measurement, thus lift and drag reduction were not quantified.

Pulsed jets are also used to control the wing tip vortex. Heyes and Smith [57] carried out an experimental study to modify wing tip vortex by pulsed span-wise air jets. A NACA0012 section wing was tested in a flow of 22 m/s, with a Reynolds number of 2.2×10^5 and at an angle of attack of 5°. The pulsed jets were supplied by compressed air via a tube passing through the wing, as shown in Figure 2-20. The results showed that the tip vortex was displaced with a magnitude

proportional to the blowing rate. Although no lift increase is mentioned in their study, this displacement of tip vortex would alleviate the negative effect of wing tip vortex and enhance the lift of the wing model.

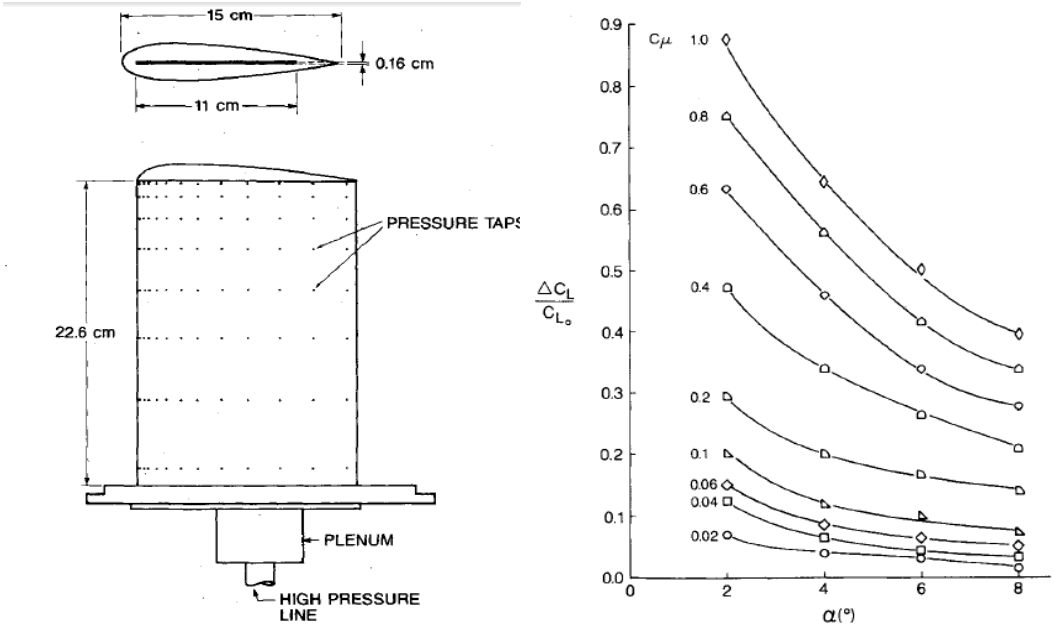

Figure 2-18 A wing model (a) and the relative lift increase by wing tip blowing (b) [55]

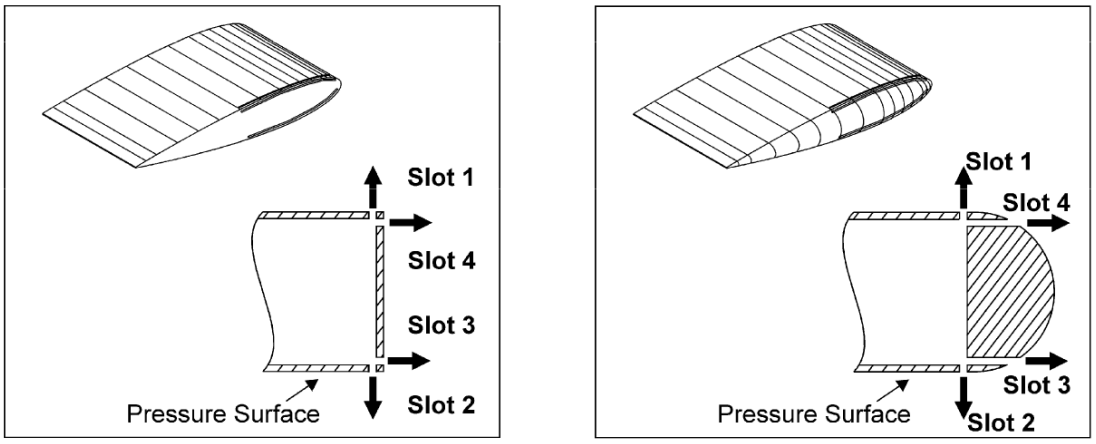

(a) (b)

Figure 2-19 Blowing configurations tested for a square tip (a) and a rounded tip (b) [56]

While there are many studies of the wing tip blowing, very few study have been focused on wing tip suction. Okada and Hiraoka [58] tested a NACA0016 airfoil at AOA=±9° for a mainstream velocity of 13.1 m/s and a Reynolds number of about 1.5×10^5. Four slots were arranged near the wing tip for suction, which were connected with a suction hose inside the wing model, as shown

in Figure 2-21. The results showed that the wing tip vortex was not affected by suction on pressure side, but was effectively diffused by wing tip suction on suction side, especially at the wing tip of trailing edge. However, the effect of wing tip suction on lift and drag was not investigated precisely, neither the reasons for the different effect on tip vortex between suction and pressure suction.

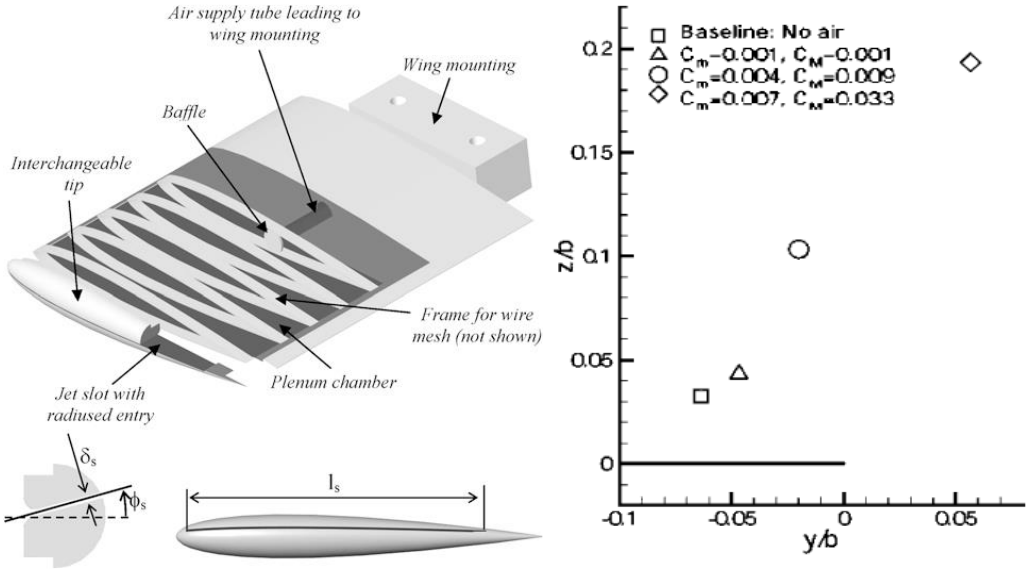

Figure 2-20 Wing with pulse jet and vortex center position with varying flow rate [57]

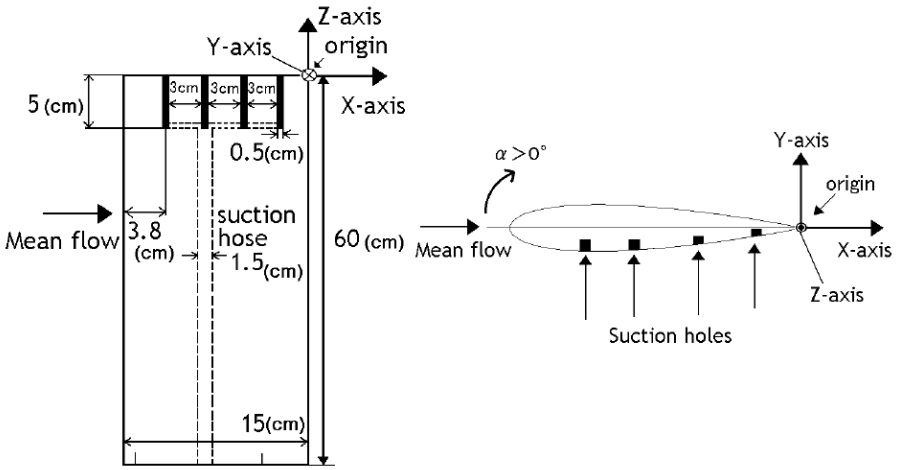

Figure 2-21 Wing model and the suction holes [58]

The above results show that the pneumatic techniques can be effective for temporary lift alteration for flight control. However, they usually require a hollow chamber inside the wing as well as pressure or vacuum sources, all of which complicate their integration and maintenance in commercial aircraft application. As in Section 2.1, one solution would be the use of synthetic jets.

Margaris and Gursul [59] applied synthetic jets on a rectangular wing NACA0015 with the same configuration as in their previous wing tip blowing investigation [56], with a free stream velocity of 10 m/s, Reynolds number of 10^5, and angle of attack of 10°. Experimental results showed that the synthetic jet was comparable to a continuous jet, which could produce a clearly diffused vortex with a low blowing coefficient.

Marouen *et al.* [60] used laser smoke flow visualization and hot wire anemometry to study the effect of synthetic jet actuation on wing tip vortex. A NACA0012 airfoil was studied in a low-speed wind tunnel, with a free stream velocity of 8 m/s, a Reynolds number of 80,000, and an angle of attack of 5°. The synthetic jet was placed near the wing tip, driven by a loudspeaker through a hollow rectangular chamber inside the wing model, as shown in Figure 2-22. Experimental results showed that the axial vorticity was reduced by nearly 30% by actuation, which was accompanied by a decreased cross-flow velocity (in y-z plane shown in Figure 2-22) and a diffused vortex core.

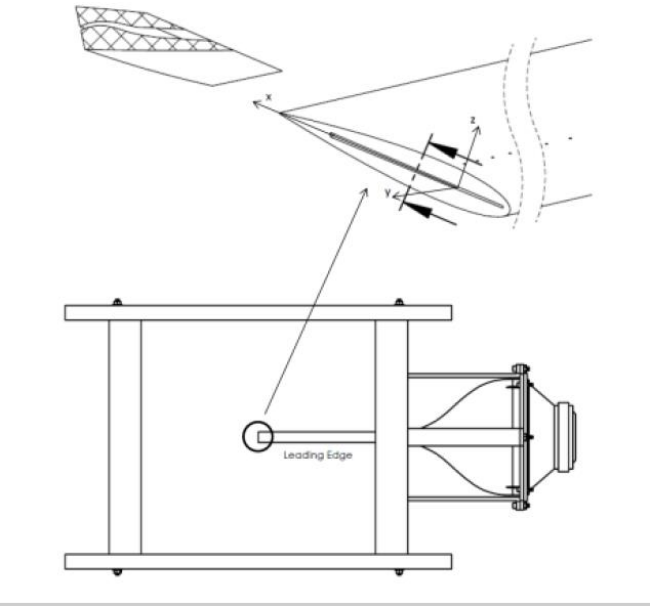

Figure 2-22 Wing model and wind tunnel set up [60]

Sudak [61] built a combined dual synthetic jet for wing tip vortex control on a NACA 0015 wing with a span of 0.427 m, and an aspect ratio of 4.2. As shown in Figure 2-23(a), the vertical jet was used for suction side actuation and the horizontal jet for wing tip spanwise actuation. The synthetic jet increased the section lift coefficient near the wing tip at $Re=1 \times 10^5$, and AOA=6 – 10°, but had no effect at high Reynolds number of 2×10^5. With actuation on (see Figure 2-23(b)), the footprint of tip vortex visualized by oil film interferometry technique disappeared suggesting the vortex was

pushed off the wing tip by the jet. The footprint was caused by low pressure created by tip vortex, therefore if vortex was diffused, or pushed away, it could not produce low enough pressure to form footprint. Nevertheless, as before, synthetic jets have maintenance issues associated with potential clogging of the holes in realistic aircraft operating environments.

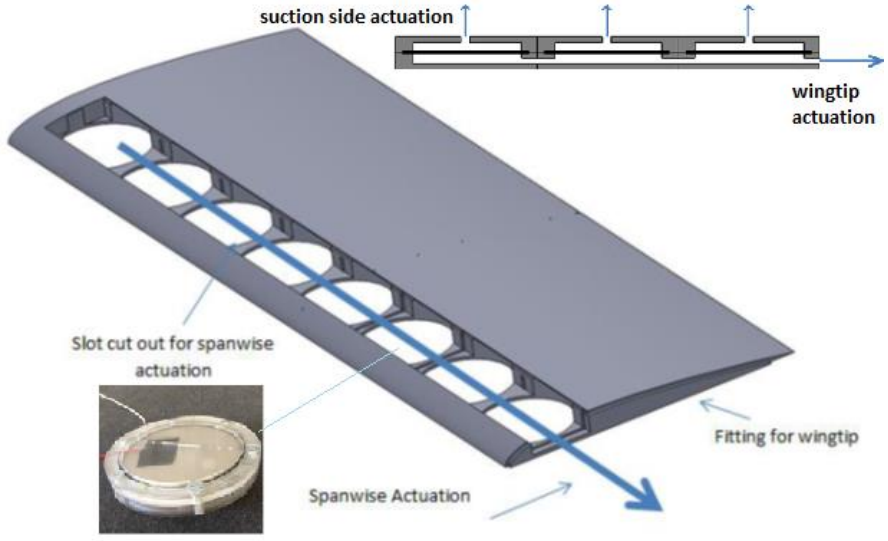

(a)

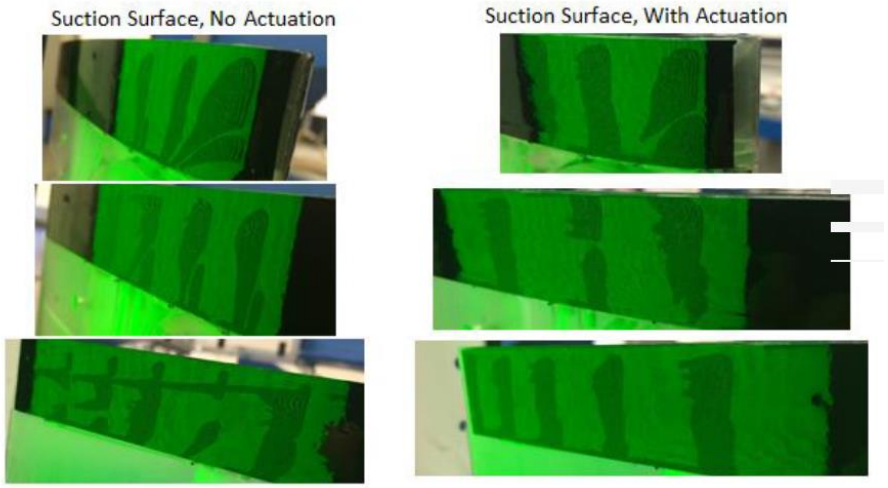

(b)

Figure 2-23 (a) Combined dual synthetic jet and (b) its effect on tip vortex footprint of a NACA0015 wing suction side [61]

Plasma actuation technology may overcome these drawbacks because of its solid-state and electrical nature. Ramakumar and Jacob [62] and Santhanakrishnan *et al.* [63] tested wings with plasma actuators placed on the suction and pressure sides near the wing tip blowing outward (called

plasma winglets), in combination with actuators placed on the suction and pressure sides near the trailing edges blowing downstream (called *plasma ailerons*). However their experiments were performed at very low Reynolds and were limited to very high angle of attack (14°) for which plasma actuation at the leading edge would be more effective, defeating the purpose of the concept for flight control application at low angle of attack.

Boesch *et al.* [6] studied wing tip actuators on an asymmetrical NACA4418 wing and a symmetric NACA0018 airfoil with a rounded wing tip at a low angle of attack, as shown in Figure 2-24. Results from CFD simulations showed that the vorticity field downstream of NACA4418 trailing edge was significantly changed, diffusing the tip vortex, as shown in Figure 2-25 which led to an increase of lift up to almost 20% for a mainstream flow velocity of 15 m/s and a Reynolds number of 1.5×10^5. Due to the limited strength of plasma actuators (maximum 40 mN/m), wind tunnel experiments were carried out at lower speeds, but the test results concur relatively well in trend with the corresponding CFD simulations. While the CFD simulations performed on a symmetric airfoil at zero angle of attack with the proposed actuator configuration showed that it could generate lift, no experiments was carried out to demonstrate this concept.

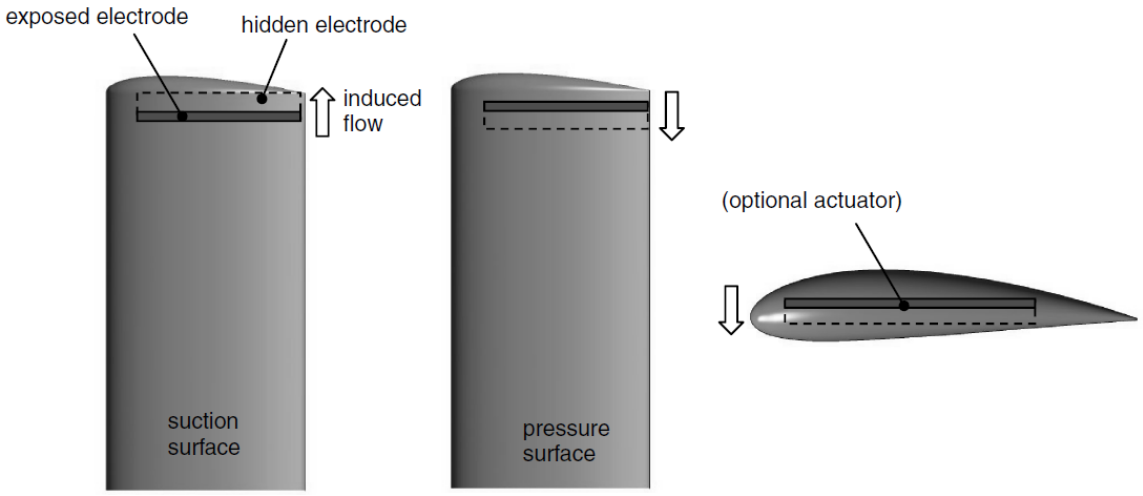

Figure 2-24 Wing geometry and plasma actuator locations [6]

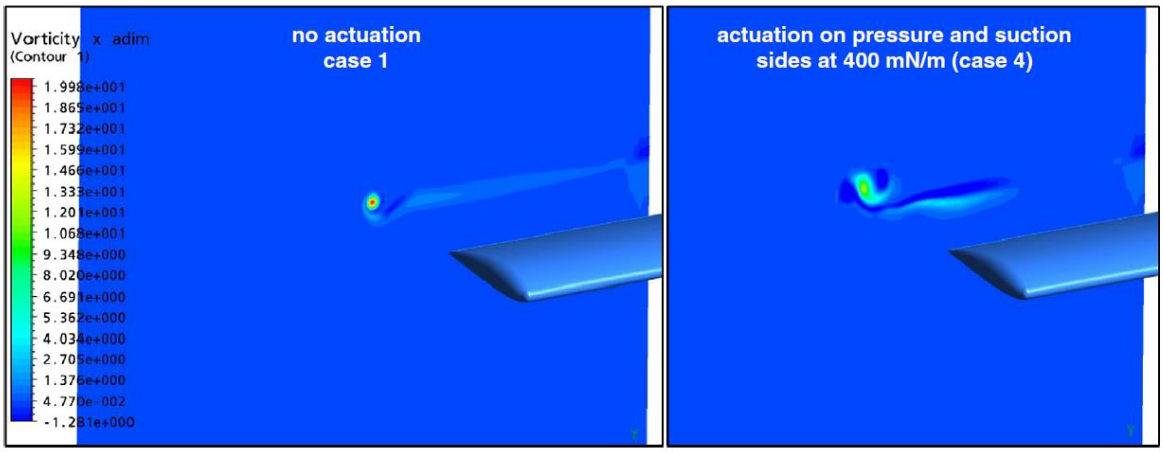

Figure 2-25 Vorticity contours downstream of trailing edge without and with plasma [6]

Hasebe *et al.* [64] used both direct numerical simulation (DNS) and wind tunnel experiments with Particle Image Velocimetry (PIV) to analyze wing tip plasma actuator operated in blowing and suction modes on the suction side of a finite NACA0012 wing. The Reynolds number based on the chord length was 3,000 for simulation and 1.44×10^5 for experiments. The AOA was fixed at 10°. PIV results showed that vortex centers move outwards (+z direction) in blowing cases but no significant change in suction cases.

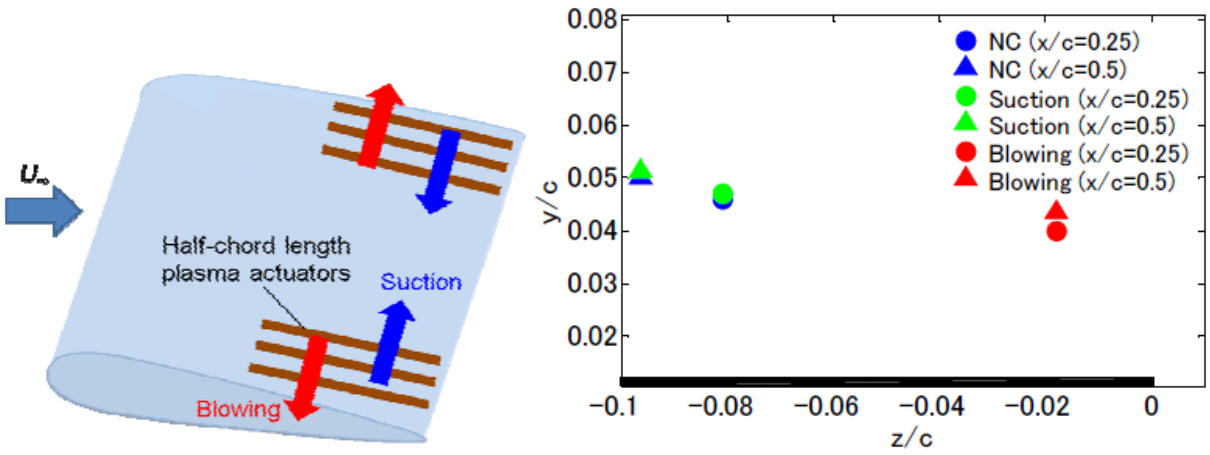

Figure 2-26 Wing tip plasma actuator configurations and experimental results [64]

Mizokami *et al.* [65] used similar DNS code to study DBD plasma actuators on a NACA0012 wing with squared wing tip at AOA=10°, Re=3,000. Four different placements of plasma actuators were considered: blowing at upper side (blow-up), blowing at bottom side (blow-down), suction at upper side (suction-up), and suction at bottom side (suction-down). A normalized induced velocity W_{PA}/U_∞ is introduced to represent plasma strength. He found that with induced velocity of 2.6,

lift increased by 188% in blow-up case and decreased by 161% in blow-down case, while slightly increased in suction-up and is nearly unaffected in suction-down case, as shown in Figure 2-27. A negative pressure field and a new vortex were created by the plasma actuation, leading to the increase of lift around wing outboard to the center region. However, they didn't specify the value of freestream velocity, making these conclusions hard to compare with existing literatures.

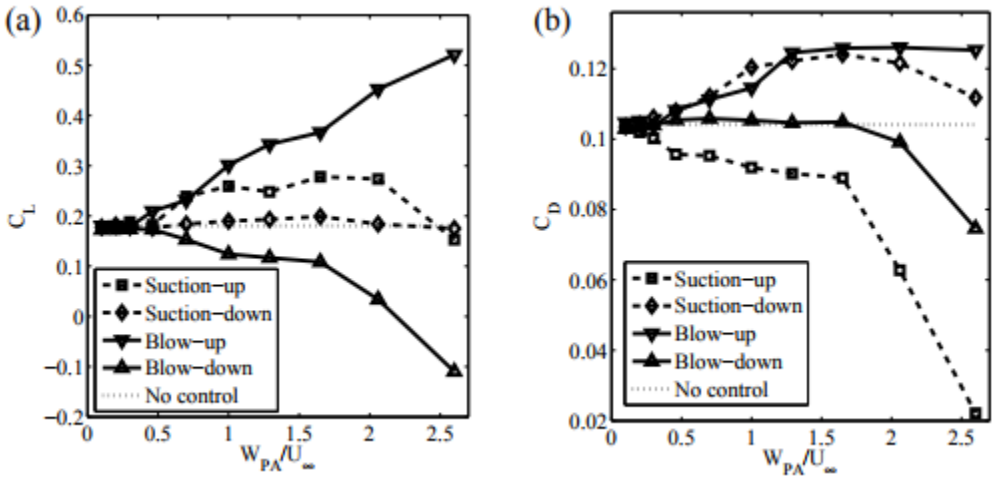

Figure 2-27 Force coefficients as a function of wing tip plasma actuator induced velocity [65]

Leroy *et al.* [66] carried out a detailed experimental study of wing tip dielectric barrier discharge (DBD) plasma actuators on a rectangular wing of a symmetric profile (AFV82) with a straight tip of sharp edges. The angle of attack was set at 6°, and mainstream velocity at 10 m/s corresponding to a Reynolds number of 2×10^5. The plasma actuators were tested on both pressure and suction sides blowing inwards and outwards, and finally only four configurations were found to be able to alter the tip vortex (DBD 1, DBD 3, DBD 6 and DBD 7 as shown in Figure 2-28). They concluded that plasma actuation in the pressure side was not as efficient as actuation in the suction side, and inward blowing decreased tip vortex vorticity but outward blowing reinforced it. However, no explanations were given. The increase of freestream velocity from 10 -19 m/s can stabilize the main vortex, but a displacement of the main wake vortex and a reduction of its streamwise vorticity are still observable with plasma actuation. The plasma effect decreased when the velocity reached above 25 m/s. However, aerodynamic force measurements were not made in their experiments, thus the lift increase and drag reduction were not quantified precisely.

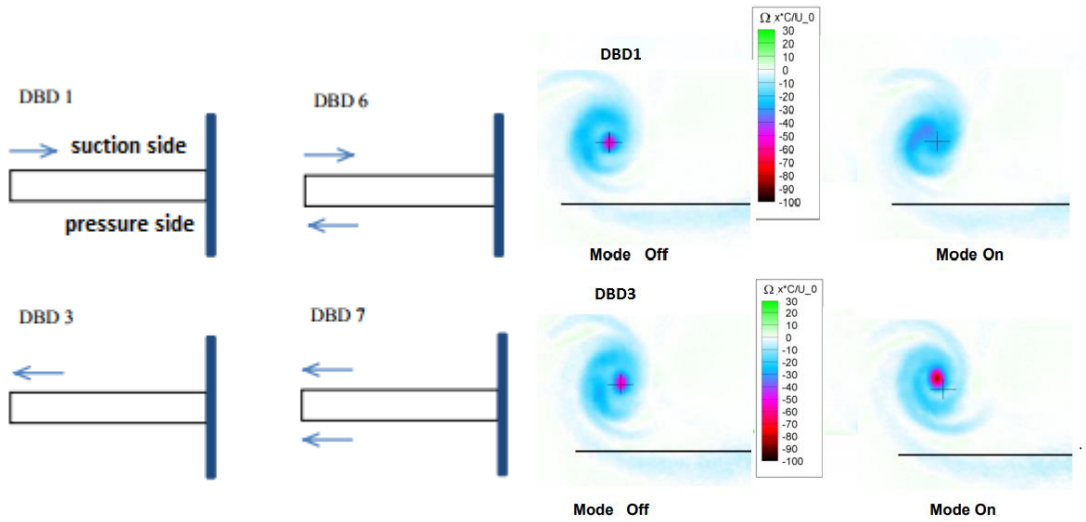

Figure 2-28 Schematic of the DBD plasma actuator arrangements (left) and the effect on trailing edge downstream tip vortex vorticity (right) [66]

Chappell and Angland [67] carried out PIV measurements of NACA0015 wing with wing tip actuators with a free stream velocity up to 15 m/s and Reynolds number up to 2.8×10^5. The configuration of plasma actuators was similar to that used by Boesch *et al.* [6], as shown in Figure 2-29. Tip vortex was found to be diffused at low angles of attack (AOA = 2, 6°), due to the blockage of the flow around the wing tip and the reduction of the tip vortex downwash. However, the effectiveness was found to decrease at high angle of attack (14°) and they hypothesized the vorticity generated by the suction side plasma actuator was fed into the vortex core at high angle of attack. However, no lift increase was mentioned in their study.

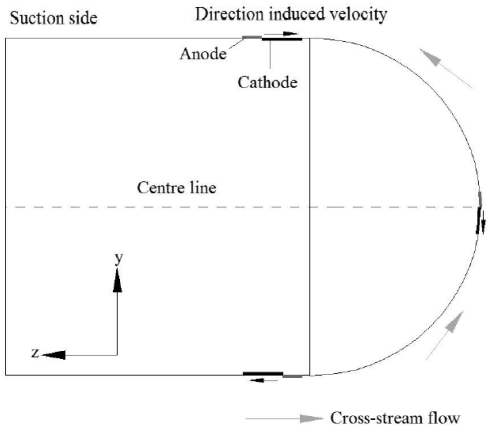

Figure 2-29 Schematic of wing tip plasma actuators [67]

In summary, many wing tip vortex control strategies have been proposed and studied over the past half century. However, only the active flow control strategies would be practical for flight control application at low angles of attack. While strategies involving plasma actuators would have the best potential of commercial applications due to their simplicity in term of integration, they have only been assessed at low Reynolds numbers or at high angles of attack and on 2D extruded wings only. Few work is to assess generation of lift on zero-lift airfoil for applications on aircraft tail planes.

2.3 Plasma Actuation for In-Flight Application

Currently most dielectric barrier discharge (DBD) plasma actuators are only investigated at low speeds, typically 5-15 m/s. Pavon *et al.* [68] carried out a detailed study of surface dielectric barrier discharges at high speed up to Mach number of 1.1. They showed that the plasma glow is reduced and the discharge becomes more filamentary at higher flow speed. A reduction of the light pulse emission duration from photomultiplier tube by one order of magnitude is found, from 500 to 50 ns, when airflow velocity is increased from zero up to an isentropic Mach number of 0.7. These measurement indicate that there is a change in the plasma breakdown mechanism when airflow velocity is increased. However, the effect of velocity on plasma actuation was not quantitatively analyzed.

The air flow's influence on the discharge performance of DBD plasma actuators was quantitatively investigated by Kriegseis [69] for flow with Mach number from 0 to 0.75. A non-dimensional relative performance index is defined by equation (2.2) with quiescent air reference,

$$\Pi_{\phi} = \frac{\phi(M)}{\phi|_{M=0}} \tag{2.2}$$

where M is the Mach number and ϕ is a general variable, which represents different quantities, such as plasma length or applied voltage.

The relative performance drop is then studied under different Mach number, however it turns out that the $\Pi_{\phi} - M$ plots varies under different applied voltages. To compensate the voltage dependency, a new reference number K is used to better address the effect of operating voltage of plasma actuators on performance drop, which is defined by equation (2.3) ,

$$K = \frac{U_{\infty}}{v_d} = \frac{U_{\infty}}{\mu E} \tag{2.3}$$

where U_∞ is freestream velocity, v_d is the drift velocity of the momentum imparting ions, μ is the ion mobility, and can be chosen as constant value of 2×10^{-4} m^2/(V-s). E is the electric field strength which scales linearly with the applied operating voltage, and can be calculate by V/d, where V denotes applied voltage and d represents the dielectric thickness.

Figure 2-30 shows the relative performance of power consumption and performance drop as a function of K. Kriegseis showed that the plasma actuator performance is reduced by 10% at Mach numbers below 0.2, and can drop by 30% at Mach numbers below 0.5. Kriegseis's work provides a new insight to quantify the plasma effect at real in-flight condition, and also explains the general over-predicted CFD results for plasma flow control concepts, such as in references [6] [12].

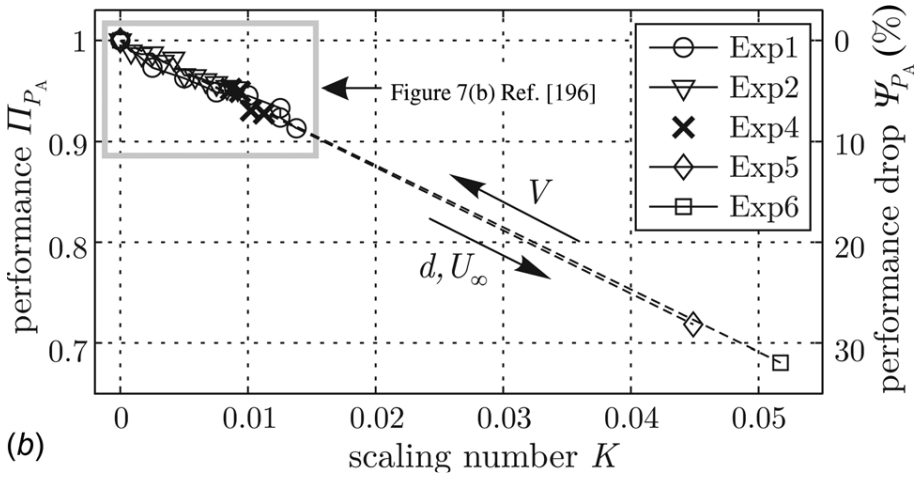

Figure 2-30 High speed influence on the relative plasma actuator performance and corresponding drop as a function of scaling number K [69]

For higher Mach number, there are very limited publications reported. Coumar and Lago [70] have studied the influence of Mach number and static pressure on plasma flow control of supersonic and rarefied flows around a sharp flat plate. The study was carried out with three contoured nozzles (Figure 2-31): first one (called NG) gives an airflow at Mach 2 and a static pressure of 8Pa, the second (NT) an airflow at Mach 4 and a static pressure of 8Pa and the third (N3) an airflow at Mach 4 and a static pressure of 71Pa. The shock wave angle increased by 1.15° for NG, by 1.21° for NT and by 1.28° for N3, showing that the discharge effect is even more significant when boosting the flow speed. It was also concluded that the morphology of the plasma discharge strongly depended on the static pressure.

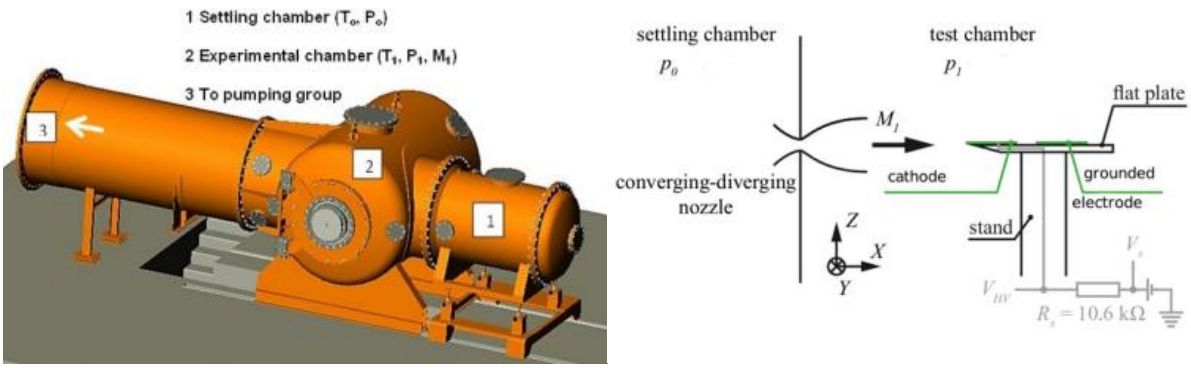

(a) (b)

Figure 2-31 Wind tunnel layout (a) and experimental setup [70]

On the other hand, while most investigations are currently carried out under laboratory conditions at low Reynolds number and small chord lengths, Duchmann [71] employed plasma actuators on the pressure side of a natural laminar flow wing section under free-flight conditions on a full-sized motorized glider. The DBD plasma actuator extends over the whole span of the trapezoidal wing which has a taper ratio of 0.55, a sweep angle at the leading edge of zero. With a flight speed of 38.5 - 39 m/s, Reynolds number of 2.8×10^6, a transition delay of 2 - 2.5% of the chord length is achieved when applying plasma actuators. The effect of pressure and humidity on actuator power consumption was also studied and it showed that a pressure increase of 3% would result in a power decrease of 4%, and a relative humidity drop of 70% would lead to a power variation of 5%.

In summary, there are still very limited studies of plasma actuation on aircraft wings at high Reynolds numbers. Compared with experiments under laboratory conditions, the plasma actuators for aircraft application are operating under a different environment, namely higher Mach number, lower pressure and density, varying humidity etc. Moreover, none of current studies have investigated quantitatively the effect of real wing geometries on plasma actuator performance.

2.4 Plasma Model

Many engineering models have been developed in the past decades to simulate the effect of DBD actuators for flow control simulations. The most common and successful approach is to simulate the DBD actuator as a spatial plasma body force distribution. Shyy *et al*. [41] proposed the first of such model with a linear two-dimensional body-force distribution. In this model, the electrical-

field was assumed to decrease linearly from exposed electrode to hidden electrode. However, the model did not take into account the exact actuator geometry, the properties of the dielectric such that the body-force vector direction and actuator strength (integral net induced body force) prediction versus the AC voltage input were inconsistent with experiments. Suzen and Huang [72] developed a model based on actuator geometry and the nature of the fluid and dielectric material. The model calculated the body force produced both by the external electrical field and electrical field by the charged particles. The body-force in this model was more realistic but the scaling with AC voltage was still incorrect, being proportional to V_{AC}^{2} instead of $V_{AC}^{3.5}$ in experiment.

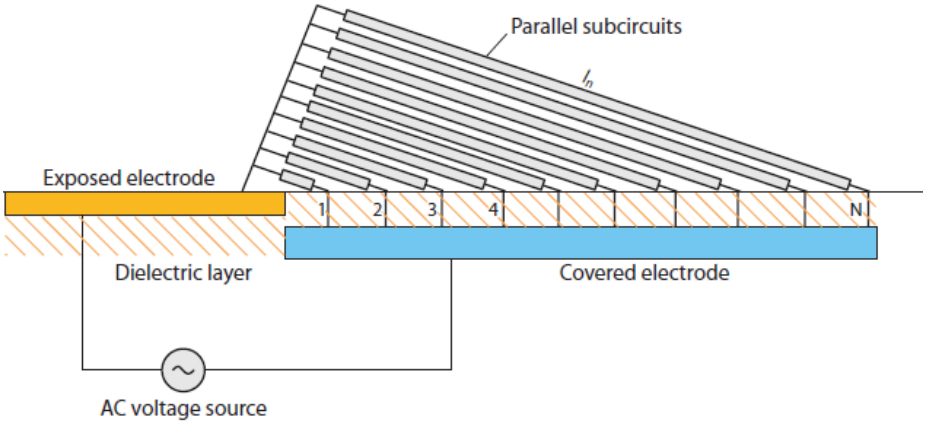

Figure 2-32 A multi-network model for a DBD plasma actuator [73]

Orlov *et al.* [73] developed a multi-network model by dividing the domain over covered electrode into several parallel parts, as shown in Figure 2-32. The property of each network depended on their distances from exposed electrode. This model successfully predicted the AC scales of $V_{AC}^{3.5}$, and an optimum AC frequency which generated the maximum body force. But Orlov's model cannot not explain the effect of gas property on negative and positive ions.

A new plasma model for engineering application was proposed by Lemire and Vo [74], combing features from models of Suzen & Huang and Orlov *et al*. This model used the most accurate time-averaged spatial body-force distribution with a low-cost model, and scale it to obtain the desired body force. The body-force distribution shown in Figure 2-33 was obtained by solving equations on a very fine mesh, and then mapped onto coarser CFD mesh of plasma actuator surface. An evaluation of different engineering models by Palmeiro and Lavoie [75] showed that this is the best engineering model of DBD plasma actuators at the time they published their paper. This plasma model is therefore used in the current work.

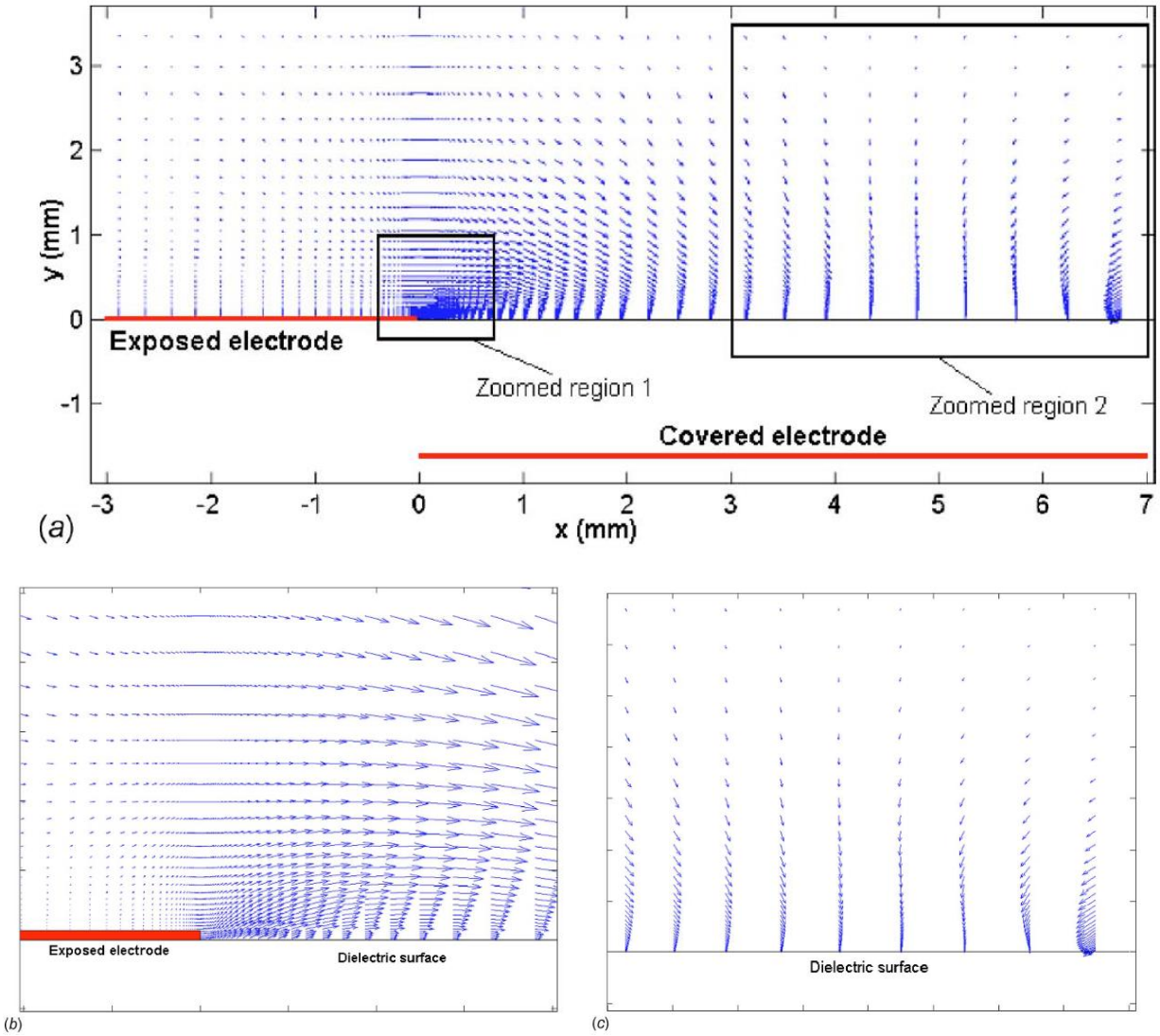

Figure 2-33 Time average spatial distribution of the force from plasma actuator [74]

CHAPTER 3 METHODOLOGY

3.1 General Approach

The methodology used to achieve the objectives of this project is fundamentally based on a computational approach backed up by experimentation. The limited strength of existing plasma actuators limits flow control testing to low speeds (below 30 m/s). On the other hand, most CFD codes can be used for aircraft simulations from low-speed ground conditions up to realistic operating conditions. In view of these constraints, the approach consists of validating a RANS CFD code with an implemented plasma actuator model, using low-speed wind tunnel testing on extruded wings with the two plasma actuation concepts, and then using this code to assess these concepts for real wing geometries and realistic operating conditions. The project can be divided into three phases as described below.

Phase 1 consists of numerical setup and experiment design. This phase starts with selecting and implementing the plasma actuation model in a commercial CFD code. In parallel, the wing geometries and dimensions and planned test conditions are chosen in consideration of the requirements of the plasma actuation concepts, plasma actuator strength limitations and available wind tunnel test facilities. Subsequently, the computational simulations with plasma actuation model for each test case are set up and carried out to validate the planned experiments and to select the adequate instrumentation.

Phase 2 involves wind tunnel testing and code validation. This phase begins with the detailed design of the test wings and components for integration of the wings, instrumentation and plasma actuation equipment in the wind tunnel. These tasks are followed by the fabrication and assembly of the experimental setup, characterization of the wind tunnel and calibration of the instrumentation. The wind tunnel experiments are carried out with and without plasma actuation, with force measurements as well as detailed measurement of the flow field, and the corresponding CFD simulations set up and performed. The numerical setup can then be refined following comparison of the numerical and experimental results.

Phase 3 is the assessment of the plasma actuation concepts for realistic wing geometries and real operating conditions. The plasma actuation concept is assessed on tapered and swept wing geometries to see the tapered and sweep effect on the plasma actuation concept. Thereafter, a realistic tapered swept wing is simulated at realistic operating conditions (cruising speed and

landing/takeoff speed) and low angles of attack, using the previous solver and plasma actuator model to estimate the plasma actuation requirement for replacing aircraft control surfaces, such as ailerons and elevators.

The next section begins with a description of the experiment setup, including wind tunnel, wings, plasma actuators, aerodynamic force measurement and flow field measurement *etc.* Subsequently the numerical setup (CFD tools and plasma actuation model) is explained in details for wind tunnel simulations, tapered and swept wing simulations, and realistic wing simulations.

3.2 Experimental Study

3.2.1 Wind Tunnel

All the tests were carried out in a close-looped wind tunnel (Figure 3-1), located in École Nationale D'Aérotechnique, St-Hubert, Québec, Canada. As shown in Figure 3-2, the test section has a cross section of 30 in × 30 in, and a length of 72 in (0.762 × 0.762 ×1.829 m). The design speed of test section is 30 m/s, with an averaged turbulence intensity of 0.44% measured by a hot wire anemometer (see Appendix A). The test section is mounted on rollers and is interchangeable with other test sections. The test section is equipped with clear glass side walls or windows to allow optical access to view test models.

Upstream of the test section is a contraction cone with a ratio 5.3:1. Multiple layers of honey comb and screens (shown in Figure 3-1) are installed at the inlet of the contraction cone to provide a low turbulence intensity in the test section. Downstream of the test section is the diffuser which gradually decelerates the air and alters the flow direction by 90° using turning vanes. The 30 HP motor of the wind tunnel is controlled by a control panel (on the right of Figure 3-2). The inlet velocity of the test section is adjusted by changing the motor frequency.

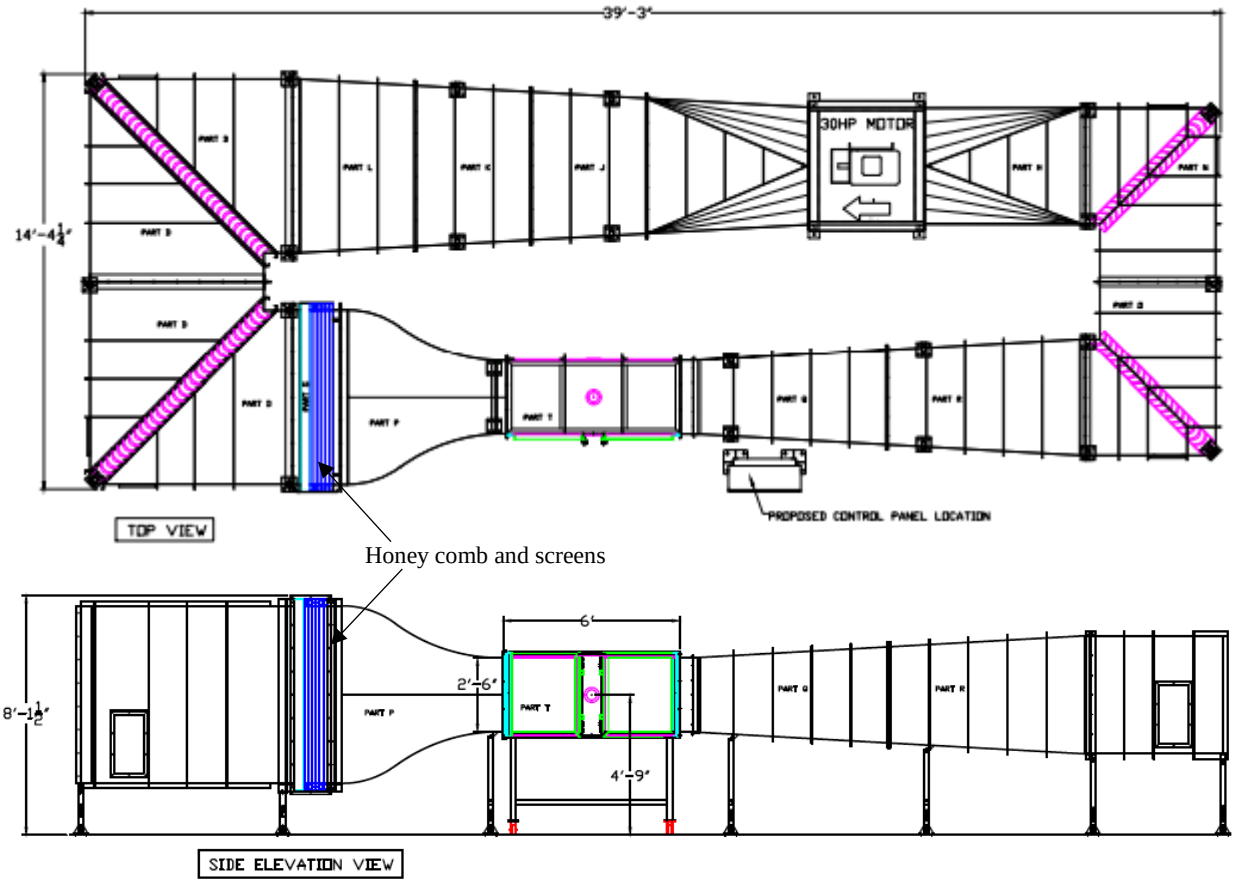

Figure 3-1 Top and side elevation view of closed-loop wind tunnel

Figure 3-2 Wind tunnel test section

3.2.2 Wings

Traditionally, asymmetrical airfoil sections are used in aircraft wings to provide lift and symmetrical airfoil sections are used in aircraft tail plane, typically rudder, horizontal tails, and elevators for flight control. Two profiles are chosen to design test wings, one asymmetrical Aerospatiale-A profile (see Figure 3-3(a)), and one symmetrical NACA 0012 profile (see Figure 3-3(b)). Aerospatiale-A has a max thickness 16% at 30% chord and a max camber 2% at 20% chord. NACA 0012 has a max thickness 12% at 30% chord and a max camber 0% at 0% chord. Both have been extensively studied by previous researchers and therefore there are existing data for comparison with current numerical and experimental study.

Four extruded wings are designed and built, as shown from Figure 3-4 to Figure 3-8. Two Aerospatiale-A wings for plasma Gurney flaps (called AG) and plasma wing tip actuators (called AT). Two NACA 0012 wings for plasma Gurney flaps (called NG) and plasma wing tip actuators (called NT).

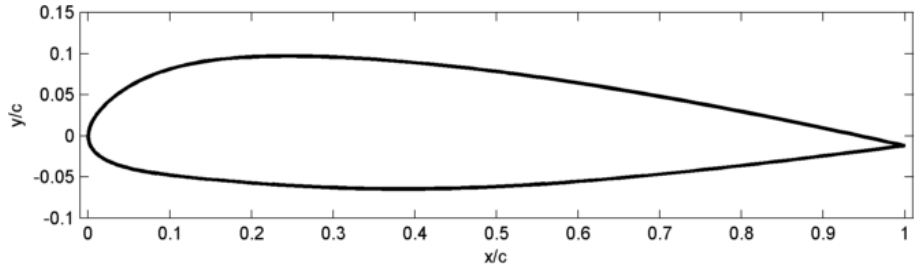

(a)

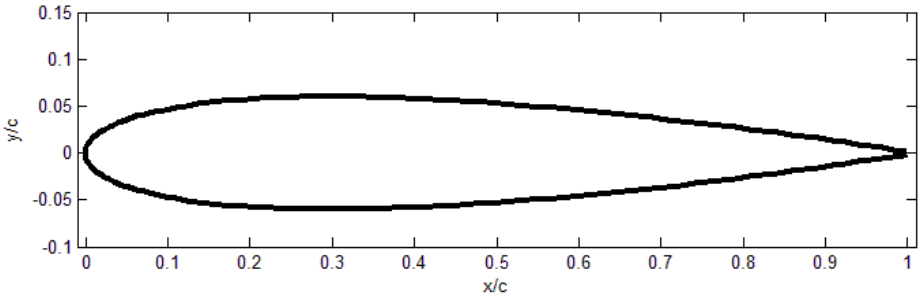

(b)

Figure 3-3 Airfoil profiles (a) Aerospatiale-A (b) NACA 0012

The airfoil chord is 10 inches (0.254 m), and the inlet velocity varies from 8 to 20 m/s, resulting in Reynold number ranging from 1.33×10^5 to 3.33×10^5. The AG and NG wings are assembled with endplates on two sides, while AT and NT wings have one endplate near the wing root. The AG and

NG wings have spans of 18 inches (0.4572 m) for an aspect ratio of 1.8, and the AT and NT wings have a span of 17 inches (0.4318 m), excluding the rounded wing tip, for an aspect ratio of 1.7. To reduce the cost of fabrication, each wing is designed to consist of four pieces, two wing blocks printed by an in-house low-cost Fused Deposition Modelling (FDM) 3D printer and two panels outsourced to *Axis Prototype Inc.* to be printed by Stereolithography (SLA) printers, which gives smoother surfaces and can prototype small pressure taps on wing tip surfaces. The SLA material also serves as the dielectric for the DBD actuators. As shown in Figure 3-4 and Figure 3-5, the wings with plasma Gurney flap consist of two spanwise hollowed blocks, one suction side panel and one pressure side panel. As shown in Figure 3-6 and Figure 3-7, the wings with wing tip actuators consist of two full chord hollowed blocks, one suction side panel with wing tip, and one pressure side panel.

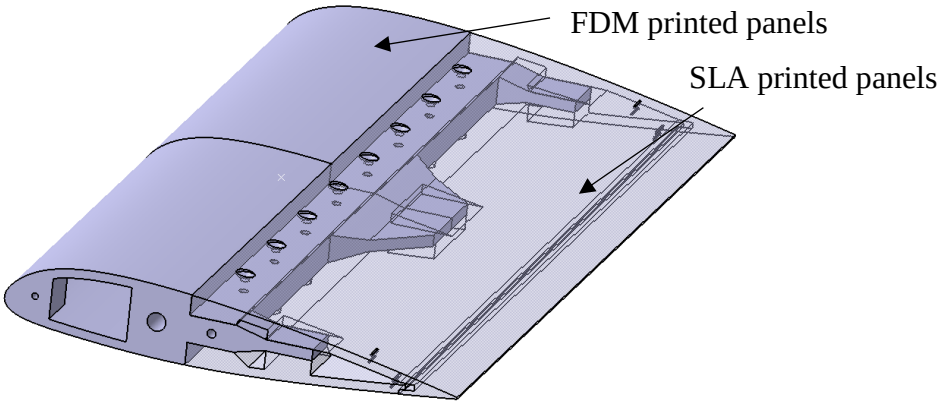

Figure 3-4 Design of Aerospatiale-A extruded wing for plasma Gurney flap (AG)

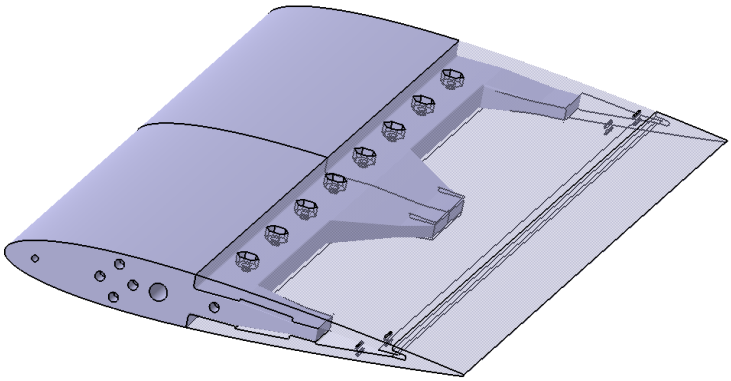

Figure 3-5 Design of NACA 0012 extruded wing for plasma Gurney flap (NG)

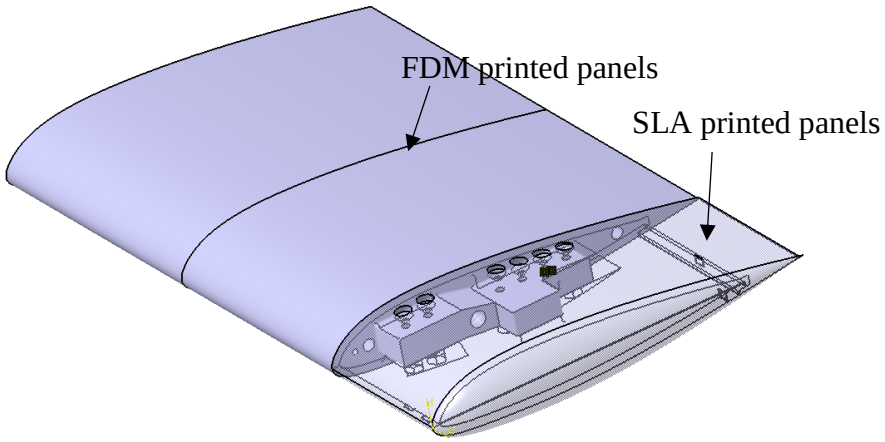

Figure 3-6 Design of Aerospatiale-A wing for wing tip plasma actuator (AT)

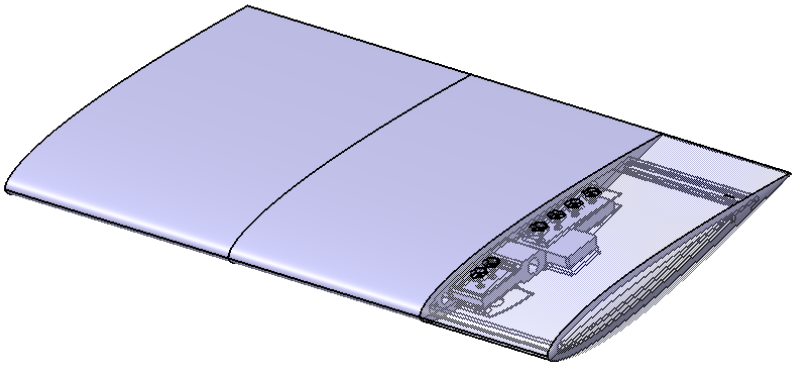

Figure 3-7 Design of NACA 0012 wing for wing tip plasma actuator (NT)

The wing blocks are printed using in-house FDM SeeMeCNC® ROSTOCK MAX™ V2 Desktop 3D Printer Kit with PLA/PHA filaments. The trailing edge panels and wing tip panels are printed by SLA printer from Axis Prototype using DSM Somos® WaterShed XC 11122 photopolymer. The average cost for SLA 3D printing is CAD$20 per cubic inch, while the material cost for in-house 3D printing is less than CAD$1 per cubic inch. The assembled AG and AT wings without endplates are shown in Figure 3-8 and Figure 3-9. All test wings are covered by plastic film to make surface smooth and eliminate any surface discontinuity at the junctions between the wing blocks and panels.

A steel wire is attached to the wing surfaces to trip the flow and set the position of transition from laminar to turbulent flow. Erm [76] indicates the trip wire diameter should be larger than 0.2 mm and placed near 10% chord. If the wire is placed too close to the leading edge, the flow may reattach

to the surface easily and remain laminar. Therefore, trip wires with a diameter of 0.5 mm are placed around 9 -13% chord for test wings.

To validate CFD simulation results in more detail, pressure taps are designed chordwise on surfaces near wing tips for the AT and NT wings. Pressure taps are not designed for the AG and NG wings because plasma actuators would block pressure taps near trailing edges. The tap positions are determined from preliminary CFD simulations, as well as physical constrains from the limited space in the wing block to accommodate associate pressure tubes.

The chordwise tap positions for the AT wing are x/c= 0.01, 0.05, 0.1, 0.3, 0.375, 0.4, 0.425, 0.45, 0.5, 0.65, 0.85, 0.9 for the suction side and x/c=0.05, 0.8 for the pressure side, where is x the chordwise distance to leading edge, and c is chord length. Tap positions for the NT wing are x/c = 0, 0.0125, 0.03, 0.05, 0.2, 0.3, 0.415, 0.6, 0.8, 0.85, 0.875, 0.925 for the suction side, x/c = 0.05, 0.8 for the pressure side. All taps are located in the same plane with a distance of 15 inches (0.381 m, 88% span) from the wing root.

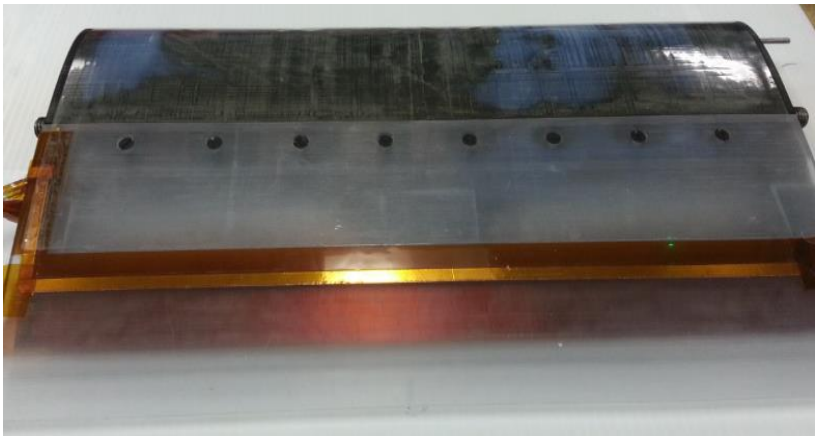

Figure 3-8 Assembled Aerospatiale-A wing with plasma Gurney flap (AG)

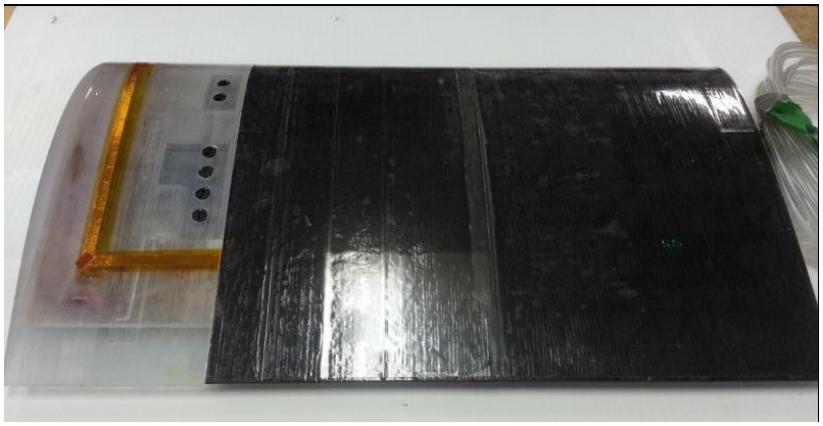

Figure 3-9 Assembled Aerospatiale-A wing with wing tip plasma actuators (AT)

Experiments are carried out at inlet velocities of 8, 15, 20 m/s for asymmetrical wings (AG and AT), AOA = 0°, Reynolds numbers ranging from 1.33×10^5 to 3.33×10^5. For symmetrical wings, the measured lift from test has a big fluctuation at high speeds at AOA = 0°. Therefore, the NG and NT wings are tested at 8, 12, 15 m/s, AOA = 0°, Reynolds numbers ranging from 1.33×10^5 to 2.57×10^5. All wings are not tested at higher velocities above 20 m/s because plasma effect becomes very weak.

3.2.3 Plasma Actuators

The dielectric barrier discharge (DBD) plasma actuator used in this research is shown in Figure 3-10. The actuator consists of two offset electrodes, which are made of 0.0035 inches (0.089 mm) thick self-adhering copper foil tape, separated by 5 mm-thick SLA wing panel wall which serves as the main dielectric. One electrode with a width of 6.35 mm (1/4 in) is exposed on the wing surface and the other electrode with a width of 25.4 mm (1 inch) is hidden beneath the wing surface. The axial gap between the exposed electrode and hidden electrode is chosen to be zero (see Figure 3-10), as used in previous studies [77, 78]. Several thin layers of 0.001 inches (0.0254 mm) and 0.005 inches (0.127 mm) thick DuPont Kapton® polyimide film are applied to protect the SLA material from degradation under repeated plasma actuation. The Kapton® tapes are also used to cover electrodes to avoid parasitic plasma, which is plasma that forms on the upstream edges of the two electrodes which produces some flow acceleration in the wrong direction.

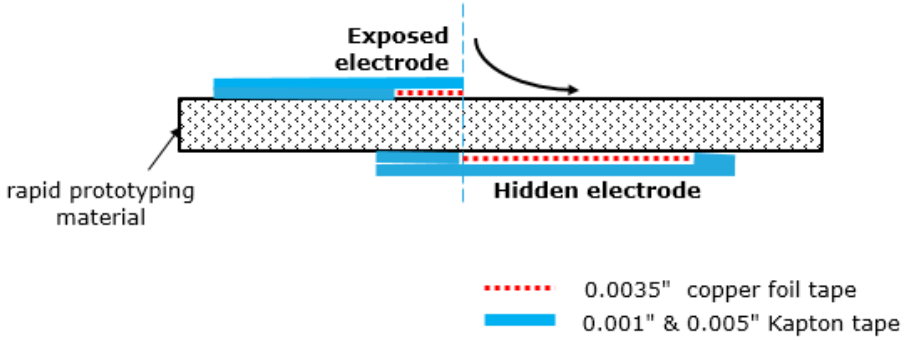

Figure 3-10 Schematic of plasma actuators

A negative saw tooth high-voltage input is provided to the plasma actuator electrodes by an in-house generation system, as shown in Figure 3-11. Details about the high-voltage generation system are given in Appendix C. This setup has been shown in a previous study [77] to generate

an actuator strength of 100 mN/m, the estimated required value for noticeable effects at 20 – 30 m/s, which is noticeably higher than conventional DBD actuators with sinusoidal AC voltage input (20 to 40 mN/m). The actuator strength is defined as the total body force in the streamwise direction (parallel to the surface) generated by the actuator per unit length of actuator.

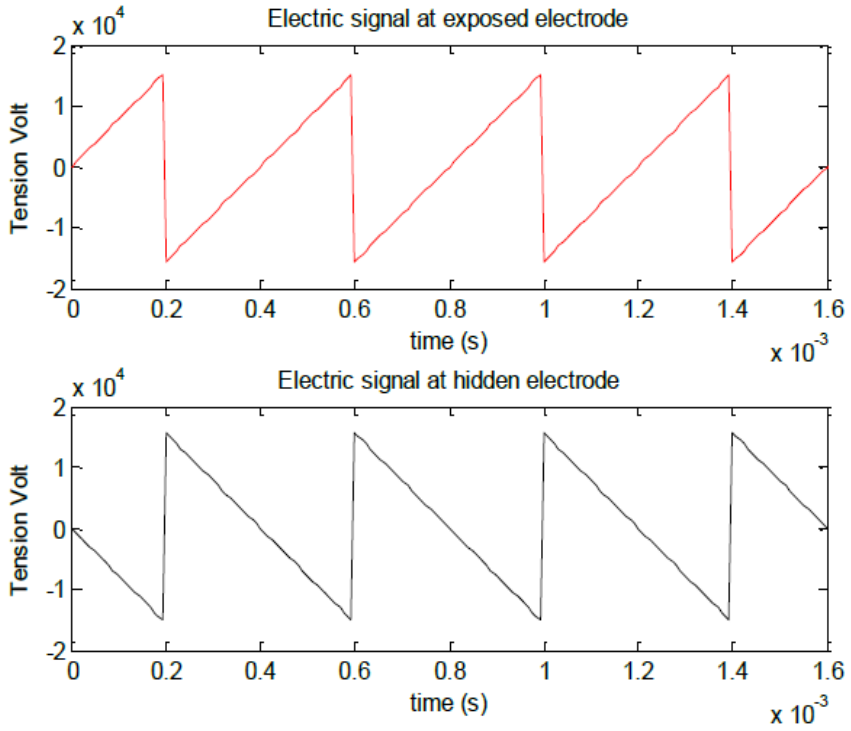

Figure 3-11 Negative saw tooth input signal for plasma actuator electrodes

While the plasma Gurney flap and wing tip actuation concepts require the plasma actuator to be positioned as closely as possible to the trailing edge and wing tip, respectively, the actual placement of the DBD actuators on the test wings is constrained by the geometries of the test wings. Figure 3-12 illustrates the positions of the DBD actuator for two airfoil profiles, where the short and long red lines represent, respectively, the exposed and hidden electrodes. The induced flow (ionic wind) is directed downstream on the suction side and upstream on the pressure side. With the location of the actuator defined by the center of the axial gap between the two electrodes, the suction side and pressure side actuators for the NG wing are located at 76% and 82% chord (Figure 3-12 (a)), respectively. The suction side and pressure side actuators for the AG wing are located at 80% and 85% of the chord (Figure 3-12(b)), respectively. Figure 3-13 shows the geometrical layout of plasma Gurney flap on the suction side, which has a length of 1.6 chord in the spanwise direction.

The plasma actuators do not cover the full wing span to avoid sparking between the hidden and exposed electrodes at the edge of the wing span.

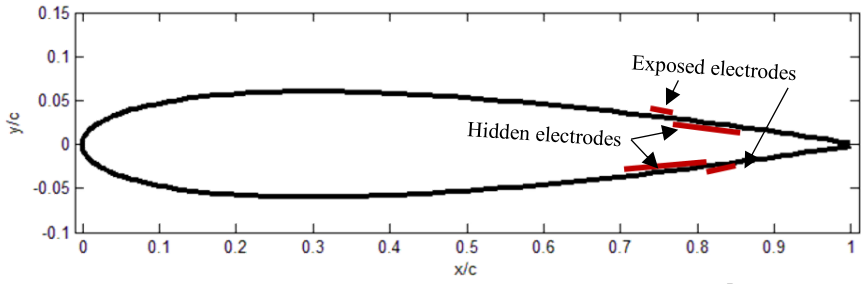

(a) NG

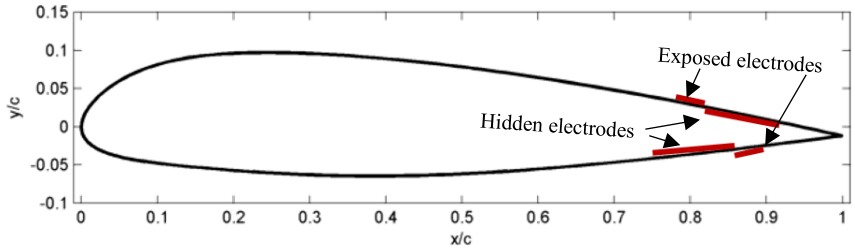

(b) AG

Figure 3-12 Positions of plasma Gurney flap for the NG and AG wings

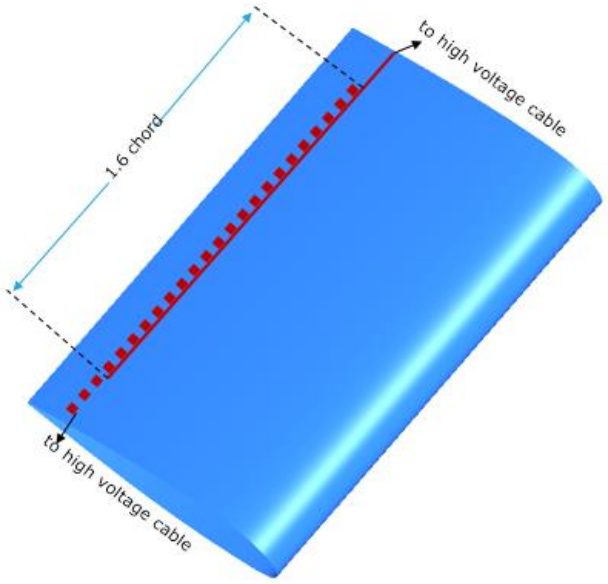

Figure 3-13 Geometrical layout of plasma Gurney flap on the suction side

Figure 3-14 shows the geometrical layout of the wing tip actuators, which avoids the complexity of placing electrodes on the three-dimensional curved wing tip surface. The plasma actuator on the suction side is positioned to induce an outward flow while the one on the pressure side induces an inward flow. As shown in the cross-section view, the pressure side actuator is located at 97% of the flat span (excluding the rounded wing tip) while the suction side one is at 88% of the flat span. The actuators axially cover from 4% to 83% of the chord with a length of 0.8 chord because of the geometrical limitations.

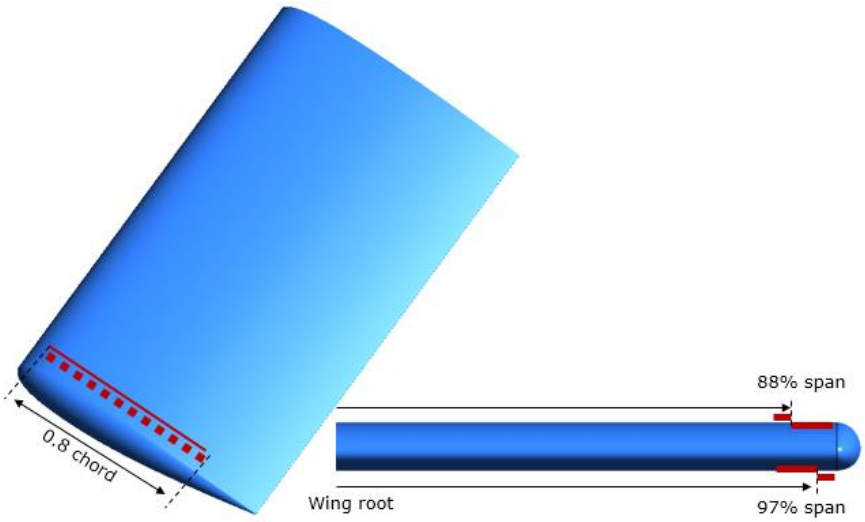

Figure 3-14 Geometrical layout of plasma wing tip actuators (left: top view; right: cross section view from upstream)

To generate a large plasma body force with high voltage, it is very important to have good insulation between hidden and exposed electrodes and good connections between electrodes and the high-voltage wires, to avoid any spark or electrical breakdown. Moreover, plasma actuators need to be visually checked to ensure a uniform plasma distribution. Figure 3-15 shows an example of relatively uniform plasma distribution (in purple) generated by wing tip plasma actuators.

To obtain the desired plasma actuation strength, the characterisation of plasma actuators is carried out through the measurement of thrust generated by actuator placed on a wing panel. As shown in Figure 3-16, the force measurement is done on a Sartorius I8100P electronic scale with precision of 0.01 g (equivalent to 0.1 mN). More details on the plasma characterisation can be found in Appendix C.

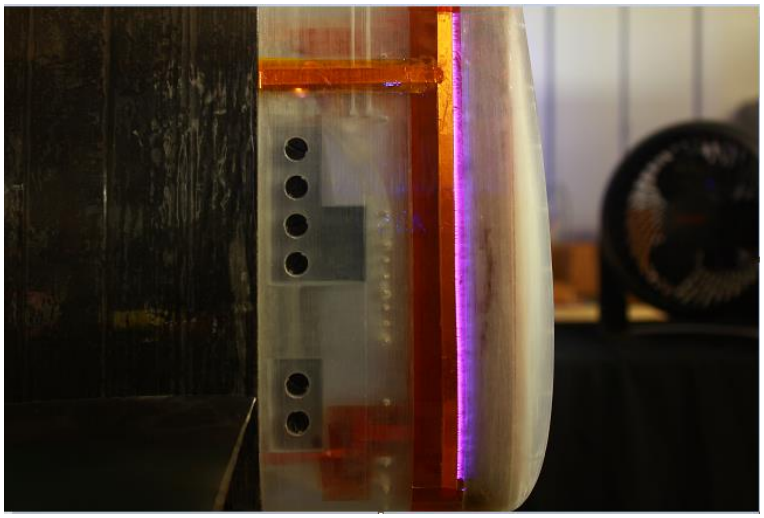

Figure 3-15 Plasma distribution for wing tip plasma actuators

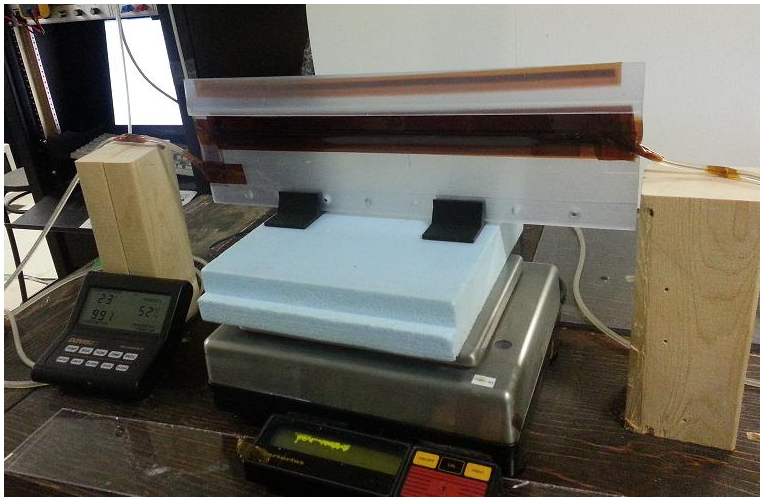

Figure 3-16 Characterisation of plasma actuators

3.2.4 Endplates

Endplates are used in the experimental test to improve aerodynamic performance by achieving a two-dimensional flow over the entire wingspan with plasma Gurney flap, and near the wing root for wings with plasma wing tip actuators. As shown in Figure 3-17, endplates are of rectangular shape and made of 6 mm-thick plexiglass. The edges of the endplates are machined to have wedge shapes, with 3mm thickness at the wedge ends, as shown in the cross section view. The four corners of the endplates are chamfered to avoid sharp corners and thus to reduce shedding vortices from

the endplates during tests. The endplates are attached to the wings using screws and foam tapes are applied between wings and endplates to ensure good insulation and to avoid flow leakage from pressure side to suction side.

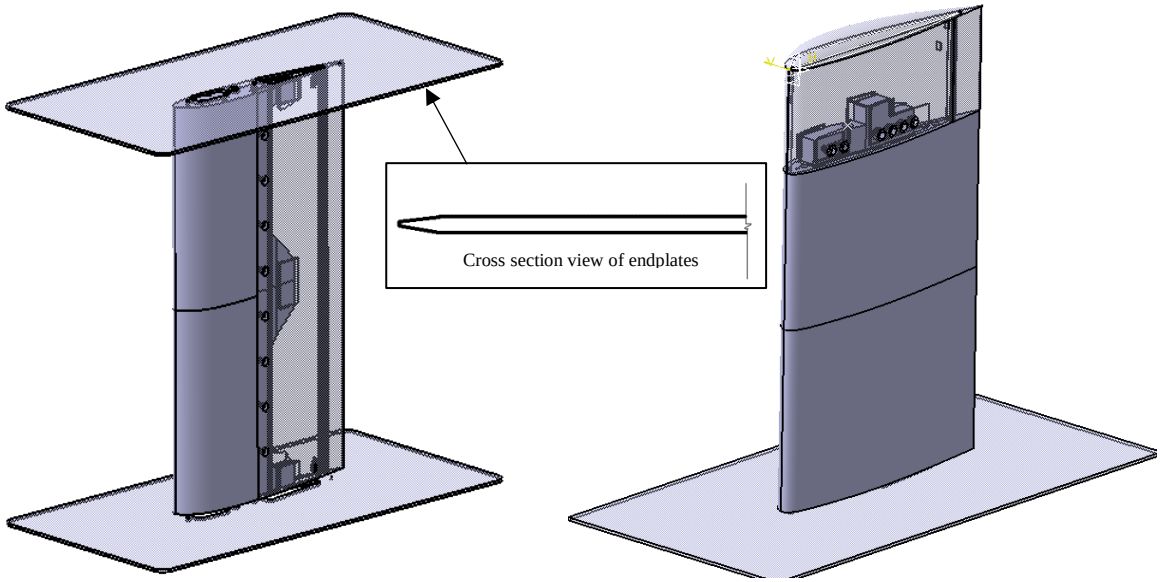

Figure 3-17 Wing models with endplates

The dimension of the endplate is an important factor which influences the flow characteristics over the test wings. Ahmed *et al.* [79] decided to use two endplates of 2.6 chord length (0.83 chord ahead of wing leading edge), 1.5 chord height to ensure two-dimensional flow. A short distance may fail to create a two-dimensional flow. However, a long distance between leading edges of endplates and airfoils may result in a thick boundary layer on the inner side of endplates, leading to an inward spanwise flow component along the wing. Moreover, longer endplates will tend to vibriate more easily at high speeds and affect force reading. The length of endplate was therefore choosen as 2.4 chord (with the endplate's leading edge at 0.8 chord ahead of wing leading edge) and its height as 1.2 chord.

The assembled wing and endplates (or test model) is positioned in the middle of the test section and is connected to L-shaped force balance by NPT 1/2" nipples and couples. High voltage input wires from plasma acutuators go through the holes on nipple/couple and pipe inside vertical arm of force balance to plasma generator system (the force balnace will be introduced in next section). With these configurations, the wires connected to test model will have negligible effect on the force measurement.

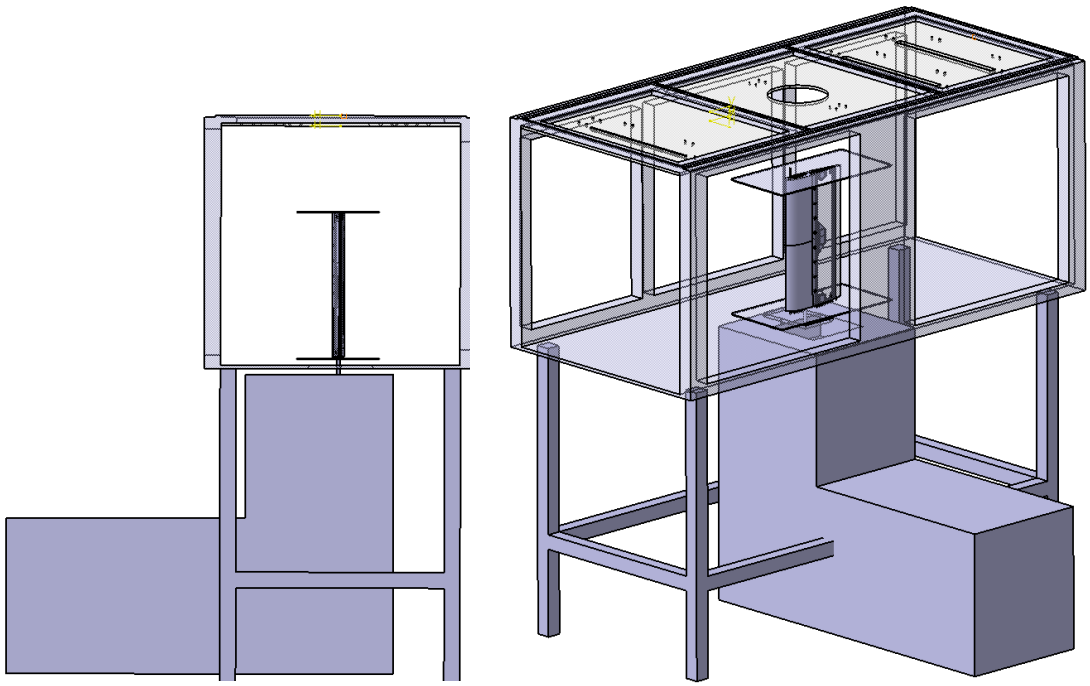

Figure 3-18 Test model and L-shaped force balance

A needle is attached to the trailing edge of the wing for angle of attack measurement (see Figure 3-19). The needle has a diameter of 1.1 mm, length of 50 mm. A printed protractor with the origin located at vertical arm of force balance is placed on bottom surface of test section. The protractor has a range from -10 to +10°, with an accuracy of 0.25°. The angle of attack is changed at one quarter chord of test wings.

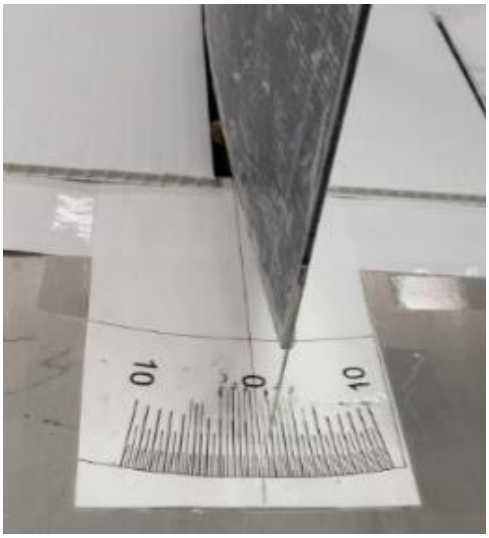

Figure 3-19 Angle of attack measurement for test model

3.2.5 Force Measurements

As shown in Figure 3-20, an L-shaped beam balance is used to measure the lift of the test wings. This setup converts the lift measurement into moment measurement by the change in the force exerted on an electronic scale. The balance is made of two orthogonal wood arms, which are specially designed to enhance their stiffness to avoid electrical sparking when applying high voltages on plasma actuators. A pipe is embedded inside the vertical arm, allowing high voltage wires go through it and connecting to plasma generator system. A wedge block is attached to the horizontal arm and can adjust the distance to the pivot thus change measurement sensitivity. The shape of the wedge block is contacted with the scale, which can be treated as line contact with the surface. The pivot of the balance consists of a hollow tube mounted on a set of ball bearings through which high-voltage wires pass, to minimize any effect of the wires on the measured moment.

The L-shaped balance is placed inside a wood box, which has a length of 42 inches, a height of 37.5 inches, and a width of 18 inches. The ball bearings are fixed on a heavy wood block inside the box, to ensure the stability of the pivot. An electronic scale (model MyWeigh CTS 30000) and a pressure scanner NetScanner 9116 are placed inside the box for acquiring force and pressure data, respectively. The electronic scale has a capacity of 30 kg (equivalent to 300 N), an accuracy of 0.5 g (5 mN), and can be connected to computer using serial port. The scale is placed far away from the pivot to avoid electromagnetic effect from high-voltage wire. A window on the box also allows visual reading of the electronic scale. As shown in Figure 3-20, the distance L_1 from the wing root to the balance pivot is 0.746 $\pm$0.005 m for wings with endplates, 0.801 $\pm$0.005 m for wings with wing tips. The distance L_2 from the contact point between wedge block and scale to the balance pivot is 0.428 $\pm$0.005 m.

The section lift of the test wing varies in spanwise as well as its distance to the balance pivot varies. This integral moment is ideally equal to the moment measured by the scale because of the level principle. The force balance was calibrated by hanging known weights through a pulley at measured attached points and measuring the scale reading, as shown in Figure 3-21. Calibration for four different positions were performed, with at least three repeated cases for each position (more details are given in Appendix B).

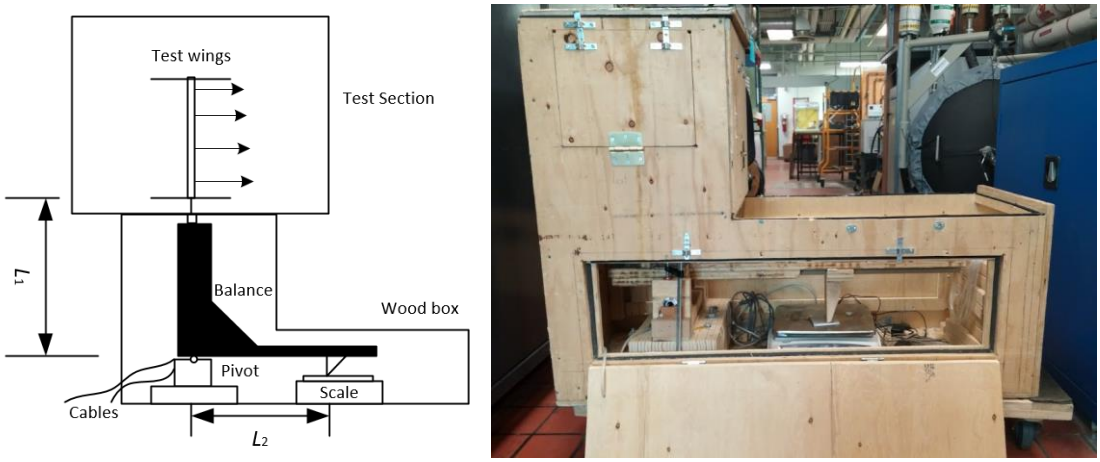

Figure 3-20 Schematic and picture of L-shaped force balance

Figure 3-21 Calibration setup for L-shaped force balance

3.2.6 Pressure Measurements

The pressure distribution on wing surfaces is measured by an Ethernet-based Pneumatic intelligent pressure scanner, NetScanner^{TM} System 9116. The scanner has built-in re-zero, purge and leak check features, and can measure pressure of 16 channels up to 10 inches water (2.5 kPa) with an accuracy of $\pm$ 0.15 % full scale, a resolution of $\pm$ 0.003 % full scale.

A pitot-static tube is placed at 2.7 chord upstream of the wing leading edge to measure the upstream velocity. The tube is connected to the pressure scanner by plastic tubes with an inner diameter of 1/4” (6.4mm). Pressure taps on the wing surfaces are connected using plastic tubes of 1/16” (1.6 mm) and 1/32” (0.8 mm), in order to have the maximum number of pressure taps for wing tip pressure distribution measurement. According to the experimental study from Whitmore *et al.*[80], for a tube with an inner diameter of 0.04” (1 mm) with a length of 8 ft (2.4 m), the attenuation of

signal above 50 Hz is larger than -20 dB. This means that high frequency components above 50 Hz are damped out. Therefore, the frequency of pressure scanner is set to be 50 Hz.

3.2.7 PIV Setup

Because of the limitation in operating time length of existing plasma actuators (in a few minutes), it would be impossible to use wake survey to capture the flow field in the wake, which could take hours using a pitot tube on a traverse. On the other hand, Particle Image Velocimetry (PIV) is a full-field, non-intrusive and instantaneous flow measurement technique. As such, it is the best method for flow field measurement of wings with plasma actuators.

The PIV system used for this research consists of a NewWave Solo pulsed Nd/YAG laser, a cooling pump, a timer box for synchronizing, two FlowSense 2M/E CCD cameras equipped with 62 mm Nikon F-mount lens, and a PIVTEC GmbH seeding generator. The NewWave Solo laser is a compact, dual laser-head laser designed to provide highly stable green light with output energy from 65 to 200 mJ at wavelength $\lambda = 532$ nm. The laser beam has a diameter of 4 mm, and is transformed into a laser sheet by a cylindrical lens. The flow is seeded with olive oil droplet (the average size of droplet is ~1 μm) by the seeding generator.

PIV images are acquired by CCD cameras which are connected to a computer by National Instrument PCIe 1433 acquisition cards, triggered by a synchronizing timer box. The CCD camera sensor has both 8-bit and 10-bit output, and a resolution of 1600 × 1200 pixels. Two hundred double-framed PIV pictures are sampled at 15 Hz and then averaged to obtain the mean and root-mean-square (RMS) velocity fields. The time delay between two laser pulses (or time delay for two frames of PIV pictures) is set to 100μs. The software Dantec Dynamic Studio is used to control the laser and camera, as well as to acquire and post-process the pictures. An adaptive correlation method is applied to calculate the vector maps, with an interrogation area size of 32 × 32 pixels and a 50% overlap.

As shown in Figure 3-22, the PIV setup for plasma Gurney flap consists of having the laser sheet aligning horizontally with the mid-span of the wing to measure the flow velocity field near the trailing edge region. The laser sheet has a thickness of around 2 mm and the camera is positioned on the top of the test section, looking downward and focusing on the airfoil trailing edge region.

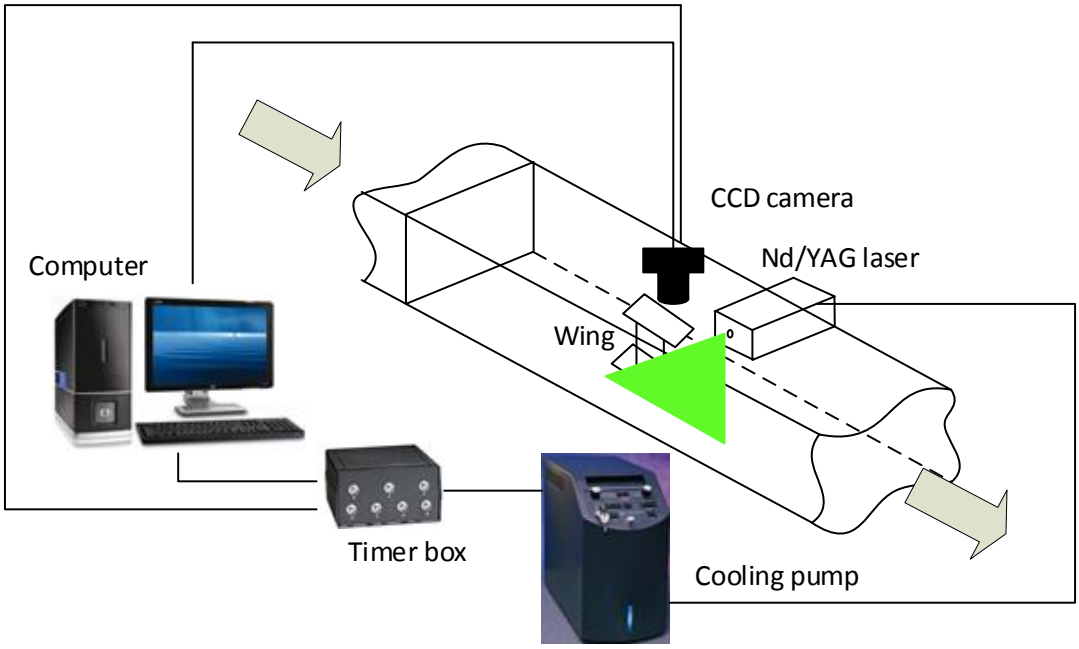

Figure 3-22 Schematic of PIV setup for plasma Gurney flap

3.2.8 LabVIEW Program

A LabVIEW program as shown in Figure 3-23 is used for data acquisition during test. This program can record the temperature reading from the thermocouple, as well as pressure data from the pressure scanner and balance reading from the electronic scale. The pressure distribution in the wing tip region can be displayed in a real-time graph, to compare with CFD results. The balance reading is acquired through a RS232 serial port which connects the electronic scale to the computer. Ambient temperature, pressure, and humidity are read from a meteorological station and manually input into the program.

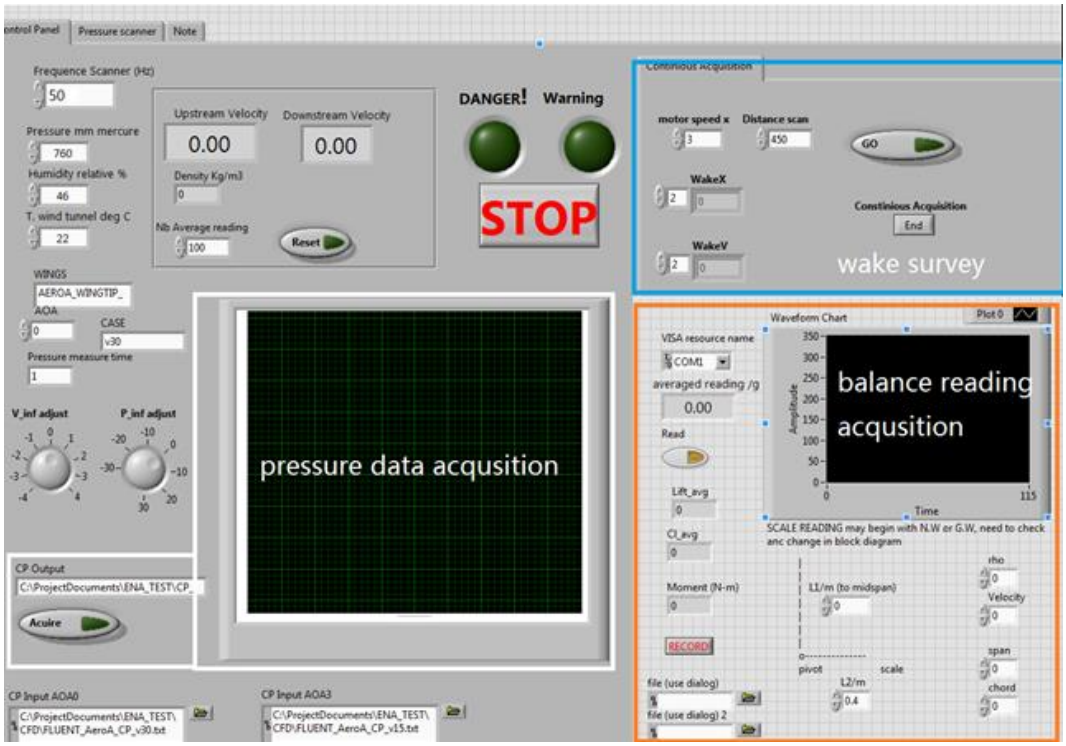

Figure 3-23 Display Panel of LabVIEW Acquisition Program

3.2.9 Data Reduction

Test Condition Data

The angle of attack is measured by a sharp needle and a protractor, with an uncertainty of ±0.25°. The temperature is measured by a thermocouple with an uncertainty of ±0.5℃. The pressure measured by the pressure scanner has an accuracy of ±0.15% of full scale (2.5 kPa), with an uncertainty of 3.8 Pa. The relative humidity and ambient temperature are measured by a metrological station, with uncertainties of 0.5% and 67 Pa, respectively.

The pressure coefficient is calculated according to equation (3.1)

$$C_p = \frac{p - p_s}{p_t - p_s} \tag{3.1}$$

where p is static pressure from wing surface, p_s is upstream static pressure used as reference pressure, p_t is upstream total pressure. The upstream velocity is obtained from equation (3.2).

$$U_\infty = \sqrt{2(p_t - p_s)/\rho} \tag{3.2}$$

The density ρ is calculated from equation (3.3)

$$\rho = M_d \frac{p_{atm}}{RT} + (M_v - M_d) HR \frac{610.78}{RT} 10^{\frac{7.5(T-273.15)}{T-35.15}} \quad (3.3)$$

where p_{atm} is ambient absolute pressure, T the ambient temperature (in Kelvin), RH the relative humidity, M_v and M_d the molar mass of water vapor (0.018016 kg/mol) and dry air (0.028964 kg/mol), and R the universal gas constant 8.314 J/(K-mol) .

Force Measurement Data

The balance reading $\overline{R}$ is obtained by equation (3.4).

$$\bar{R} = \frac{(\bar{R}_1 - R_{1,offset}) + (\bar{R}_2 - R_{2,offset}) + (\bar{R}_3 - R_{3,offset})}{3} \quad (3.4)$$

where $\bar{R}_i$(i=1,2,3) is averaged balance data over at least 30 seconds, $R_{i,offset}$ the reading offset with wind tunnel off. The averaged moment by wing lift is calculated by equation (3.5).

$$\bar{M}_1 = \frac{\bar{M}_2}{a} = \frac{\bar{R} L_2}{a} \quad (3.5)$$

where L_2 is the distance between pivot and scale (see Figure 3-20) and a=0.969$\pm$0.005 from calibration. The moment difference by plasma actuation is then calculated by equation (3.6).

$$\Delta\bar{M}_1 = \bar{M}_{1,plasma} - \bar{M}_1 \quad (3.6)$$

The measured moment is the integral moment to the pivot for wing (the lift varies in spanwise direction), therefore it cannot converted into lift or lift coefficient. Therefore, the moment will be compared directly with simulation results.

PIV Data

The captured images from PIV are processed using adaptive correlation in Dantec PIV software Dynamic Studio v3.1, and averaged flow field vector maps are then obtained over 200 vectors maps for each test case, as shown in Figure 3-24. The mean vector maps are imported to MATLAB as text files. A MATLAB program is written to compute streamlines (shown in Figure 3-25) and to compare trailing edge streamlines with and without plasma to visualize plasma effect.

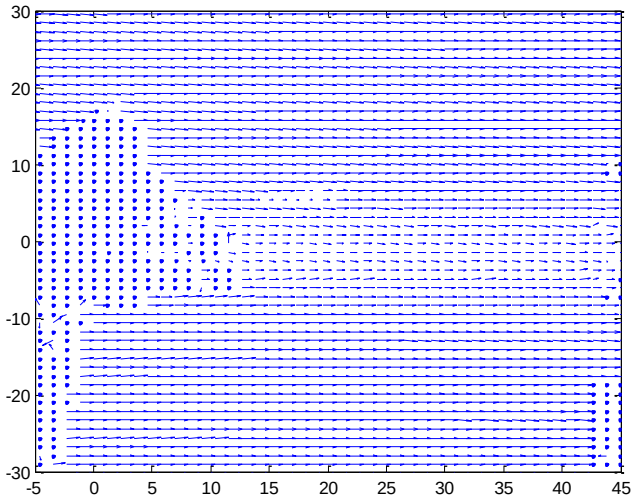

Figure 3-24 PIV averaged vector map from Dynamic Studio

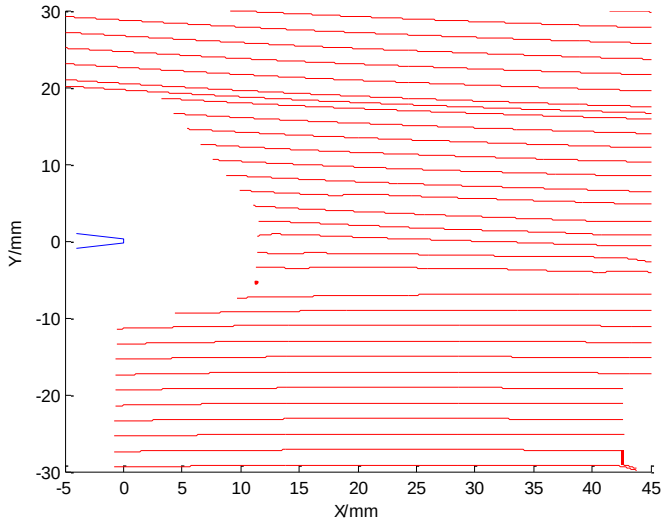

Figure 3-25 Computed streamlines from MATLAB

3.3 Numerical Study

In this section, the CFD solver and the implementation of plasma model are introduced first. The simulations for the test wings at low-speed wind tunnel are then presented, followed by simulations for tapered and swept wing. Finally, simulations for realistic wings of a typical full-scale high subsonic commercial airliner are presented.

CFD Solver

A three-dimensional, pressure-based, double precision, steady segregated solver is chosen for CFD simulations with commercial software ANSYS FLUENT. Two turbulence models, Spalart-Allmaras full turbulence model, and Shear Stress Transport are applied in FLUENT. The Spalart-Allmaras model is designed specifically for aeronautics and aerospace applications involving wall-bounded flows and has been shown to give good results for boundary layers subjected to adverse pressure gradients. The Shear Stress Transport turbulence model is a combination of the k-epsilon model in the free stream and the k-omega models near the walls, and can be modified to simulate laminar-turbulent transition of wall boundary layers. The standard SST model (k–omega SST) is used in FLUENT.

Some of the solver settings in FLUENT are listed in Table 3-1. Green-Gauss Node-Based is chosen for gradient reconstruction. At least second order discretization schemes are used for pressure, momentum and turbulent quantities. Under-relaxation factors are set to be 0.5.

Plasma Implementation

In the present work, Lemire and Vo's [74] engineering model is applied to calculate the spatial distribution of plasma body force. The original code is written in MATLAB, and can generate a desired plasma actuation strength in 2D space and be imported into FLUENT. To incorporate the plasma actuators in the CFD simulations, the spatial body force distribution on the very fine 2D Cartesian mesh is mapped onto the curved CFD mesh, using the process described by Lemire and Vo [74].

Preliminary validations for the plasma model have been carried out by previous colleagues. Xu [77] had simulated instantaneous vorticity fields for a plasma actuator on a flat plate with plasma actuator strength of 30 mN/m. CFD simulation results with Lemire's plasma model is consistent with documented wall jet experiments, as shown in Figure 3-26. CFD simulation showed similar vortex structures with PIV measurement, which validate the application of current plasma model with CFD tools.

Table 3-1 Solver settings in FLUENT

Turbulence Model	SST	Spalart-Allmaras
Time mode	Steady, Pressure-based	
Pressure-Velocity Coupling Scheme	SIMPLE	
Gradient	Green-Gauss Node Based	
Spatial Discretization		
Pressure	Second Order	
Momentum	Second Order Upwind	
Turbulent Kinetic Energy Specific Dissipation Rate	Second Order Upwind	N/A
Modified Turbulent Viscosity	N/A	Second Order Upwind
Under-Relaxation Factors		
Pressure, Density, Body Forces, Momentum, Turbulent Viscosity	0.5	
Modified Turbulent Viscosity	N/A	0.5
Turbulent Kinetic Energy Specific Dissipation Rate	0.5	N/A

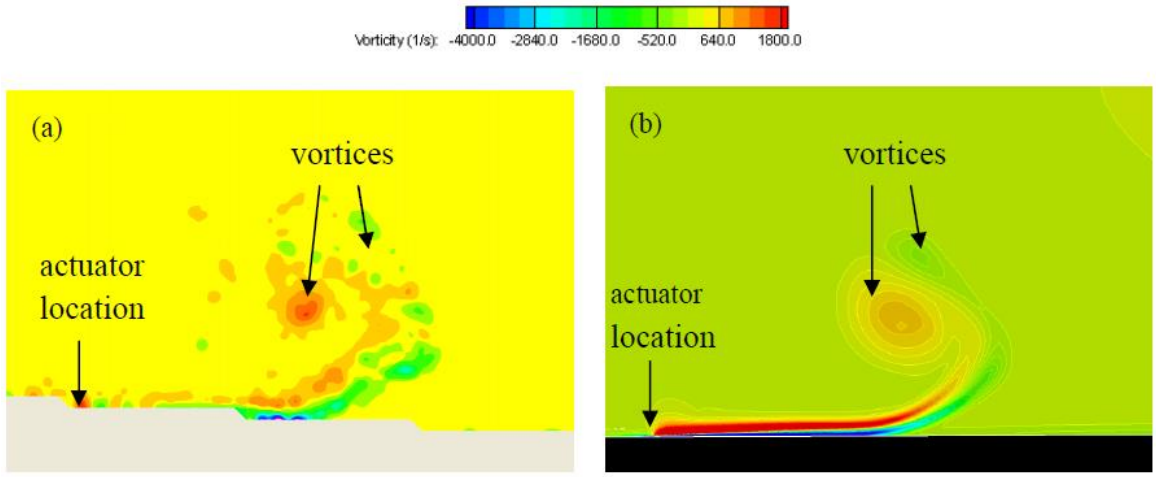

Figure 3-26 Instantaneous vorticity fields for plasma actuator in quiescent air from (a) measured PIV and (b) CFD [77]

To accelerate the plasma implementation process and to make it feasible for 3D CFD mesh geometry, a new MATLAB code named PLASMA2GO was developed. The spatial body force distribution can be generated for both suction and pressure sides, blowing spanwise and chordwise. This new code uses block information files (which contain node coordinates of structured meshes)

from ICEM CFD meshes, and maps the body force spatial distribution from the plasma model onto each mesh layer with desired direction, position and plasma actuation strength. More details are given in Appendix F.

For plasma Gurney flap on wings with endplates, the body force is mapped on multiple spanwise layers at desired actuator locations near the trailing edge as shown in Figure 3-27. For wings with rounded wing tips, the body force is mapped onto multiple chordwise layers at desired actuator locations near wing tip region as shown in Figure 3-28. The locations of plasma actuators on both sides are set to match those of test wings. The actuation strengths of plasma actuators (F_B) in wind tunnel tests are provided by plasma characterisation results (see Appendix C). The actuation strengths F_B of plasma Gurney flap for wing AG and NG are 55±5, 60±5 mN/m, respectively. The actuation strengths of plasma wing tip actuators for wing AG are 65±10 and 90±5 mN/m, for NG wing 80±10 mN/m. The actuation strengths of plasma Gurney flap for tapered wing ATtap, swept wing ATsw in Chapter 5 are all 100 mN/m.

The generated body force files from MATLAB includes mesh nodes coordinates, cell ID for FLUENT, and body force components in three directions. These files are then implemented into FLUENT using a user defined function by C++, which enables FLUENT to read cell ID from files, match cells and assign corresponding body force components to cells. These body force values are stored in the user-defined memory of FLUENT, and then are applied into CFD simulations as source terms. The implementation result of plasma body force can be shown as user-defined memory contours in FLUENT, as shown in Figure 3-29 for plasma Gurney flap and Figure 3-30 for plasma wing tip actuators (only one component of body force is shown).

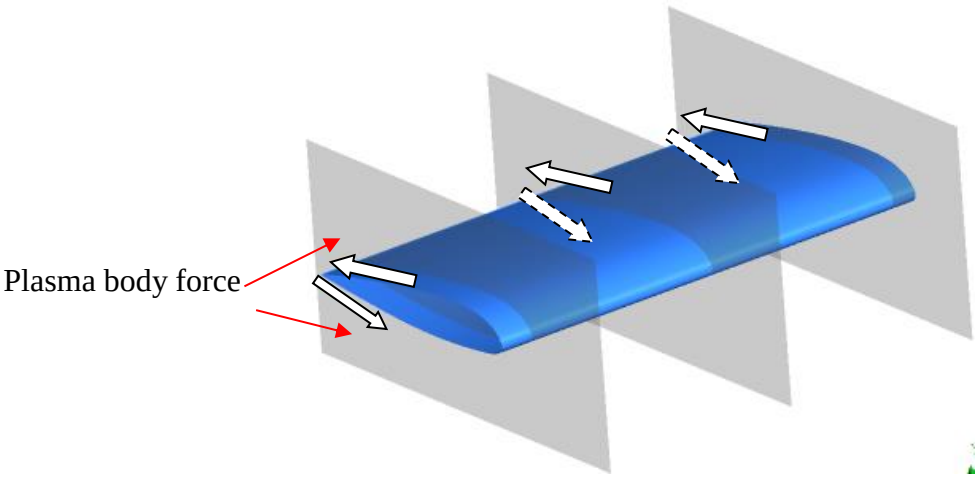

Figure 3-27 Body force implementation for the AG wing

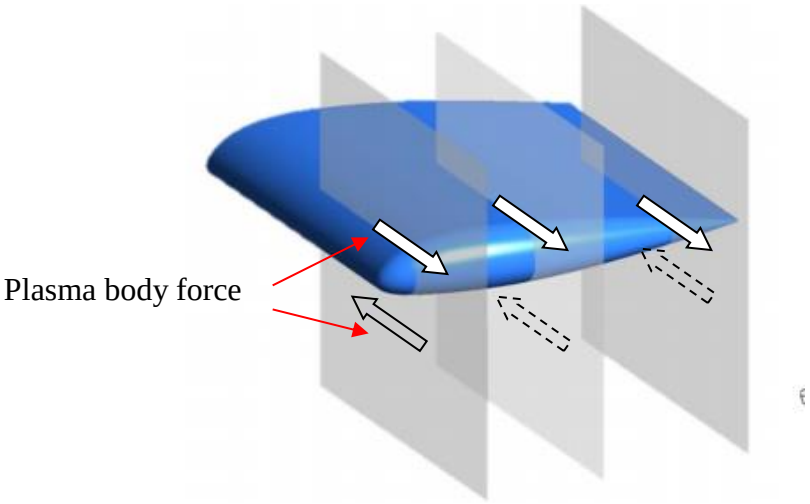

Figure 3-28 Body force implementation for AT wing

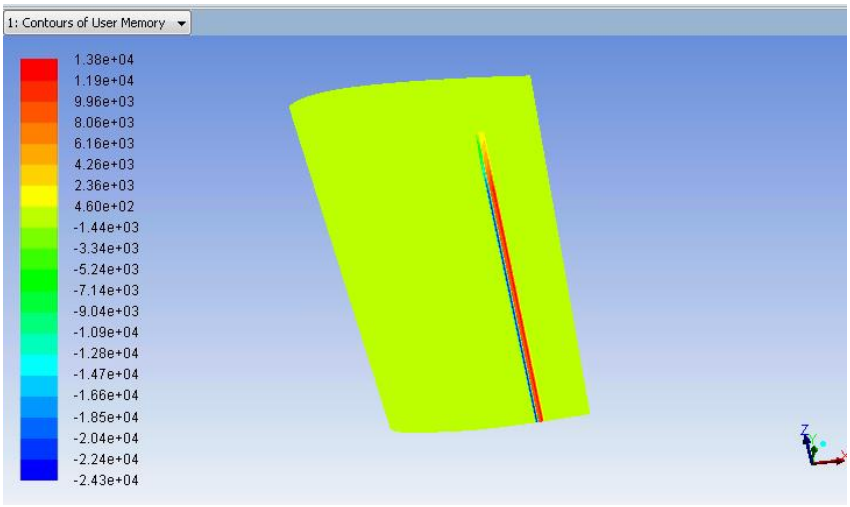

Figure 3-29 Plasma body force distribution of AG wing

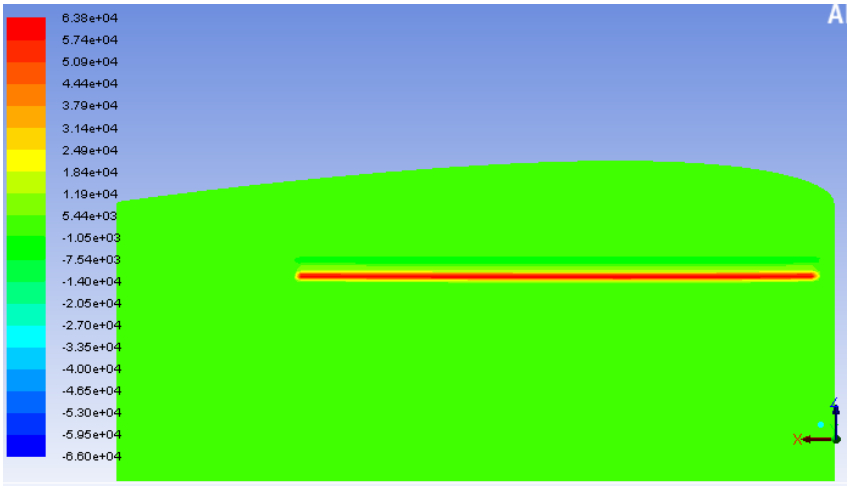

Figure 3-30 Plasma body force distribution of AT wing

3.3.1 Test Wing Simulations

Fluid Domain and Boundary Conditions

The fluid domain for test wing simulations is shown in Figure 3-31 (cross section) and Figure 3-32 (3D). The blue dash rectangle in Figure 3-31 represents the wind tunnel test section (see Section 3.2.1), which is 7.2 chord long, and 3 chord high. The inlet and outlet of the simulation domain is far from the wing (15.4 chord) to avoid simulation divergence. The test section walls are modified slightly by empirical flat plate boundary layer displacement thickness to account for the growth of boundary layer near walls.

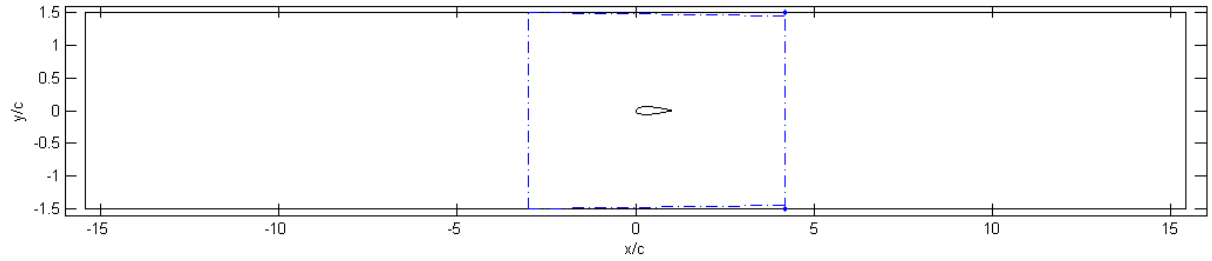

Figure 3-31 Schematic of fluid domain

Figure 3-32 also shows the boundary conditions used in wind tunnel simulations. Boundary conditions for upstream inlet and downstream outlet are velocity inlet and pressure-outlet. The turbulence intensity of velocity inlet is 0.44% according to wind tunnel characterisation. Boundary conditions for wind tunnel side walls are symmetry. Wing and endplates use no-slip walls as boundary conditions.

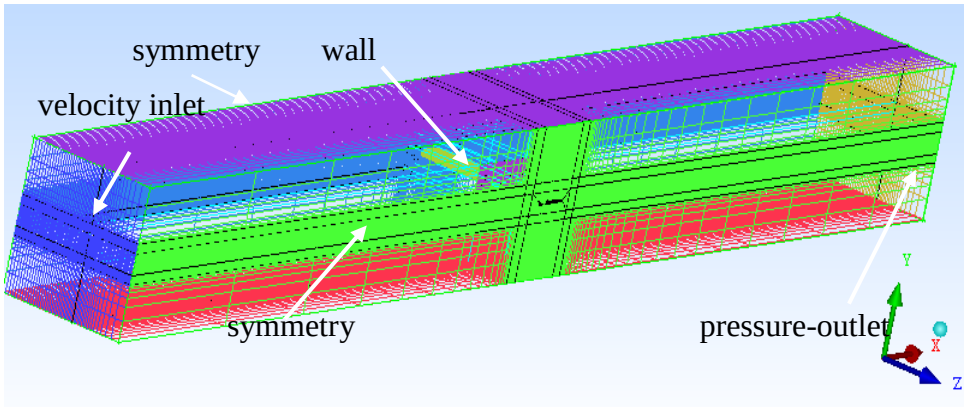

Figure 3-32 Flow domain and boundary conditions for wind tunnel simulations

Meshes

As shown in Figure 3-33, the fluid domain is split into multi-block in ANSYS ICEM CFD to generate structured meshes. Figure 3-34 and Figure 3-35 show the mesh structure and surface meshes for AG and AT wings. For AG wing, one zero-thickness endplate is meshed to simplify the mesh generation. Mesh near trailing edges and wing tips are refined to have enough mesh density for implementation of plasma actuators, as show in Figure 3-36. The first layers of meshes near wing surfaces have a height of 2.4×10^{-5} chord to ensure y+ is lower than 1. The structural meshes are then imported into FLUENT for CFD simulations, and also converted into block information files to generate plasma body force as mentioned before. Mesh studies are carried out to ensure mesh independency as shown in Appendix D. The mesh size is 2,838,523 for the AG and NG wings, and 2,087,478 for the AT and NT wings.

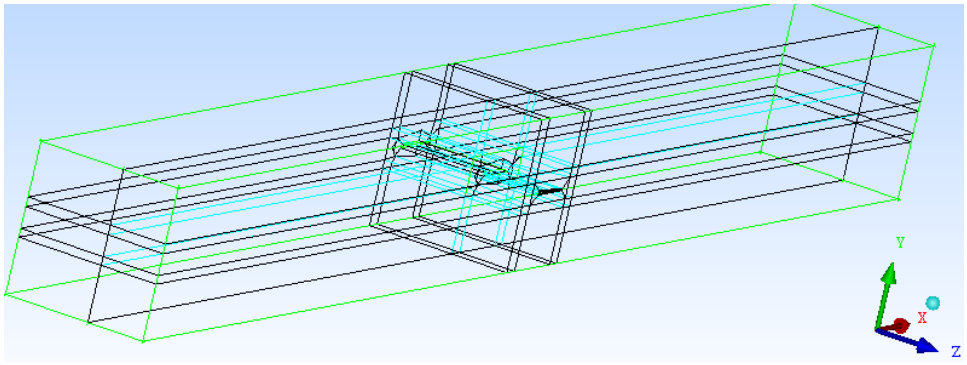

Figure 3-33 Mesh topology for wings in wind tunnel

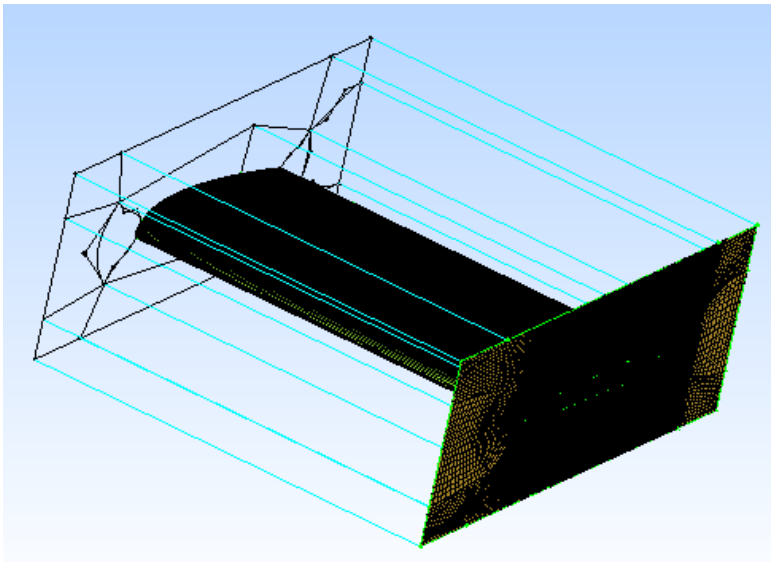

Figure 3-34 Mesh topology and surface mesh of AG wing

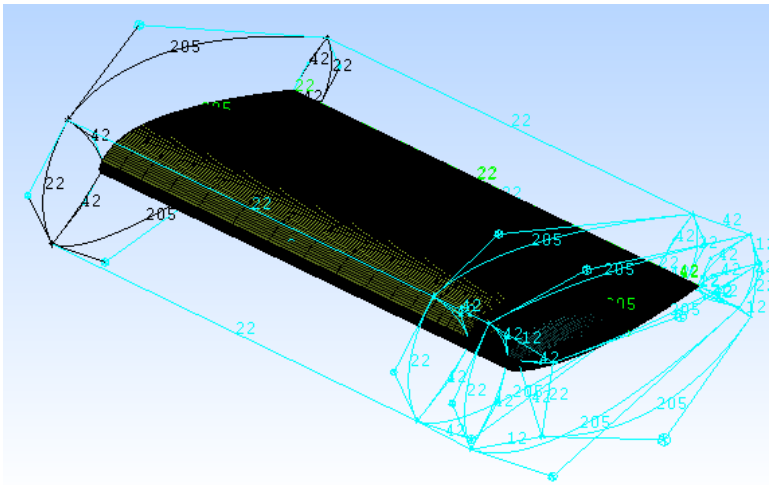

Figure 3-35 Mesh topology and surface mesh of AT wing

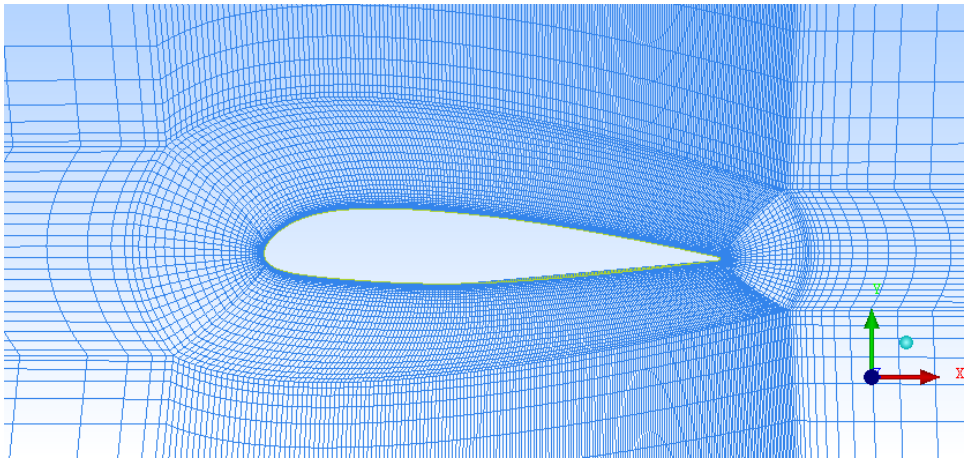

(a)

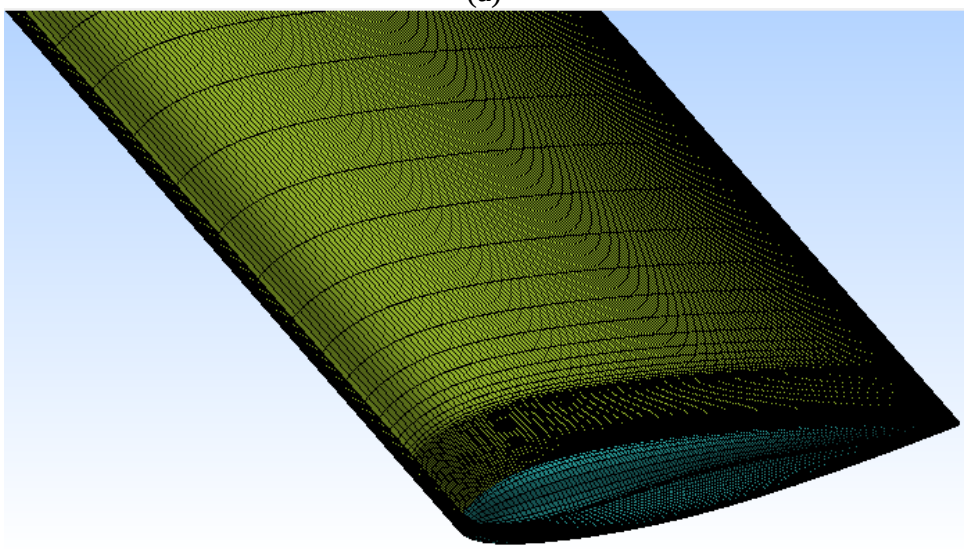

(b)

Figure 3-36 Cross section mesh (spanwise plane) for AG wing and surface mesh for AT wing

Validation

CFD tools are firstly validated with experimental wind tunnel data from existing literature to check the reliability of the CFD solver in the preliminary stage. Martínez-Aranda *et al.* [81] had studied an 3D NACA 0012 wing with wing tip (AR=2) at low-to-moderate Reynolds numbers (3.33×10^4 – 1.33×10^5) and summarized the aerodynamic characteristics for NACA 0012 airfoil with rounded wing tip for any aspect ratio, as shown in equation (3.7).

$$\frac{\Delta C_L}{\Delta \alpha} = \begin{cases} 0.00012 AR^{0.5} Re_c^{0.51}, Re_c < 10^5 \\ 0.042 AR^{0.5}, Re_c > 10^5 \end{cases} \quad (3.7)$$

The aspect ratio of the current test wing is AR=1.8, and Reynolds number is larger than 10^5, therefore the slope $\Delta C_L/\Delta\alpha$ is 0.0563 deg^{-1}.

Figure 3-37 compares the calculated lift coefficients from CFD simulations with test data for NACA 0012 at three angles of attack with free stream velocity of 20 m/s, Re=1.33×10^5, and inlet turbulence intensity of 2.3% [81]. It can be observed that simulation results with both SA and SST models agree with the test data of Martínez-Aranda *et al.*, with a slope $\Delta C_L/\Delta\alpha$ of 0.056 – 0.057 deg^{-1}, proving the reliability of the CFD process in the mesh generation and solver settings.

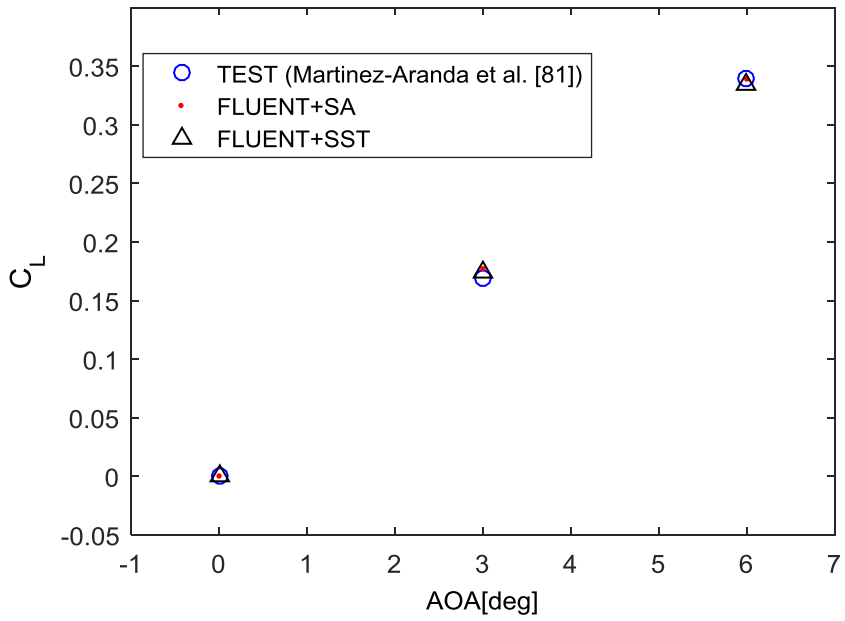

Figure 3-37 Lift coefficients of experiments and simulations for NACA0012 with wing tip

3.3.2 Tapered & Swept Wing Simulations

Most of current research for plasma actuators on wings are focused on extruded 2D wings, and there are only limited publications on tapered or swept wings. Duchmann *et al.* [71] have tested plasma actuators on a trapezoidal wing to study turbulence transition under in-flight condition. The DBD plasma actuator extends over the whole spanwise length of the measurement region on pressure side, located at 0.33 chord from leading edge. Patel *et al.* [82] studied the leading-edge and trailing edge plasma actuators on different full-span and half-span unmanned air vehicles (1303 UCAV scaled models), with plasma actuators aligning parallel to the leading edge or trailing edge. Optimum lift enhancement was achieved by placing the actuators at a chordwise location that was close to the leading edge on the suction side at 0.03 chord. However, no force measurements are reported for these studies.

To investigate the possibility of applying plasma actuators on real wing geometries, the AT wing is tapered and swept, while keeping span and lift coefficients the same. As shown in Figure 3-38, the tapered wing (referred as ATtap) has an aspect ratio of 2.2, a taper ratio of 0.56 and a swept angle of zero for one-quarter position. The swept wing (referred as ATsw) has an aspect ratio of 1.7, a swept angle 26.7° for one-quarter position and a taper ratio of zero. Meshes are generated using the same topology as the AT wing, and mesh studies are carried out to ensure mesh independency. Mesh sizes for tapered wing and swept wing are 2,312,220 and 2,817,208, respectively.

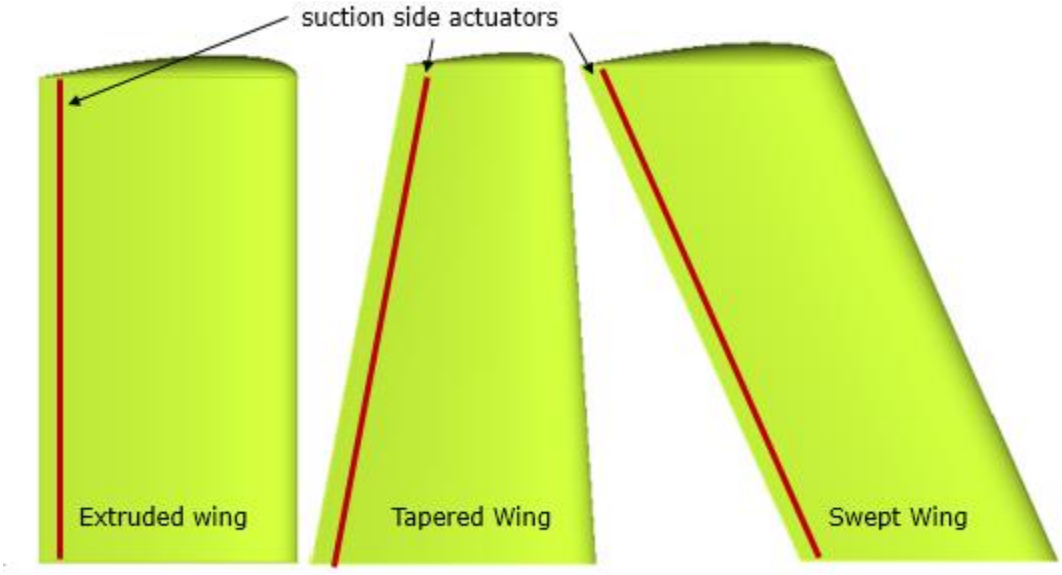

Figure 3-38 Extruded, tapered and swept wings with plasma Gurney flap

The CFD solver and fluid domain for tapered wing and swept wing simulations can refer to previous test wing simulations. Free stream velocity is set to be 20 m/s, AOA = 0°, Re = 3.33 × 10^5. To study the taper and swept effect on plasma actuation, the tapered ATtap and swept ATsw wings without plasma actuation are scaled chordwise to have the same 3D total lift with plasma actuation as the extruded AT wing by trial and error, while keeping AOA, Reynolds number and Mach number constant. Plasma actuators are then applied at trailing edges of each scaled wing, to estimate plasma effect on lift coefficients. The plasma Gurney flap is placed at 76 % chord for suction side, 82% chord for pressure side on wing root, extending spanwise from wing root to near wing tip (90% span) parallel to trailing edge. The plasma actuator on pressure side blows upstream and the suction side actuator blows downstream. The wing tip plasma actuator is not studied for the tapered and swept wings because the geometry change only affect spanwise plasma distribution and not chordwise plasma distribution. Moreover, the tapered wing has smaller lift than extruded wing at same spanwise locations. Since plasma wing tip actuation only affect the lift in the tip region, the effect of this concept will be even smaller than that for the extruded wing.

3.3.3 Realistic Wing Simulations

To simulate plasma actuation on realistic wing geometries under real-flight conditions, a three-dimensional, pressure-based, double precision, steady solver is chosen for CFD simulations with ANSYS FLUENT. Spalart-Allmaras and Shear Stress Transport turbulence models are used with energy equation turned on.

A symmetrical swept-tapered transonic wing ONERA M6 [83] (which has a max thickness 10% at 38% chord) is chosen because of availability numerous of CFD and experimental data from literatures. The original wing (referred as M6) has a root chord of 31.73 inches, span of 47.1 inches, aspect ratio of 3.8, taper ratio of 0.56, swept angle of 26.7° for one-quarter position. To investigate the possibility of replacing traditional control surfaces, plasma Gurney flap and plasma wing tip actuators are simulated on two scaled ONERA M6 wings to present the geometries of wings and horizontal tails of commercial jet Boeing 737 (as shown in Figure 3-39). One wing (referred as M6t) has a chord of 2.5 m to represent 737 horizontal tail, and one wing (referred as M6w) has a chord of 8.0 m to represent 737 wing.

The two plasma actuation concepts are studied on M6w and M6t wings. The plasma Gurney flap is placed as close as possible to the trailing edge, with both pressure and suction side actuators located at 90 - 95 % chord, spreading from wing root to 85% span. The plasma wing tip actuators are located at 96% span on pressure and suction sides and cover the full chord.

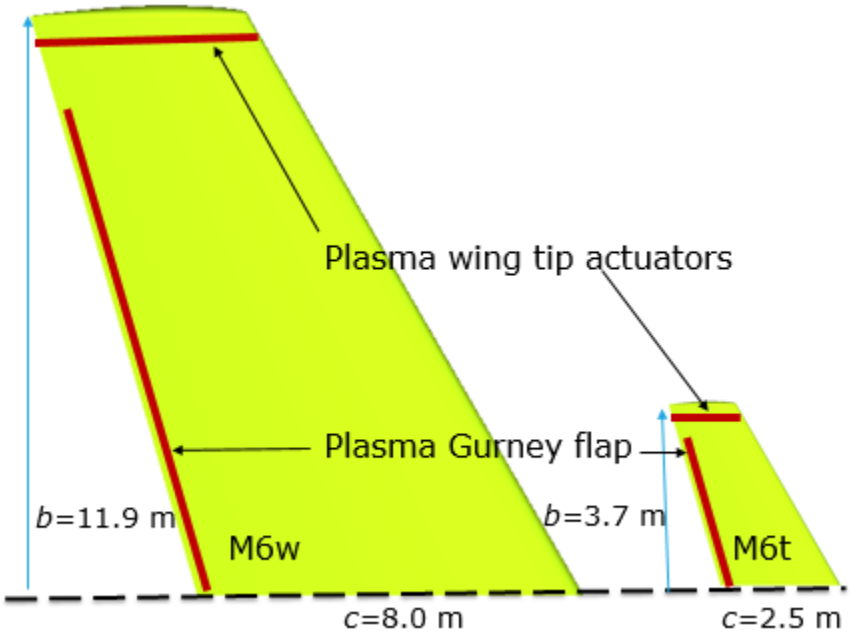

Figure 3-39 M6w and M6t wings with two plasma actuation concepts

The wings are located inside a flow domain of 60 chord long, 30 chord high, and 30 chord wide, with the inlet located at 16 chord upstream of airfoil leading edge, as shown in Figure 3-40. Boundary conditions are no-slip walls for wing surfaces, symmetry for wing root wall, and pressure far field for the rest side walls, upstream inlet and downstream outlet.

To compare with existing experimental data, the M6 wing was firstly calculated at AOA = 3.06°, Mach = 0.84, Re = 1.172×10^7 to validate generated mesh and solver settings. The temperature of far-field is around 255 K (-18 ℃), absolute ambient pressure 80.5 kPa, air density 1.1 kg/m^3.

To simulate the full-scale wings at cruise condition, the freestream velocity for the M6t wing is AOA = 0°, Mach = 0.84, Re = 1.54×10^7, and for the M6w wing is AOA = 3°, Mach = 0.84, Re = 4.94×10^7. At flight level (around 30 000 ft=10 km), the far-field temperature is around 223 K (-50 ℃), absolute pressure 25 kPa, air density 0.4 kg/m^3.

To simulate wings at landing/takeoff conditions, the freestream velocity for the M6t wing is AOA = 0, Mach = 0.3, Re = 1.93×10^7, and for M6w wing, AOA = 3°, Mach = 0.3, Re = 6.21×10^7. The temperature of far-field is 283 K (10 ℃), absolute pressure 101.325 kPa, air density 1.25 kg/m^3. All meshes for the M6, M6t and M6w are generated using the same topology as the AT wing, as shown in Figure 3-40 and Figure 3-41, and mesh studies are carried out to ensure mesh independency. The mesh size is finally chosen as 2,234,988.

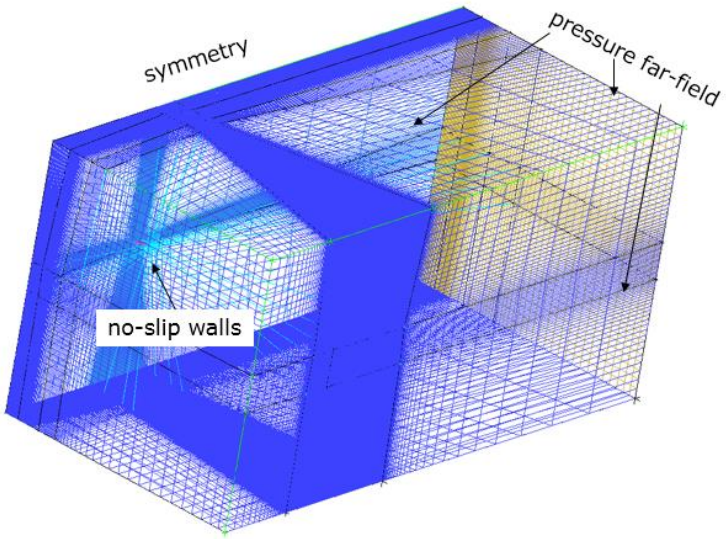

Figure 3-40 Fluid domain and boundary conditions for realistic wing simulations

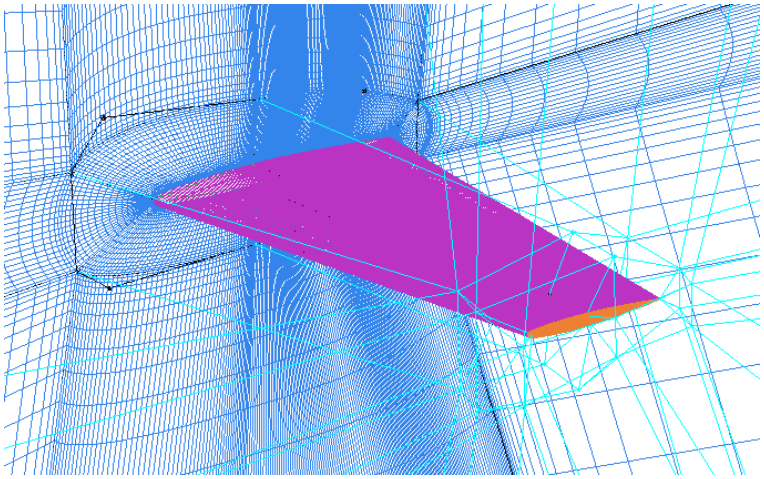

Figure 3-41 Surface mesh for the realistic wing simulations

CHAPTER 4 EXPERIMENTAL & CFD RESULTS

This chapter presents the results for the wind tunnel studies of the test wings to validate the numerical setup. First the test and CFD results without plasma actuation are introduced. Then, the plasma Gurney flap and wing tip actuation concepts for both asymmetrical and symmetrical wings are presented, followed by some discussions.

4.1 Wings without Actuation

Figure 4-1 and Figure 4-2 present the measured lift moments (TEST) from the L-shaped balance in the wind tunnel versus the equivalent CFD predictions from FLUENT using different turbulence models for the AG and AT wings at AOA = 0°, respectively. The averaged values of measured moments from repeated test cases are also shown in the figures. It can be concluded that at AOA = 0°, simulation results with both turbulence models match well with wind tunnel test data for the AG wing, while the simulation results with SST model match the test data better for the AT wing.

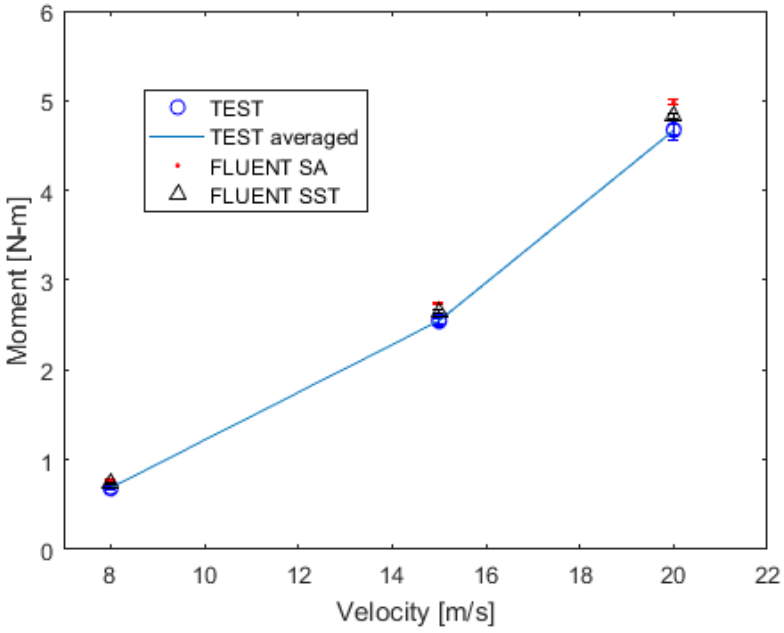

Figure 4-1 Moments comparison of TEST versus CFD for AG wing (AOA = 0°)

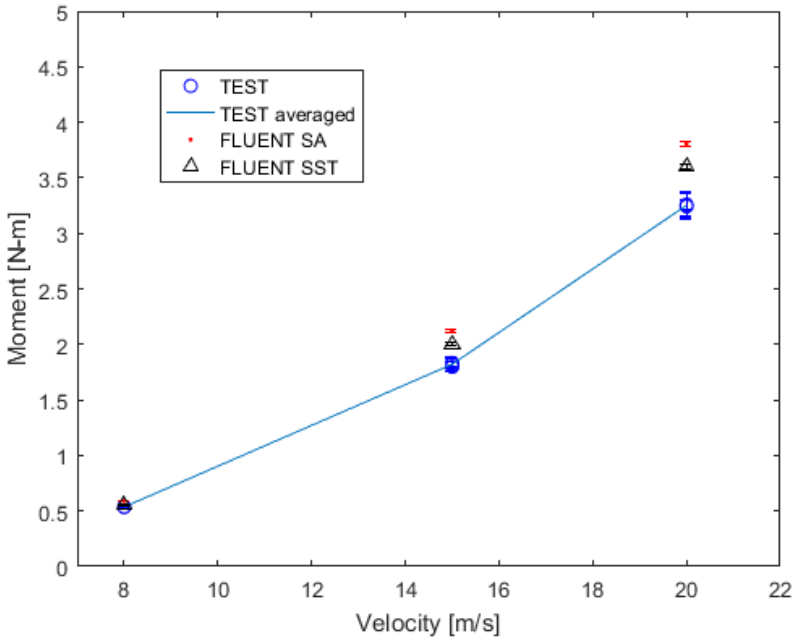

Figure 4-2 Moments comparison of TEST versus CFD for AT wing (AOA = 0°)

The pressure distributions on suction sides near the wing tip can be measured from pressure taps to further compare with CFD results. The pressure error is ~4.0 Pa for all speeds (including reading error ~0.3 Pa and instrument error ~3.8 Pa), therefore the pressure coefficient error is larger at 8 m/s than that at 20 m/s. Figure 4-3 and Figure 4-4 present the surface pressure distributions near wing tip for the AT and NT wings at different velocities at AOA = 0°. The results show that the CFD simulation results generally match with experimental data.

Figure 4-5 presents the effect of AOA on lift moments for the AG wing at 8 m/s. The moment increases at higher AOA as expected, and SA model predicts closer moment to test data than SST model at higher AOA. Figure 4-6 presents the same data for AT wing at three speeds. The results indicate that SA model over-predicts the moment for the AT wing at AOA = 3°, especially at high speeds. Nevertheless, the numerical predications are relatively quite good at both AOA values, with the SST results within 5% of test data at 15 – 20 m/s while the SA results are within 10%.

The pressure distributions for the AT wing at AOA = 3° are also simulated and compared with measured results (see Figure 4-7). Predicted pressure distributions near wing tip from SST model and SA model both generally match the experimental data.

Overall, for wings without plasma actuation, simulation results with SST and SA models generally match with experimental results and SST model performs better at higher AOA and speeds.

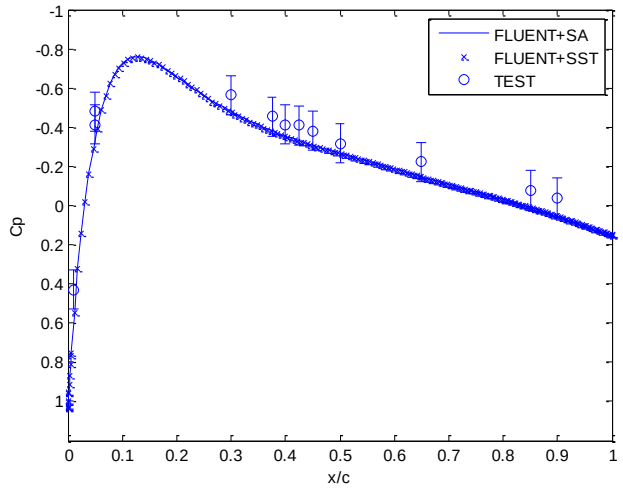

(a) 8 m/s

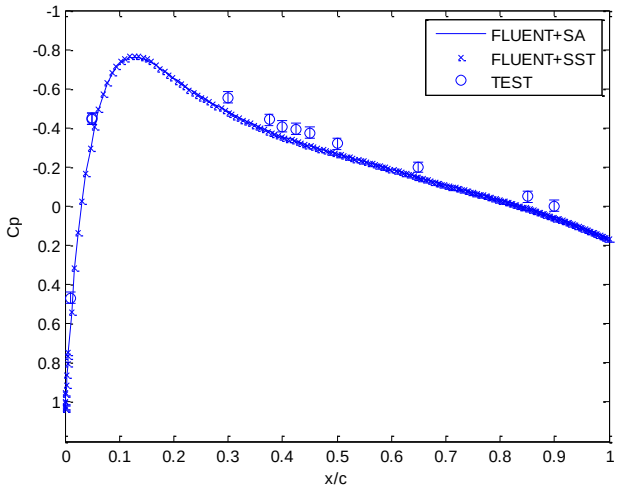

(b) 15 m/s

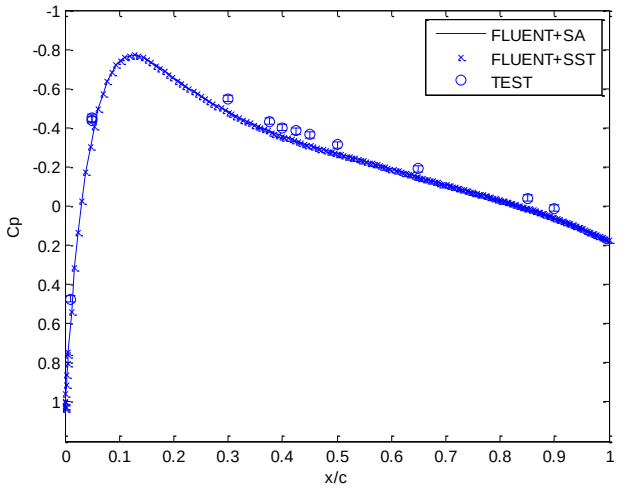

(c) 20 m/s

Figure 4-3 Pressure distribution of experiments and simulations for AT wing (AOA = 0°)

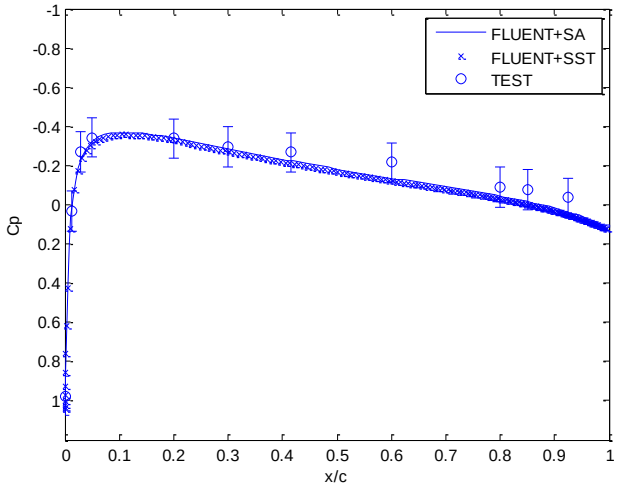

(a) 8 m/s

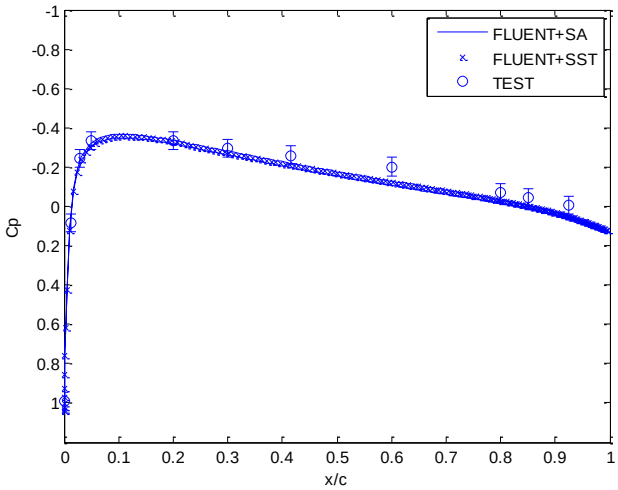

(b) 12 m/s

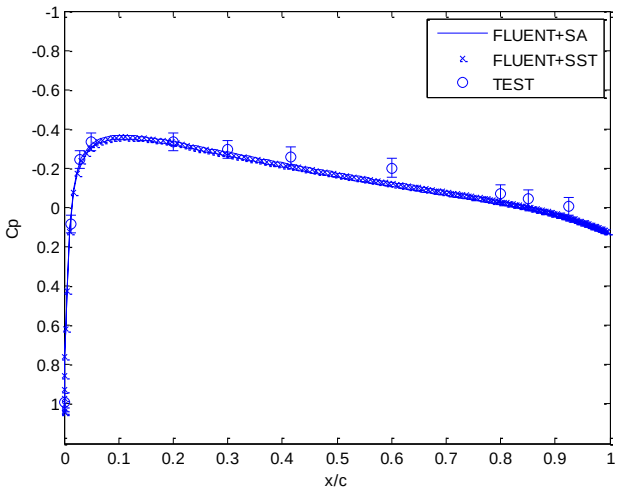

(c) 15 m/s

Figure 4-4 Pressure distribution of experiments and simulations for wing NT (AOA = 0°)

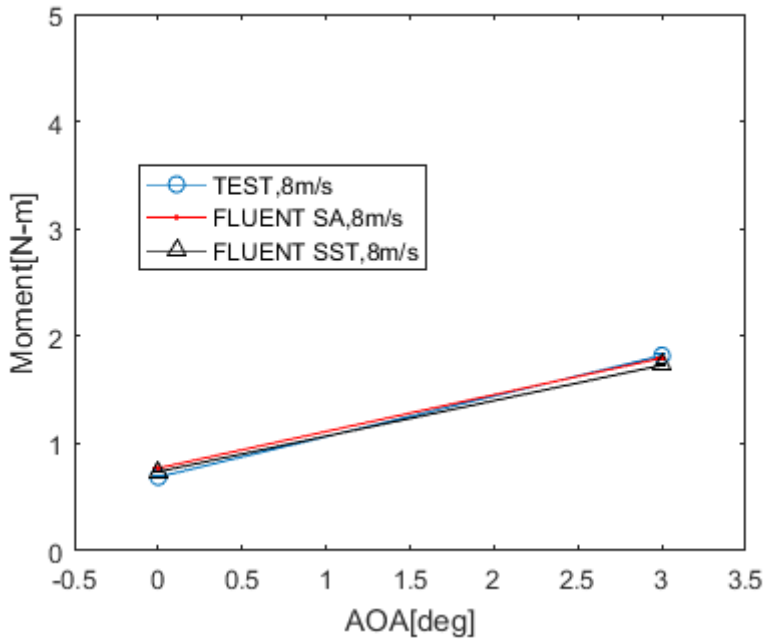

Figure 4-5 Effect of AOA on lift moments of TEST and CFD for AG wing

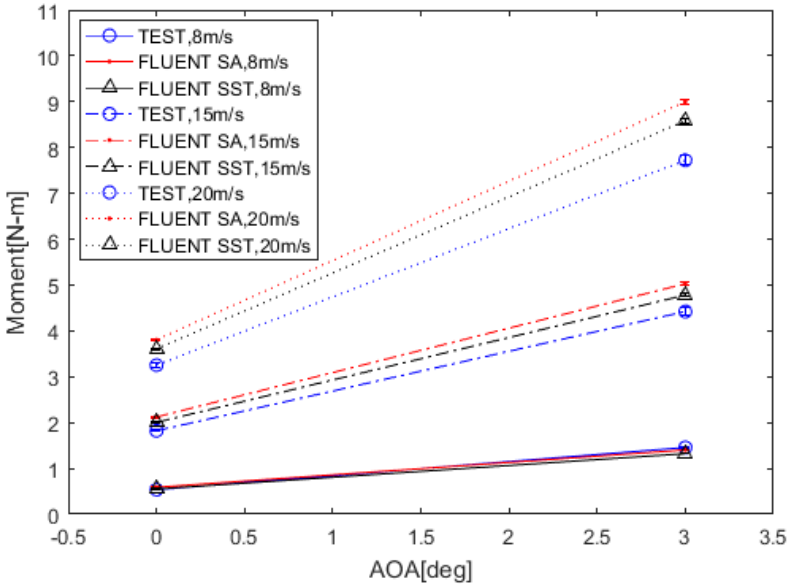

Figure 4-6 Effect of AOA on lift moments of TEST and CFD for AT wing

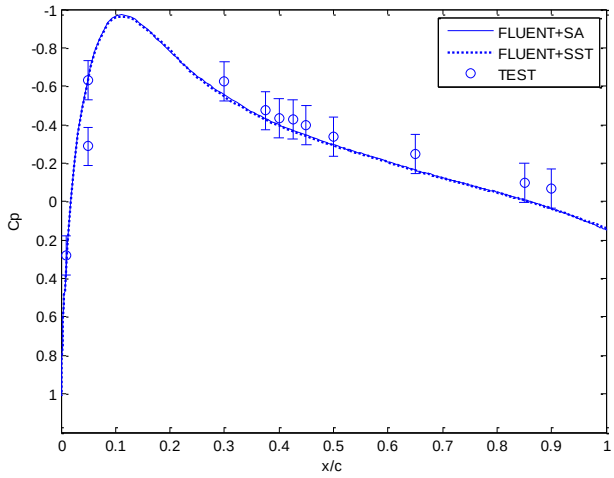

(a) 8 m/s

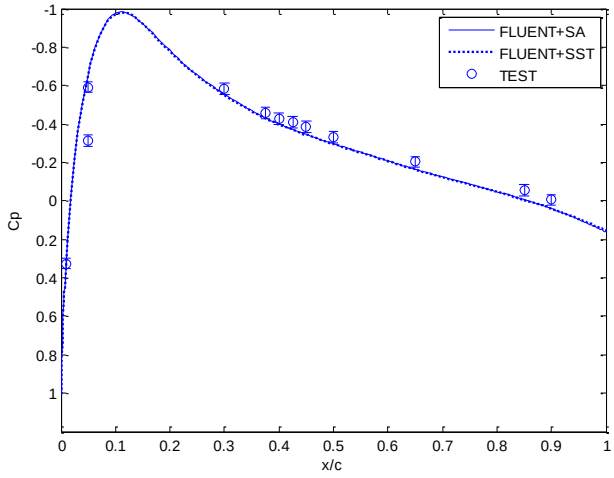

(b) 15 m/s

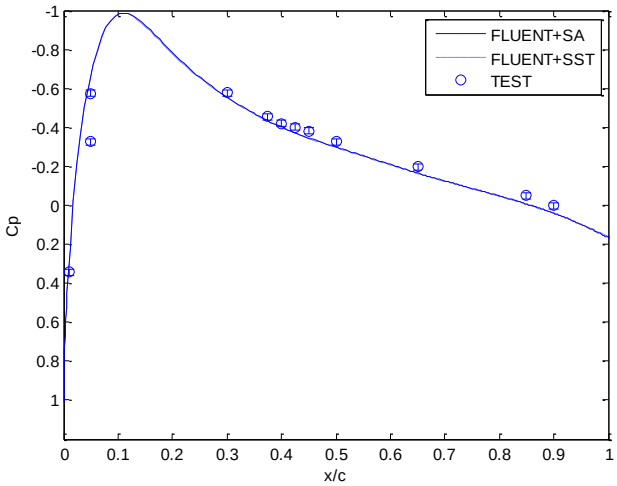

(c) 20 m/s

Figure 4-7 Pressure distribution of experiments and simulations for AT wing (AOA = 3°)

4.2 Wings with Plasma Gurney Flap

4.2.1 Asymmetrical Wing (AG)

Figure 4-8 presents the change in measured lift moment due to the plasma Gurney flap (in absolute value and in percentage of the nominal, i.e. without actuation, moment) at the three tested incoming flow velocities for the AG wing at AOA = 0° versus the corresponding CFD simulations. The plasma actuation strength is 55 mN/m for both test and simulations. The scale reading fluctuates when the wind tunnel is running, resulting in a time varying reading. In the figures, the error bars of scatters in experiments include this reading oscillation and instrument errors of the scale and the L-shaped balance, as well as reading changes with and without plasma actuation. The instrument error is about 0.5 g (0.005 N), and the reading fluctuation ranges from 0.5 to 40 g (0.005 to 0.4 N) depending on the flow velocity. The moment difference error in Figure 4-8(a) becomes larger at high speeds because of larger reading fluctuations. The error bars for the measured moment increase percentage in Figure 4-8(b) is smaller than in Figure 4-8(a) because the nominal moment increases with speed. The error bars of CFD data come from the measurement uncertainty of the distance L_1 from wing root to pivot (see Figure 3-20), which is used as force arm length to calculate the moment in FLUENT.

To study the reliability of the plasma model, CFD simulations with plasma actuations were carried out with different turbulence models. As shown in Figure 4-8, the CFD simulations with the SST

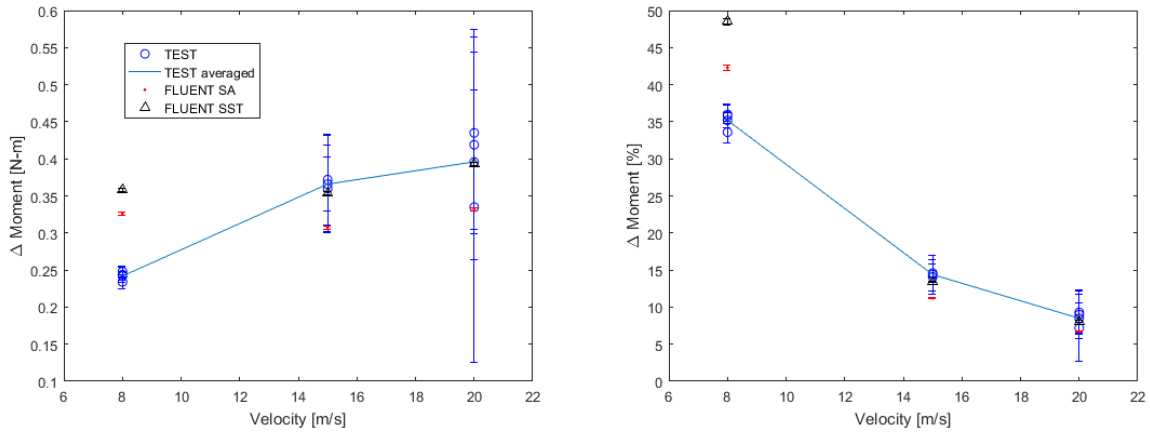

(a) (b)

Figure 4-8 Effect of plasma Gurney flap on AG wing at AOA = 0°, F_B =55 mN/m

model appears to show the least difference with test data at high speeds (15 – 20 m/s), while the SA model performs better at 8 m/s. Both the test results and CFD data in Figure 4-8(b) show that at constant actuation strength the effectiveness of the plasma Gurney flap decreases with flow velocity.

Figure 4-9 to Figure 4-11 show the surface pressure distributions at mid-span from CFD simulation with and without plasma at three speeds. Because of plasma actuation local effect, the pressure near actuators has a sudden increase and drop on both sides. As seen in these figures, the net pressure drop on the suction side and net pressure increase on the pressure side lead to an increase in lift and moment. Simulations with SA and SST models have similar pressure distribution at all three speeds.

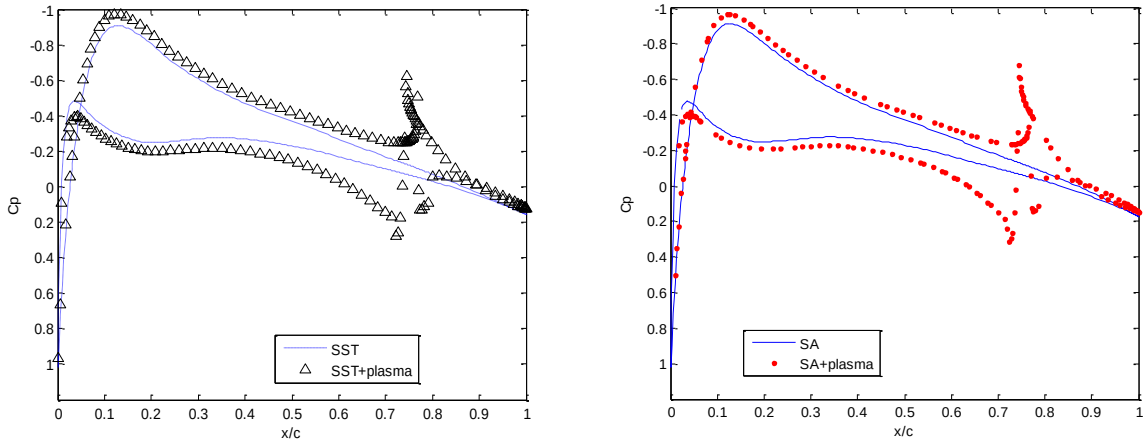

(a) (b)

Figure 4-9 Predicted mid-span pressure distribution of AG wing (8 m/s, AOA = 0°)

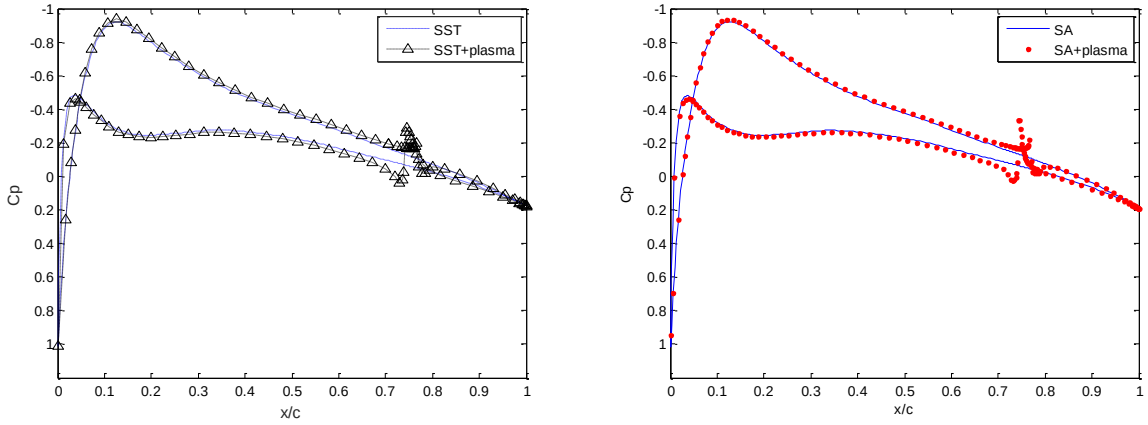

(a) (b)

Figure 4-10 Predicted mid-span pressure distribution of AG wing (15 m/s, AOA = 0°)

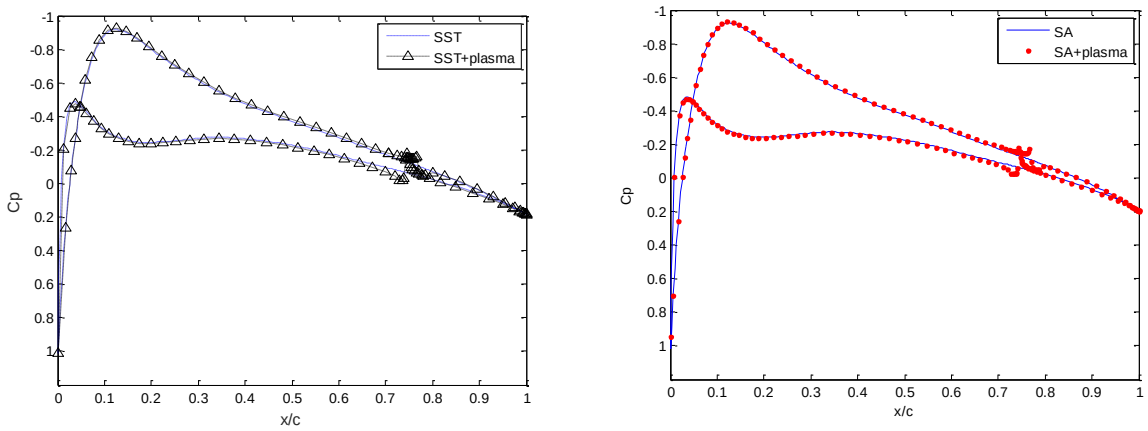

(a) (b)

Figure 4-11 Predicted mid-span pressure distribution of AG wing (20 m/s, AOA = 0°)

Figure 4-12 to Figure 4-14 compare streamline changes near the trailing edges of the AG wing with and without plasma Gurney flap at AOA = 0°, 8 – 20 m/s. The streamlines are extracted from the mid-span of the CFD simulation results and then compared with PIV measurements. Due to the laser scatter reflection during PIV measurement, streamlines close to the wing trailing edge are not well captured and thus omitted.

As shown in Figure 4-12 (c), the PIV streamlines at the trailing edge bend downwards at 8 m/s with plasma Gurney flap. As discussed in Section 2.1, streamlines with smaller radius lead to a smaller pressure (horizontal streamlines have infinite radius). The trailing edge bending downwards, leading to smaller radius on suction side streamlines and bigger radius on pressure side streamlines. Therefore, pressure reduces on suction side and increase on pressure side, resulting in an increase in lift, as shown with the force measurement results. CFD simulations with both SA and SST models are presented in Figure 4-12 (a) and Figure 4-12(b), which show nearly the same streamlines with and without plasma actuation. For simplicity, the following streamline comparison will henceforth use CFD simulations with SST model and PIV measurements.

At higher speeds, there is a very small change for streamlines at speed of 15 m/s (Figure 4-13) and 20 m/s (Figure 4-14), for both CFD simulations and PIV measurements. This means the effect of the plasma Gurney flap becomes weaker as the flow velocity increasing from 8 m/s to 20 m/s.

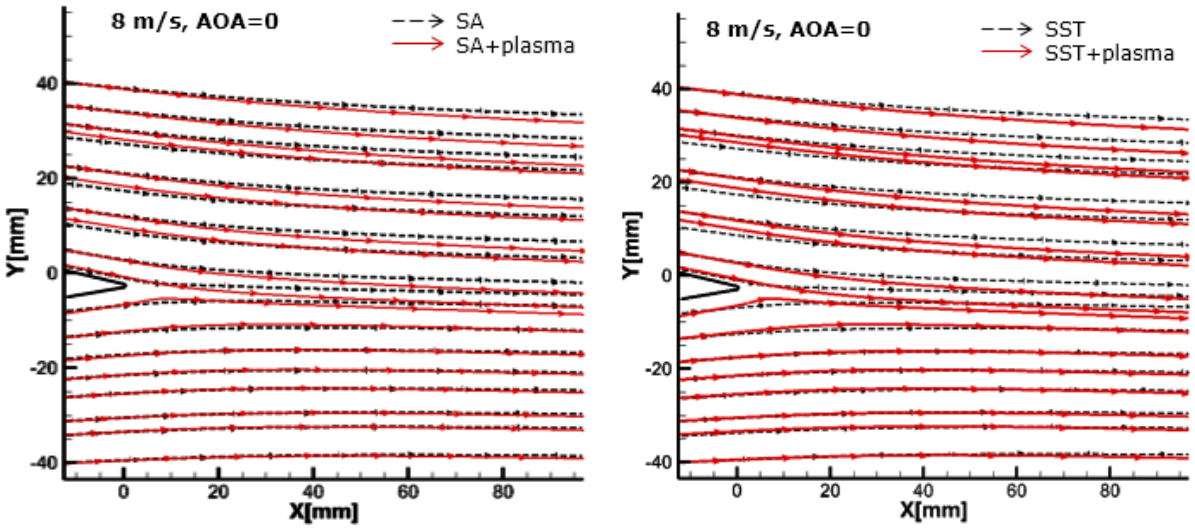

(a) (b)

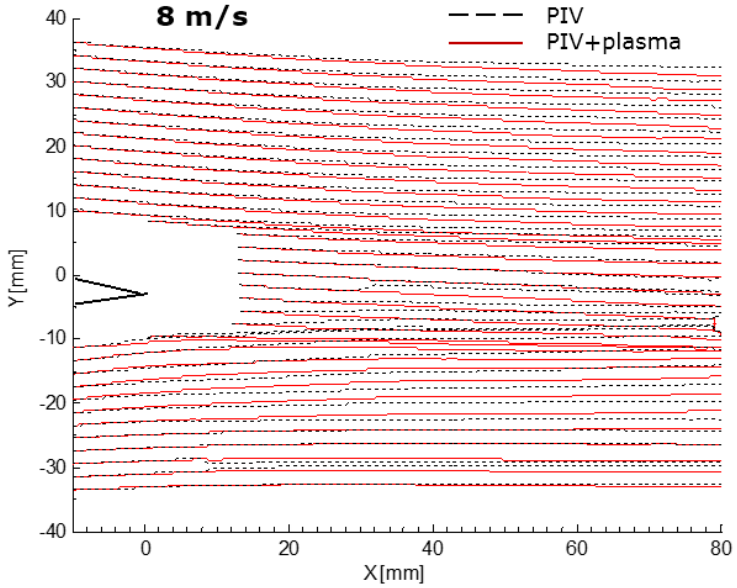

(c)

Figure 4-12 Streamlines near trailing edge of AG wing from CFD and PIV (8 m/s, AOA = 0°)

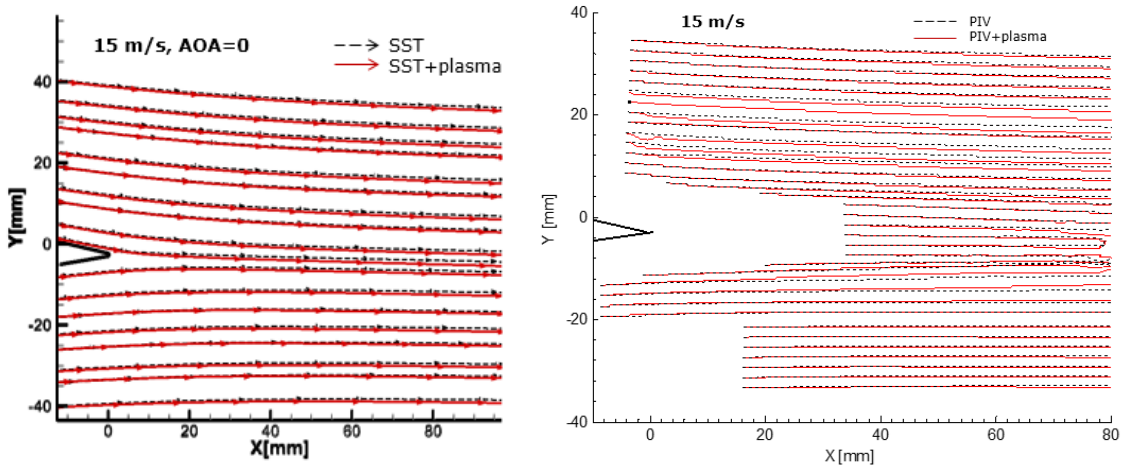

(a) (b)

Figure 4-13 Streamlines near trailing edge of AG wing from CFD and PIV (15 m/s, AOA = 0°)

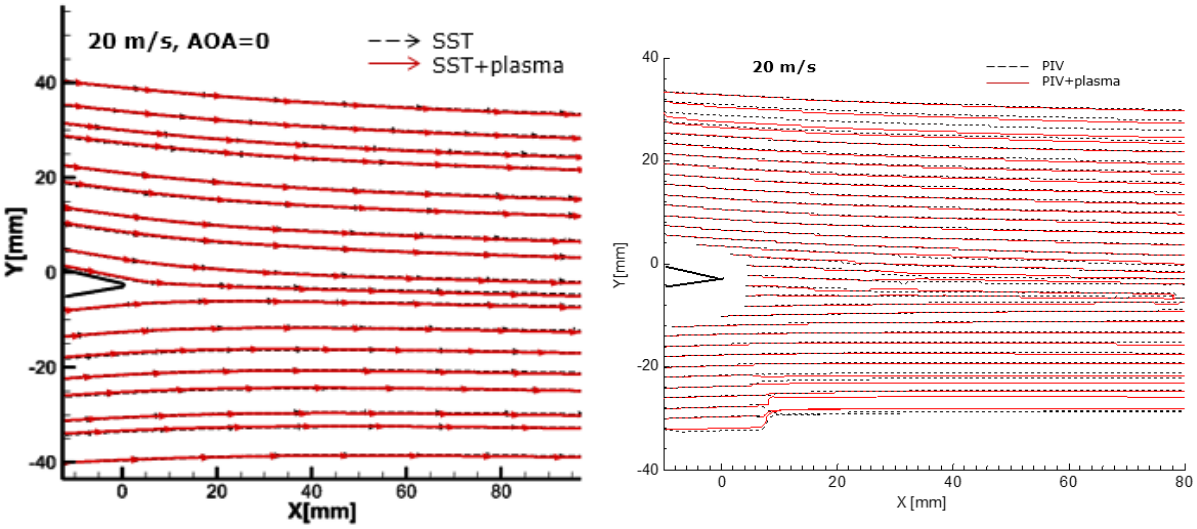

(a) (b)

Figure 4-14 Streamlines near trailing edge of AG wing from CFD and PIV (20 m/s, AOA = 0°)

Figure 4-15 presents the effect of AOA on measured lift moment due to the plasma Gurney flap for the AG wing at 8 m/s versus the corresponding CFD simulation with plasma actuation strength of 55 mN/m and different turbulence models. It can be concluded that the measured moment changes decrease at higher AOA. This shows that plasma Gurney flap tends to become weak at higher AOA. CFD results predict the right trend but overestimate the plasma effect. CFD simulations with the SA model appear to show the least difference with test data at 8 m/s.

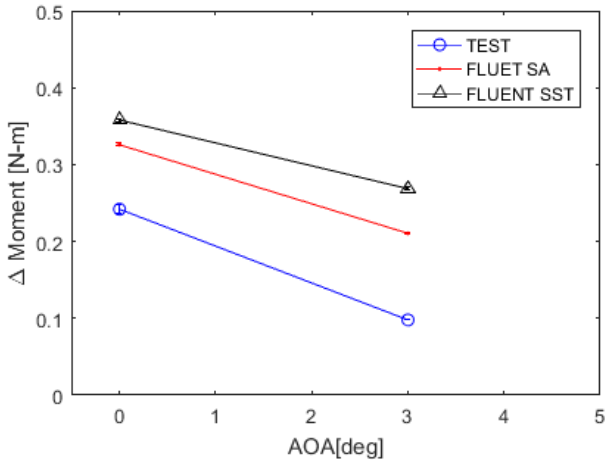

Figure 4-15 Effect of AOA on plasma Gurney flap for AG wing at 8 m/s, F_B = 55 mN/m

From the above comparisons between simulations and experiments for moment and streamline changes, it can be concluded that SST model can better predict the force (moment) change and streamline change of AG wing by plasma Gurney flap at higher speeds, while SA model only provide good predictions at low speeds (~8 m/s). SST model is therefore recommended for CFD simulation of plasma Gurney flap on the asymmetrical wings.

Figure 4-16 investigate the effect of AOA on streamline changes near trailing edge of the AG wing with and without plasma Gurney flap at 8 m/s. From CFD simulations with the SST model, it can be observed that streamlines bend downwards at zero angle of attack, while have almost no change at AOA =3°. This result matches previous moment change in Figure 4-15.

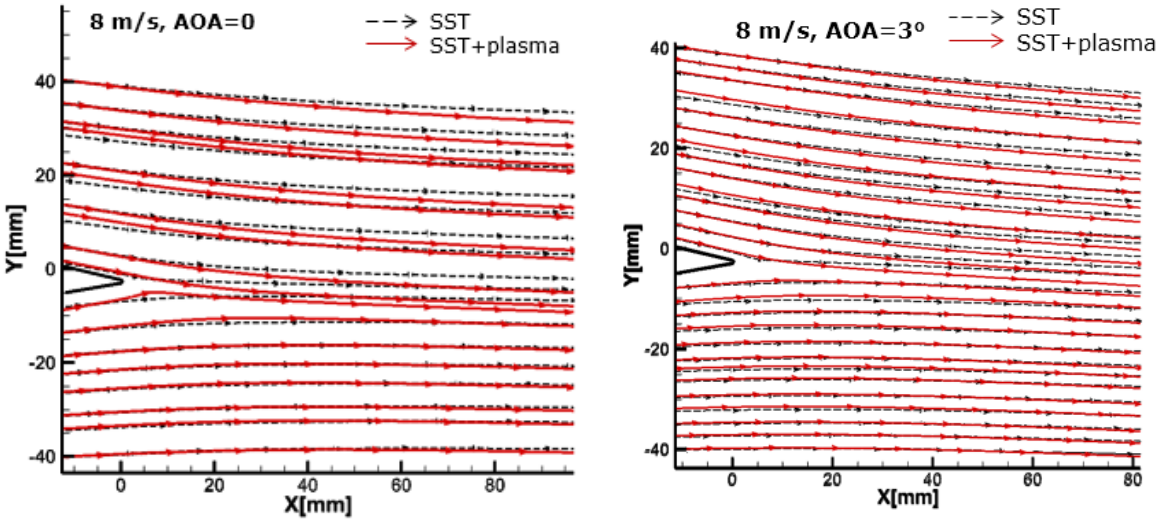

(a) (b)

Figure 4-16 Streamlines near trailing edge of AG wing at 20 m/s, AOA = 0° and 3°

The plasma Gurney flap becomes weaker at high angle of attack, which is observed from both experiment and simulations. To explain this behaviour, Figure 4-17 overlays the streamlines in the trailing edge region from CFD simulations for the AOA = 3° and AOA = 0° cases. As expected, the suction side streamlines have higher curvature for the AOA = 3° case, which would require higher generated moment from the plasma Gurney flap concept (thus higher actuation strength) to bend the streamline curvature in the other direction (downward). This would explain the decreased effectiveness of the plasma Gurney flap at higher AOA for the same actuation strength.

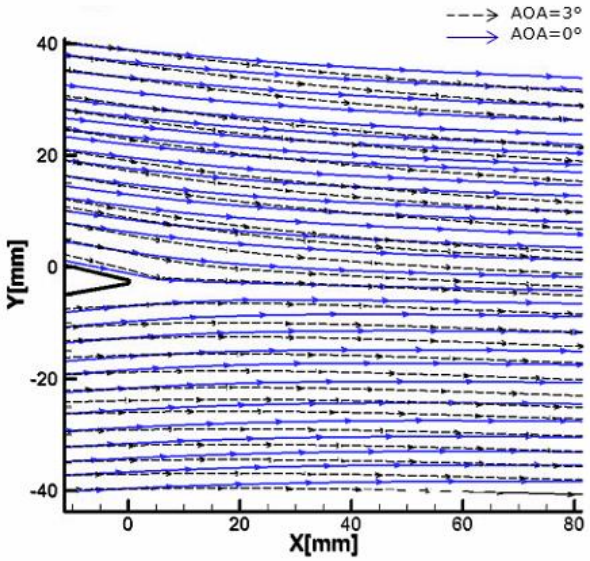

Figure 4-17 Streamlines near trailing edge of AG wing at 20 m/s without plasma, AOA = 0° & 3°

4.2.2 Symmetrical Wing (NG)

Figure 4-18 shows the measured change in lift moment from plasma Gurney flap (plasma actuation strength F_B = 60 mN/m) on the NG wing versus the corresponding simulation from CFD with different turbulence models. The measured moment difference increases when velocity increases, which matches well with the prediction from simulations with SST and SA turbulence models at 12 – 15 m/s. Similar to the AG wing, the CFD simulations with the two turbulence models over-predict the plasma effect at 8 m/s and slightly underestimate the plasma effect at 12 – 15 m/s. The SST model performs better than the SA model at the three speeds.

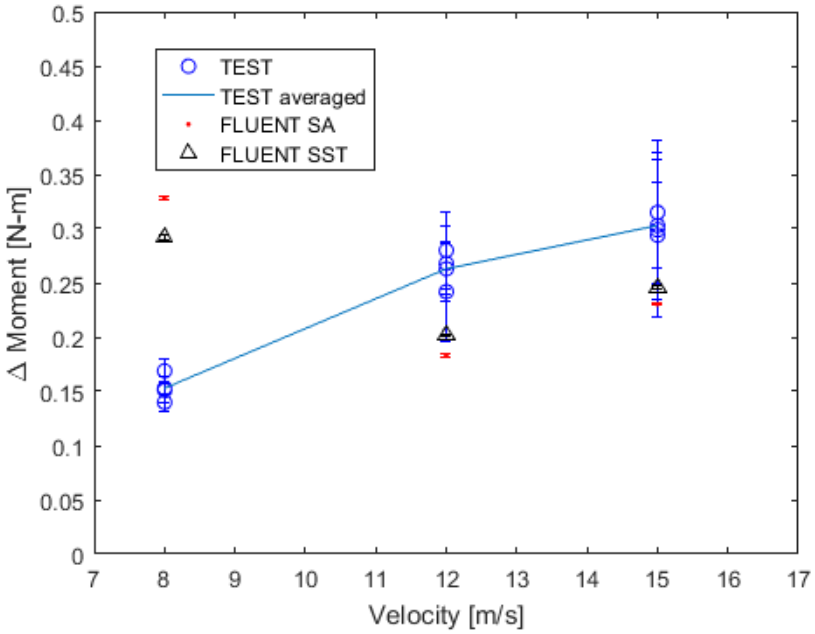

Figure 4-18 Effect of plasma Gurney flap on NG wing at AOA = 0°, F_B = 60 mN/m

Figure 4-19 shows the predicted (CFD) pressure distributions on the mid-span plane of the NG wing at AOA = 0°. Without plasma actuation, pressure and suction sides have identical pressure because of the symmetrical profile at AOA = 0°. The CFD simulations with the SST and SA models indicate that the pressure is only locally affected by plasma actuation at 12 and 15 m/s, but the surface pressure distribution upstream of the actuator is greatly altered at 8 m/s, which is consistent with force moment results in Figure 4-18. The pressure distribution near the plasma actuators exhibits the similar behavior as in the case of the AG wing. There is not any observable difference between the results with the SA model and those with the SST model.

The flow field near the trailing edge of the symmetrical wing can be studied from both CFD simulation and PIV measurement, as shown in Figure 4-20, Figure 4-21 and Figure 4-22. Streamlines bend downwards when applying plasma Gurney flap at 8 m/s AOA = 0° in Figure 4-20 (a), but the changes are more significant from simulation, with a recirculation vortex occurring near the trailing edge on the pressure side, which is consistent with the over-estimation of force measurement in Figure 4-18. PIV measurements show that the plasma effect becomes weaker as velocity increases and very small streamline changes can be observed at 12 m/s (see Figure 4-21) and 15 m/s (see Figure 4-22). The simulation results match well with PIV measurements.

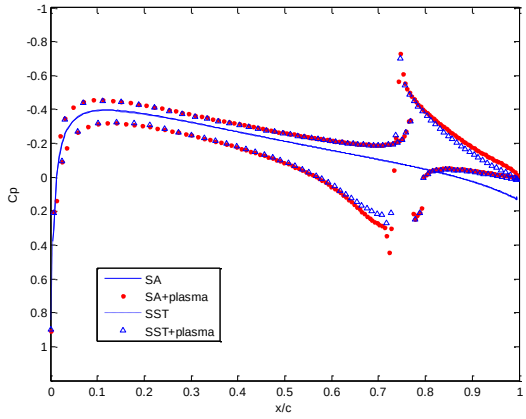

(a) 8 m/s

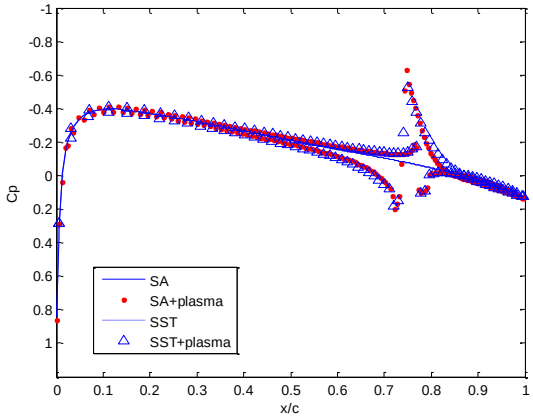

(b) 12 m/s

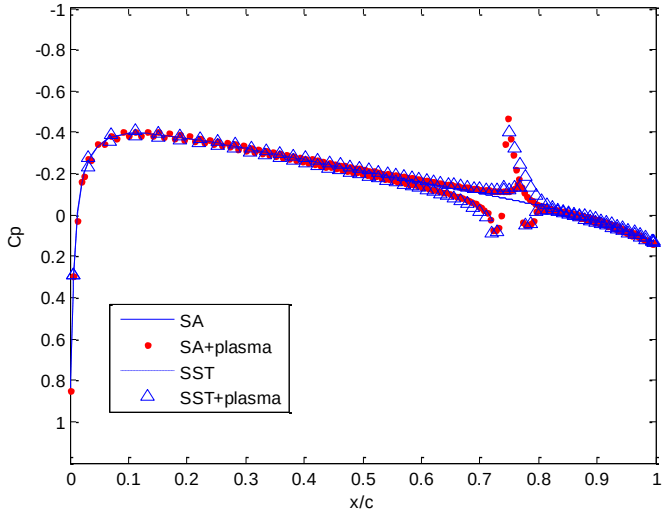

(c) 15 m/s

Figure 4-19 Mid-span pressure distributions for NG wing (AOA = 0°, F_B = 60 mN/m)

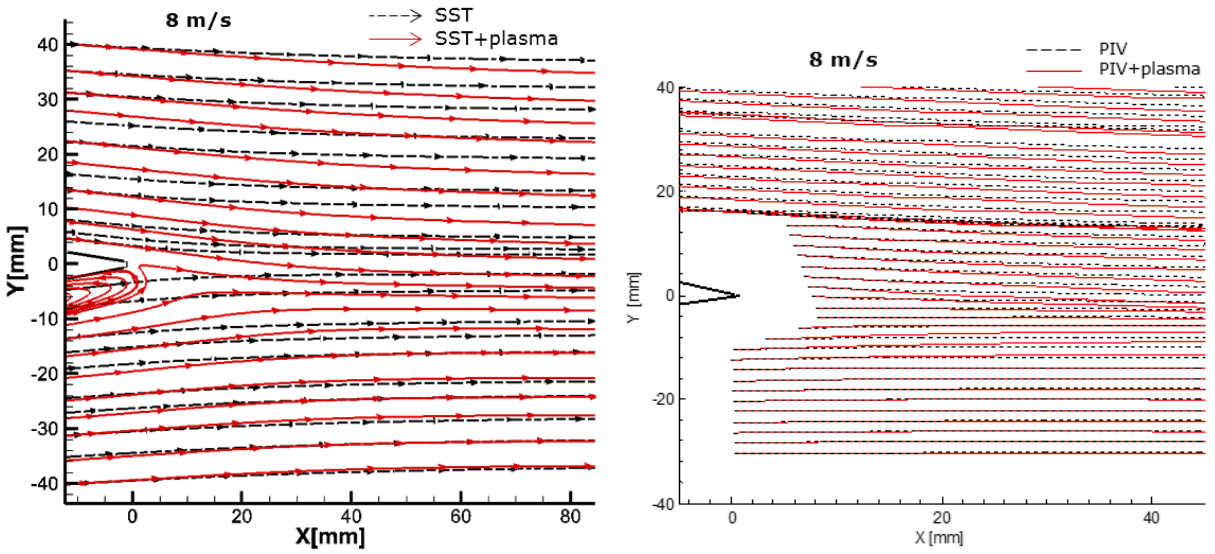

(a) (b)

Figure 4-20 Streamlines near trailing edge of NG wing from CFD and PIV (8 m/s, AOA = 0°)

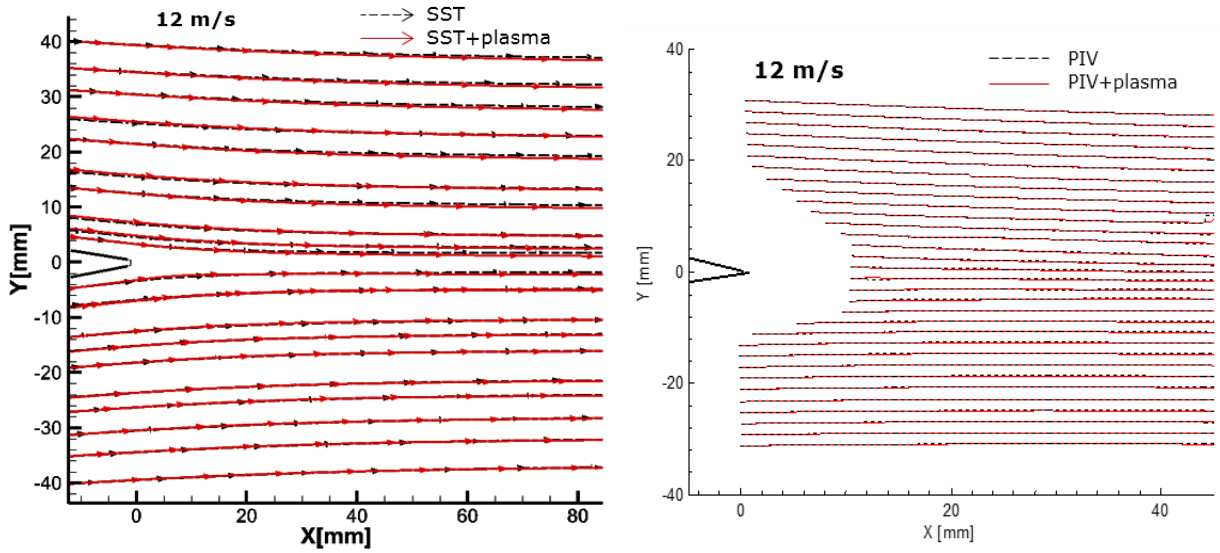

(a) (b)

Figure 4-21 Streamlines near trailing edge of NG wing from CFD and PIV (12 m/s, AOA = 0°)

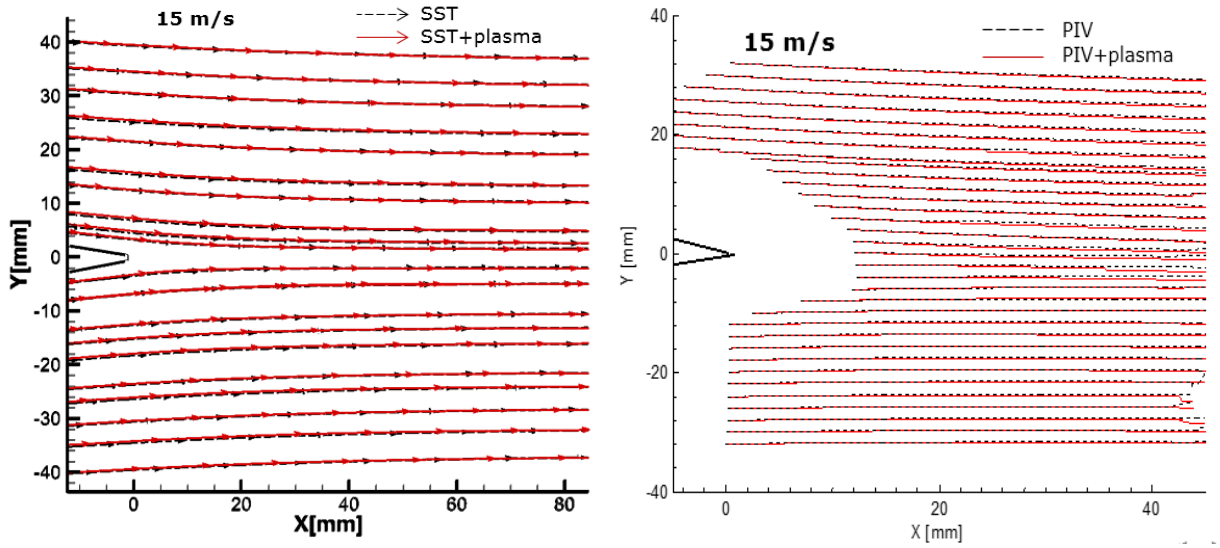

(a) (b)

Figure 4-22 Streamlines near trailing edge of NG wing (15 m/s, AOA = 0°)

From above comparisons between simulations and experiments for moment and streamline changes, it can be concluded that SST model can also predict the force (moment) change and streamline change of the NG wing by the plasma Gurney flap at different speeds. The SST model is therefore relatively better for simulation of the plasma Gurney flap for both symmetrical and asymmetrical wings.

4.3 Wings with Plasma Wing Tip Actuation

4.3.1 Asymmetrical Wing (AT)

Figure 4-23 presents the measured change in lift moment (in absolute value and in percentage of nominal, i.e. no actuation, moment) due to the wing tip actuation (plasma actuation strength F_B = 65 mN/m) for the AT wing versus corresponding CFD simulations with different turbulence models at AOA = 0°. The results show that the wing tip plasma actuators have smaller effect on the force measurement than the plasma Gurney flap. Indeed, the plasma wing tip actuation can only have maximum lift moment difference of 0.1 N-m at test conditions, while plasma Gurney flap can provide a 0.3 – 0.4 N-m change in lift moment. This is expected as the wing tip actuation only affects lift in the wing tip region, while the plasma Gurney flap affect the lift over nearly the whole span. In other words, the ultimate lift coefficient achieved by wing tip actuation on an extruded

wing is that of a corresponding 2D wing profile, while plasma Gurney flap increases the lift coefficient of the 2D wing profile itself.

From Figure 4-23, good predictions are observed for simulations with SST and Spalart-Allmaras models, especially at low speeds. The predicted average moment difference increases with inlet velocities, while test data remains constant. The moment differences at higher plasma strength (F_B =90 mN/m) are presented in Figure 4-24, which are only larger by 0.01−0.02 N-m than those with actuation strength of 65 mN/m. Both the test results and CFD data in Figure 4-23(b) and Figure 4-24(b) show that at constant actuation strength the effectiveness of wing tip actuation decreases with flow velocity.

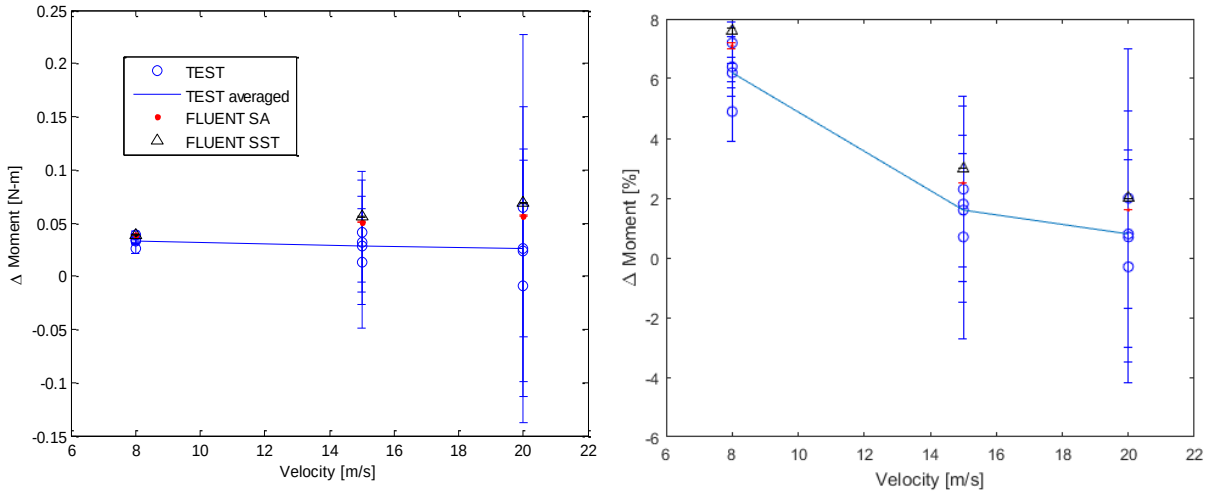

(a) (b)

Figure 4-23 Effect of wing tip actuation on lift moment for wing AT (AOA = 0°, F_B =65 mN/m)

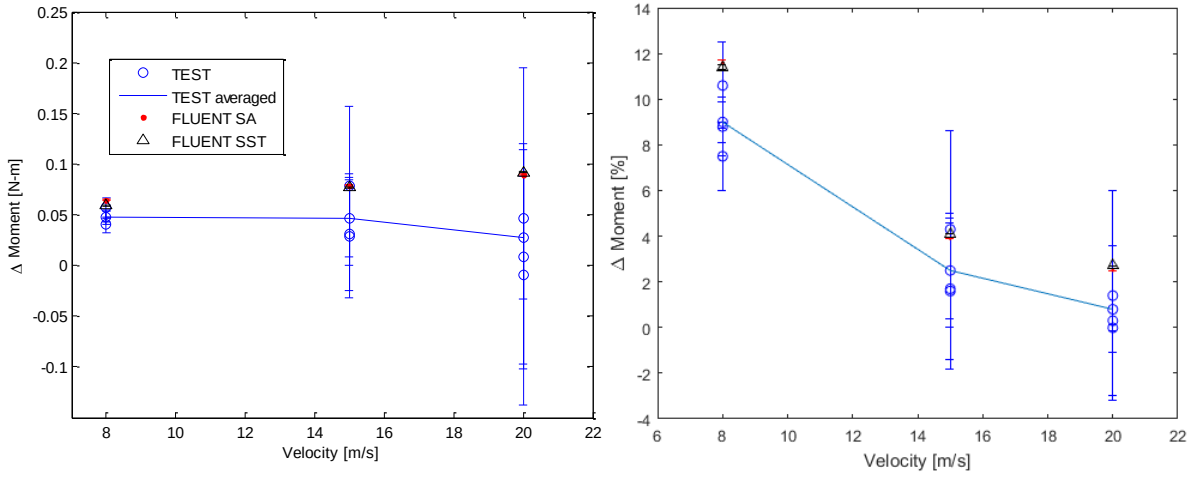

(a) (b)

Figure 4-24 Effect of wing tip actuation on lift moment for AT wing (AOA = 0°, F_B =90 mN/m)

Figure 4-25 presents the change in spanwise lift distributions from CFD at three speeds with plasma strength of 65 mN/m at AOA = 0°. It can be observed that spanwise lift distribution from CFD results with SST model and SA model are about the same, with only small differences near tip region. This agrees with the same lift moment change in Figure 4-23.

In term of the effect of plasma wing tip actuation on the tip vortex, Figure 4-26 shows the vorticity distribution at an axial plane one chord downstream of the AT wing trailing edge for CFD simulation with SST model at AOA = 0° and plasma actuation strength of 65 mN/m. For clarify, only CFD results with SST model are presented in Figure 4-26.

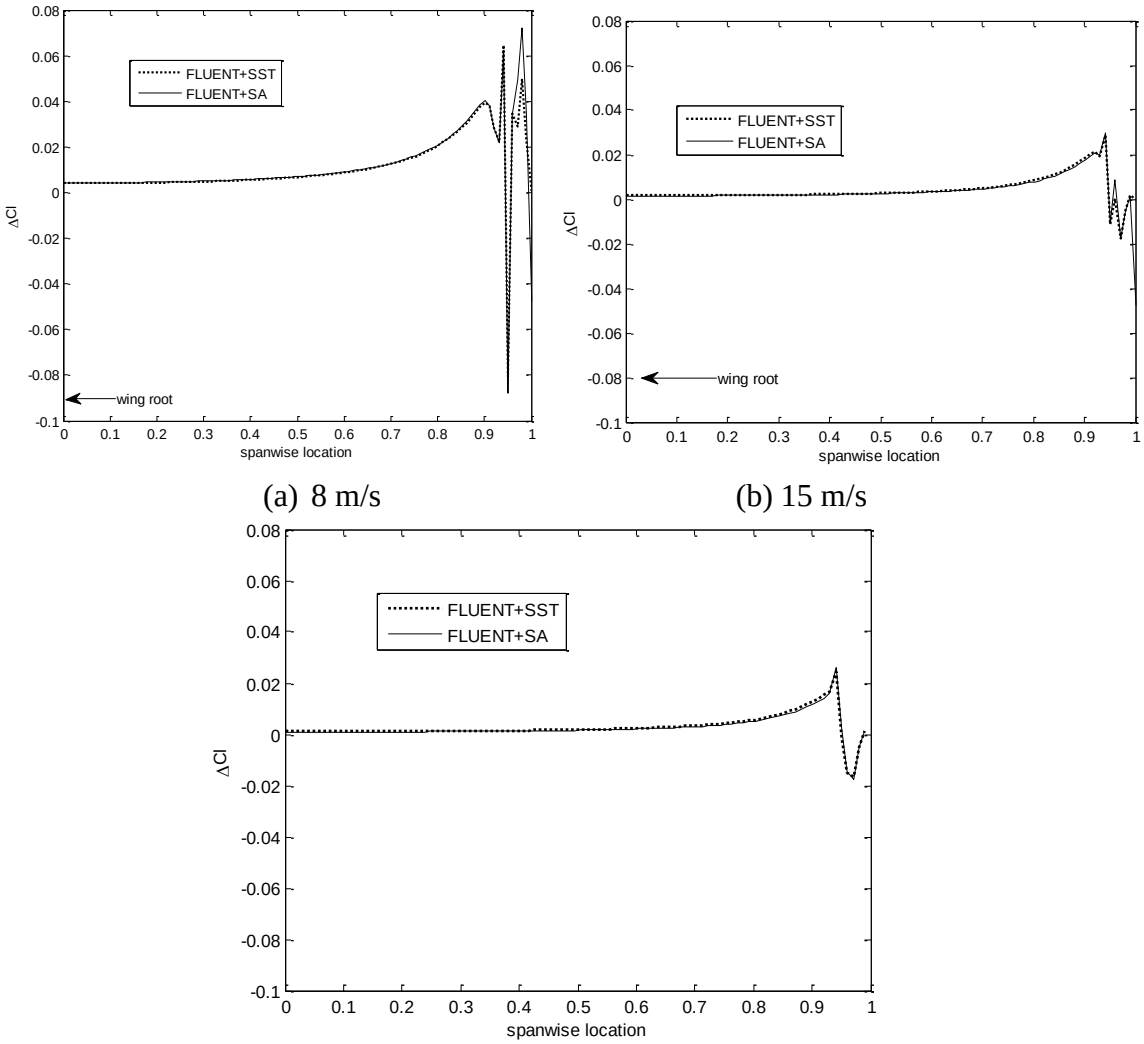

(a) 8 m/s (b) 15 m/s

(c) 20 m/s

Figure 4-25 Predicted (CFD) spanwise lift change by plasma for AT wing (AOA = 0°, F_B = 65 mN/m)

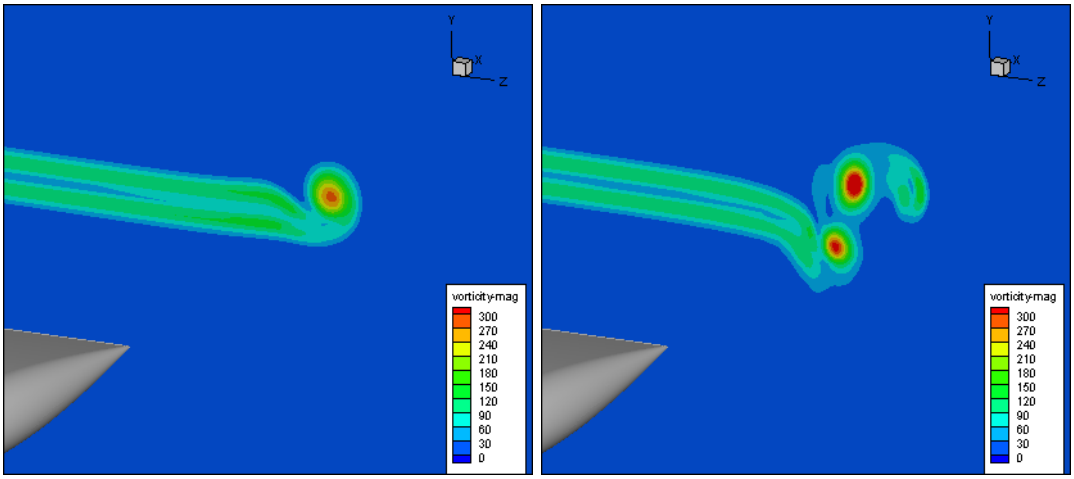

(a) 8 m/s

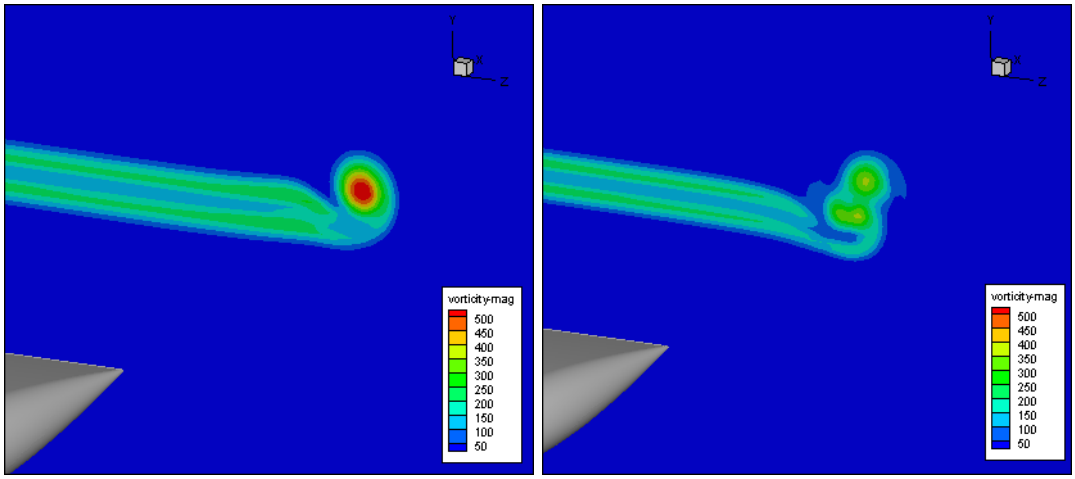

(b) 15 m/s

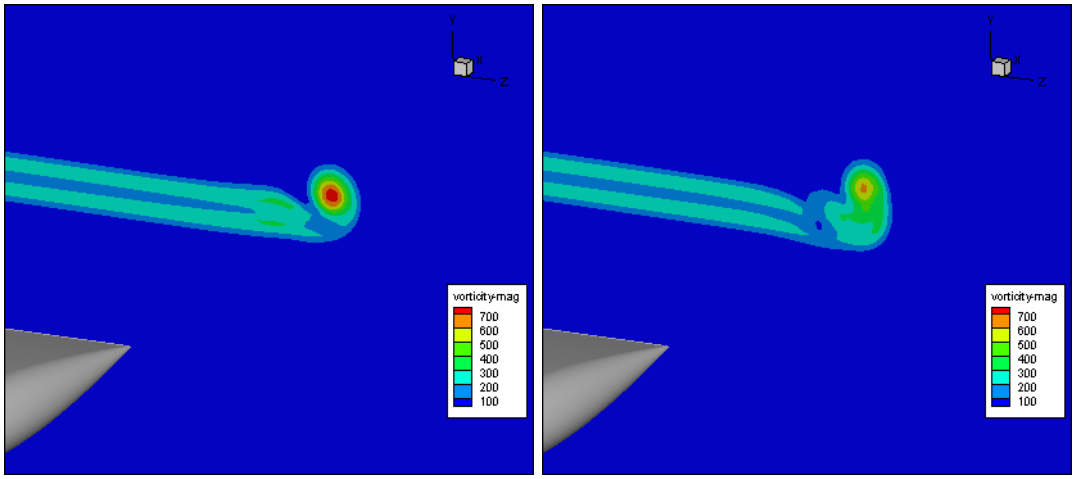

(c) 20 m/s

Figure 4-26 Predicted (CFD) contours of wake vorticity one chord downstream for AT wing (AOA = 0°) without (left) and with plasma actuation (right, F_B =65 mN/m)

The results show that the induced flow generated by the plasma wing tip actuators is able to alter the tip vortex. Indeed, the tip vortex is displaced away from the wing tip and separated into two bigger vortices at 8 m/s. The asymmetrical vortices can induce large spanwise variation in the tip-region lift coefficient change as shown in Figure 4-25(a). At higher speeds, the plasma effect becomes weaker and the vorticity magnitude of tip vortices is reduced which indicates that the tip vortices are diffused by the plasma wing tip actuation, resulting in lower spanwise variation in the tip-region lift coefficient change at 15 and 20 m/s.

The effect of plasma wing tip actuation can also be studied by local AOA near wing leading edge. As depicted in Figure 1-3 in Chapter 1, the tip vortex induces a downwash that is largest near the wing tip, causing the incoming flow to bend downward, thus reducing the local angle of attack. Figure 4-27 presents predicted spanwise local AOA (SST model) at 0.1 chord upstream the AT wing leading edge with and without plasma actuation (AOA = 0°, F_B =65 mN/m). It is observed that the local AOA decreases from wing root to wing tip without plasma actuation. The plasma wing tip actuation improves the AOA over the whole span, indicating a reduction in the downwash. In Figure 4-27, the AOA increases by about 0.1°, 0.04° and 0.02° at 8, 15 and 20 m/s, respectively, which shows that plasma effect on downwash decreases with increasing flow speed.

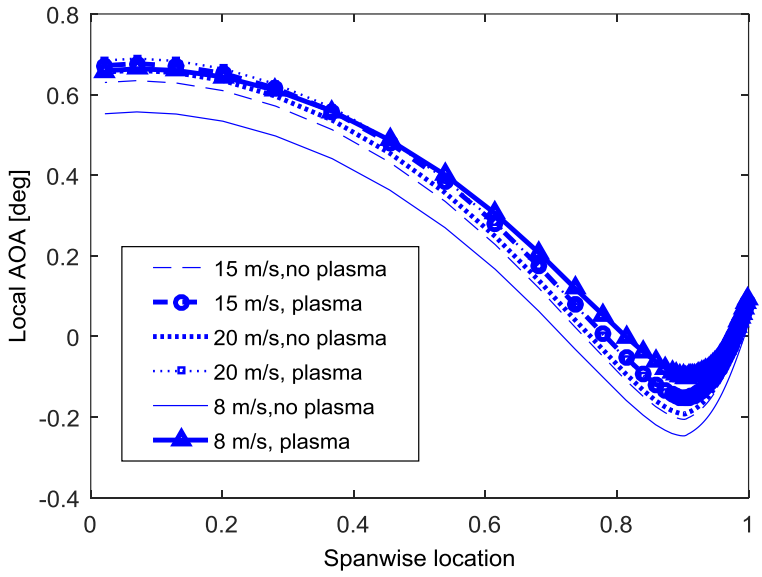

Figure 4-27 Predicted (CFD) local AOA at 0.1chord upstream leading edge of AT wing with and without plasma (AOA = 0°, F_B =65 mN/m)

Figure 4-28 presents the effect of AOA on wing tip plasma actuator for AT wing at AOA = 3° with F_B = 65 mN/m. The test data has higher error bars at high speeds (12-15 m/s) due to the reading

fluctuation. At 8 m/s, measurement moment show that the change in AOA does not have much effect on plasma wing tip actuation. The CFD simulations show a slight increase at higher angle of attack and SA model appear to have smaller difference compare with test data. Figure 4-29 presents predicted local AOA at 0.1 chord upstream leading edge for the AT wing at AOA = 3°, F_B =65 mN/m. The data indicates that plasma wing tip actuation increases the local AOA by about 0.12°, 0.05° and 0.03° at 8, 15 and 20 m/s, respectively, which are about the same as those at AOA = 0°. This observation is consistent with lower sensitivity in effectiveness with AOA increase for the plasma wing tip actuation relative to the plasma Gurney flap.

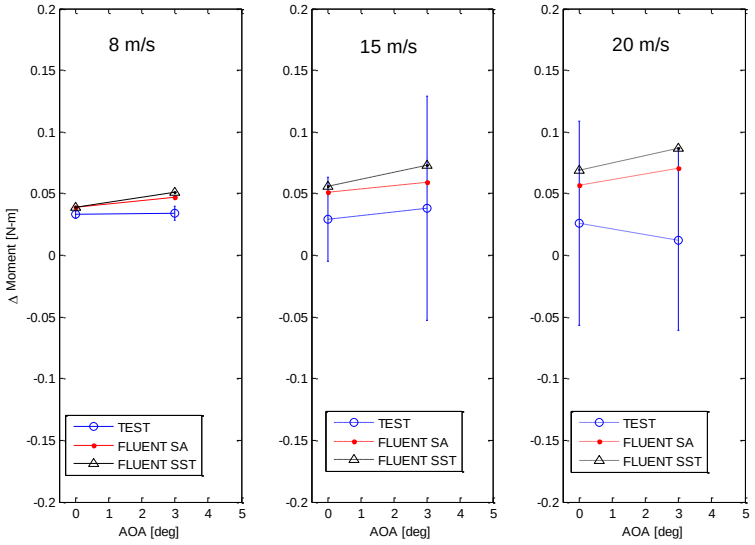

Figure 4-28 Effect of AOA on wing tip actuation effectiveness for AT wing (F_B = 65 mN/m)

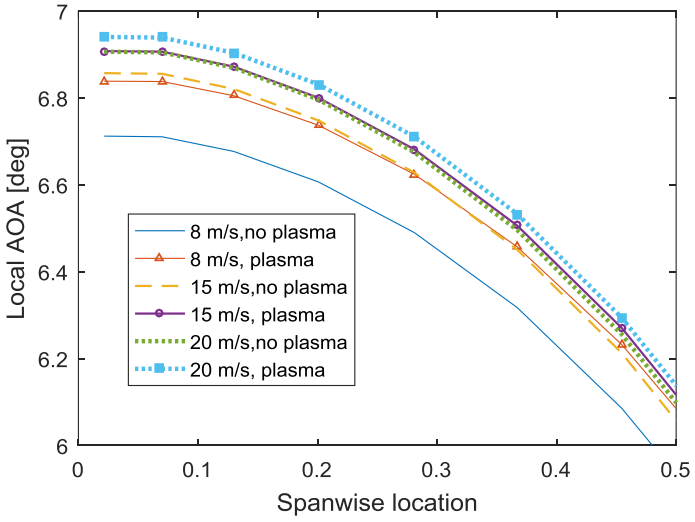

Figure 4-29 Predicted (CFD) local AOA at 0.1chord upstream leading edge of AT wing with and without plasma (AOA = 3°, F_B =65 mN/m)

From the above comparisons between experimental and CFD simulation results, it can be concluded that both SST and SA models can provide close match with test data for plasma wing tip actuation for asymmetrical wing. The increase in angle of attack doesn't affect the plasma wing tip actuation performance.

4.3.2 Symmetrical Wing (NT)

The moment differences by plasma wing tip actuation for symmetrical NT wing are shown in Figure 4-30 (AOA = 0°, F_B =80 mN/m)). The average moment change increases slightly from 8 to 12 m/s, then decreases at 15 m/s. The measured lift moments are well predicted by both turbulence models at 8 – 12 m/s, and slightly overestimated at 15 m/s. Considering the error bars, it can be concluded that both turbulence models seem adequate for simulations of plasma wing tip actuators on symmetrical wings. The SST model predicts the C_L increases by 0.01 at 8 m/s, by 0.004 at 20 m/s, indicating that the actuation effect becomes weak at high speeds.

Figure 4-31 presents the predicted (CFD) spanwise lift change for the NT wing at AOA = 0°, F_B = 80 mN/m. The spanwise lift change exhibits similar behavior than that of AT wing at AOA = 0° in Figure 4-25, with big fluctuations near wing tip due to plasma effect. The plasma effect becomes weaker at 15 m/s as expected, as shown in Figure 4-31 (c). Simulations of the two model have similar spanwise lift change, which explain the close moment change in Figure 4-30.

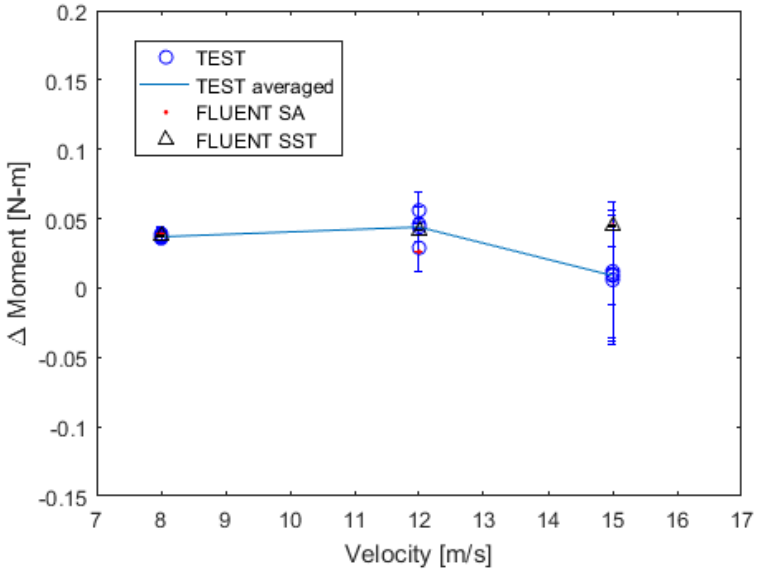

Figure 4-30 Effect of wing tip actuation on lift moment for NT wing (AOA = 0°, F_B =80 mN/m)

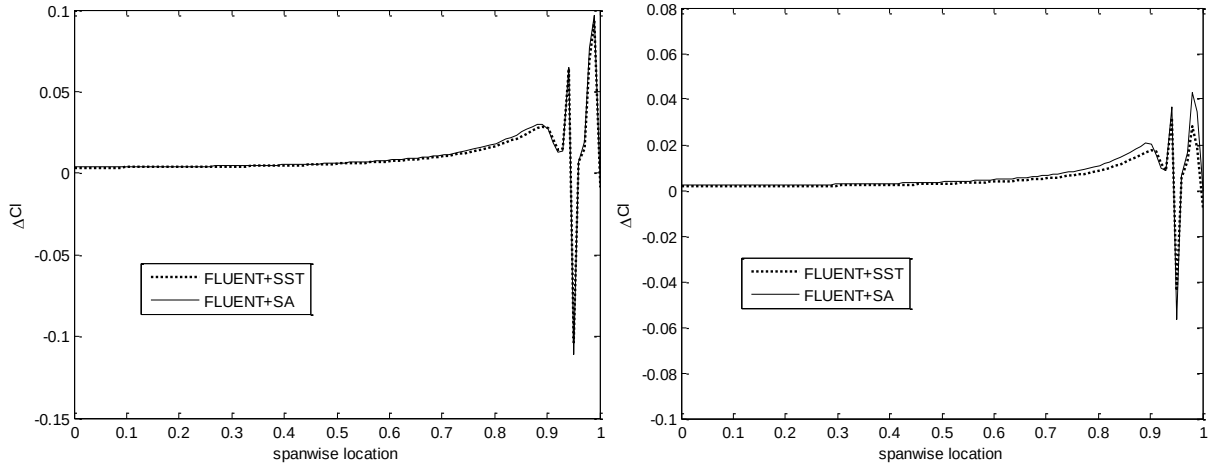

(a) 8 m/s (b) 12 m/s

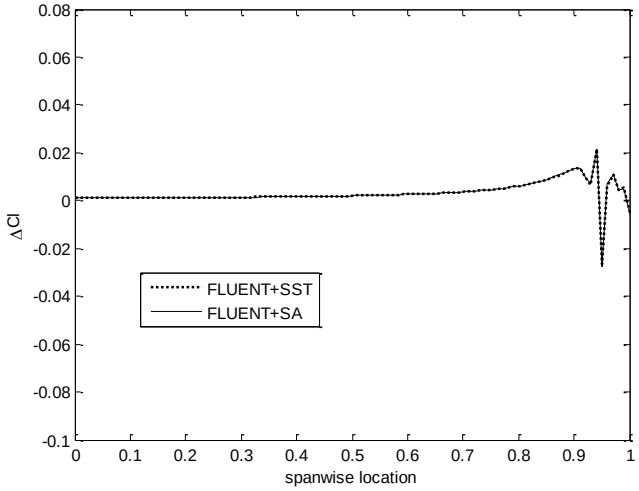

(c) 15 m/s

Figure 4-31 Spanwise lift for symmetrical wing with wing tip actuation (AOA = 0°, F_B = 80 mN/m)

Figure 4-32 shows the predicted (CFD) vorticity at an axial plane one chord downstream of the NT wing trailing edge with and without plasma actuation (AOA = 0°, F_B =80 mN/m). The results show that there is no tip vortex in the no actuation case. With plasma wing tip actuation, a pair of asymmetrical counter-rotating tip vortices are generated for the three speeds. The asymmetry of the tip vortex results in lift generation and thus explains the moment increase by plasma actuation seen in Figure 4-30. Similar to the AT wing, Figure 4-31 and Figure 4-32 indicate that the amplitude of spanwise variation in the tip-region lift coefficient change increases with the asymmetry of the wing tip vortices, which is higher at low velocity for the same actuation strength.

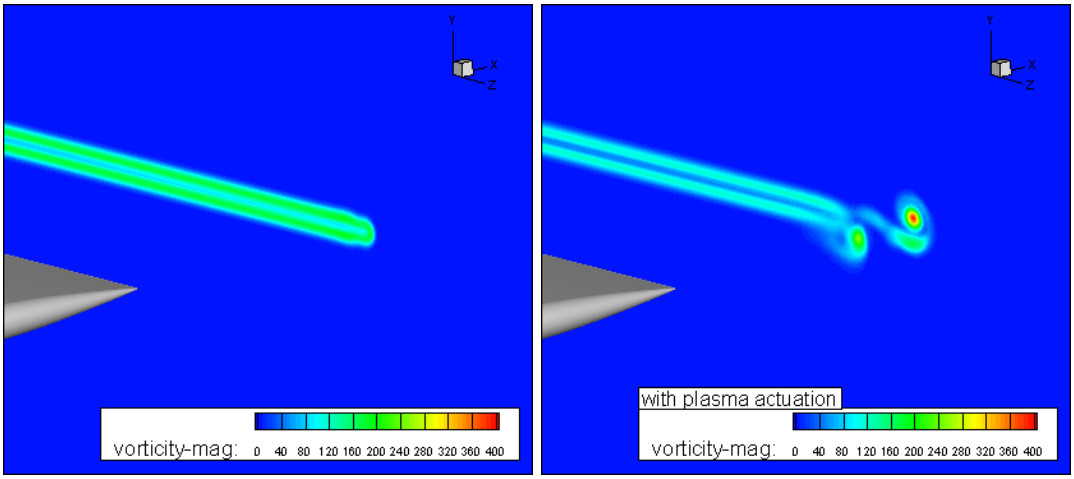

(a) 8 m/s

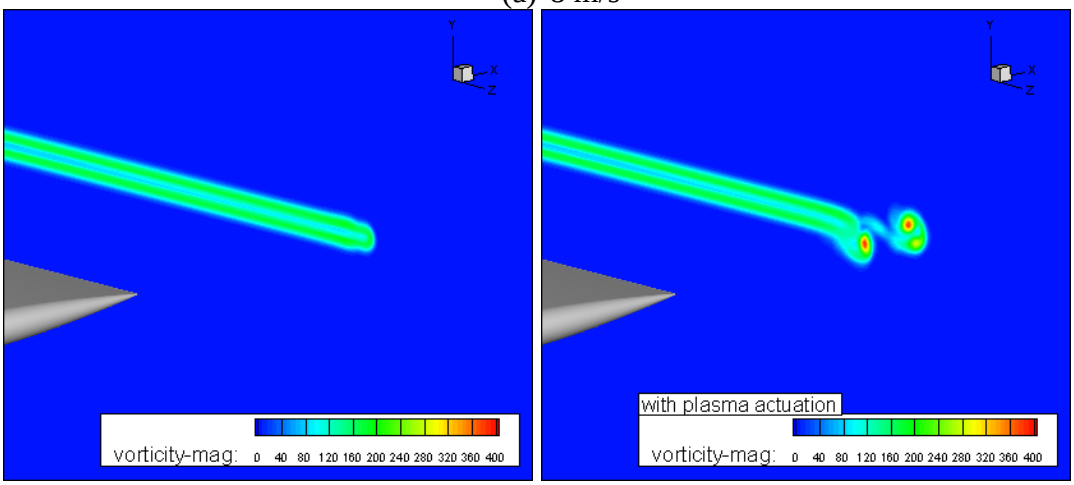

(b) 12 m/s

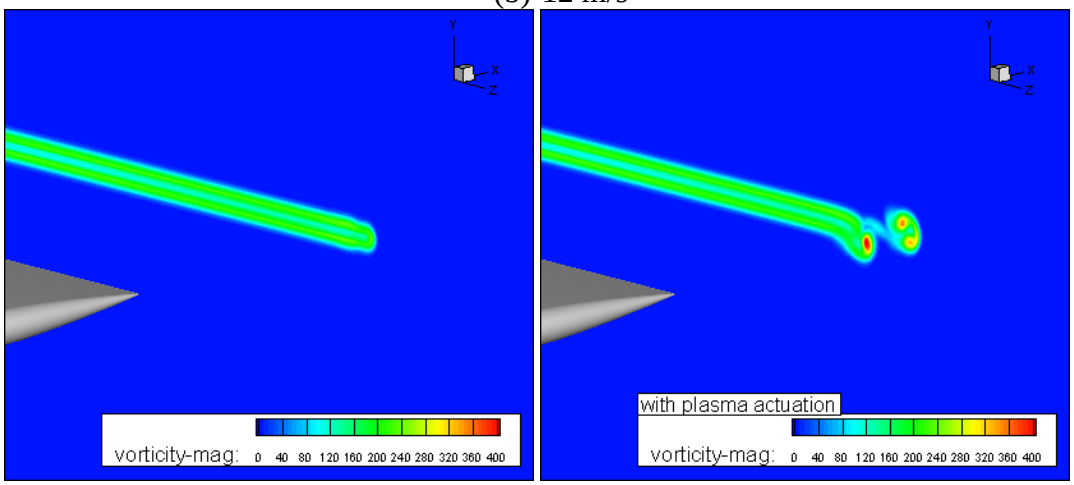

(c) 15 m/s

Figure 4-32 Predicted (CFD) contours of wake vorticity one chord downstream for NT wing (AOA = 0°) without and with plasma actuation (right, F_B =80 mN/m)

Figure 4-33 presents predicted local AOA (SST model) at 0.1 chord upstream NT wing leading edge with and without plasma actuation (AOA = 0°, F_B =80 mN/m). It can be observed that the velocity angle is zero without plasma actuation. The plasma wing tip actuation improves the AOA significantly over the full span at 8 m/s, especially near the wing tip (up to 0.15° increase). The improvement of AOA indicates a generation of upwash (opposite effect of downwash) which results in lift increase. However, the plasma actuators have very limited effect on the angle change at higher velocity (above 12 m/s), which is consistent with the spanwise lift change in Figure 4-31.

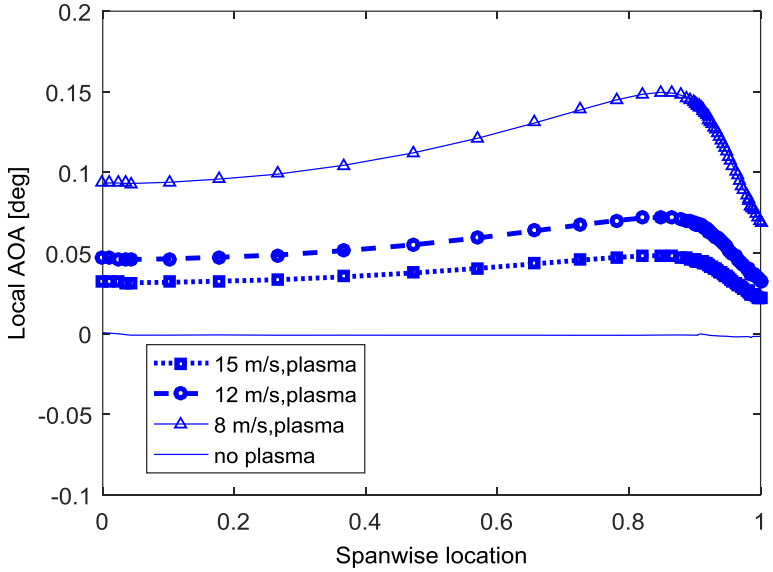

Figure 4-33 Predicted (CFD) local AOA at 0.1chord upstream leading edge of NT wing without and with plasma (AOA = 0°, F_B =80 mN/m)

Overall, the comparisons among test data, simulations with the SA model and those with the SST model indicates the two turbulence models provide close results with test data for symmetrical wings with plasma wing tip actuators.

4.4 Discussion

In this chapter, experimental and numerical results of plasma Gurney flaps and plasma wing tip actuators were presented for asymmetrical and symmetrical wings. Two turbulence models, namely Spalart-Allmaras (SA) and SST, were applied for numerical simulations. The CFD tools were first validated with current experimental results without plasma actuation. Then it was used to assess the two plasma concepts on four wings (AG, NG, AT, NT) at different speeds and different AOAs.

Generally, SST and SA models predict similar changes in wing lift moment for two plasma concepts, with SST providing a closer match with test data.

From the experimental results, it can be concluded that these two plasma concepts can help to improve lift and their effect reduce as flow velocity increasing. The plasma Gurney flap has better performance than wing tip plasma actuators in terms of lift enhancement.

Both CFD simulations and flow field measurement (PIV) results indicate that streamlines near wing trailing edge bend downwards (towards the pressure sides) with the plasma Gurney flap, resulting in lift increase. CFD simulations show with plasma wing tip actuation, the tip vortices of the asymmetrical wing are diffused at high speeds and a pair of counter-rotating tip vortex is generated for the symmetrical wing, both of which contributes to lift increment.

The effect of AOA on two plasma concepts are also presented in this chapter. Based on current test data, the plasma Gurney flap tends to become weaker at higher AOA while the wing tip plasma actuator remains the same.

Similar plasma actuators near the wing trailing edge have been experimentally studied before by He *et al.* [8] and Ueno [12]. He *et al.* [8] tested plasma actuators at 0.9 chord on the suction side of a NACA 0015 airfoil. With a velocity of 21 m/s and a Reynold number of 1.8×10^5, the lift coefficient was uniformly increased by plasma actuation for a given angle of attack. The lift coefficient change was approximately 0.051, as shown in Figure 4-34. Ueno [12] measured the plasma Gurney flap on both suction side and pressure side near the trailing edge of a NACA 4424 airfoil. With velocity ranging from 6 – 16 m/s, the Reynolds number is from 1.0×10^5 to 2.6×10^5. Figure 4-34 compares current results with existing experiment data. Since lift coefficients cannot be obtained directly from experiments, the lift coefficients from simulations with SST model are used. The lift coefficient change in the present work is lower than those of Ueno's results, but the trend tends to coincide with data of He *et al*.. Considering the differences in airfoil shapes, applied voltages, and actuation geometries, the results presented are in the same order of magnitude as previous results.

Wing tip plasma actuators have been studied quantitatively by Boesch *et al.* [6] for NACA 4424 with plasma body force of 40 mN/m at AOA = 0°, U_∞= 8.5 – 19.4 m/s, Re = $0.9 \times 10^5 – 2.0 \times 10^5$. Results are shown in Figure 4-35 in terms of moment change, in percentage. Current work covers a wider range of Reynolds numbers than Boesch's results and has higher moment change because of a higher plasma body force (65 – 90 mN/m).

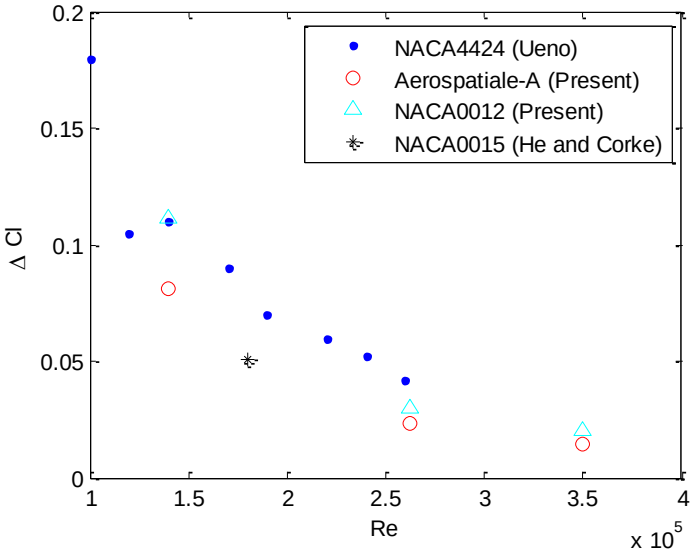

Figure 4-34 Comparison of lift increase by plasma Gurney flap with existing data

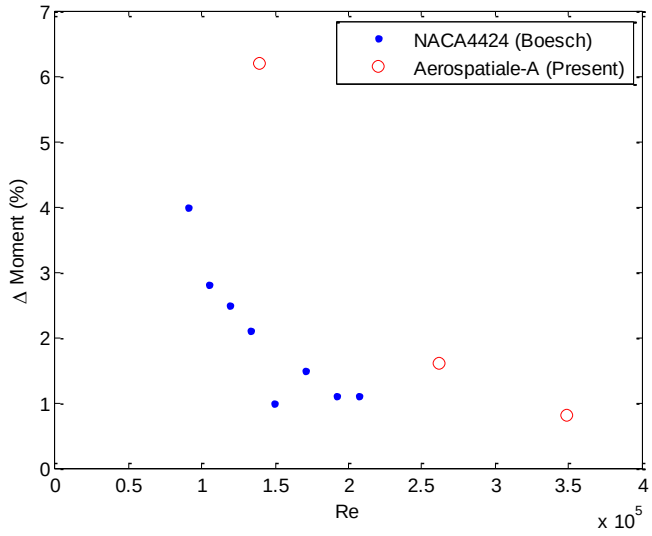

Figure 4-35 Comparison of moment increase by wing tip plasma actuators with existing data

Even though those two plasma actuation concepts have been studied before, these study did not validate CFD tools with detailed force and flow field measurements nor were the effect of AOA on their effectiveness. In the current work, the CFD tools are validated against the experiment tests and a comparison of turbulence models is also carried and a selection is made to best predict the plasma actuation effect for each actuation concept. This tool will be used to predict the effectiveness of the two concepts for real wing geometries under real flight conditions, for which the results will be presented in the Chapter 5.

CHAPTER 5 CFD STUDY ON REAL WING GEOMETRIES AND REAL FLIGHT CONDITIONS

5.1 Performance of Plasma Gurney Flap on Tapered & Swept Wings

Figure 5-1 presents the simulation results for the extruded (AT), tapered (ATtap) and swept wings (ATsw), with and without the plasma Gurney flap at 20 m/s, AOA = 0°, F_B=100 mN/m. The lift increases by 15.6%, 16.3%, 18.3%, respectively. The results indicate that plasma actuation has a better performance on tapered and swept wings than the extruded wing. This can be explained by Figure 5-2, which shows the velocity triangles at the trailing edges of the three wings. The trailing edges on the tapered and swept wings are not perpendicular to the free stream velocity U, therefore the velocities seen by the wings are only the trailing edge normal components of the free stream velocity ($U_{N,tap}$ and $U_{N,sw}$ in Figure 5-2). As the plasma actuation has a larger effect at lower speeds, it has larger lift increment for tapered and swept wings than the extruded wing. This can be further validated by simulating the extruded wing with plasma Gurney flap at free stream velocities of $U_{N,tap}$ and $U_{N,sw}$. Results in Figure 5-3 show that the lift coefficient increases by 16.1% with plasma Gurney flap at free stream velocity of $U_{N,tap}$, and by 19.0% at $U_{N,sw}$, respectively. This indicates that the better effectiveness of plasma Gurney flap on tapered and swept wings come from the reduction of the velocity component normal to the plasma actuators.

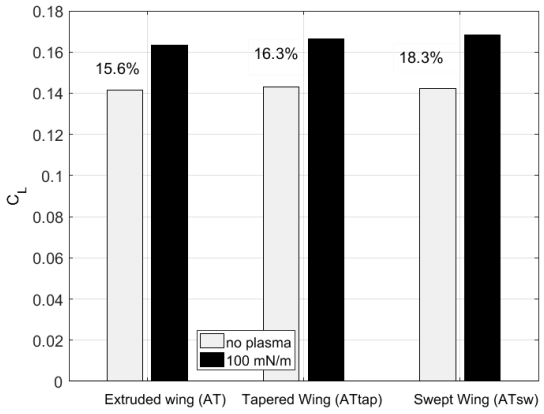

Figure 5-1 Effect of 3D wing geometry on plasma Gurney flap effectiveness (20 m/s, AOA = 0°, F_B= 100 mN/m)

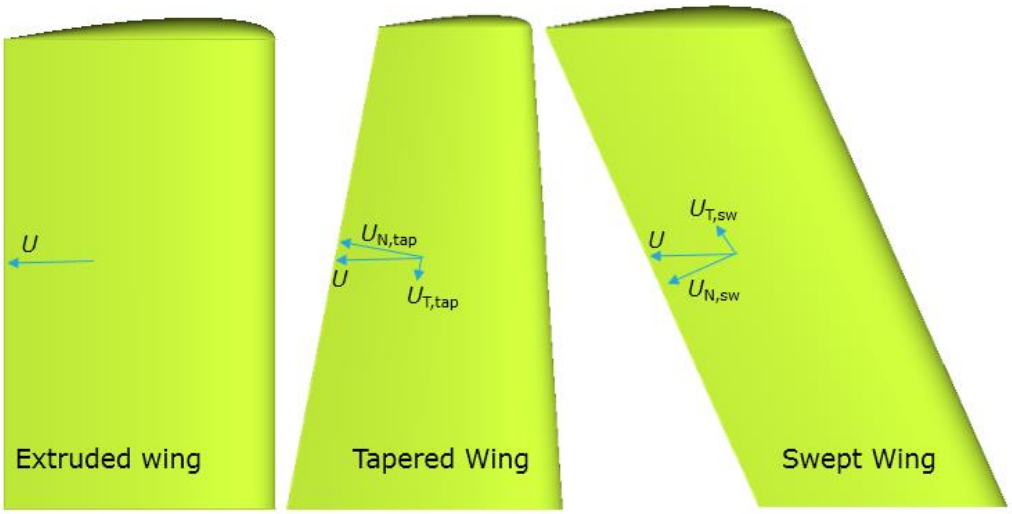

Figure 5-2 Velocity triangles at trailing edges of extruded, tapered and swept wings

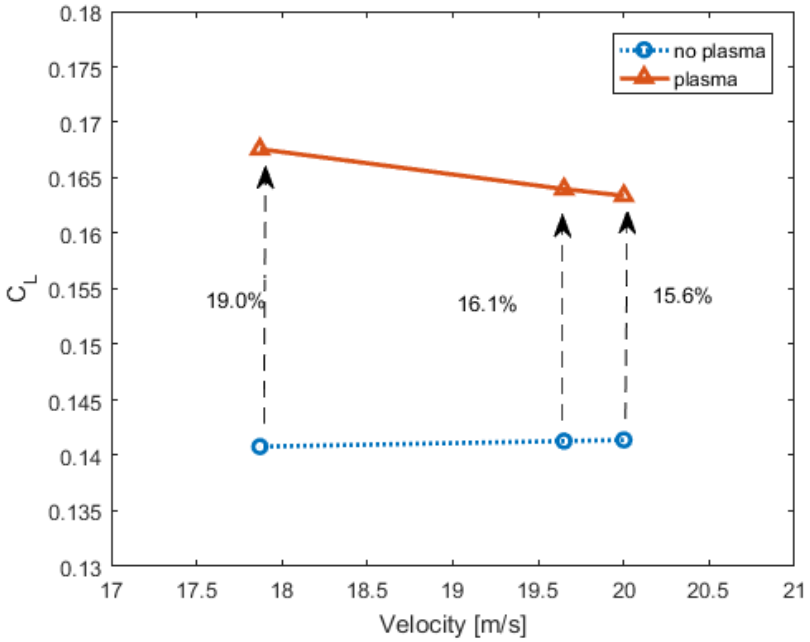

Figure 5-3 Effect of velocity on lift for AT wing with and without plasma Gurney flap

Figure 5-4 presents the mid-span streamlines near trailing edges for the three wings with and without plasma Gurney flap at 20 m/s, AOA = 0°. It can be observed that the tapered and swept wings are slightly better at bending streamlines downwards, which is consistent with previous conclusions.

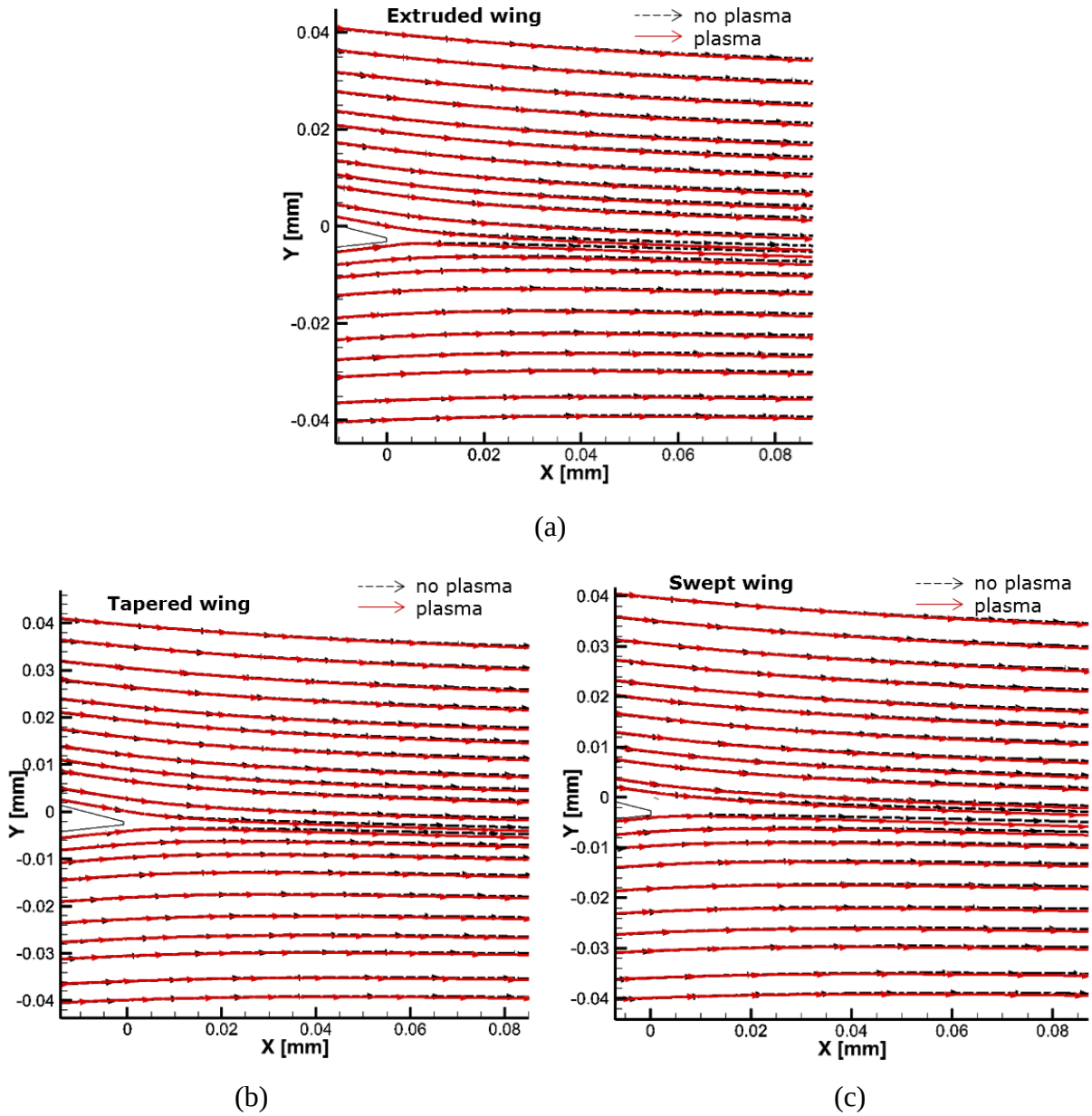

Figure 5-4 Predicted streamlines near trailing edges (CFD) of AT, ATtap and ATsw wings at mid-span (20 m/s, AOA = 0°, F_B= 100 mN/m)

5.2 CFD Tool Assessment at High Speed

To simulate the two plasma concepts on full-scale wings at flight conditions, the CFD tools are first validated at high speed with wind tunnel experimental data [83] and NASA CFD code (WIND) results [84] for M6 wing at AOA = 3.06°, Mach = 0.84, Re = 1.172×10^7. The full turbulence

models (SST and SA) are chosen because the flow is at high speed, and they predict similar changes in wing lift moment for the two plasma concepts (see Chapter 4).

Figure 5-5 presents the pressure contours from FLUENT with SA model and WIND. The figure shows that FLUENT result with SA model matches with WIND results, both capturing the shock wave on the wing surface. Simulation with SST model presents similar contours and is not presented here.

Figure 5-6 to Figure 5-9 show the pressure distributions at four spanwise sections (20%, 65%, 80%, 99% span). Results show that FLUENT results with the SA model match experimental data well, but fail to capture the two shocks on the upper surface at 80% span (see Figure 5-8), which are similar to the WIND results. At wing tip region (99% span), FLUENT with the SA model has better prediction than WIND. The SST model, however, only predicts well for pressure distributions from 20% to 65% span (Figure 5-6 and Figure 5-7). It fails to predict the two shocks at 80% span (see Figure 5-8) and has waving pressure distribution from 0.4 chord to 0.7 chord at 99% span (see Figure 5-9).

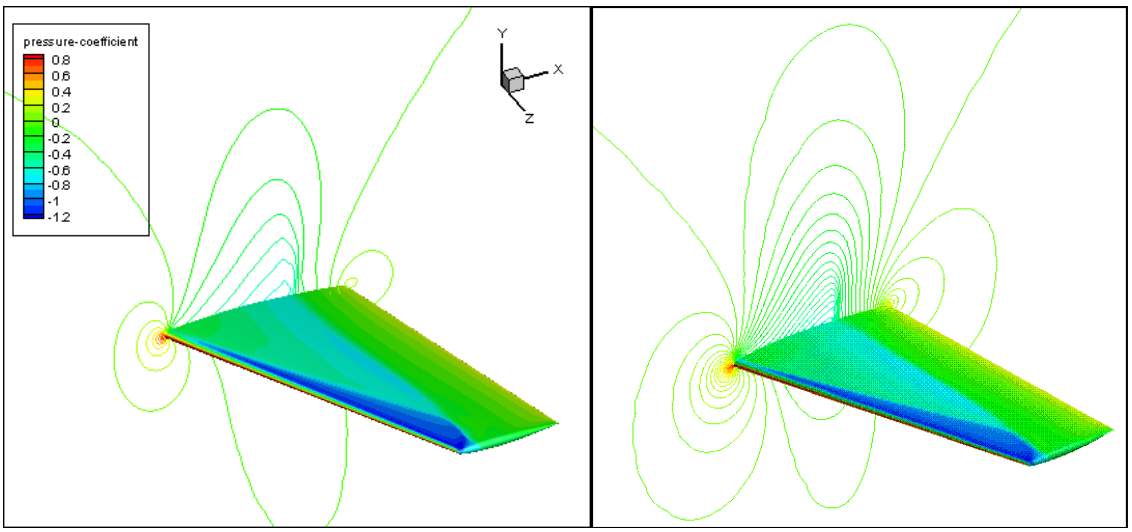

Figure 5-5 Pressure contour by FLUENT (left) compared with WIND results [84] (right) for M6 wing (Mach = 0.84, AOA = 3.06°, Re = 1.172×10^7)

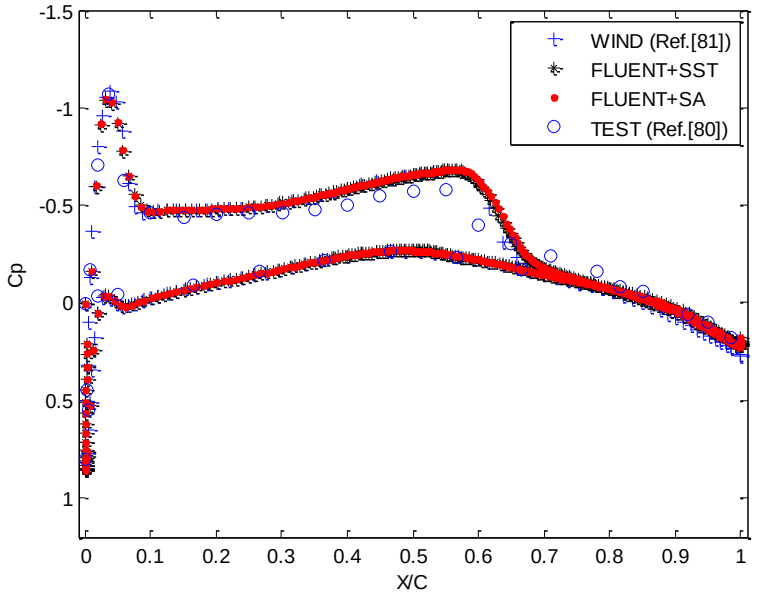

Figure 5-6 Pressure distributions of FLUENT, WIND, and experiment at 20% span for wing M6 (Mach = 0.84, AOA = 3.06°, Re = 1.172×10^7)

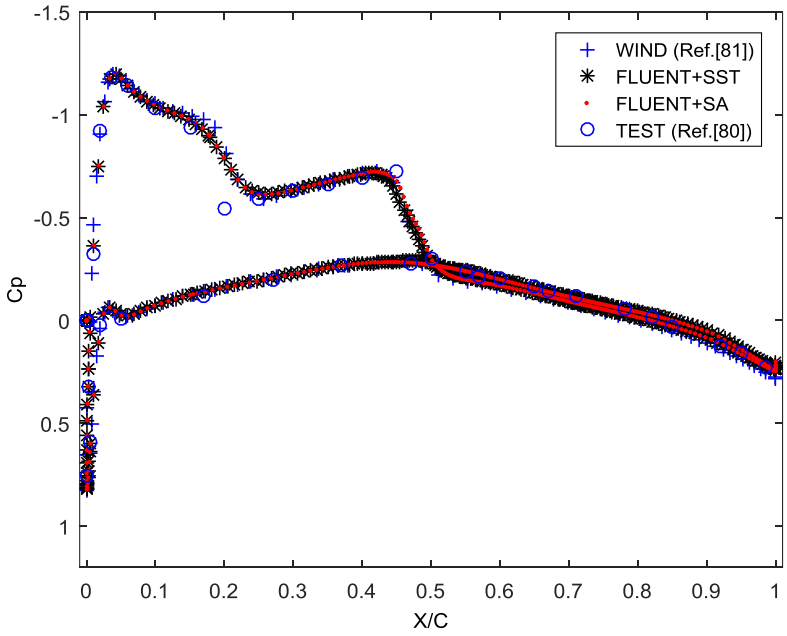

Figure 5-7 Pressure distributions of FLUENT, WIND, and experiment at 65% span for wing M6 (Mach = 0.84, AOA = 3.06°, Re = 1.172×10^7)

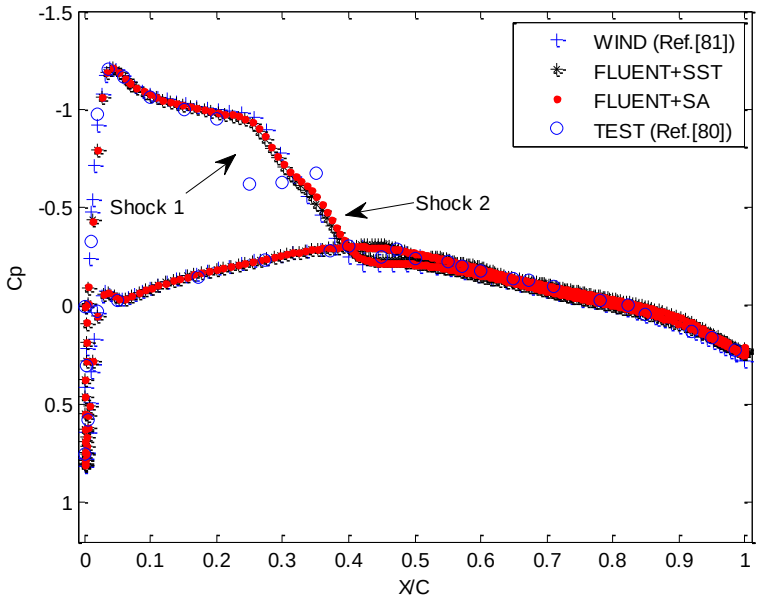

Figure 5-8 Pressure distributions of FLUENT, WIND, and experiment at 80% span for wing M6 (Mach = 0.84, AOA = 3.06°, Re = 1.172×10^7)

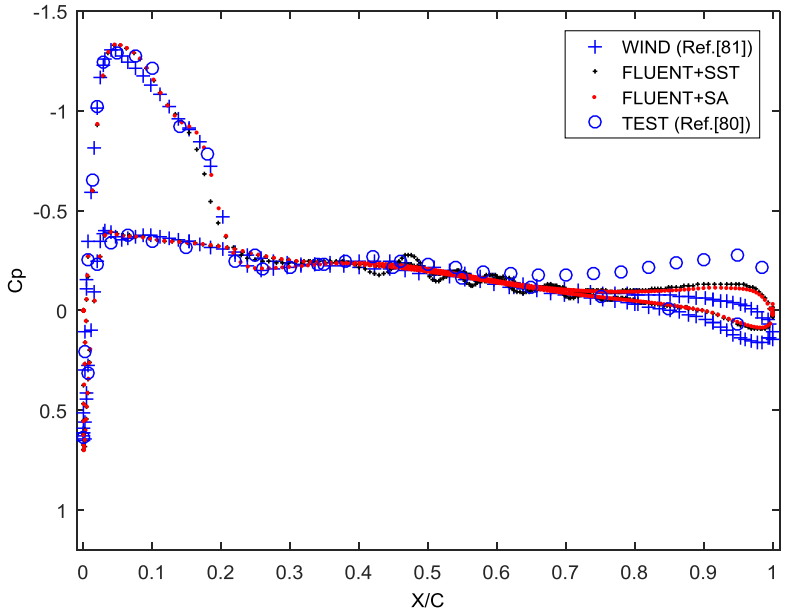

Figure 5-9 Pressure distributions of FLUENT, WIND, and experiment at 99% span for wing M6 (Mach = 0.84, AOA = 3.06°, Re = 1.172×10^7)

Table 5-1 compares the predicted lift and drag coefficients from FLUENT with CFD results from existing literature [85-87]. The simulation results vary for different CFD solvers, but generally lift coefficient is around $0.25 - 0.27$, and drag coefficient around $168-180$ counts. The predicted force

results from FLUENT with two turbulence models fall in line with the above ranges. Therefore, FLUENT can predict force results and the flow characteristics over the wing surface well. The Spalart-Allmaras model provides better prediction and will be used in the following study.

Table 5-1 Comparison of CFD simulation with data from literatures

	Lee [85]	Neilsen [86]	MERLIN [87]	FLUENT+SST	FLUENT+SA
C_L	0.2622	0.253	0.2697	0.2644	0.2690
C_D (counts)	175.1	168	173.6	180.4	178.8

5.3 Assessment of Plasma Actuation Concepts for Full-scale Aircraft

To estimate plasma actuator requirements for full-scale aircraft, the plasma actuator strength is scaled and then implemented on wing trailing edges and wing tips. The plasma Gurney flap is first studied on M6w and M6t trailing edges, with both pressure and suction side actuators located at 90 - 95 % chord. The plasma wing tip actuator is then investigated on wing tips of M6w and M6t, located at 96% span on pressure and suction sides.

As detailed in Appendix G, the rolling moment coefficient for Boeing 737 wing is about 0.04 with a maximum aileron deflection of 10° and the lift coefficients for horizontal tails are about 0.12 for Mach = 0.84, and 0.15 for Mach = 0.3. To compare with the above data, the same non-dimensional coefficients, moment coefficient and lift coefficient are computed in FLUENT.

In FLUENT, the wing lift L is the sum of the spanwise lift on the whole wing surface, and the moment M is the integral moment of spanwise lift to wing root, as shown in Figure 5-10. The lift and moment coefficients C_L and C_M are defined by equation (5.1) and (5.2)

$$C_L = \frac{L}{qS} \tag{5.1}$$

$$C_M = \frac{M}{qbS} \tag{5.2}$$

where L is the total lift, M the integral moment to wing root, q the dynamic pressure, b the wing span, S the wing area.

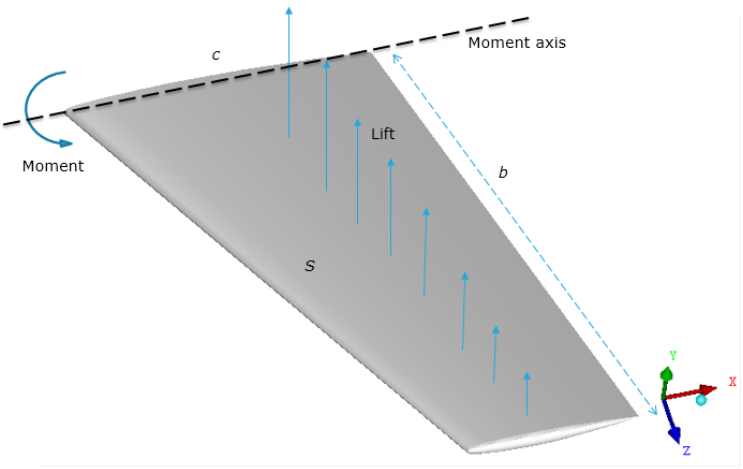

Figure 5-10 Moment and lift for M6t and M6w wings

Plasma Gurney Flap Performance at High Speed

Figure 5-11 presents the moment coefficient change under different plasma actuation strengths for M6w wing at AOA = 3°, Mach = 0.84, Re = 4.94 × 10^7. The far-field temperature is around 223 K (-50 ℃), absolute pressure 25 kPa, density 0.4 kg/m^3. A smooth spline is applied to fit the CFD data points for actuation strength prediction. In order to have the equivalent moment change as traditional mechanical aileron with a maximum deflection of 10°, the required rolling moment change ΔC_M = is 0.04, therefore the plasma Gurney flap should have an actuation strength of about 27 N/m.

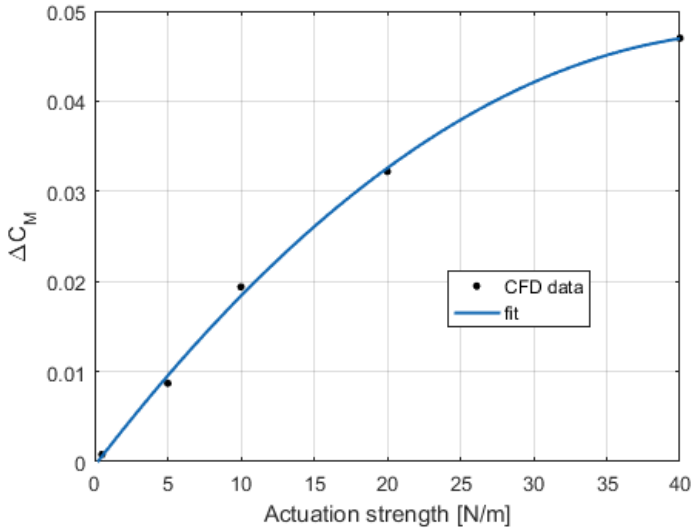

Figure 5-11 Moment coefficient increase for M6w wing with plasma Gurney flap (AOA = 3°, Mach = 0.84, Re = 4.94 × 10^7)

Figure 5-12 presents the pressure contours on the suction side of M6w wing, without and with plasma Gurney flap (actuation strength of 20 N/m). It can be observed that the pressure drops along the leading edge because of plasma actuation, as shown by a bigger and darker region near leading edge in Figure 5-12. A low-pressure region also appears in the middle of pressure side because of the plasma actuation at the trailing edge. A plot of the Mach number contours at mid-span in Figure 5-13 indicates that plasma actuation strengthen the shock on the wing suction surface and moves it downstream.

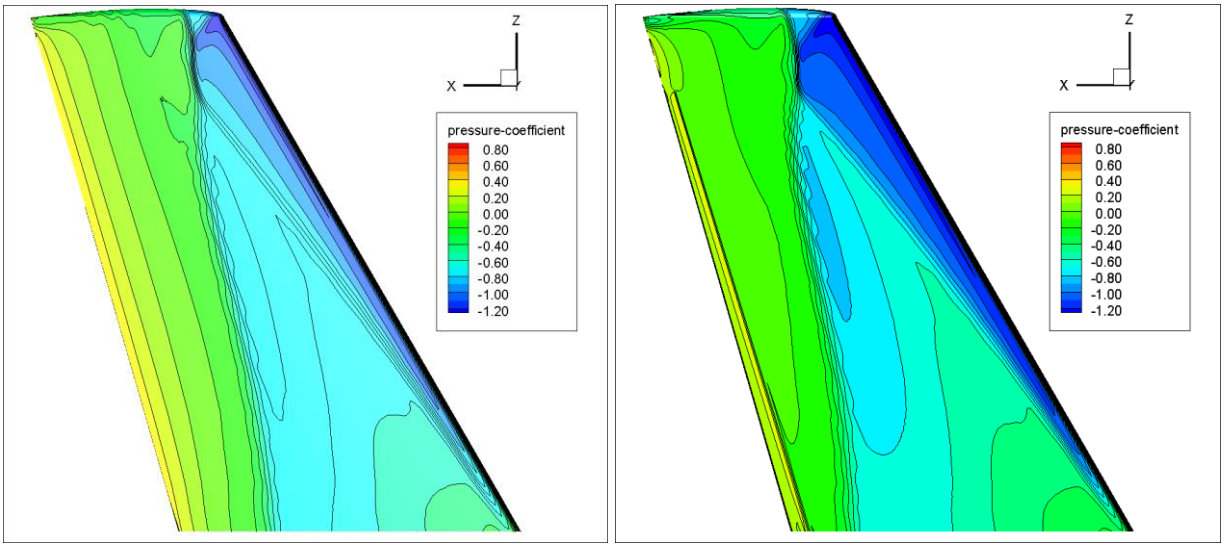

Figure 5-12 Pressure contours for M6w wing suction side without (left) and with (right) plasma Gurney flap (AOA = 3°, Mach = 0.84, Re = 4.94×10^7, F_B= 20 N/m)

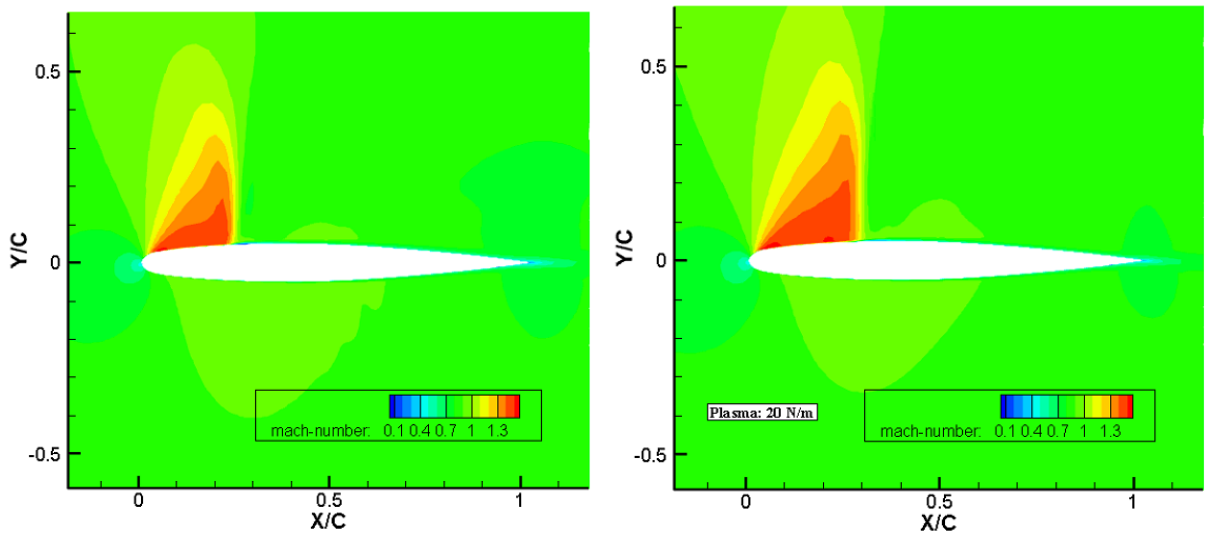

Figure 5-13 Mach number contours for M6w wing mid-span without (left) and with (right) plasma Gurney flap (AOA = 3°, Mach = 0.84, Re = 4.94×10^7, F_B= 20 N/m)

This can be observed clearly from the pressure distribution at different spanwise sections, as shown in Figure 5-14 for 0% (wing root), 50%, 75% and 99% span. Shock is observed at this Mach number and AOA, and it is sensitive to perturbations. The shock on the suction side therefore moves downstream by about 0.1 chord from wing root to 75% span. The suction side has a lower pressure peak (the y axis is reversed in the figures). Moreover, the pressure on the pressure side increases near trailing edge and decreases on the suction side. The results show that the upstream and wing tip pressure distributions are affected significantly by the plasma Gurney flap. This is because the shock wave is very sensitive to the trailing edge actuation. The wing surface pressure change greatly when shock wave moves downstream. This shows that the presence of shock improves plasma Gurney flap effect.

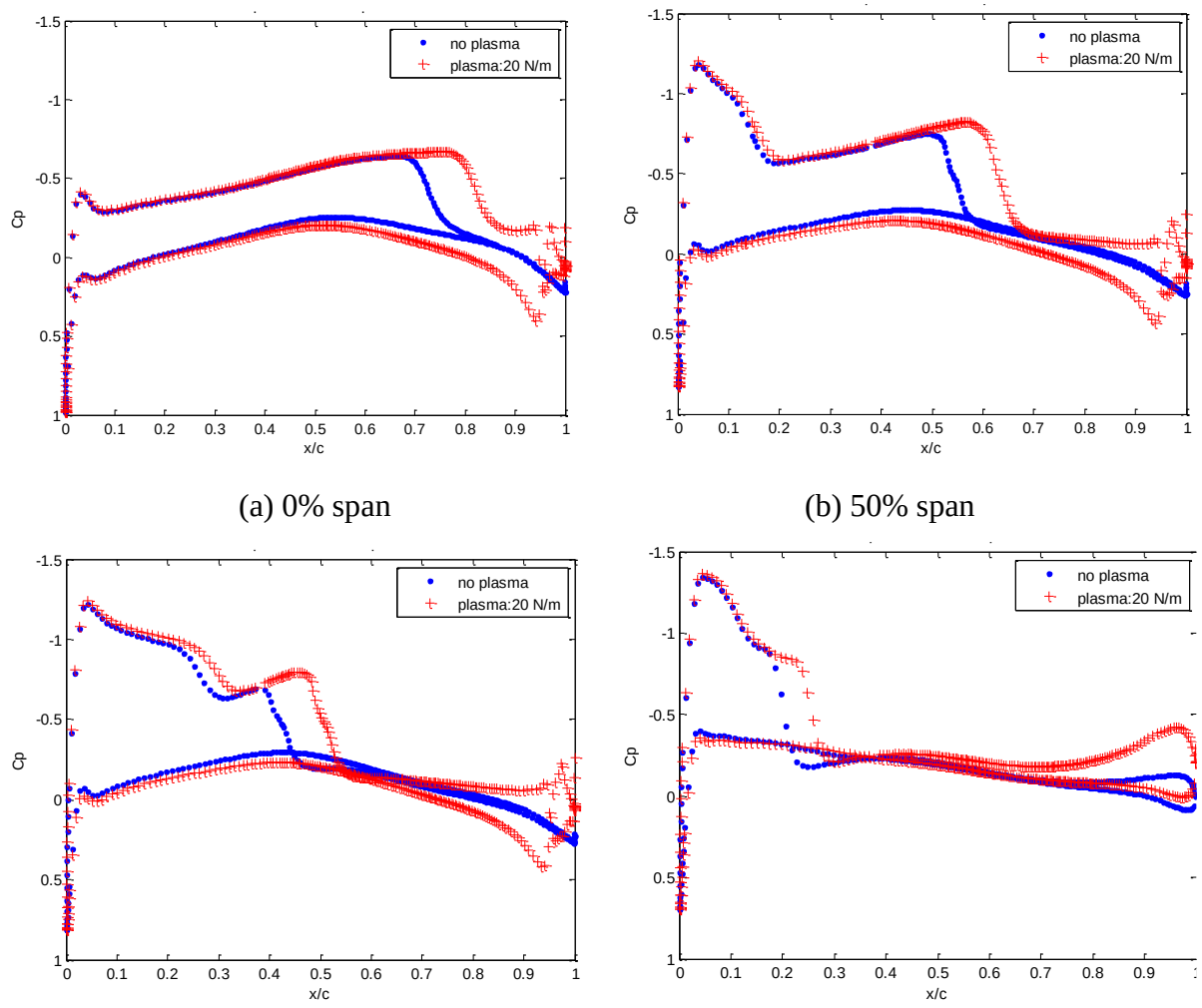

(a) 0% span

(b) 50% span

(c) 75% span

(d) 99% span

Figure 5-14 Pressure distributions for M6w wing with and without plasma Gurney flap at different spanwise positions (AOA = 3°, Mach = 0.84, Re = 4.94×10^7, F_B= 20 N/m)

Figure 5-15 presents the middle-span streamlines near the trailing edge of the M6w wing with and without plasma Gurney flap (F_B= 5 and 20 N/m) at AOA = 3°. With a plasma actuation strength of 5 N/m, streamlines bend downwards towards the pressure side, resulting in lift increase. With a strength as high as 20 N/m, the streamlines bend downwards significantly, with a recirculation vortex occurring near the trailing edge. The streamline changes are consistent with the moment/lift increase from Figure 5-11, where stronger actuation strength leads to larger moment increase and streamline changes.

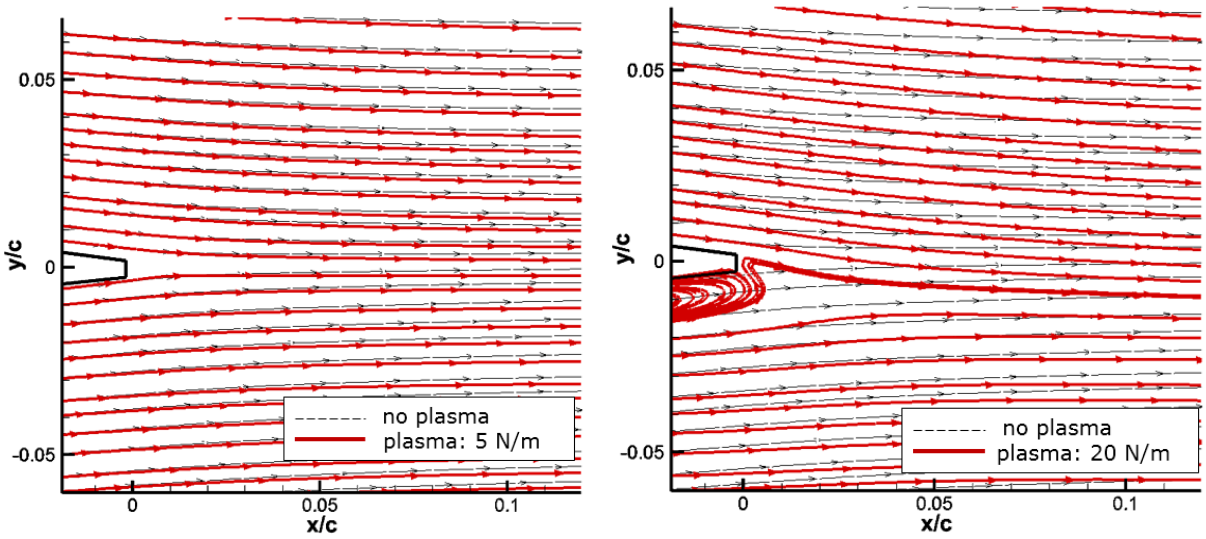

Figure 5-15 Middle-span streamlines for M6w wing with and without plasma Gurney flap (AOA = 3°, Mach = 0.84, Re = 4.94×10^7, F_B=5 and 20 N/m)

Figure 5-16 presents the lift coefficient change under different plasma actuation strengths for the M6t wing at AOA = 0°, Mach = 0.84, Re = 1.54×10^7. A smooth spline is used to fit the CFD data. As shown in Figure 5-16, to obtain the same lift coefficient as traditional horizontal tails at cruising speed (ΔC_L = 0.12, see Appendix G), the plasma actuators should have an actuation strength as high as 72 N/m.

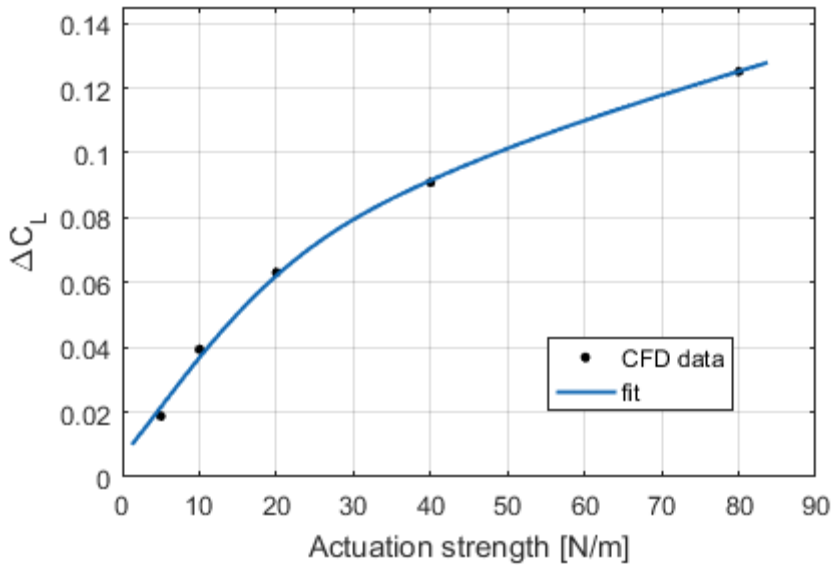

Figure 5-16 Lift coefficient increase for M6t wing with plasma Gurney flap (AOA = 0°, Mach = 0.84, Re = 1.54×10^7)

The pressure distributions for the M6t wing with and without plasma Gurney flap (F_B =20 N/m) at different spanwise locations are shown in Figure 5-17. At zero angle of attack, the pressure without plasma actuation on pressure and suction sides is identical because of the symmetrical profile. With an actuation strength of 20 N/m, the suction side pressure decreases and pressure side pressure increases over most of the wing span (except near wing tip). Moreover, the plasma actuation not only affects the local region, but also alters the upstream pressure greatly. Unlike the M6w wing, the plasma Gurney flap has less effect for pressure near the wing tip with the same actuation strength as M6w wing. At AOA = 0, no shock is observed without plasma but the conditions for shock exists. With plasma actuation, a weak shock occurs on M6t wing and this leads to upstream pressure change (around 0.4-0.6 chord). This shows the condition for shock can also improve plasma Gurney flap effect.

Figure 5-18 shows the mid-span streamlines near the trailing edge of the M6t wing with and without the plasma Gurney flap (F_B= 5 and 20 N/m) at AOA = 0°. Similar to M6w wing, the plasma Gurney flap with actuation strength of 5 N/m only bends streamlines slightly. When the actuation strength reaches 20 N/m, streamlines bend significantly downwards with a recirculation vortex generated near the pressure side trailing edge.

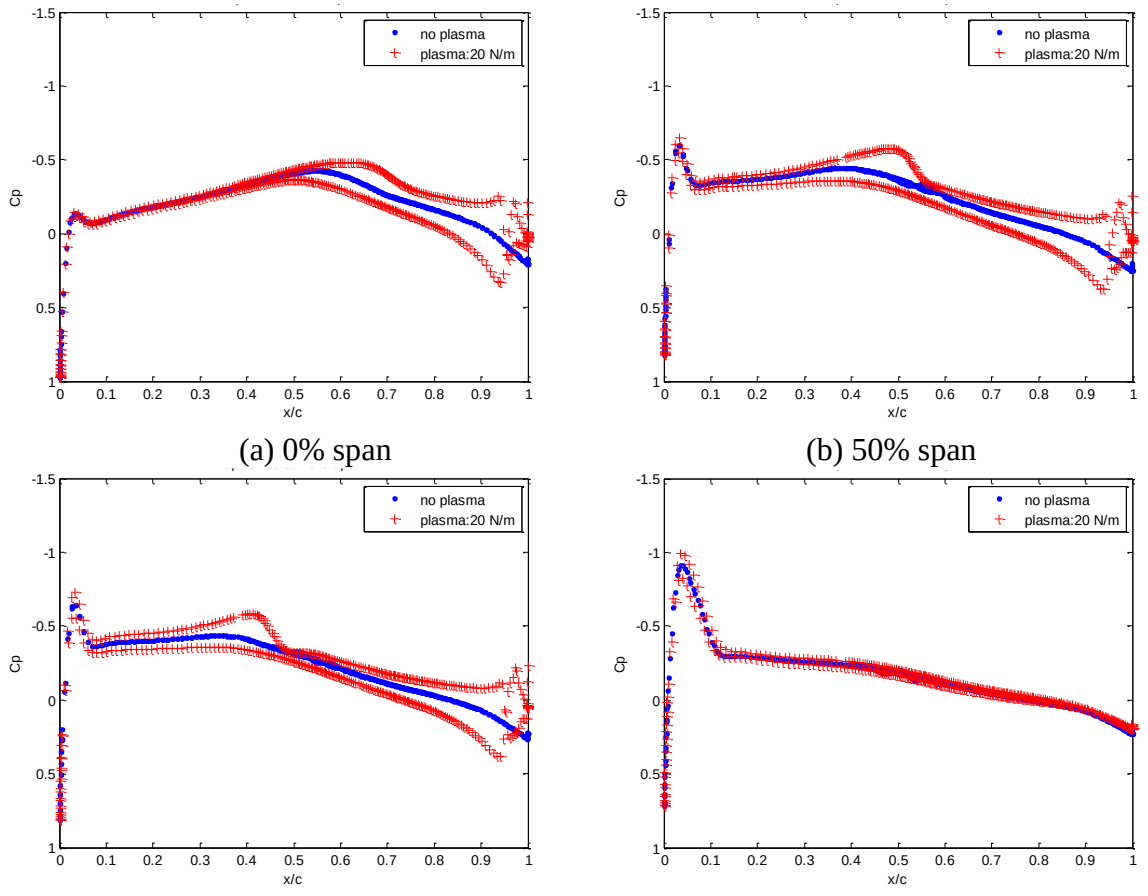

(a) 0% span (b) 50% span

(c) 75% span (d) 99% span

Figure 5-17 Pressure distributions for M6t wing with and without plasma Gurney flap at different spanwise positions (AOA = 0°, Mach = 0.84, Re = 1.54×10^7, F_B =20 N/m)

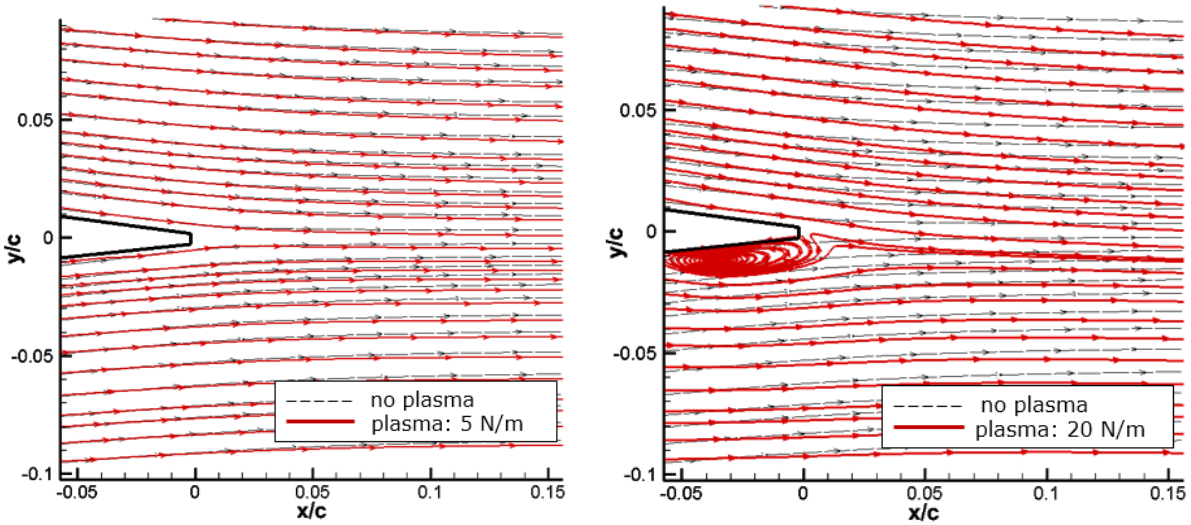

Figure 5-18 Mid-span streamlines for M6t wing with and without plasma Gurney flap (AOA=0°, Mach = 0.84, Re = 1.54×10^7, F_B=5 and 20 N/m)

Plasma Wing Tip Actuator Performance at High Speed

Plasma wing tip actuation has very limited effect at high speed conditions (AOA = 0° & 3°, Ma = 0.84, Re=1.54 – 4.94 × 10^7). For the M6w wing, the moment coefficient only changes by 0.006 for a plasma actuation strength of 40 N/m. For M6t wing, the lift coefficient increases only by 0.002 with plasma body force of 40 N/m. The moment and lift coefficient increases are about one tenth of those achieved by plasma Gurney flap. As mentioned before, to replace traditional wing ailerons and horizontal tails for flight control at cruise speed, the moment coefficient change and lift coefficient change is 0.04 and 0.12, respectively. However, plasma wing tip actuators could only bring a change of 0.002 - 0.006 for moment coefficient and lift coefficient and couldn't sufficient lift/moment for flight control. Therefore, it would not provide much added value when combined with plasma Gurney flaps.

Figure 5-19 shows the vorticity contours at an axial plane one chord downstream of the M6w wing trailing edge, without and with plasma wing tip actuation (F_B = 20 and 40 N/m). The vortices are pushed away from the wing tip and separated into one small and one big vortex because of the plasma actuation. With 40 N/m plasma actuation strength, lift has better lift improvement than 20 N/m, leading to a larger tip vortex with higher core vorticity as expected.

Figure 5-20 presents the vorticity contours at an axial plane one chord downstream of the M6t wing trailing edge, without and with plasma wing tip actuation (F_B = 20 and 40 N/m). Similar to NT wing in Section 4.3.2, the wing tip plasma actuators generate a pair of counter-rotating vortices at downstream plane. The vortex cores have higher vorticity with stronger plasma actuation strength, which is similar to previous M6w wing with plasma wingtip actuation.

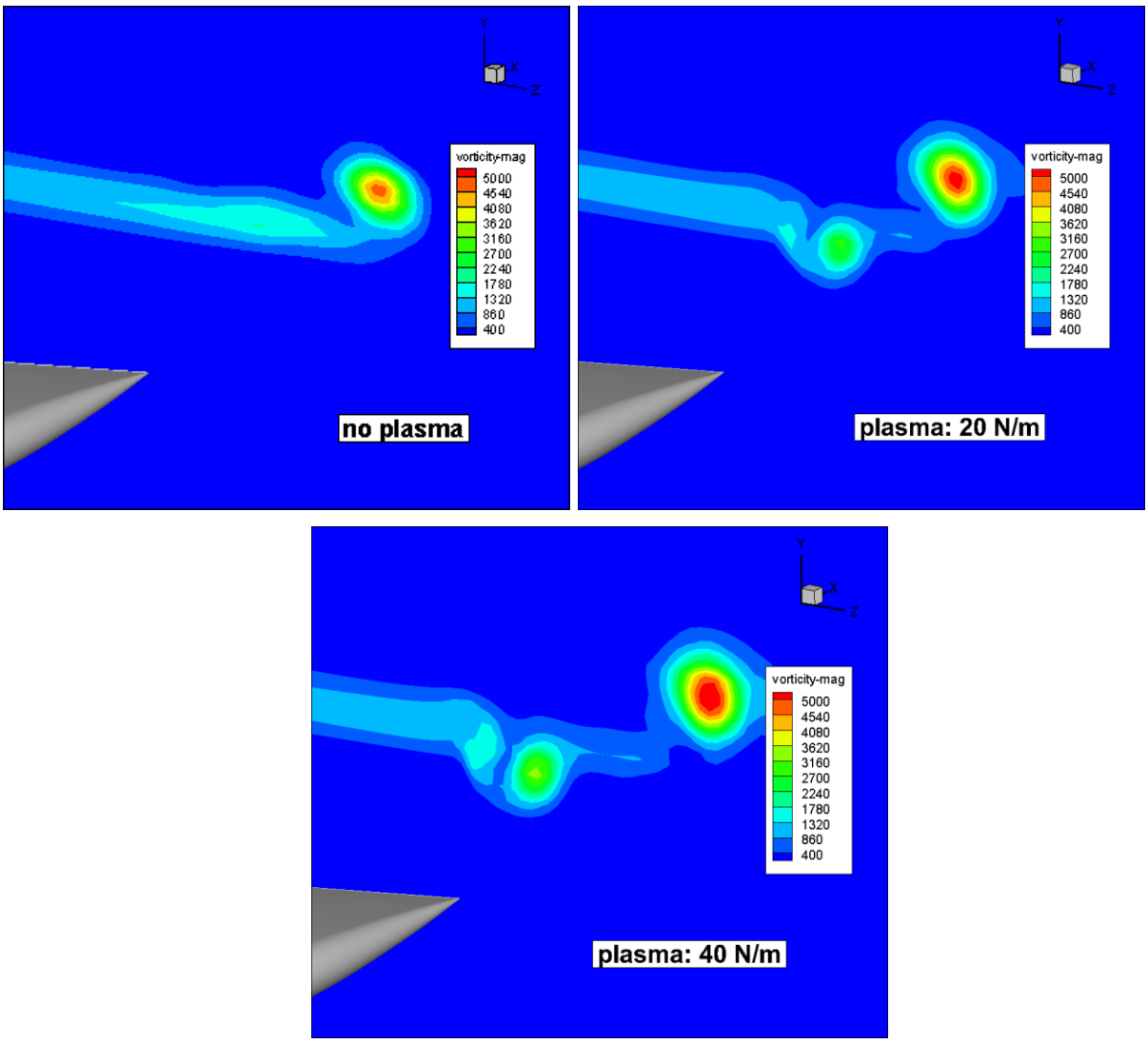

Figure 5-19 One chord downstream of trailing edge vorticity contours for M6w wing with and without plasma wing tip actuation (AOA=3°, Mach = 0.84, Re = 4.94×10^7, F_B=20 and 40 N/m)

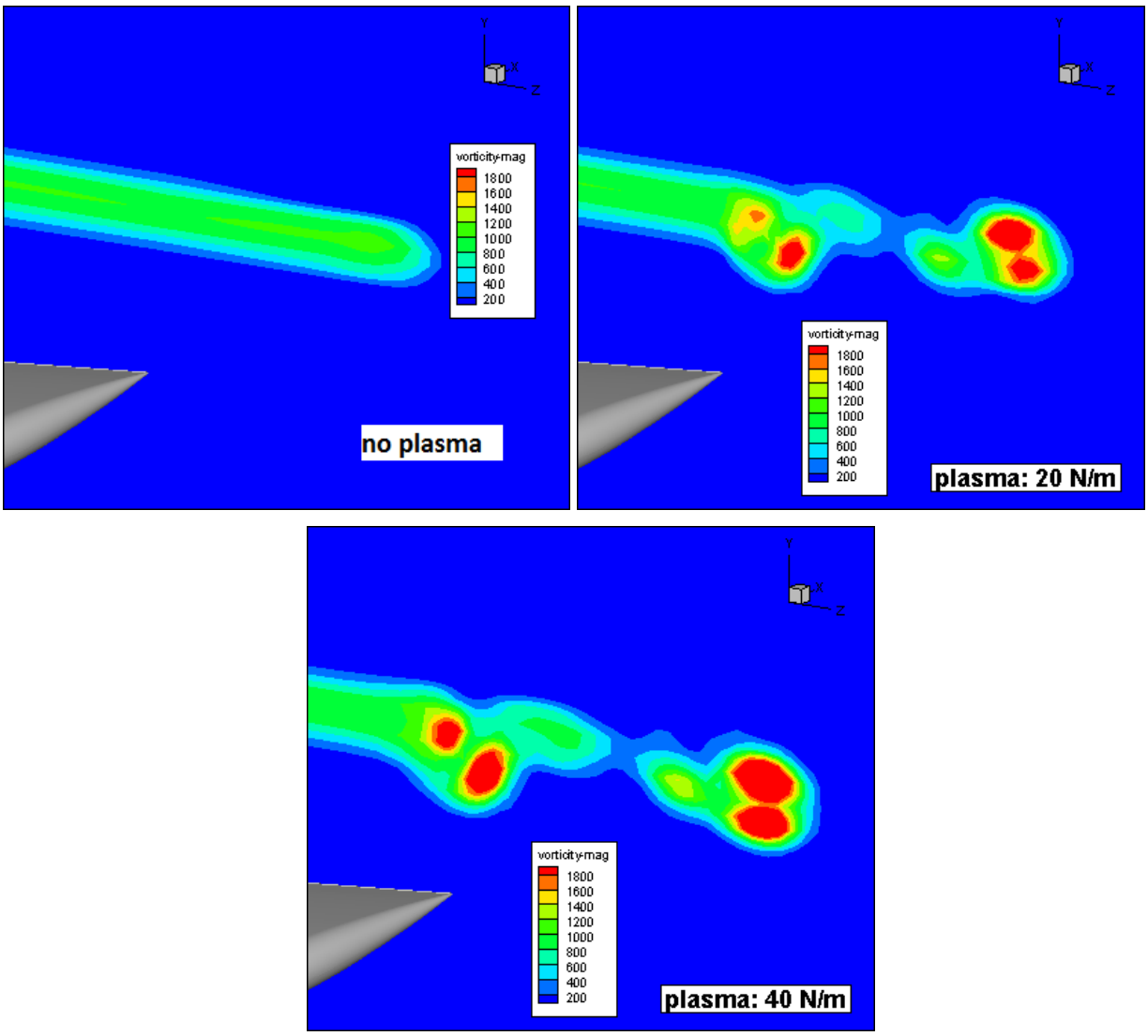

Figure 5-20 One chord downstream of trailing edge vorticity contours for M6t wing with and without plasma wing tip actuation (AOA=0°, Mach = 0.84, Re = 1.54×10^7, F_B=20 and 40 N/m)

The plasma wing tip actuation can be also investigated by local AOA at a spanwise location 0.1 chord upstream of wing leading edges. Figure 5-21 and Figure 5-22 show the results with and without plasma for wing M6w and M6t, respectively. The local AOAs of both wings increase with plasma actuation by a maximum angle of 0.02° with plasma actuation strength of 40 N/m, which can be observed clearly in Figure 5-22. These results are in the same order of velocity angle change for AT and NT wings in Section 4.3.

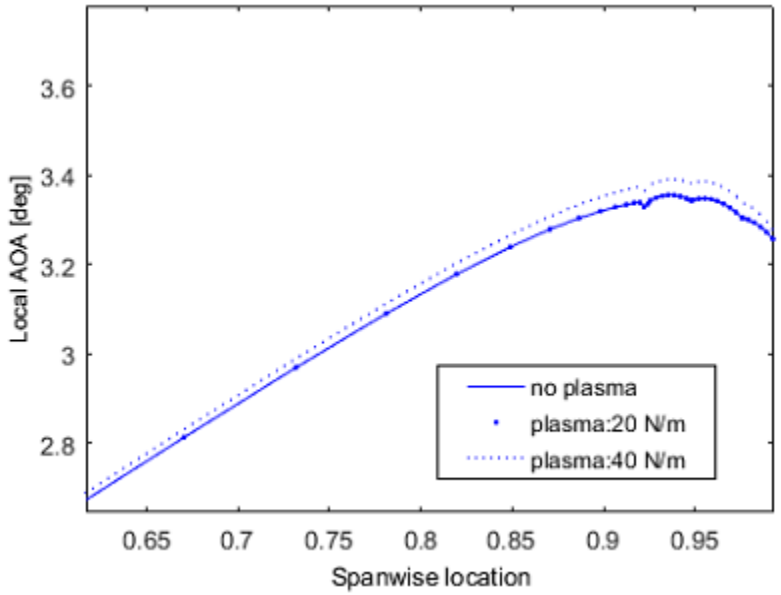

Figure 5-21 Local AOA at 0.1 chord upstream leading edge of M6w wing with and without plasma wing tip actuation (AOA = 3°, Mach = 0.84, Re = 4.94×10^7)

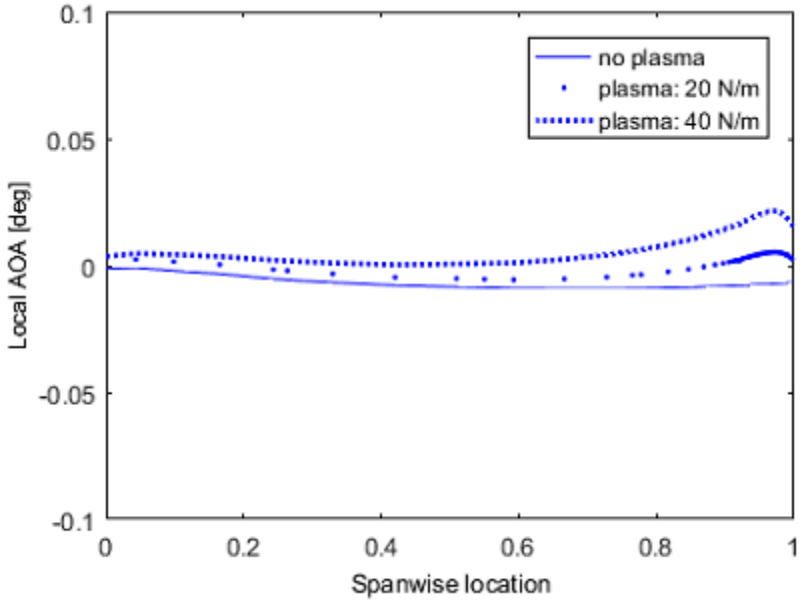

Figure 5-22 Local AOA at 0.1 chord upstream leading edge of M6t wing with and without plasma wing tip actuation (AOA = 0°, Mach = 0.84, Re = 1.54×10^7)

Plasma Gurney Flap Performance at Takeoff/Landing Speed

To simulate the aircraft takeoff/landing conditions, the M6t wing is simulated at AOA = 0°, Mach = 0.3, Re = 1.93 × 10^7, and the M6w wing at AOA = 3°, Mach = 0.3, Re = 6.21 × 10^7. The temperature of far-field is 283K (10 ℃), absolute pressure 101.325 kPa, air density 1.25 kg/m^3.

For takeoff/landing conditions, the plasma actuation strength is scaled up to 160 N/m and then implemented on trailing edges of the M6w and M6t wings, as shown in Figure 5-25 and Figure 5-26. For M6w and M6t wing, when plasma actuation strength grows above 80 N/m, the moment and lift coefficient change by plasma Gurney flap reach a plateau, with a maximum of ΔC_M = 0.038 for M6w at F_B =~100 N/m and ΔC_L = 0.080 for M6t at F_B =160 N/m. Traditional aileron with a deflection angle of 9.5° can provide a rolling moment ΔC_M of 0.038. Therefore, at takeoff/landing conditions, the plasma Gurney flap on M6w can provide adequate rolling moment with an actuation strength of about 100 N/m. However, the plasma Gurney flap on M6t wing cannot provide sufficient moment for pitch control. Thus, the plasma Gurney flap concept is less effective at takeoff/landing conditions than cruise condition.

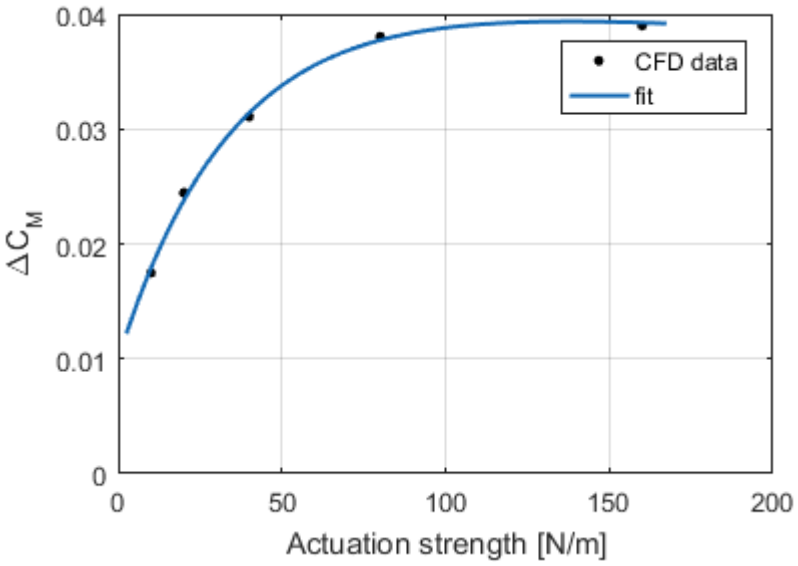

Figure 5-23 Moment coefficient increase for M6w wing with plasma Gurney flap (AOA = 3°, Mach = 0.3, Re = 6.21 × 10^7)

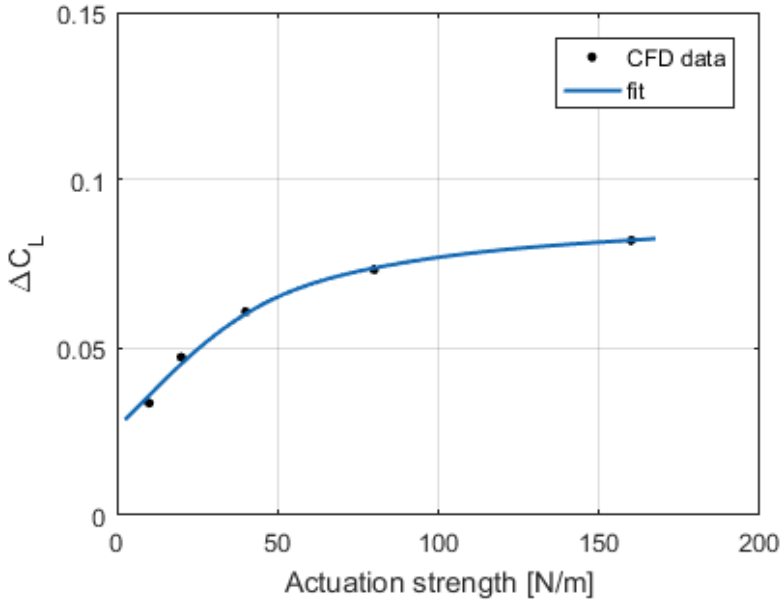

Figure 5-24 Lift coefficient increase for M6t wing with plasma Gurney flap (AOA = 0°, Mach = 0.3, Re = 1.93×10^7)

Figure 5-25 presents the pressure distributions at two spanwise positions (0%, 50% span) for the M6w wing with and without plasma Gurney flap at AOA = 3°. With an actuation equal to that at cruising speed in Figure 5-14 (20 N/m), the pressure on the pressure side increases and that on the suction side drops, mainly near trailing edge, leading to lift/moment increase. Unlike the M6w wing at high speed, no shock appears at Mach =0.3 and plasma actuation with the same strength only has a limited effect on upstream pressure. This can explain the weaker effect of moment/lift change by plasma Gurney flap at Mach=0.3.

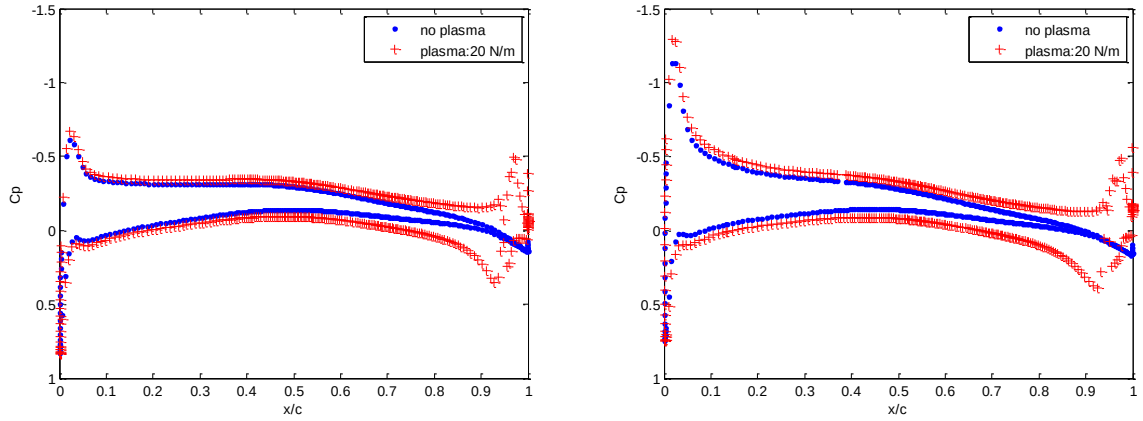

(a) 0% span (b) 50% span

Figure 5-25 Pressure distributions for M6w wing with and without plasma Gurney flap at different spanwise positions (AOA = 3°, Mach = 0.3, Re = 6.21×10^7, F_B=20 N/m)

The mid-span streamlines near the trailing edge for the M6w wing at takeoff/landing conditions exhibit similar patterns as those at high speed. As shown in Figure 5-26, streamlines bend downwards with a recirculation vortex occurring near trailing edge when apply 20 N/m plasma actuation.

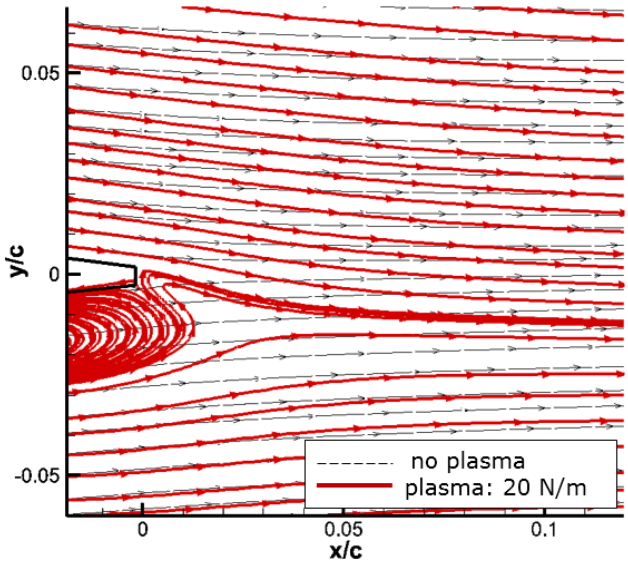

Figure 5-26 Mid-span streamlines for M6w wing with and without plasma Gurney flap (AOA = 3°, Mach = 0.3, Re = 6.21×10^7, F_B=20 N/m)

Figure 5-27 presents the pressure distributions at two spanwise positions (0%, 50% span) for the M6t wing with and without plasma Gurney flap at AOA = 0°, Mach = 0.3. At this Mach number, the plasma Gurney flap only affects the local pressure distribution near the trailing edge, much as the plasma Gurney flap on the M6w wing at the same Mach number (Figure 5-25). Moreover, the effect is also less significant than that at high speed (Mach=0.84). With the absence of shock wave at Mach = 0.3, the plasma Gurney flap can only affect local pressure distribution for the M6t wing.

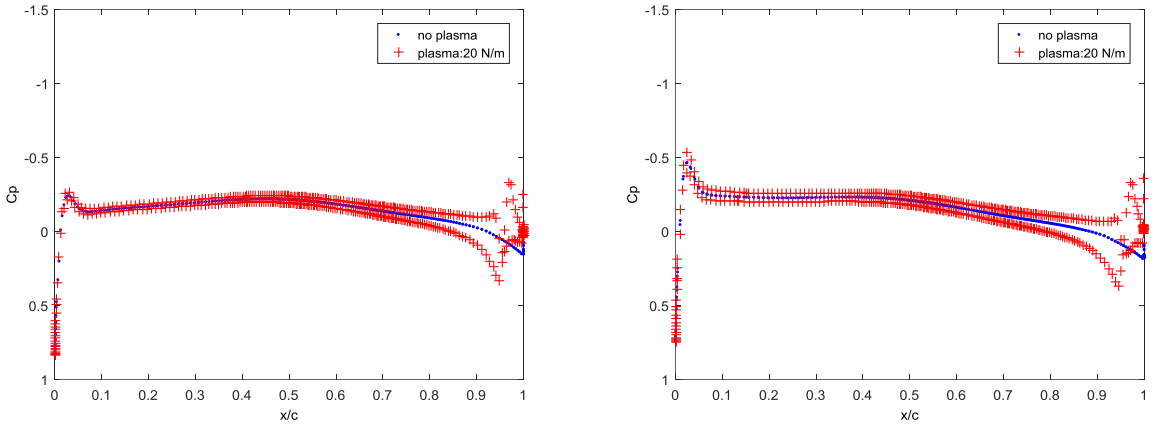

(a) 0% span (b) 50% span

Figure 5-27 Pressure distributions for M6t wing with and without plasma Gurney flap at different spanwise positions (AOA = 0°, Mach = 0.3, Re = 1.93×10^7, F_B=20 N/m)

Plasma Wing Tip Actuator Performance at Takeoff/Landing Speed

For wing tip actuations at Mach =0.3, the moment coefficient of the M6w wing increase by 0.0027 and the lift coefficient of M6t increases by 0.0019 with plasma body force of 20 N/m, which are much smaller (less than one tenth) than those by plasma Gurney flap with the same actuation strength. Similar as in the high-speed conditions, the wing tip plasma actuators have very limited effect on M6w and M6t wings at landing/takeoff conditions. Figure 5-28 and Figure 5-29 present the vorticity contours at axial planes one chord downstream of the trailing edges of M6w and M6t wings, respectively. Similar conclusions can be drawn for plasma wing tip actuators for the two wings, when comparing with Figure 5-19 and Figure 5-20 at Mach = 0.84. For the M6w wing, the tip vortex is pushed away but with higher core vorticity due to plasma actuation. For M6t wing, a small pair of counter-rotating vortices is generated when plasma actuation is applied.

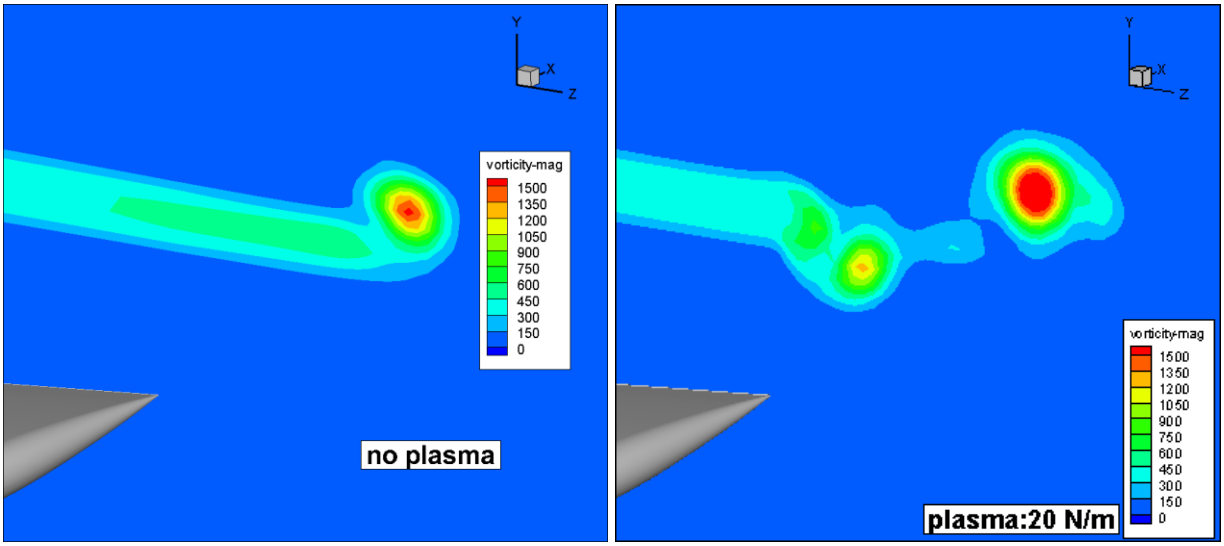

Figure 5-28 One chord downstream of trailing edge vorticity contours for M6w wing with and without plasma wing tip actuation (AOA = 3°, Mach = 0.3, Re = 6.21×10^7)

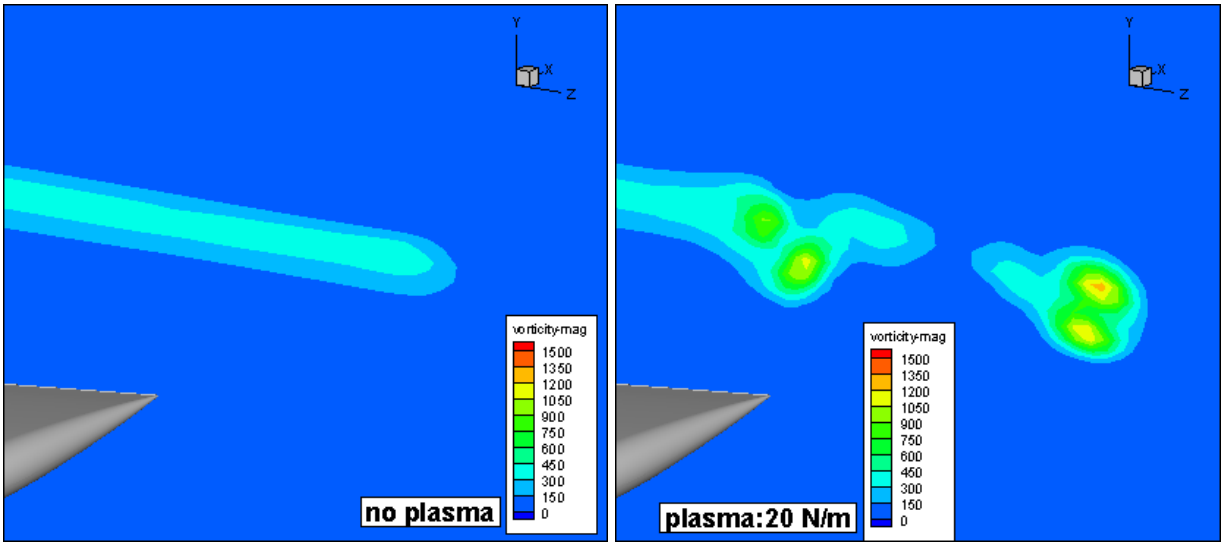

Figure 5-29 One chord downstream of trailing edge vorticity contours for M6t wing with and without plasma wing tip actuation (AOA = 0°, Mach = 0.3, Re = 1.93×10^7)

5.4 Discussion

In this chapter, the plasma actuation effect on tapered and swept wings is first studied. It is found that the plasma Gurney flap has better performance on tapered and swept wings because of the reduction of the effective velocity component normal to the plasma actuator. Then, a 3D transonic wing within a far field domain is simulated to assess the required plasma actuation strength for

aircraft application. It is concluded that the plasma Gurney flap requires a plasma actuation strength of about 27 N/m to provide sufficient rolling moment, and about 72 N/m to replace horizontal tails at high speed (Mach = 0.84). At landing/takeoff conditions (Mach = 0.3), the plasma Gurney flap requires a plasma actuation strength of about 100 N/m to provide sufficient (or close) rolling moment, but cannot provide enough moment to replace movable pitch control surfaces on the horizontal tail. It is observed that the presence and condition of shock can improve the performance of plasma Gurney flap. On the other hand, the wing tip plasma actuator is too weak to provide sufficient force by itself for aircraft control.

Currently, there has not been any study of the flow velocity effect on plasma actuation strength at high Mach number (above 0.3). Therefore, the plasma actuation strengths from CFD simulations are considered as effective plasma actuation strength at the desired operating flow velocity.

The simulations in this thesis provide the target actuation strength required for the application of the proposed plasma actuation concepts for typical full-scale high subsonic commercial airliners. With the actuation strength of current AC driven DBD plasma actuator ranging only from 0.1- 0.5 N/m, much research work in terms of plasma actuator development remain to be done to improve actuator strength to the level required for the proposed concepts to work in real commercial aircraft applications.

CHAPTER 6 CONCLUSION AND RECOMMENDATIONS

The primary objective of the present work is to provide a deeper assessment of two concepts of DBD plasma actuators for lift enhancement on wings at low angles of attack, namely the plasma Gurney flap and wing tip plasma actuator. Wind tunnel tests are carried out on four wings with plasma actuators to validate the CFD tools, which are then used to assess the two concepts on realistic wing geometries at real fight conditions.

The research was carried out in three phases. Phase 1 consisted of preliminary numerical study and experimental design. ANSYS FLUENT was chosen as the CFD solver with the engineering plasma model by Lemire and Vo [74] to provide lift estimation for experimental design. Four wings were designed, fabricated and tested at wind tunnel conditions in the second phase to validate the CFD tools by force, pressure and flow field measurements. In the last phase, the validated CFD tools were used to assess the viability of the two concepts on realistic wing geometries at real flight conditions.

The main conclusions/finding are as follows:

1) The RANS CFD code ANSYS FLUENT with the engineering plasma actuator model by Lemire and Vo [74], is capable to predict the effect of plasma Gurney flap and plasma wing tip actuators on the aerodynamic forces moments. The effect of the plasma Gurney flap on the flow field near the wing trailing edge is also well captured by CFD when compared with experiment measurements.
2) The CFD tools are evaluated with two turbulence models, namely Shear Stress Transportation and Spalart-Allmaras models. In general, the two turbulence models predict similar changes in wing lift moment for the two plasma concepts, with the SST model providing a closer match with wind tunnel test data.
3) The plasma Gurney flap and plasma wing tip actuation concepts can both help to improve lift for wings with asymmetrical and symmetrical profiles. However, the plasma Gurney flap provides higher lift enhancement, but the effectiveness of both concepts decreases with increasing flow velocity.
4) The plasma Gurney flap effect tends to decrease at higher angle of attack (3°) while plasma wing tip actuator remains about the same.

5) The tapered and swept effects on wing geometries can help improve plasma Gurney flap performance by reducing the effective velocity component normal to the plasma actuator.
6) To apply plasma Gurney flap on the full-scale aircraft, the plasma Gurney flap needs to have an effective plasma actuation strength on the order of $25 - 70$ N/m at high subsonic cruising conditions, and about 100 N/m at landing/takeoff conditions. The presence of shocks can help improve the effectiveness of plasma Gurney flap.
7) Plasma wing tip actuators are relatively too weak to provide sufficient force for aircraft at both cruising and takeoff/landing conditions. Therefore the combination of the two plasma concepts would not add much value for lift improvement beyond the use of the plasma Gurney flap alone.

The contributions of this project are:

1) Assessment of the predictive accuracy of CFD tools (ANSYS FLUENT with the plasma model by Lemire and Vo[74]) for two plasma actuation concepts for low AOA flight control.
2) First detailed measurement of the two plasma concepts and at higher flow velocity than before (up to 20 m/s instead of previous 16 m/s) with high plasma actuation strength (up to 90 mN/m instead of previous 40 mN/m).
3) First comparative assessment of the effectiveness between the two concepts.
4) First assessment of the sensitivity of angle of attack on two plasma concepts
5) First investigation of the two concepts on taper and swept wings.
6) First assessment of the two concepts on realistic wing geometries at flight conditions with the estimation of plasma actuation strength requirements.

Based on this research, the recommendations for future works include:

1) Carry out flow field measurement for plasma wing tip actuators. Use Stereo PIV to validate the plasma wing tip actuation effect on the tip vortex for wings with asymmetrical and symmetrical profiles.
2) Develop new plasma actuators with higher actuation strength. Look for new dielectric materials with higher breakdown voltage, lower cost, and better machinability. Develop faster and easier way to assemble plasma actuators with better insulation.

BIBLIOGRAPHY

1. Englar, R.J., Hemmerly, R.A., Taylor, D.W., Moore, W.H., Seredinsky, V., Valckenaere, W., and Jackson, J.A., *Design of the Circulation Control Wing STOL Demonstrator Aircraft.* Journal of Aircraft, 1981. **18**(1): p. 51-58.
2. Kaups, K. and Cebeci, T., *Compressible laminar boundary layers with suction on swept and tapered wings.* Journal of Aircraft, 1977. **14**(7): p. 661-667.
3. Amitay, M., Smith, D.R., Kibens, V., Parekh, D.E., and Glezer, A., *Aerodynamic flow control over an unconventional airfoil using synthetic jet actuators.* AIAA journal, 2001. **39**(3): p. 361-370.
4. Grosjean, C., Lee, G.B., Hong, W., Tai, Y.C., and Ho, C.M. *Micro balloon actuators for aerodynamic control*. in *Micro Electro Mechanical Systems, 1998. MEMS 98. Proceedings., The Eleventh Annual International Workshop on*. 1998.
5. Tai,Y.C.. *Aerodynamic control of a delta-wing using MEMS sensors and actuators*. in *Micromechatronics and Human Science, 1997. Proceedings of the 1997 International Symposium on*. 1997.
6. Boesch, G., Vo, H.D., Savard, B., Wanko-Tchatchouang, C., and Mureithi, N.W., *Flight Control Using Wing-Tip Plasma Actuation.* Journal of Aircraft, 2010. **47**(6): p. 1836-1846.
7. Enloe, C.L., McLaughlin, T.E., VanDyken, R.D., Kachner, K.D., Jumper, E.J., Corke, T.C., Post, M., and Haddad, O., *Mechanisms and responses of a single dielectric barrier plasma actuator: Geometric effects.* AIAA Journal, 2004. **42**(3): p. 595-604.
8. He, C., Corke, T.C., and Patel, M.P., *Plasma flaps and slats: an application of weakly ionized plasma actuators.* Journal of Aircraft, 2009. **46**(3): p. 864-873.
9. Huang, J., Corke, T.C., and Thomas, F.O., *Unsteady plasma actuators for separation control of low-pressure turbine blades.* Aiaa Journal, 2006. **44**(7): p. 1477-1487.
10. Grundmann, S. and Tropea, C., *Delay of Boundary-Layer Transition Using Plasma Actuators*, in *46th AIAA Aerospace Sciences Meeting and Exhibit*. 2008, AIAA-2008-1369.
11. Vo, H.D., *Control of Rotating Stall in Axial Compressors Using Plasma Actuators*, in *37th AIAA Fluid Dynamics Conference and Exhibit*. 2007, AIAA-2007-3845.

12. Ueno, S., *Investigation of a Plasma Gurney Flap for Lift Enhancement*. 2010, École Polytechnique de Montréal.
13. Coanda effect - Wikipedia. Updated on Dec 4, 2017, Accessed on Dec 30, 2017. Available from: https://en.wikipedia.org/wiki/Coand%C4%83_effect.
14. Novak, C., Cornelius, K., and Roads, R., *Experimental investigations of the circular wall jet on a circulation control airfoil*, in *25th AIAA Aerospace Sciences Meeting*. 1987, AIAA-87-0155.
15. Raspet, A., *Flight Measurements of Automatic Trailing Edge Suction on a Sailplane*. 1952, Mississippi State Coll Starkville Engineering Research Station, USA.
16. Hazen, D.C., R.F.Lehenert, T.E.Sweeney, and F.O.Ringleb, *Preliminary report on circulation control by means of trailing edge suction and the cusp effect*. 1953, Office of Naval Research, USA.
17. Zhang, P., Wang, J., and Feng, L., *Review of zero-net-mass-flux jet and its application in separation flow control.* Science in China Series E: Technological Sciences, 2008. **51**(9): p. 1315-1344.
18. Chatlynne, E., Rumigny, N., Amitay, M., and Glezer, A., *Virtual aero-shaping of a Clark-Y airfoil using synthetic jet actuators*, in *39th Aerospace Sciences Meeting and Exhibit*. 2001, AIAA-2001-0732.
19. Amitay, M., Horvath, M., Michaux, M., and Glezer, A., *Virtual aerodynamic shape modification at low angles of attack using synthetic jet actuators*, in *15th AIAA Computational Fluid Dynamics Conference*. 2001, AIAA-2001-31306.
20. Farnsworth, J.A.N., Vaccaro, J.C., and Amitay, M., *Active flow control at low angles of attack: stingray unmanned aerial vehicle.* AIAA Journal, 2008. **46**(10): p. 2530-2544.
21. Liebeck, R.H., *Design of Subsonic Airfoils for High Lift.* Journal of Aircraft, 1978. **15**(9): p. 547-561.
22. Neuhart, D. and Pendergraft, O., *A water tunnel study of Gurney flaps*, in *NASA Technical Memorandum 4071*. 1988.
23. Jeffrey, D., Zhang, X., and Hurst, D.W., *Aerodynamics of Gurney flaps on a single-element high-lift wing.* Journal of Aircraft, 2000. **37**(2): p. 295-301.
24. Storms, B.L. and Jang, C.S., *Lift Enhancement of an Airfoil Using a Gurney Flap and Vortex Generators.* Journal of Aircraft, 1994. **31**(3): p. 542-547.

25. Jang, C.S., Ross, J.C., and Cummings, R.M., *Numerical investigation of an airfoil with a Gurney flap.* Aircraft Design, 1998. **1**(2): p. 75-88.
26. Ross, J.C., Storms, B.L., and Carrannanto, P.G., *Lift-Enhancing Tabs on Multielement Airfoils.* Journal of Aircraft, 1995. **32**(3): p. 649-655.
27. Myose, R., Papadakis, M., and Heron, I., *Gurney flap experiments on airfoils, wings, and reflection plane model.* Journal of Aircraft, 1998. **35**(2): p. 206-211.
28. Gai, S.L. and Palfrey, R., *Influence of trailing-edge flow control on airfoil performance.* Journal of Aircraft, 2003. **40**(2): p. 332-337.
29. Matalanis, C.G. and Eaton, J.K., *Wake vortex control using static segmented Gurney flaps.* AIAA Journal, 2007. **45**(2): p. 321-328.
30. Lee, T., *PIV study of near-field tip vortex behind perforated Gurney flaps.* Experiments in Fluids, 2011. **50**(2): p. 351-361.
31. Lee, T. and Ko, L.S., *PIV investigation of flowfield behind perforated Gurney-type flaps.* Experiments in Fluids, 2009. **46**(6): p. 1005-1019.
32. Tang, D. and Dowell, E.H., *Aerodynamic loading for an airfoil with an oscillating gurney flap.* Journal of Aircraft, 2007. **44**(4): p. 1245-1257.
33. Gerontakos, P. and Lee, T., *Particle image velocimetry investigation of flow over unsteady airfoil with trailing-edge strip.* Experiments in Fluids, 2008. **44**(4): p. 539-556.
34. Kinzel, M.P., Maughmer, M.D., and Lesieutre, G.A., *Miniature trailing-edge effectors for rotorcraft performance enhancement.* Journal of the American Helicopter Society, 2007. **52**(2): p. 146-158.
35. Yeo, H.S., *Assessment of active controls for rotor performance enhancement.* Journal of the American Helicopter Society, 2008. **53**(2): p. 152-163.
36. Fuglsang, P., Bak, C., Gaunaa, M., and Antoniou, L., *Design and verification of the Riso-B1 airfoil family for wind turbines.* Journal of Solar Energy Engineering-Transactions of the Asme, 2004. **126**(4): p. 1002-1010.
37. Tongchitpakdee, C., Benjanirat, S., and Sankar, L.N., *Numerical studies of the effects of active and passive circulation enhancement concepts on wind turbine performance.* Journal of Solar Energy Engineering-Transactions of the ASME, 2006. **128**(4): p. 432-444.

38. Nakafuji, D.T.Y., van Dam, C.P., Smith, R.L., and Collins, S.D., *Active load control for airfoils using microtabs.* Journal of Solar Energy Engineering-Transactions of the ASME, 2001. **123**(4): p. 282-289.
39. Byerley, A.R., Stormer, O., Baughn, J.W., Simon, T.W., Van Treuren, K.W., and List, J., *Using Gurney flaps to control laminar separation on linear cascade blades.* Journal of Turbomachinery-Transactions of the ASME, 2003. **125**(1): p. 114-120.
40. Zhang, P.F., Liu, A.B., and Wang, J.J., *Aerodynamic Modification of NACA 0012 Airfoil by Trailing-Edge Plasma Gurney Flap.* AIAA Journal, 2009. **47**(10): p. 2467-2474.
41. Shyy, W., Jayaraman, B., and Andersson, A., *Modeling of glow discharge-induced fluid dynamics.* Journal of Applied Physics, 2002. **92**(11): p. 6434-6443.
42. Feng, L.H., Jukes, T.N., Choi, K.S., and Wang, J.J., *Flow control over a NACA 0012 airfoil using dielectric-barrier-discharge plasma actuator with a Gurney flap.* Experiments in Fluids, 2012. **52**(6): p. 1533-1546.
43. Feng, L.H., Shi, T.Y., and Liu, Y.G., *Lift Enhancement of an Airfoil and an Unmanned Aerial Vehicle by Plasma Gurney Flaps.* AIAA Journal, 2017. **55**(5): p. 1622-1632.
44. Dacles-Mariani, J., Zilliac, G.G., Chow, J.S., and Bradshaw, P., *Numerical/experimental study of a wingtip vortex in the near field.* AIAA Journal, 1995. **33**(9): p. 1561-1568.
45. Michele, R. Winglets|Aerospace Engineering. Accessed on 2017 Dec 29. Available from: http://www.aerospacengineering.net/?p=177.
46. Gudmundsson, S., *General Aviation Aircraft Design: Applied Methods and Procedures*. 2013: Elsevier Science.
47. Houghton, E.L. and Carpenter, P.W., *Aerodynamics for Engineering Students*. 2003: Elsevier Science.
48. Udris, A. This is How Winglets Work | Boldmethod. Updated onDec 23rd, 2017, Accessed on 2017 Dec 29th. Available from: http://www.boldmethod.com/learn-to-fly/aerodynamics/winglets-and-wingtip-vortices/.
49. Whitcomb, R.T., *A design approach and selected wind tunnel results at high subsonic speeds for wing-tip mounted winglets*, in *NASA Technical Note D-8260*. 1976.
50. Sohn, M.H. and Chang, J.W., *Visualization and PIV study of wing-tip vortices for three different tip configurations.* Aerospace Science and Technology, 2012. **16**(1): p. 40-46.

51. Ayers, R.F. and Wilde, M.R., *An Experimental Investigation of the Aerodynamic Characteristics of a Low Aspect Ratio Swept Wing with Blowing in a Spanwise Direction from the Tips*, in *College of Aeronautics Report, Note 57*. 1956: Cranfield, England, U.K.
52. Wu, J., Vakili, A., Shi, Z., and Mo, J., *Investigation of phenomena of discrete wingtip jets*. 1988, DTIC Document.
53. Schwind, R.G. and Briggs, M.M., *Effects of Blowing Spanwise from the Tips of Low-Aspect Ratio Wings of Varying Taper Ratio, with Application to Improving STOL Capability of Fighter Aircraft*. 1983: Defense Technical Information Center.
54. Mineck, R.E., *Study of Potential Aerodynamic Benefits from Spanwise Blowing at Wingtip*. 1995: National Aeronautics and Space Administration, Langley Research Center.
55. Tavella, D.A., Wood, N.J., Lee, C.S., and Roberts, L., *Lift modulation with lateral wing-tip blowing.* Journal of Aircraft, 1988. **25**(4): p. 311-316.
56. Margaris, P. and Gursul, I., *Vortex topology of wing tip blowing.* Aerospace Science and Technology, 2010. **14**(3): p. 143-160.
57. Heyes, A.L. and Smith, D.A.R., *Spatial perturbation of a wing-tip vortex using pulsed span-wise jets.* Experiments in Fluids, 2004. **37**(1): p. 120-127.
58. Okada, S. and Hiraoka, K., *Experimental Studies of Reduction of the Wing Tip Vortex by Suction*, in *21st AIAA Applied Aerodynamics Conference*. 2003, AIAA-2003-3533.
59. Margaris, P. and Gursul, I., *Wing tip vortex control using synthetic jets.* Aeronautical Journal, 2006. **110**(1112): p. 673-681.
60. Marouen, D., Mohsen, F., and Maher, B., *Control of Wing Tip Vortex Structure Using Fluidic Actuation*, in *7th AIAA Flow Control Conference*. 2014, AIAA-2014-2792.
61. Sudak, P.J., *Experimental Investigation of Active Wingtip Vortex Control Using Synthetic Jet Actuators*, in *Aerospace Engineering*. 2014, California Polytechnic State University.
62. Ramakumar, K. and Jacob, J.D., *Flow Control And Lift Enhancement Using Plasma Actuators*, in *35th Fluid Dynamics Conference*. 2005: Toronto, ON.
63. Santhanakrishnan, A., Pern, N.J., Ramakumar, K., Simpson, A., and Jacob, J.D., *Enabling Flow Control Technology for Low Speed UAVs*, in *AIAA Infotech@Aerospace*. 2005, AIAA-2005-6960.
64. Hasebe, H., Naka, Y., and Fukagata, K., *An Attempt for Suppression of Wing-Tip Vortex Using Plasma Actuators.* Journal of Fluid Science and Technology, 2011. **6**(6): p. 976-988.

65. Mizokami, T., Noguchi, D., and Fukagata, K. *Lift and drag control using dielectric barrier discharge plasma actuators installed on the wingtips*. in *21st AIAA Computational Fluid Dynamics Conference*. 2013. AIAA-2013-2456.

66. Leroy, A., Molton, P., Carpels, Y., and Pons, J., *Experimental studies of DBD actuator effects on wing tip vortex topology*, in *6th AIAA Flow Control Conference*. 2012, AIAA-2012-2951.

67. Chappell, S. and Angland, D., *Active Control of a Wing Tip Vortex with a Dielectric Barrier Discharge Plasma Actuator*, in *6th AIAA Flow Control Conference*. 2012, AIAA-2012-2952.

68. Pavon, S., Dorier, J.L., Hollenstein, C., Ott, P., and Leyland, P., *Effects of high-speed airflows on a surface dielectric barrier discharge.* Journal of Physics D-Applied Physics, 2007. **40**(6): p. 1733-1741.

69. Kriegseis, J., Grundmann, S., Tropea, C., *Airflow influence on the discharge performance of dielectric barrier discharge plasma actuators.* Physics of Plasmas, 2012. **19**(7): p. 073509.

70. Coumar, S. and Lago, V., *Influence of Mach number and static pressure on plasma flow control of supersonic and rarefied flows around a sharp flat plate.* Experiments in Fluids, 2017. **58**(6).

71. Duchmann, A., Simon, B., Tropea, C., and Grundmann, S., *Dielectric Barrier Discharge Plasma Actuators for In-Flight Transition Delay.* AIAA Journal, 2014. **52**(2): p. 358-367.

72. Suzen, Y. and Huang, P., *Simulations of flow separation control using plasma actuators*, in *44th AIAA Aerospace Sciences Meeting and Exhibit, Aerospace Sciences Meetings*. 2006, AIAA-2006-877.

73. Orlov, D.M., Corke, T.C., and Patel, M., *Electric circuit model for aerodynamic plasma actuator*, in *44th AIAA Aerospace Sciences Meeting and Exhibit, Aerospace Sciences Meetings*. 2006, AIAA-2006-1206.

74. Lemire, S. and Vo, H.D., *Reduction of fan and compressor wake defect using plasma actuation for tonal noise reduction.* Journal of Turbomachinery, 2011. **133**(1): p. 011017.

75. Palmeiro, D. and Lavoie, P., *Comparative analysis on single dielectric barrier discharge plasma actuator models*, in *7th International Symposium on Turbulence and Shear Flow Phenomena*. 2011: Ottawa, Canada.

76. Erm, L., Jones, M., and Henbest, S. *Boundary layer trip size selection on streamlined bodies of revolution*. in *18th Australian Fluids Mechanics Conference*. 2012. Launceston, Australia.

77. Xu, X., *Plasma Actuation for Boundary Layer Separation Control in Engine Ducts*. 2011, École Polytechnique de Montréal.

78. Demers, F., *Amélioration de l'Aérodynamisme des Ailes d'Avion par Actionnement Plasma*. 2015, École Polytechnique de Montréal.

79. Ahmed, M.R., Takasaki, T., and Kohama, Y., *Aerodynamics of a NACA4412 Airfoil in Ground Effect.* AIAA Journal, 2007. **45**(1): p. 37-47.

80. Whitmore, S.A., Lindsey, W.T., Curry, R.E., and Gilyard, G.B., *Experimental characterization of the effects of pneumatic tubing on unsteady pressure measurements*, in *NASA Technical Memorandum 4171*. 1990.

81. Martínez-Aranda, S., García-González, A., Parras, L., Velázquez-Navarro, J., and Del Pino, C., *Comparison of the Aerodynamic Characteristics of the NACA0012 Airfoil at Low-to-Moderate Reynolds Numbers for any Aspect Ratio.* International Journal of Aerospace Sciences, 2016. **4**(1): p. 1-8.

82. Patel, M.P., Ng, T.T., Vasudevan, S., Corke, T.C., and He, C., *Plasma actuators for hingeless aerodynamic control of an unmanned air vehicle.* Journal of Aircraft, 2007. **44**(4): p. 1264-1274.

83. Schmitt, V. and Charpin, F., *Pressure distributions on the ONERA-M6-Wing at transonic Mach numbers*, in *Experimental Database for Computer Program Assessment, Report of the Fluid Dynamics Panel Working Group 04, AGARD AR 138*. 1979.

84. Slater, J.W. ONERA M6 Wing: Study #1. Updated on August 30, 2002, Accessed on Sep 29, 2017. Available from: https://www.grc.nasa.gov/www/wind/valid/m6wing/m6wing01/m6wing01.html.

85. Lee, B., Kim, C., Kim, C., Rho, O., and Lee, K., *Parallelized design optimization for transonic wing using aerodynamic sensitivity analysis*, in *40th AIAA Aerospace Sciences Meeting & Exhibit, Aerospace Sciences Meetings*. 2002, AIAA-2006-264.

86. Nielsen, E.J. and Anderson, W.K., *Recent improvements in aerodynamic design optimization on unstructured meshes.* AIAA Journal, 2002. **40**(6): p. 1155-1163.

87. Le Moigne, A., *A discrete Navier-Stokes adjoint method for aerodynamic optimisation of Blended Wing-Body configurations*, in *School of Engineering*. 2002, University of Cranfield, UK.
88. Sadraey, M.H., *Aircraft Design: A Systems Engineering Approach*. Vol. 71. 2012: Wiley.
89. Brady, C. Boeing 737 Detailed Technical Data. Accessed on Nov 10, 2017. Available from: http://www.b737.org.uk/techspecsdetailed.htm.

APPENDIX A – WIND TUNNEL CHARACTERISATION

A.1 Experimental Setup

The experimental setup is shown in Figure A- 1. The hot wire, pitot-static tube and thermocouple were mounted on one steel rod, traversed in a cross section plane 5 inches from test section inlet, to measure flow turbulence intensity, velocity and temperature. The hot-wire system is a Dantec constant temperature anemometer, with single-sensor normal probe (55P11). The acquisition system consists of Dantec Dynamics Multichannel CTA 54N82, National Instruments PXI-4495 and PXI 1042, National Instruments PXI-8360 MXI Express Card, and National Instruments PXI-6229 M series Multifunction DAQ. A second pitot-static tube is placed 51 in from test section inlet, measuring downstream flow velocity. The two Pitot-static tubes are connected to two Huba Control pressure indicators (0~1600 Pa) with uncertainty of ± 2 Pa powered by NIPS-15 power supply, whose data can be acquired from computer through National Instruments SCB-68 A/D board. The flow temperature is measured by P795 Reference-Thermometer, with an accuracy of 0.01°C.

(a) (b)

Figure A- 1 Experimental setup

(1. Hot wire and Pitot-static tube; 2. Pitot-static tube; 3. Pressure indicator; 4. Traverse system; 5. Thermometer; 6. Acquisition system; 7. Laptop and LabView code.)

A.2 Calibration

The Dantec miniature wire-probe 55P11 is used with 4mm L-shaped supports 55H22 (overall length 235mm). Because of the dimension limitation, the hot wire and support are bonded on a 3ft-long steel rod (with a diameter of 1/8 in) to cover the cross section plane.

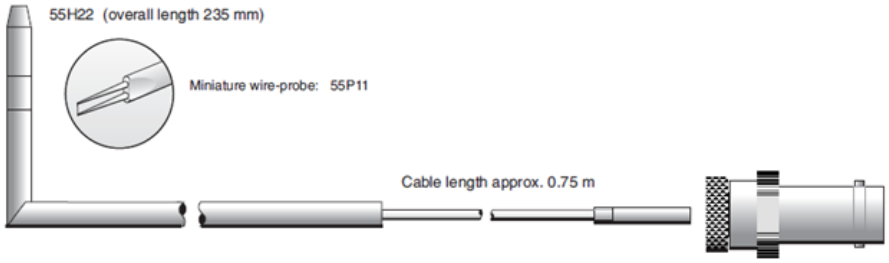

Figure A- 2 Hot wire schematic

Because of hot-wire reading is strongly affected by flow temperature, the reading (voltage E) need to be corrected using the Equation (A.1)

$$E_{corr} = E\left(\frac{T_w - T_0}{T_w - T}\right)^{0.5} \tag{A.1}$$

The hot wire sensor hot temperature $T_w = T_0 + a/\alpha$, where a is the overheating ratio (0.8 is commonly used), α is sensor temperature coefficient of resistance (0.36% for the selected probe) at refereence temperature T_0=20 ℃. Therefore T_w=242.22℃.

The measurement data are fitted by two method. The first one is to plot a power law curve E^2_{corr} vs U^n to fit King's Law

$$E^2_{corr} = A + B * U^n \tag{A.2}$$

where A, B is constant, and n=0.45. The second method is to plot U as a function of E_{corr} and create a 4th order polynomial trend line:

$$U = C_4 * E_{corr}^4 + C_3 * E_{corr}^3 + C_2 * E_{corr}^2 + C_1 * E_{corr} + C_0 \tag{A.3}$$

where C_4 = 19.886, C_3 = -121.33, C_2 = 312.34, C_1 = -375.39, C_0 =172.73

The results are compared on Figure A- 3 and Figure A- 4, and one can observe that the polynomial fit is more accurate than power law curve fit (King's law), therefore the later will be applied for the following study.

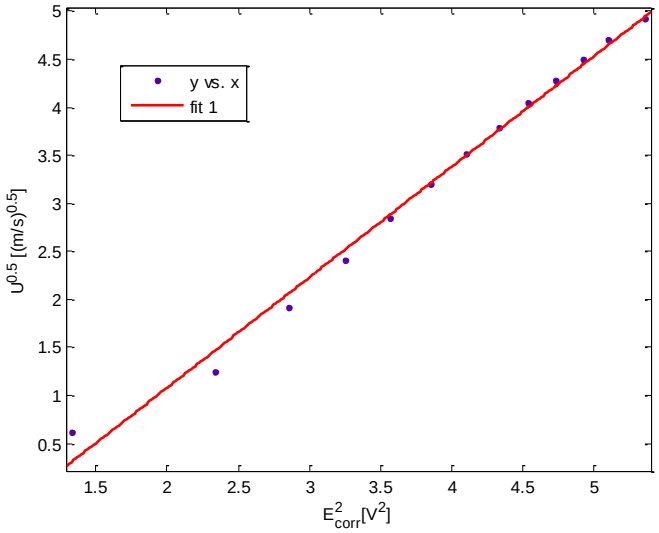

Figure A- 3 Power law curve fitting for hot wire reading (King's law)

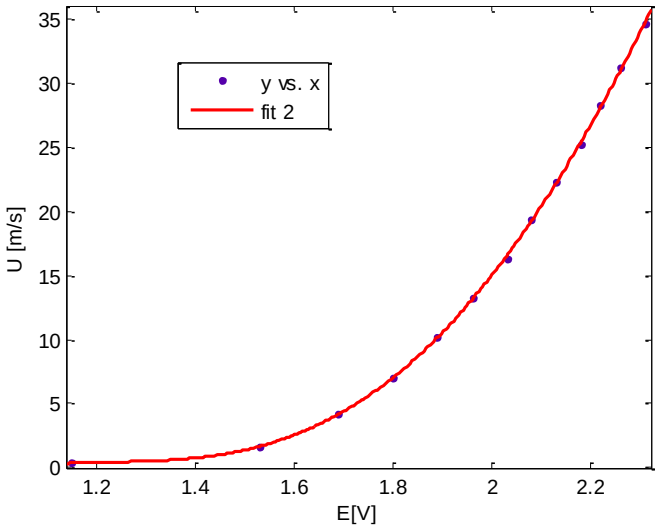

Figure A- 4 Polynomial curve fitting for hot wire reading

A.3 Response and Stability

The time response of hot wire and front Pitot - static tube velocities are first studied and can be seen in Figure A- 5**.** Both of them response quickly and the readings tend to be stable after 5 seconds. A sampling rate of 4 kHz and sampling time of more than 60 seconds per time are used for hot wire. The free stream and temperature time history during test are shown in Figure A- 6**.** The free

stream velocity remains stable during the test, with a fluctuation of about ±0.1 m/s. The flow temperature varies about ± 1 ℃ when the wind tunnel is turned on. Heat is generated from the motor and heat exchanger is used for cooling to reach the set temperature. Because of the delay in heat exchanger cooling, the temperature is fluctuating as shown in Figure A- 6.

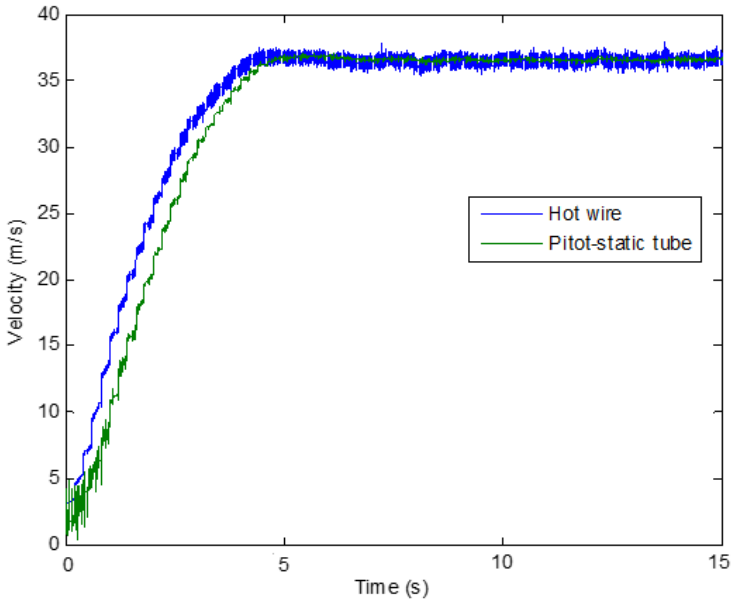

Figure A- 5 Time response of hot-wire and front Pitot - static tube

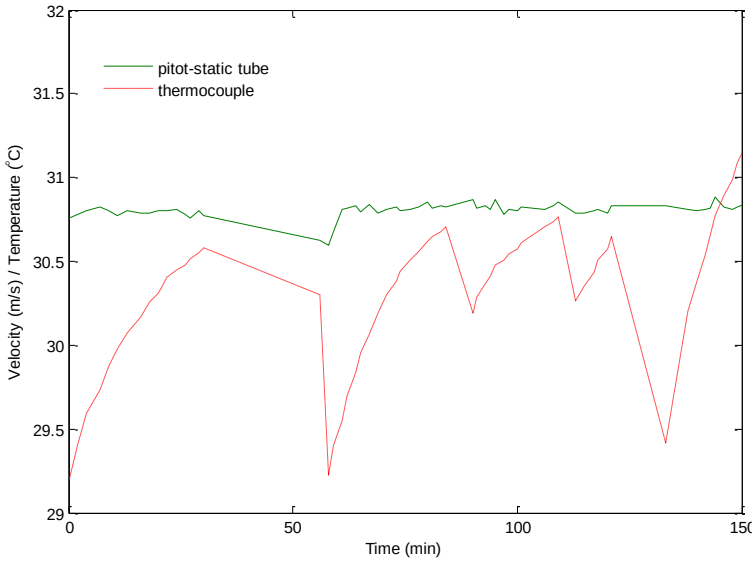

Figure A- 6 Free stream velocity and flow temperature time history

A.4 Turbulence

The hot wire is mounted on the traverse system to measure turbulence intensity distribution in cross section plane, as shown in Figure A- 7. The instantaneous fluctuating velocities in three directions is assumed to be the same $u' = v' = w'$, then the turbulence intensity in three dimensions can be obtained by measuring axial turbulence intensity *T*u. The origin X=0 Y=0 is defined as the center of cross section. The maximum distance in horizontal direction X and vertical direction Y are 16 in (406 mm), 12 in (305 mm) respectively. The traverse step is 2 in and in Figure A- 7 each intersection point corresponds to one measurement point. In order to have sufficient sample numbers, acquisition time for each point is at least 60 seconds (sampling rate 4 kHz). It takes 3~4 hours to complete the measurement of all points.

Experimental data can be analyzed using the following equations:

Mean Velocity $$U_{mean} = \sum_{i=1}^{N} \frac{U_i}{N} \quad \text{(A.4)}$$

Standard deviation of velocity $$\sigma = \sqrt{\sum_{i=1}^{N} \frac{(U_i - U_{mean})^2}{N-1}} \quad \text{(A.5)}$$

Turbulence intensity $$T_u = \sigma / U_{mean} \quad \text{(A.6)}$$

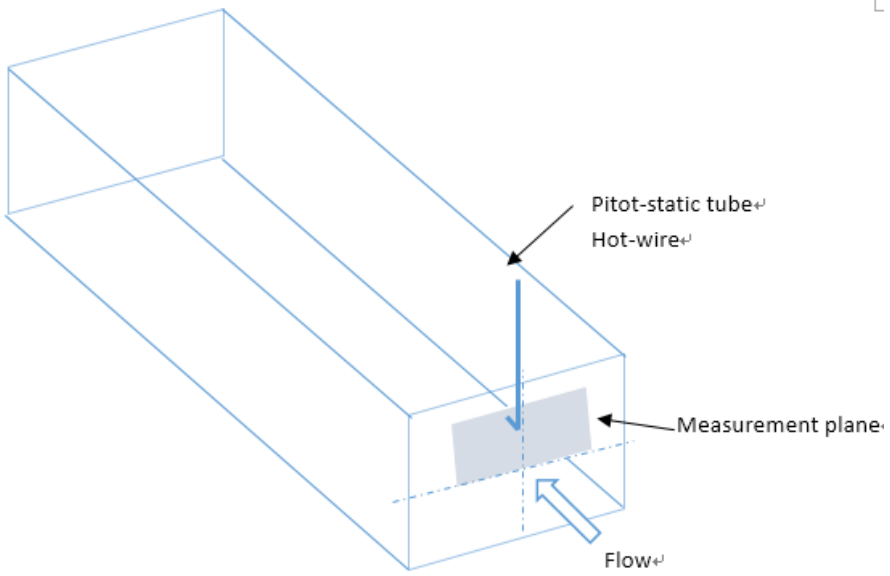

Figure A- 7 Hot wire measurement plane

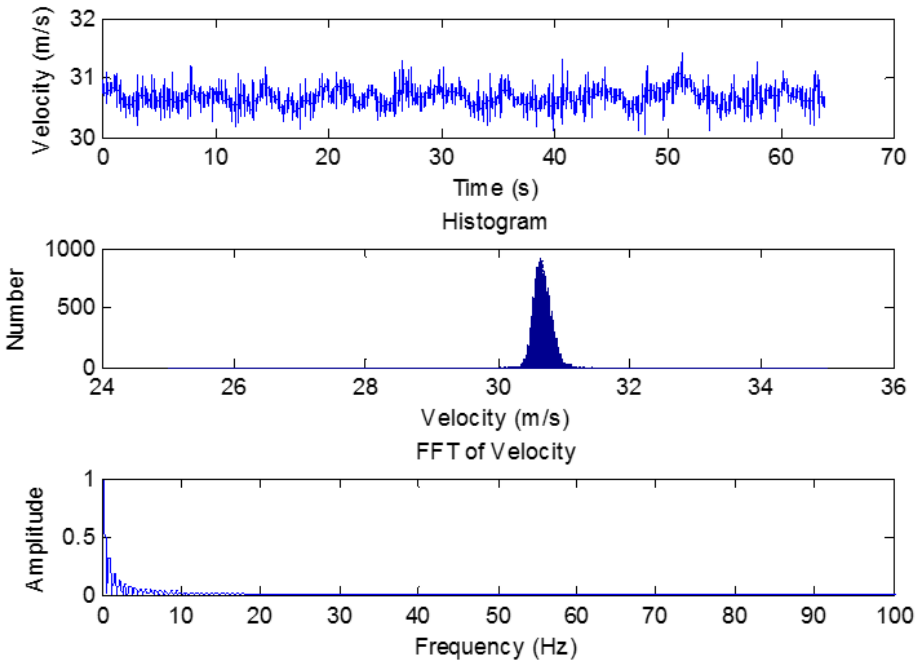

Figure A- 8 Velocity time history, histogram, and FFT result

Figure A- 8 shows the velocity time history, histogram and FFT results for one measurement point. As shown in Figure A- 8, most components of velocity signals occurs under 20 Hz, indicating there is not high frequency noise. The velocity and turbulence intensity distributions of the measurement plane are shown in Figure A- 9 and Figure A- 10. The velocity on the measurement plane has a variation of 0.2 m/s, or 0.67%, which indicates a good flow uniformity. Turbulence intensity distributes uniformly for most of the cross section, with a slightly higher value near top panel of test section, and the average turbulence intensity for the whole measurement plane is 0.44%. This turbulence intensity will be used in CFD simulation.

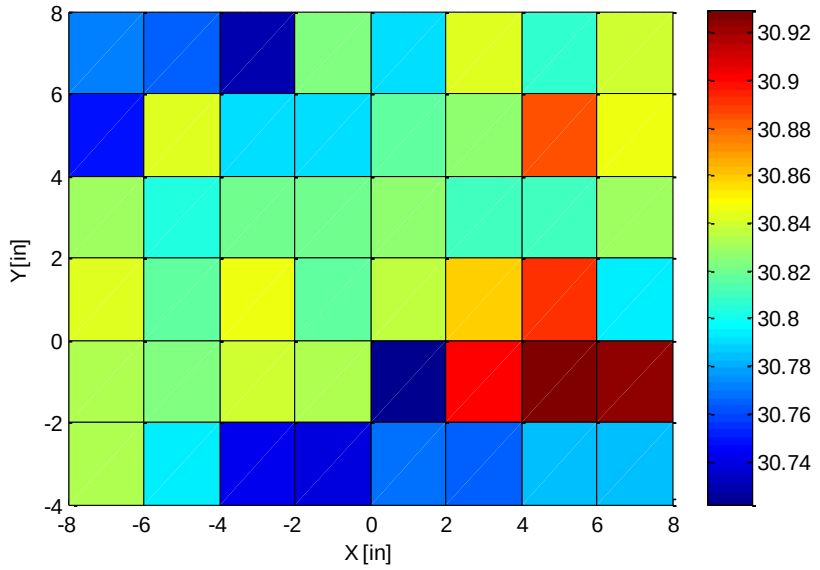

Figure A- 9 Velocity distribution of measurement plane

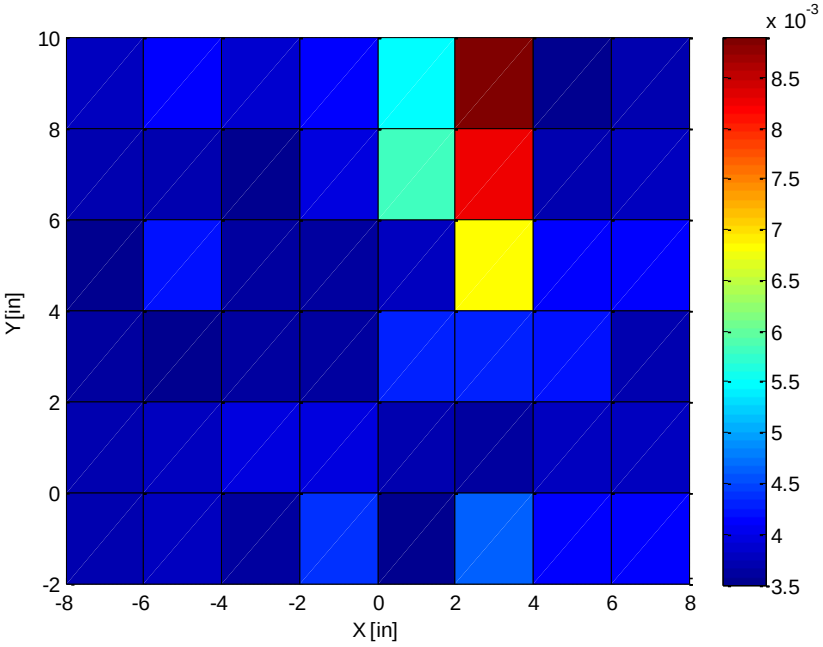

Figure A- 10 Turbulence intensity distribution of measurement plane

A.5 Boundary Layer Effect

Two pitot-static tubes are placed in the center of cross section to study the effect of boundary layer growth on the flow velocity. Aerodynamically, this effect is often evaluated by the displacement thickness of boundary layer δ^*,

$$\delta^* = \int_0^\infty (1 - \frac{U(y)}{U}) dy \tag{A.7}$$

For laminar flow in a flat plate,

$$\delta^* = 1.72/\sqrt{Re_x} \tag{A.8}$$

For turbulence flow in a flat plate,

$$\delta^* = 0.021/\sqrt[7]{Re_x} \tag{A.9}$$

where $Re_x = \rho U x/\mu$, x is the distance to the inlet, U is the free stream velocity, ρ and μ are flow density and viscosity, respectively. Because of the boundary layer growth, the flow is accerlated because cross section area of free stream flow is reduced to $(W - 2\delta^*)\text{^}2$. Considering mass conservation, for two pitot-static tubes, ideally

$$U_1 * (W - 2\delta_1^*)^2 = U_2 * (W - 2\delta_2^*)^2 \tag{A.10}$$

$$U_1/U_2 = \left((W - 2\delta_2^*)/(W - 2\delta_1^*)\right)^2 \tag{A.11}$$

where U_1 and U_2 represent upstream and downstream velocity, δ_1^* and δ_2^* upstream and downstream boundary layer displacement thickness. Upstream and downstream pitot static tube positions are x_1= 0.127m, x_2=1.257m. Flow density and viscosity are ρ =1.18 kg/m3, μ=1.8075e-5 kg-m/s^2. The measurement results U_1 /U_2 are compared with theoretical values $((W - 2\delta_2^*)/(W - 2\delta_1^*))^2$ in Table A-2, and show an average error of 0.71% between test data and predict results.

Table A - 1 Boundary effect under different velocities

f (Hz)	U_1 (m/s)	U_2 (m/s)	U_1 /U_2	$((W - 2\delta_2^*)/(W - 2\delta_1^*))^2$	Error
24.7	15.0308	15.3782	0.9774	0.9846	0.73%
32.8	19.9953	20.4536	0.9776	0.9849	0.74%
41.0	25.1174	25.715	0.9768	0.9851	0.85%
49.5	30.2195	30.8292	0.9802	0.9854	0.52%

APPENDIX B – WIND TUNNEL TEST

B.1 Balance Calibration

The force balance was calibrated by hanging known weights through a pulley at measured attached points and measuring the scale reading. Calibration for four different positions are performed (denoted by TEST 1, TEST 2, *etc* in Figure B-1), with at least three repeated cases for each position. The calibration shows that the measured moment M_2 has a linear relationship with applied moment M_1 as shown in equation (B.1)

$$M_2 = M_1 \times a \tag{B.1}$$

where M_2 and M_1 are in Nm, and $a = 0.969 \pm 0.005$.

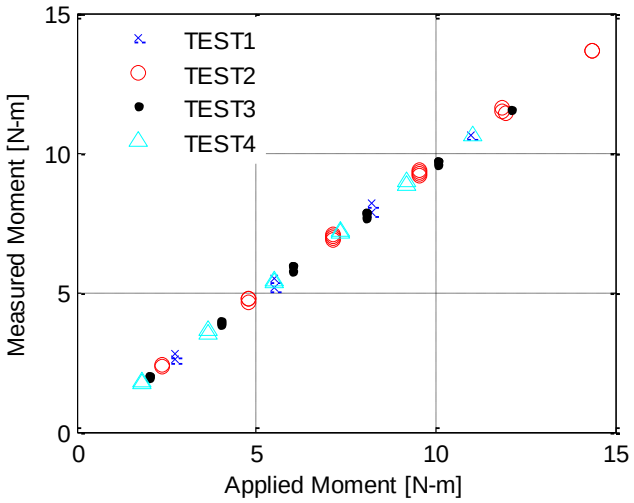

Figure B-1 Calibration results of L-shaped force balance

B.2 Test Procedure

Before Test

- Check wing surface to make sure surface is smooth.
- Test plasma actuators to make sure that they work properly without any spark.
- Check pressure ports by injecting water to find leakage or clogging.
- Lubricate pivot bearing to reduce friction.
- Connect plasma generating system, electronic scale, pressure scanner and PIV system.

- Run LabView program and Dynamic Studio v3.0 to acquire sample data.
- Make test plan and prepare test matrix.

On Site

- Install pitot-static tube, traverse and thermal couple.
- Record upstream velocity under different motor frequencies and obtain velocity vs frequency chart.
- Insert L-shaped box underneath test section. Use level to make sure balance arm inside the box is horizontal and perpendicular to flow direction.
- Install test wings and connect with plasma generating system.
- Run wind tunnel at different angels of attack at one constant velocity to find zero-lift angle of attack. Check/change angle of attack from the protractor inside test section. Tighten pipe connection to make sure angle doesn't change during test.
- Run wind tunnel at various velocities (8, 12, 15, 20 m/s) and designed angle of attack. Record scale reading, pressure data, temperature and humidity for cases without plasma actuation.
- Increase applied voltage for plasma actuators to desired values and record data.
- Install PIV cameras, laser and cooling pump. Carry out calibration using PIV targets.
- Turn on particle seeding generator and run wind tunnel at designed velocities and angles of attack. Record pictures using Dynamic Studio for cases with and without plasma actuation.

B.3 Test Data Error Analysis

The measurement of angle of attack has an uncertainty of ±0.25°, ambient temperature of ± 0.5℃, pressure of pressure scanner of 3.8 Pa, the relative humidity of 0.5% and ambient pressure of 67Pa. The density uncertainty is estimated by equation (B.2).

$$\delta\rho = \sqrt{\left(\frac{\partial \rho_{atm}}{\partial T}\delta T\right)^2 + \left(\frac{\partial \rho}{\partial HR}\delta HR\right)^2 + \left(\frac{\partial \rho}{\partial p}\delta p\right)^2}$$

$$\cong \sqrt{\left(M_d \frac{p}{RT^2}\delta T\right)^2 + \left((M_v - M_d)\frac{610.78}{RT}10^{\frac{7.5(T-273.15)}{T-35.15}}\delta HR\right)^2 + \left(M_d \frac{\delta p}{RT}\right)^2} \qquad \text{(B.2)}$$

For ambient temperature 293 – 303 K, ambient pressure 101325 Pa, density uncertainty is 0.006-0.009 kg/m^3.

Upstream velocity is calculated by equation (B.3) and its error is estimated by equation (B.3).

$$\delta U_\infty = \sqrt{\left(\frac{\partial U_\infty}{\partial \rho}\delta\rho\right)^2 + \left(\frac{\partial U_\infty}{\partial p_t}\delta p_t\right)^2 + \left(\frac{\partial U_\infty}{\partial p_s}\delta p_s\right)^2}$$

$$= \sqrt{\frac{p_t - p_s}{2\rho}\left(\frac{\delta\rho}{\rho}\right)^2 + \frac{1}{\rho(p_t - p_s)}(\delta p)^2} \quad \text{(B.3)}$$

Therefore, free stream velocities has uncertainties as shown in Table B-1.

Table B-1 Uncertainties of Free Stream Velocities

U_∞ [m/s]	8	12	15	20	30
δU_∞ [m/s]	0.56	0.38	0.30	0.23	0.15
$\delta U_\infty / U_\infty$	7.10%	3.20%	2.00%	1.10%	0.50%

The force balance is calibrated by increasing and decreasing known weights (whose weight range covers the expected force range from CFD predictions) at four different positions and at least three repeated cases for each applied weight. The balance reading would calculated by equation (B.4)

$$\bar{R}_c = \frac{R_{c1} + R_{c2} + R_{c3}}{3} \quad \text{(B.4)}$$

where R_{ci} is readings of three repeated cases (i=1, 2, 3), $\overline{\mathrm{R}}_c$ is the calibration averaged reading. Linear regression is performed between applied moment M_1 and measured moment M_2, which are calculated by equation (B.5) and (B.6)

$$M_1 = mgL_1 \quad \text{(B.5)}$$

$$M_2 = \overline{\mathrm{R}}_c g L_2 \quad \text{(B.6)}$$

where g=9.8 N/kg, L_1 is the distance from applied calibration position to pivot. L_2 is the horizontal arm of force balance (from pivot to the pin on the scale, as shown in Figure 3-20) with a length of 0.425$\pm$0.005m.

The applied moment and measured moment is linear fitting by least square method, with the intercept equal to zero. Therefore, we would need to find the best slope "a" value for the equation $y=ax$ to fit all experiment data, which is obtained by equation (B.7),

$$a = \frac{\sum_{i=1}^{n} x_i y_i}{\sum_{i=1}^{n} x_i^2} \quad \text{(B.7)}$$

And the slope error is calculated by equation (B.8).

$$\delta a = \frac{\sqrt{\sum_{i=1}^{n} x_i^2}}{\sum_{i=1}^{n} x_i^2}\sqrt{\frac{\sum_{i=1}^{n}(y_i - a x_i)^2}{n-1}} \quad \text{(B.8)}$$

where (x_i, y_i) is experimental data (applied moment and measured moment, respectively) for each test case. The final curve fitting slope between applied moment and measured moment is the averaged value of slopes of all four positions.

When wind tunnel is on, the force balance reading is fluctuating and therefore the mean balance reading $\overline{R}$ is obtained by averaging data over at least 30 seconds (maximum acquisition frequency is 6Hz).

$$\bar{R} = \frac{(\bar{R}_1 - R_{1,offset}) + (\bar{R}_2 - R_{2,offset}) + (\bar{R}_3 - R_{3,offset})}{3} \tag{B.9}$$

where $R_{i,offset}$ (i=1,2,3) is reading offset with wind tunnel off for each test case. The error of balance reading comes from the instrument accuracy (i.e. 0.5g) and the fluctuation of reading (time-varying error). The averaged moment would be calculated by equation (B.10)

$$\bar{M}_2 = \bar{R} L_2 \tag{B.10}$$

L_2 has a length of 0.428$\pm$0.005m during wind tunnel testing. The averaged moment by wing lift is

$$\bar{M}_1 = \frac{\bar{M}_2}{a} = \frac{\bar{R} L_2}{a} \tag{B.11}$$

The relative error of moment is

$$\frac{\delta \bar{M}_1}{\bar{M}_1} = \sqrt{\left(\frac{\delta \bar{M}_2}{\bar{M}_2}\right)^2 + \left(\frac{\delta a}{a}\right)^2} = \sqrt{\left(\frac{\delta \bar{R}}{\bar{R}}\right)^2 + \left(\frac{\delta L_2}{L_2}\right)^2 + \left(\frac{\delta a}{a}\right)^2} \tag{B.12}$$

The moment difference by plasma actuation and its error are then calculated by equation (B.13) and (B.14)

$$\Delta \bar{M}_1 = \bar{M}_{1,plasma} - \bar{M}_1 \tag{B.13}$$

$$\delta(\Delta \bar{M}_1) = \sqrt{\left(\delta \bar{M}_{1,plasma}\right)^2 + (\delta \bar{M}_1)^2} \tag{B.14}$$

APPENDIX C – PLASMA CHRACTERLISATION

C.1 Experimental Setup

The plasma generation system is designed and built by Xu [77], which consists of signal generator, power amplifiers, resistor module and transformers (see Figure C-1 and Figure C-2) and has been successfully used in previous projects.

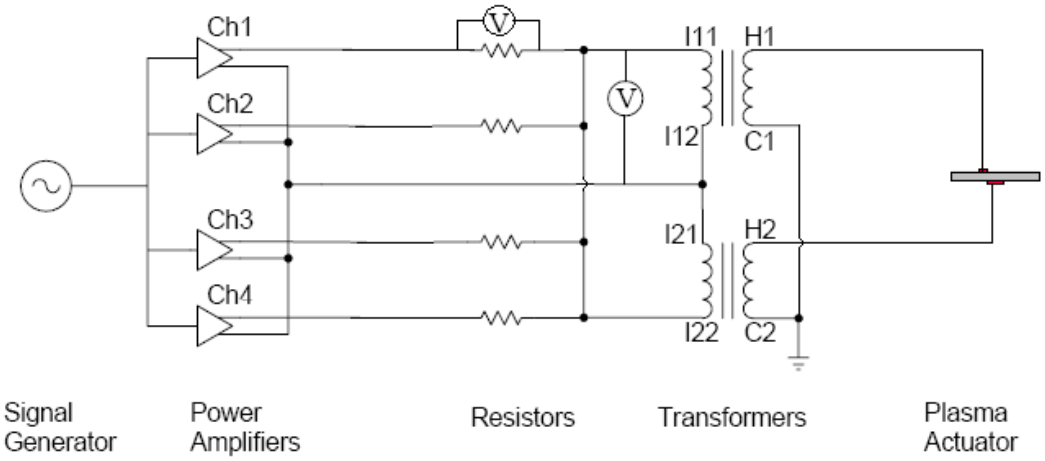

Figure C-1 A schematic diagram of plasma generation system

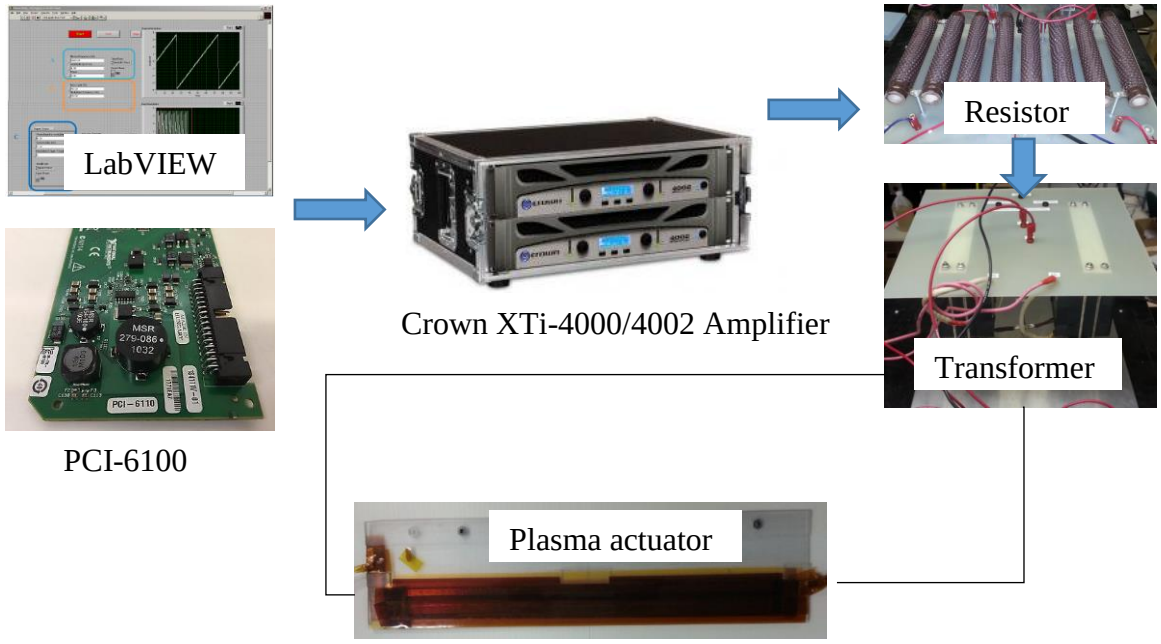

Figure C-2 Plasma generation system

The AC signal is generated by NI-DAQ card PCI-6100 and LabVIEW code as shown in Figure C-3. The signal is then sent to two Crown XTi-4000/4002 Power Amplifiers to magnify its power output to various levels. The Resistor Module consists of four ballast resistors (2 ohms, 300W), corresponding to the four channels of power amplifiers. The amplified voltage is then fed through the resistor module and connected to two transformers which has a winding ratio of 1:360, working frequency of 0.9-5 kHz and maximum output of 25 kVrms. As shown in the schematic diagram of Figure C-1, the primary coils of the transformers are connected in parallel but in the opposite polarity, with the low potential output of the secondary coils is connected to ground. The high voltage of hidden and exposed electrodes are taken from the two high potential leads of the transformers so that the effective winding ratio of this system is 1:720. Two multimeters have been used to measure the voltage and current as shown in the schematic diagram. To avoid high voltage and small current, both of them are placed before the transformer, with one measuring voltage between I11 and I12 , the other measuring voltage drop through one resistor to obtain current.

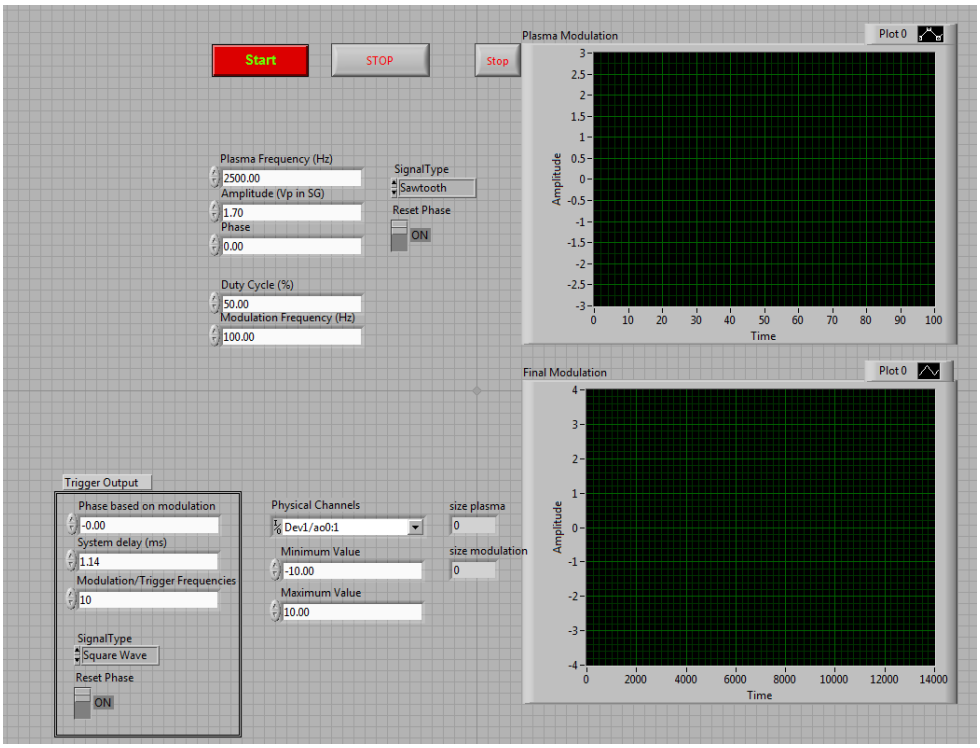

Figure C-3 LabVIEW program front panel

C.2 Experimental Results

The negative saw tooth waveform is used for input voltage because it can produce higher body force at the same voltage [77]. The effect of signal frequency on the plasma actuation strength is shown in Figure C-4 for plasma Gurney flap of NACA0012 wing. It can be observed that the thrust increases at higher voltage with higher frequency and 100 mN/m thrust can be achieved at a lower voltage with a higher frequency, for example 48 kV at 3.75 kHz. However, with high frequency, the consumed power are too much to have a stable output voltage because the amplifiers have self-protection circuits and thus would clip the output voltages. Therefore, frequency of 3 kHz is chosen in present test.

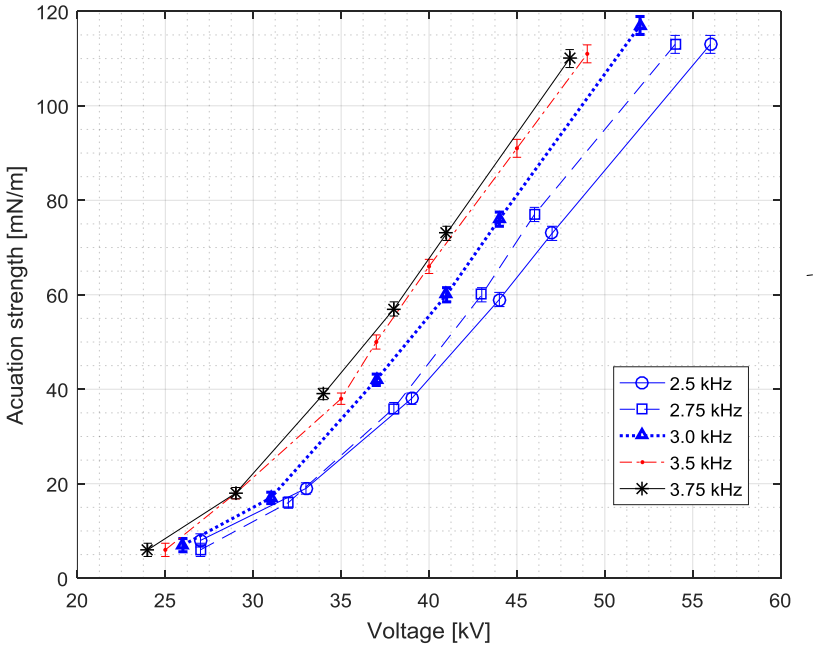

Figure C-4 Actuation strength of plasma Gurney flap on wing NG at various signal frequencies

Figure C-5 shows actuation strength of plasma Gurney flap on suction side (S.S.) and pressure side (P.S.) of wing AG under different input peak-peak voltages. Figure C-6 and Figure C-7 present the same data for plasma wing tip actuators on AT and NT wings under different input peak-peak voltages. Because of the limited space inside wing tip, hidden electrodes, exposed electrodes and high voltages wires are much easier to have sparks than plasma Gurney flap actuators. Good insulation is crucial for plasma wing tip actuators, especially near trailing edge where hidden electrodes are very close to exposed ones.

In the wind tunnel experimental tests, the measured peak-peak voltages by multimeter for plasma Gurney flap are about 42 and 46 kV, for wing tip actuators about 46 and 53 kV. Plasma actuators at lower peak-peak voltage are more stable because higher voltage tends to be clipped by the amplifiers. Moreover, higher voltage is more likely to damage the dielectric materials. Therefore, most test are carried out at 42 and 46 kV for plasma Gurney flap and plasma wing tip actuator, respectively. The plasma actuation strength is estimated from Figure C-4 to Figure C-7.

The averaged plasma actuation strength of NG wing is 60±5 mN/m, AG wing 55±5 mN/m, NT 80±10 mN/m, AT 65±5 mN/m. Several cases are tested at 53 kV for AT wing with an actuation strength of 90±5 mN/m.

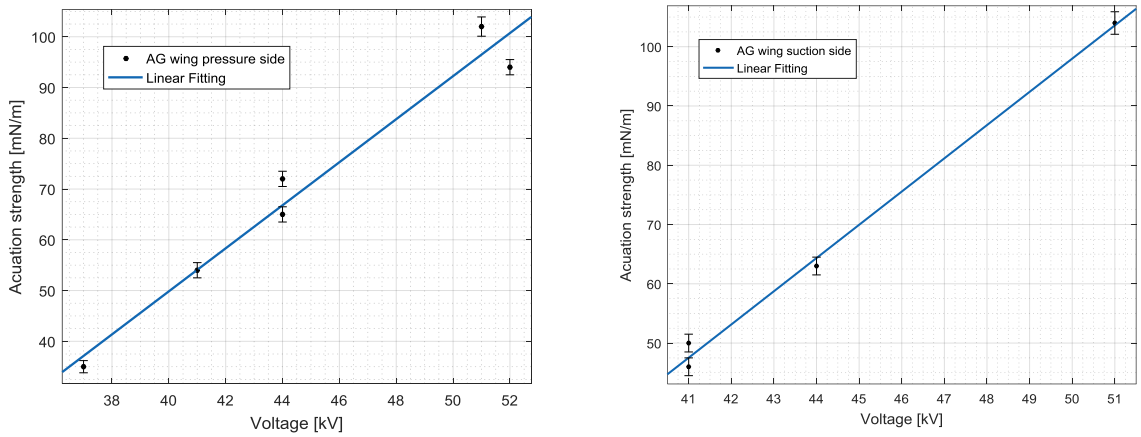

Figure C-5 Actuation strength of plasma Gurney flap on wing AG *vs* peak-peak voltage

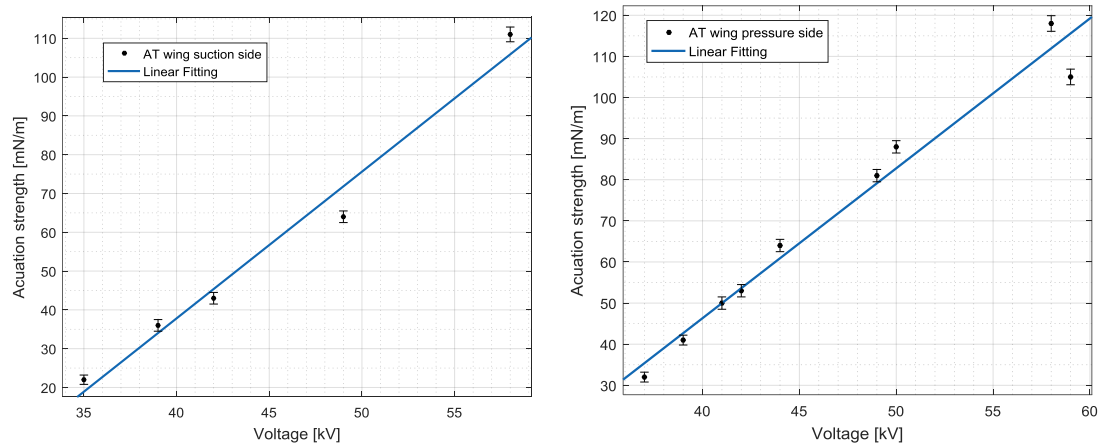

Figure C-6 Actuation strength of plasma wing tip actuation on wing AT *vs* peak-peak voltage

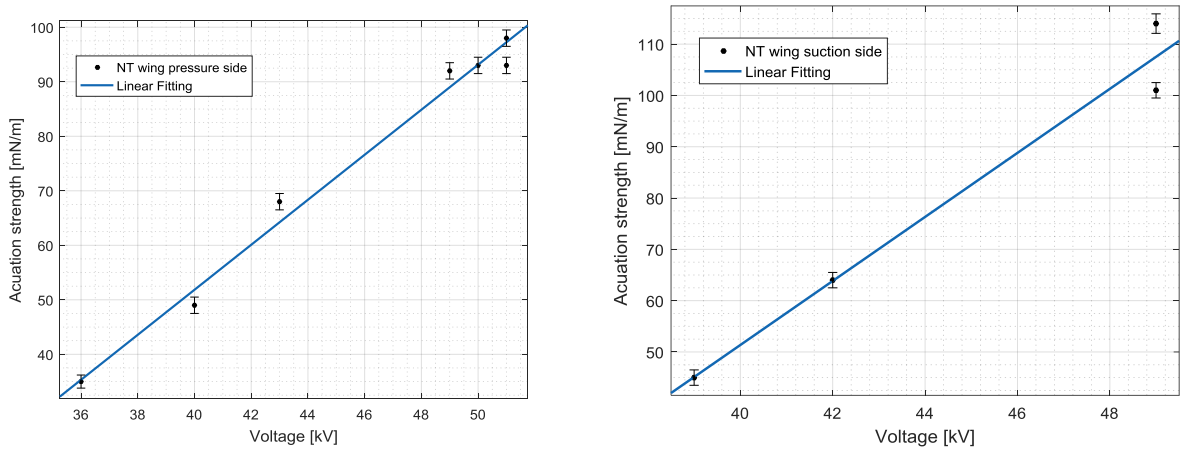

Figure C-7 Actuation strength of plasma wing tip actuation on wing NT *vs* peak-peak voltage

APPENDIX D – MESH STUDY

D.1 Mesh Study for Wings with Endplates

Figure D-1 shows the mesh study results for the AG wing. The force coefficients achieve a plateau when the mesh size increase from 2,007,040 to 4,501,504. Therefore, the mesh size for the AG wing is chosen as 2,838,528. Meshes of the NG wing have similar mesh structures and distributions.

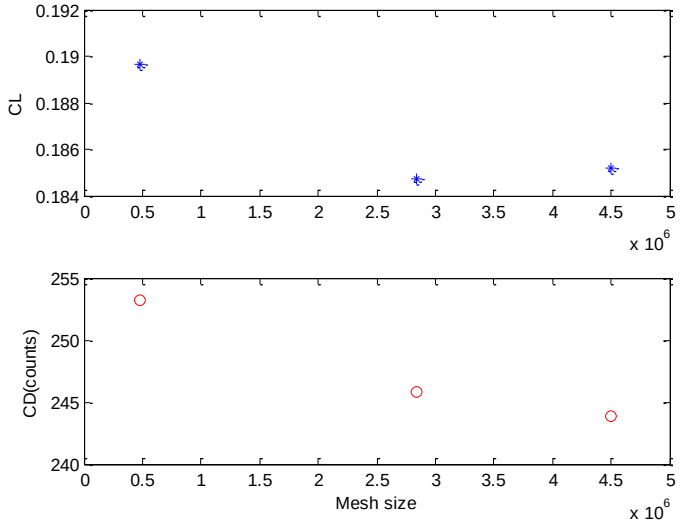

Figure D- 1 Mesh study for AG wing

D.2 Mesh Study for Wings with Wing Tips

Figure D-2 shows the mesh study results for the AT wing. With the mesh size increasing from 5×10^5 to 3.6×10^6, lift coefficient and drag coefficient reach a plateau. To ensure the mesh density for plasma actuator near wing tip, the mesh size for the AT wing is selected as 2,087,478. Meshes of the NT wing have similar mesh structures and distributions.

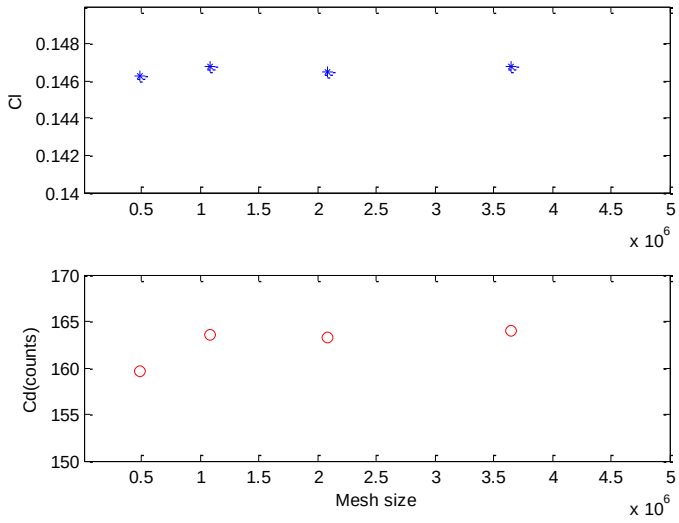

Figure D- 2 Mesh study for AT wing

D.3 Mesh Study for Tapered Wing

Figure D-3 presents the mesh study for the tapered wing ATtap. When the mesh size increases from 1,141,148 to 4,313,444, lift coefficients and drag coefficients converge and therefore the best mesh size would be 2,312,220.

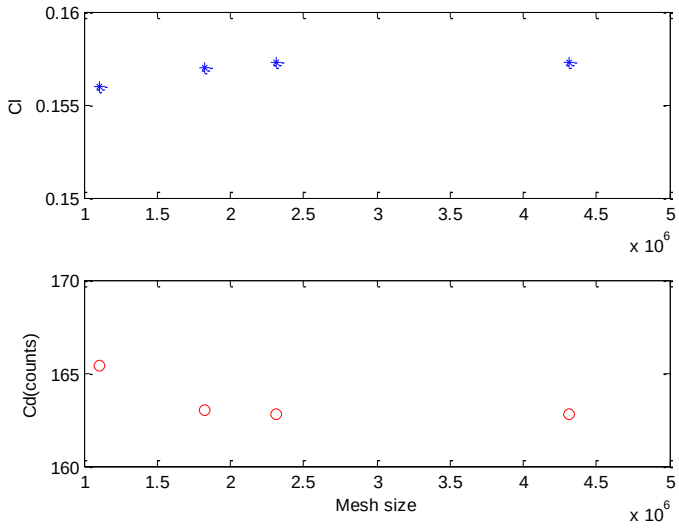

Figure D- 3 Mesh study for tapered wing

D.4 Mesh Study for ONERA M6 Wing

Figure D-4 presents the mesh study for M6 wing. Lift coefficient and drag coefficient have smaller variations when the mesh size is larger than about 1.6 million. Considering mesh density for plasma actuation, the mesh size is chosen as 2,234,988. The M6t and M6w wings have the same mesh as the M6 wing.

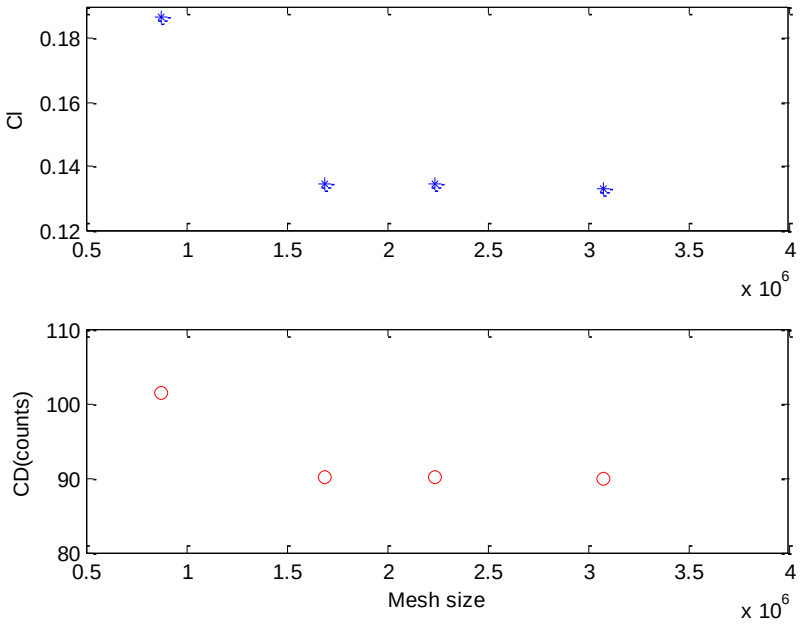

Figure D- 4 Mesh study for ONERA M6 mesh

APPENDIX E – CFD RESULTS WITH TRANSITION SST MODEL

The full turbulence models Spalart-Allmaras and SST model are chosen for simulations to compare with wind tunnel experimental results in the content. But it is not sure how effective tripping wires are and therefore transition SST model is also used for simulation. Transition SST model (also known as the gama-theta model) is based on the coupling of the SST transport equations with two other transport equations, one for the intermittency and one for the transition onset criteria, in terms of momentum-thickness Reynolds number. Proper mesh refinement and specification of inlet turbulence levels is crucial in this model.

To achieve good convergence, transition SST model is calculated with 3D unsteady pressure-based coupled solver. The spatial discretization and under relaxation factor can refer to the solver setting for fully turbulence models. CFD simulations with transition SST model are carried out for the two plasma concepts with various plasma actuation strength at different velocities and angles of attack. The results would compared with other turbulence models as well as experimental data in flowing parts.

Figure E- 1 presents the measured moments (TEST) versus the CFD predictions from FLUENT using different turbulence models for AG and AT wings (AOA = 0°), respectively. Figure E- 2 present the same data for AG and AT wings at AOA = 3°. It can be observed that transition SST model generally performs worse than SST and SA models, except for AT wing at AOA = 0°.

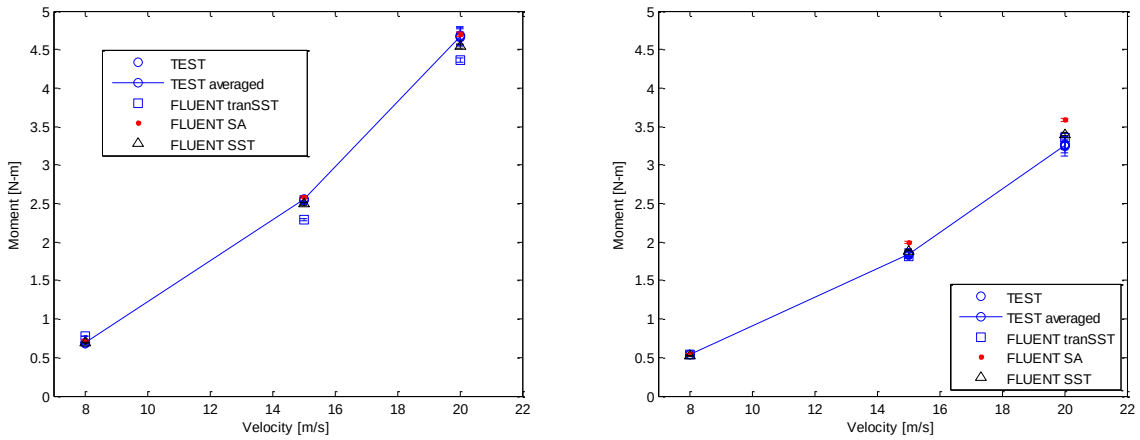

Figure E- 1 Moments of TEST and CFD for AG (left) and AT (right) wings at AOA = 0°

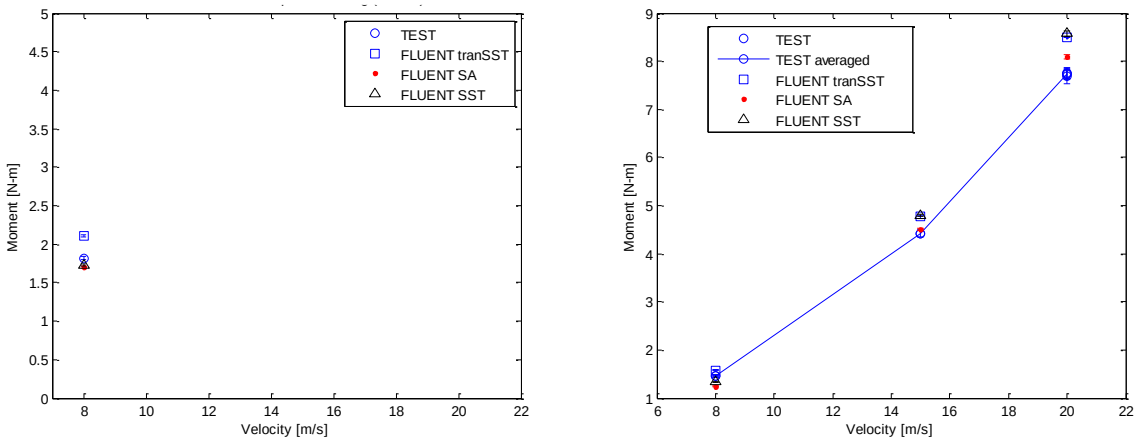

Figure E- 2 Moments of TEST and CFD for AG (left) and AT (right) wings at AOA = 3°

Figure E- 3 presents change in measured lift moment due to the plasma Gurney flap for the AG wing at AOA = 0° and 3° versus the correspondent CFD simulation with different turbulence models. Figure E- 4 the same data for NG wing at AOA = 0°. It can be observed that transition SST model fails to predict correctly the effect of plasma Gurney flap for both symmetrical and asymmetrical wings.

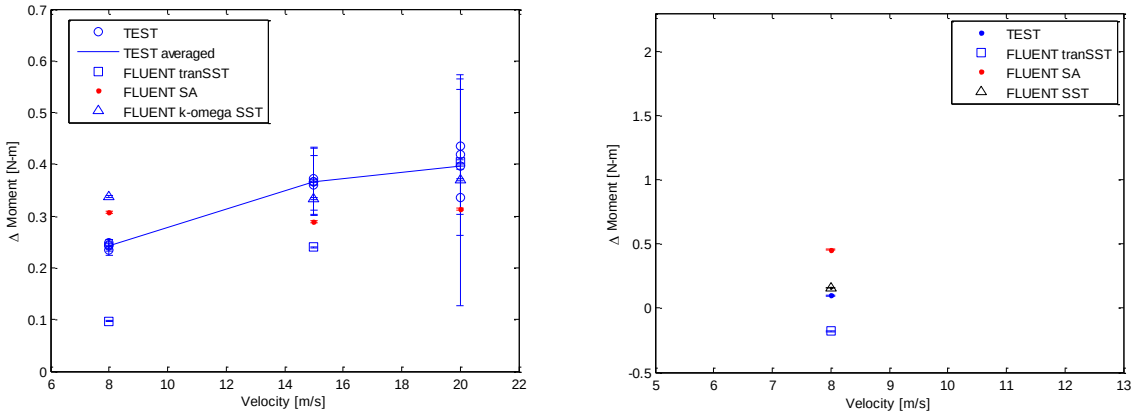

Figure E- 3 Effect of plasma Gurney flap on AG wing at AOA = 0° (left) and 3° (right)

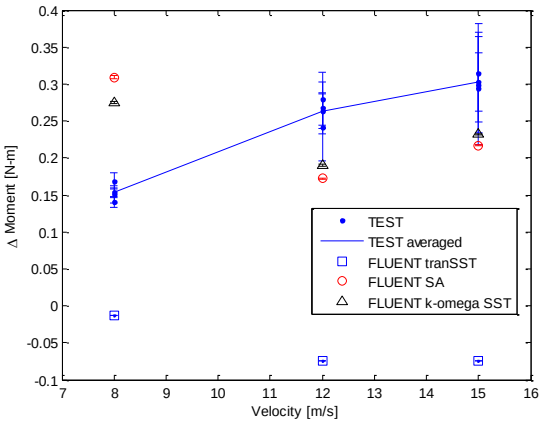

Figure E- 4 Effect of plasma Gurney flap on NG wing (AOA = 0°)

Figure E- 5 and Figure E- 6 present the measured change in lift moment due to the wing tip actuation for AT wing versus corresponding CFD simulations with three turbulence models at AOA = 0° and AOA = 3°. Figure E- 7 shows the same data for NG wing with plasma wing tip actuator at AOA = 0°. It can be observed that transition SST model provide good prediction for AT and NT wings at 12 – 20 m/s, similar as simulation results with the other two models. But it is unlikely to conclude which one is better due to the high error at the velocity ranges.

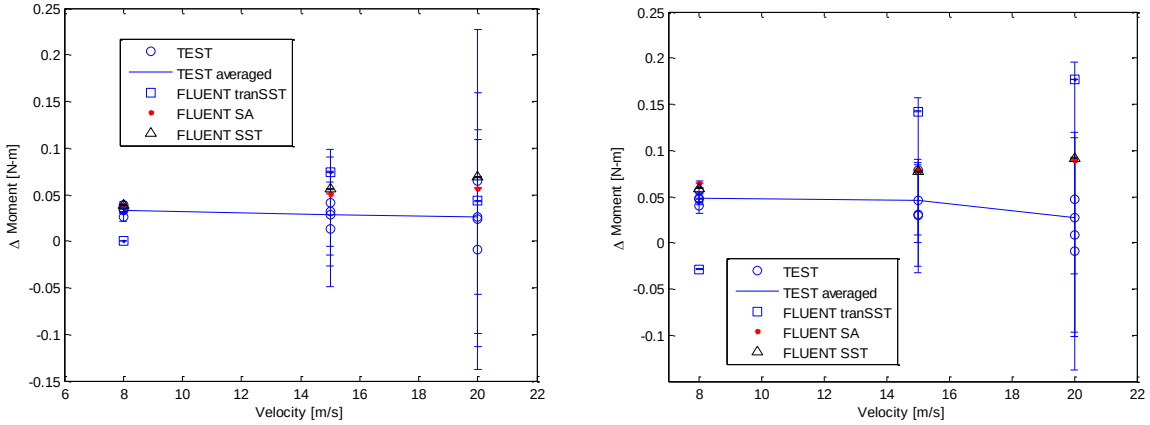

Figure E- 5 Effect of wing tip actuation on lift moment for AT wing at AOA = 0°, F_B =65 (left) and 90 (right) mN/m

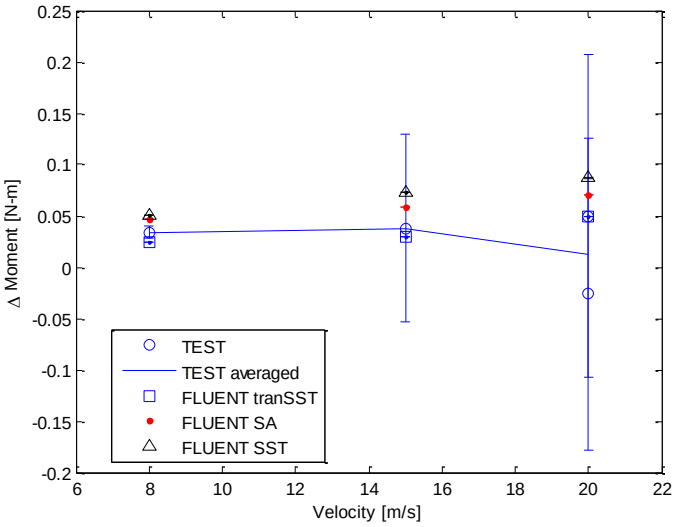

Figure E- 6 Effect of wing tip actuation on lift moment for AT wing (AOA = 3°, F_B = 65 mN/m)

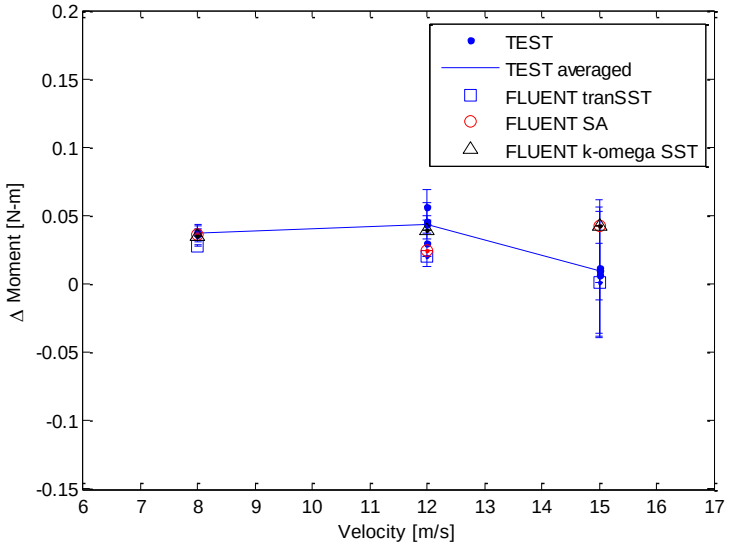

Figure E- 7 Effect of wing tip actuation on lift moment for NT wing (AOA = 0°, F_B =80 mN/m)

Finally, transition SST model is not recommended for simulating plasma Gurney flap. It may provide adequate results for wing tip actuator for certain wings, but the other models (SST and SA) can provide good predictions for most cases. Therefore, it would be a better choice to use SST or SA turbulence model to simulate the plasma Gurney flap and plasma wing tip actuator.

APPENDIX F – PLASMA IMPLEMENTATION

The plasma model developed by Lemire and Vo and its implementation into CFD mesh are described in detailed in Ref. [74]. The plasma model provide spatial average body force distribution on a very fine Cartesian mesh. The desired actuation strength for CFD simulations is obtained by multiply the force vector from plasma model by a scale factor.

In the plasma implementation code for this thesis, each 2D mesh from a cut plane covering the plasma actuator region is converted into a Cartesian mesh through rotation and unbending while keeping the total mesh area constant, as shown in Figure F-1(a). Then the spatial body force distribution from plasma model on the fine actuator mesh is superposed on the converted (coarser)

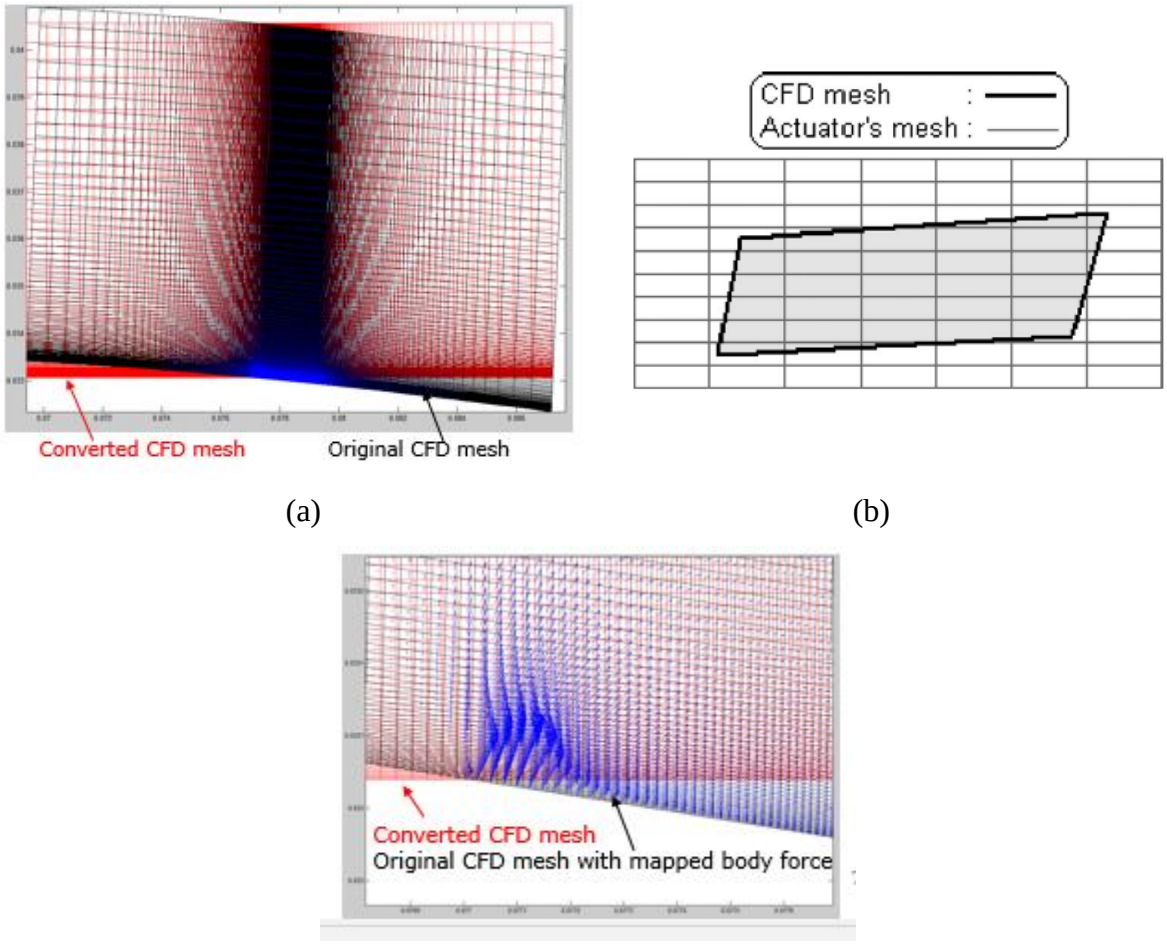

(a) (b)

(c)

Figure F-1 (a) Mesh rotation and unbending for plasma actuator region (b) Mesh superposition [74] (c) mapped body force distribution for original CFD mesh

CFD mesh and the body force distribution is mapped onto the converted CFD mesh. The mapping method is illustrated in Figure F-1(b) and based on the method in reference [74]. The body force associated with each cell in the CFD mesh is obtained by adding the body force from the each actuator cell within the CFD cell boundaries modulated by the proportion of its area that is contained in the CFD cell. The obtained force vectors are mapped back to original CFD mesh cells to obtain plasma body force distribution for original CFD mesh as shown in Figure F-1 (c).

APPENDIX G – ESTIMATION OF LIFT/MOMENT REQUIREMENT FOR BOEING 737

This part would estimate the lift/moment coefficients for traditional ailerons and horizontal tails on a commercial jet Boeing 737 based on the aircraft design calculation [88]. According to open data of Boeing 737[89], the wing has a root chord of 8 m, span of 30 m, aspect ratio of 8 -10, taper ratio of 0.25, 1/4 chord sweep angle of 25°, and twist angle of -1.1°. The horizontal tails have a root chord of 2.5 m, span of 10-14 m, aspect ratio of 4 - 6, taper ratio of 0.2 - 0.26, 1/4 chord sweep angle of 30°. Boeing 737 weight is W = 44000 - 77000 kg, wing planform area S=110 m^2, wing span b=30 m, wing sectional lift curve slope $C_{L_{\alpha_w}}$ = 4.5 rad^{-1}.

Wing lift coefficient is calculated by equation (F.1)

$$\mathrm{C}_L = \frac{2Wg}{\rho U_\infty^2 s} \tag{G.1}$$

So C_L is about 0.31 for cruise speed Mach = 0.84, about 0.85 for landing/takeoff speed Mach =0.3. The wing-fuselage pitching moment coefficient is determined by

$$C_{m_{owf}} = C_{m_{af}} \frac{AR\, cos^2(\Lambda)}{AR+2\cos(\Lambda)} + 0.01\alpha_t \tag{G.2}$$

Assuming Boeing 737 using NACA632-615 airfoil for wing profile, $C_{m_{af}}$= - 0.11. AR is 8-10, sweep angle Λ=25°, twist angle α_t= - 1.1°. Then $C_{m_{owf}}$ can be estimated as - 0.0885.

For the horizontal tail, the lift coefficient can be obtained by

$$\mathrm{C}_L = \frac{C_{m_{owf}} + \mathrm{C}_L(h-h_0)}{\overline{V_H}} \tag{G.3}$$

$\overline{V_H}$ is horizontal tail volume coefficient, typically 0.80 -1. The center of gravity of Boeing 737 is 18% MAC (mean aerodynamic chord), the aerodynamic center is assume to be 23% MAC, therefore h=0.18, h_0=0.23. Therefore, the lift coefficient for horizontal tail of Boeing 737 can be estimated about -0.12 for Mach number of 0.84, -0.15 for Mach number of 0.3.

The rolling moment coefficient derivative $\mathrm{C}_{l_{\delta_A}}$ for aileron can be calculated by

$$\mathrm{C}_{l_{\delta_A}} = \frac{2C_{L_{\alpha_w}} \tau C_r}{Sb} \int_{y_i}^{y_0} \left(\frac{y^2}{2} + \frac{2}{3} y^3 \left(\frac{\lambda - 1}{b} \right) \right) dy \tag{G.4}$$

For Boeing 737, wing root chord C_r=8, aileron angle of attack effectiveness parameter τ=0.4, the inboard and outboard position of aileron are selected as y_i=0.35b and y_0=0.5b, Therefore the $C_{l_{\delta_A}}$

can be estimated as 0.23 rad^{-1}. With a maximum defection of 10° for aileron, the maximum moment coefficient can increase to 0.04.

Finally, the rolling moment coefficient for aircraft wings is about 0.04 with a maximum aileron deflection of 10 deg. The lift coefficients for horizontal tails are about 0.12 for cruising speed, and 0.15 for landing/takeoff speed.